A single electron in a Bose-Einstein condensate

Jonathan B. Balewski

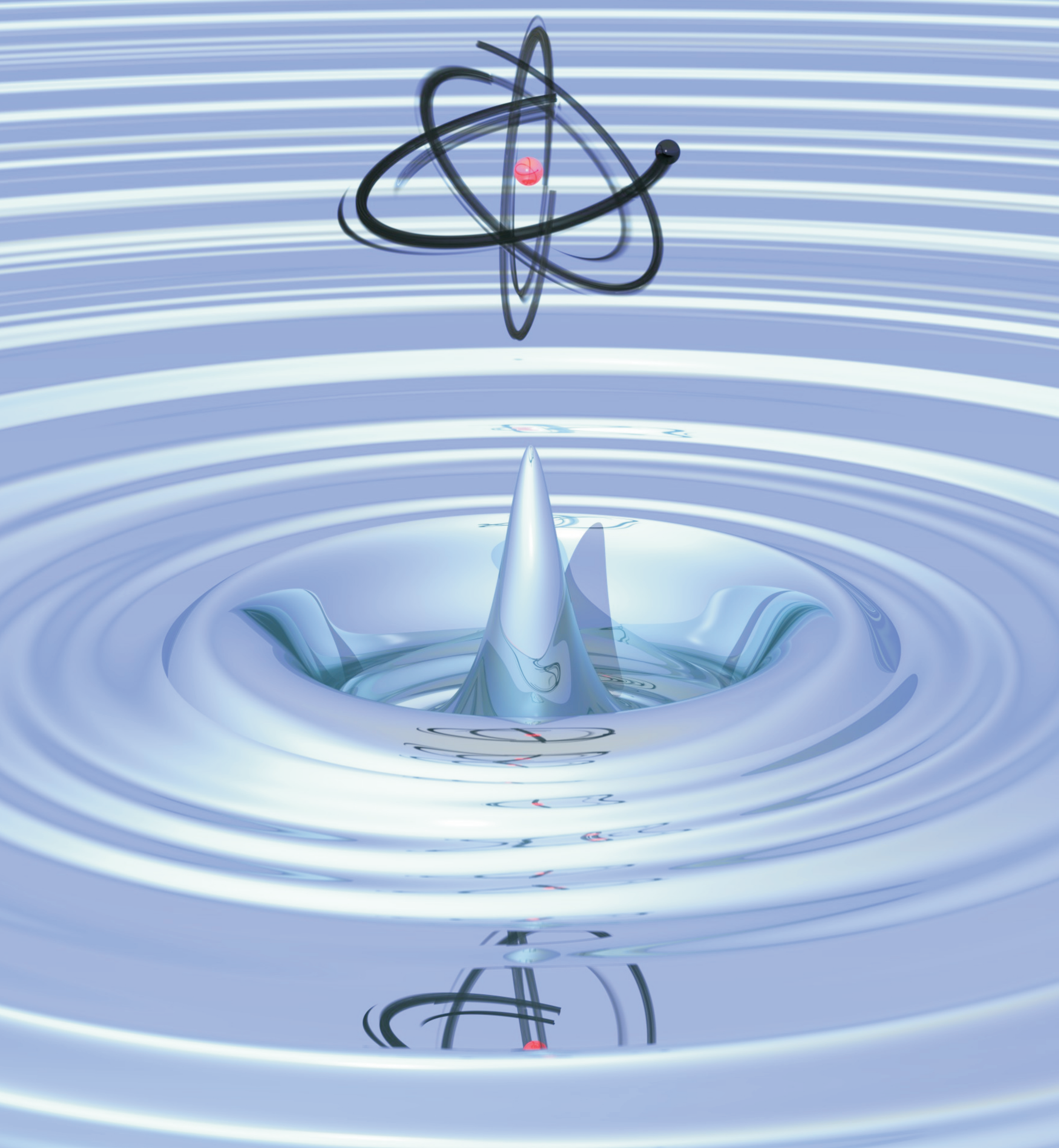

A single electron in a Bose-Einstein condensate

Von der Fakultät Mathematik und Physik der Universität Stuttgart
zur Erlangung der Würde eines Doktors der
Naturwissenschaften (Dr. rer. nat.) genehmigte Abhandlung

vorgelegt von

Jonathan Benedikt Balewski

aus Göppingen

Hauptberichter:	Prof. Dr. Tilman Pfau
Mitberichter:	Prof. Dr. Jörg Wrachtrup
Prüfungsvorsitzender:	Prof. Dr. Hans Peter Büchler
Tag der mündlichen Prüfung:	20.02.2014

5. Physikalisches Institut, Universität Stuttgart

2014

D 93

Zusammenfassung

Diese Arbeit beschäftigt sich mit der Erzeugung und Untersuchung von Rydberg-Atomen in ultrakalten Quantengasen. Die Kombination dieser beiden quantenmechanischen Objekte erlaubt es ungewöhnliche Zustände von Materie herzustellen. Insbesondere lässt sich ein Modellsystem von grundlegender Bedeutung realisieren, nämlich ein einzelnes Elektron in einem Bose-Einstein-Kondensat (BEC). Diese neue Idee, ihre experimentelle Realisierung und theoretische Beschreibung, sowie die Entwicklung von Anwendungsmöglichkeiten in einer Vielzahl von Bereichen bilden den Kern dieser Arbeit.

Als Rydberg-Atome werden Atome in einem extremen quantenmechanischen Zustand bezeichnet. Mindestens ein Elektron ist dabei hoch angeregt, gekennzeichnet durch einen sehr großen Wert der Hauptquantenzahl n. In einem klassischen Bild bewegt sich dieses so genannte Rydberg-Elektron auf einer Bahn, auf der es sich sehr weit von dem restlichen Atomrumpf entfernt. Bei der Anregung in einen Zustand mit Hauptquantenzahl $n = 200$ dehnt sich ein Atom auf das etwa 40.000-fache seiner ursprünglichen Größe aus und erreicht damit die Größe kleinster lebender Objekte, die ihrerseits aus mehreren Billionen von Atomen bestehen. Die Eigenschaften eines solchen Atoms werden dann im Wesentlichen nur noch von dem einzelnen, hoch angeregten Rydberg-Elektron bestimmt, fast unabhängig von dem jeweiligen chemischen Element. Insbesondere lässt sich der Ladungsschwerpunkt des Rydberg-Elektrons relativ leicht verschieben, da dieses nur noch schwach an den weit entfernten Atomrumpf gebunden ist. Das führt dazu, dass Rydberg-Atome sowohl stark untereinander als auch mit ihrer Umgebung wechselwirken. Rydberg-Atome sind deshalb auch interessant für die Anwendung als empfindliche Sensoren, die sogar in der Lage sind, einzelne Photonen zerstörungsfrei zu detektieren ([1], Nobelpreis 2012 für Serge Haroche). Vor diesem Hintergrund liegt die Vermutung nahe, dass das Vorkommen von Rydberg-Atomen nur auf ideale Laborbedingungen und, in der freien Natur, allenfalls auf den interstellaren Raum beschränkt ist. Erstaunlicherweise ist das nicht zutreffend, denn tatsächlich können sich innerhalb eines einzelnen Rydberg-Atoms mehrere Zehntausend andere Atome im Grundzustand befinden. Dies wurde bereits vor über 80 Jahren durch die Beobachtung der Absorption von Licht in dichten Gasen gezeigt ([2, 3] und Einführung auf Seite 4).

Der zweite Bestandteil der hier vorgestellten Experimente, das Bose-Einstein-Kondensat, weist nicht minder erstaunliche Eigenschaften auf. Nahe des absoluten Nullpunkts der Temperatur und bei relativ hohen Dichten findet in einem Gas aus schwach wechselwirkenden Bosonen ein Phasenübergang statt. In dem sich dabei ausbildenden Aggregatzustand befinden sich alle Teilchen im selben quantenmechanischen Zustand; ein Ensemble, bestehend aus typischerweise mehreren Zehntausend bis Millionen von Atomen, kann somit durch eine einzige Wellenfunktion beschrieben werden. Seit der erstmaligen Erzeugung eines solchen

Quantenzustands ([4, 5], Nobelpreis 2001 für Eric A. Cornell, Carl E. Wieman und Wolfgang Ketterle) werden Bose-Einstein-Kondensate erfolgreich zur Erforschung einer Vielzahl von grundlegenden physikalischen Fragestellungen eingesetzt.
Aufgrund ihrer hohen Reinheit und guten Kontrollierbarkeit lassen sich ultrakalte Quantengase zum Beispiel als Modell zur Simulation komplexer Vielteilchensysteme verwenden [6]. Ein wesentlicher Beitrag zu den vielversprechenden Entwicklungen auf diesem Gebiet könnte durch die Nutzbarmachung der Rydberg-Anregung geleistet werden. Die Wechselwirkung zwischen Rydberg-Atomen ist nämlich nicht nur sehr stark, sondern kann auch relativ einfach über die Wahl des Quantenzustands kontrolliert werden [7]. Dies bezieht sich nicht nur auf die Stärke der Wechselwirkung, sondern auch auf deren Winkelabhängigkeit und das Vorzeichen. Einen limitierenden Faktor stellt dabei allerdings die endliche Lebensdauer von Rydberg-Zuständen dar. In Abhängigkeit von dem jeweiligen Quantenzustand beschränkt diese Lebensdauer die mögliche Länge von Experimenten mit einzelnen Rydberg-Anregungen auf typischerweise mehrere zehn Mikrosekunden bis maximal wenige Millisekunden. Eine Möglichkeit dieses Problem zu umgehen, das so genannte Rydberg-Dressing, basiert darauf, dass jedem Atom innerhalb eines Ensembles nur zu einem geringen Anteil der Rydberg-Zustand beigemischt wird. Dies lässt sich dadurch erreichen, dass das zur Rydberg-Anregung verwendete Lichtfeld in der Frequenz leicht verstimmt wird. Es gibt eine Vielzahl von theoretischen Vorschlägen, wie dies zur Erzeugung exotischer Zustände von Materie genutzt werden kann (siehe Einleitung zu Kapitel 6).

Im ersten Teil dieser Arbeit wird untersucht, inwiefern eine erstmalige experimentelle Demonstration von Rydberg-Dressing mit dem derzeitigen experimentellen Aufbau möglich ist. Bei den hohen Dichten, die in ultrakalten Atomwolken typischerweise vorherrschen, sind kollektive Effekte zu erwarten [8]. Diese verhinderten bislang in diesem Regime ein einfaches Verständnis der dem Rydberg-Dressing zugrunde liegenden Prozesse. Aufbauend auf der Beschreibung in einer zweiatomigen Basis [9] wird deshalb zunächst ein Modell entwickelt, welches den Effekt auf ein Bose-Einstein-Kondensat auch im kollektiven Regime beschreibt. Es wird gezeigt, dass die Ergebnisse dieser analytischen Rechnungen mit den Resultaten eines numerischen Ansatzes [8] übereinstimmen. Neben dem anschaulichen Verständnis bietet dieser neu entwickelte Ansatz allerdings noch weitere wesentliche Vorteile. So erlaubt die Ausnutzung der effizienteren analytischen Form nicht nur die Simulation experimentell relevanter asymmetrischer Kondensate in drei Dimensionen, sondern auch die Berechnung des zu erwartenden Effekts in Abhängigkeit von den experimentell zugänglichen Parametern. Zudem wird die Erweiterung von Rydberg-Dressing auf Rydberg-Zustände nahe einer Förster-Resonanz vorgeschlagen, um die Flexibilität in der Kontrolle der Rydberg-Rydberg-Wechselwirkung zusätzlich zu erweitern [10, 11].
In Kombination mit experimentellen Untersuchungen werden schließlich die limitierenden Faktoren identifiziert, die eine Beobachtung von signifikanten Effekten durch Rydberg-Dressing im derzeitigen Aufbau verhindern. Dies sind im Wesentlichen eine zu hohe Dichte der verwendeten Atomwolke und eine zu geringe verfügbare Laserleistung zur Rydberg-Anregung. Bei vielen Rydberg-Zuständen, insbesondere bei Rydberg D-Zuständen, treten außerdem zusätzliche Atomverluste auf, hervorgerufen durch die Erzeugung von weit ausgedehnten Rydberg-Molekülen [12, 13]. Diese Verluste verhindern eine Realisierung von Rydberg-Dressing im Bereich kleiner roter Verstimmungen des Anregungslichts. Ohne signifikante

Veränderung der Fallengeometrie lässt sich die Anzahldichte der Atome nicht mehr wesentlich verringern, ohne den ultrakalten Temperaturbereich zu verlassen. Dieser ist aber essentiell für die Beobachtung von möglichen Effekten auf die Atomwolke, hervorgerufen durch Rydberg-Dressing. Eine mögliche Lösung bietet die Verringerung der effektiven Atomzahldichte durch die Verwendung von Ensembles mit reduzierter Dimensionalität, wie zum Beispiel durch die Verwendung optischer Gitter.

Nach diesen Erkenntnissen rückt der Schwerpunkt im zweiten Teil dieser Arbeit auf die direkte Wechselwirkung zwischen einzelnen Rydberg-Atomen und einem Bose-Einstein-Kondensat. Die bisherigen Untersuchungen werden dazu auf noch höher angeregte Rydberg-Zustände ausgedehnt. Für Zustände mit Hauptquantenzahlen $n > 110$ ist die Wechselwirkung zwischen zwei Rydberg-Atomen so stark, dass sich, bei konstanter Frequenz der Anregungslaser, innerhalb des Volumens eines Kondensats nur ein einzelnes Rydberg-Atom erzeugen lässt. Experimente in diesem Regime stellen zunächst eine ganze Reihe von technischen Herausforderungen. Mit der derzeitigen Apparatur wurden bislang nur Rydberg-Zustände mit Hauptquantenzahlen $n < 50$ untersucht. Zunächst musste die Kontrolle der elektrischen Felder in der Experimentierkammer um mehrere Größenordnungen verbessert werden, da Rydberg-Atome mit Hauptquantenzahlen um $n = 200$ eine mehr als 20.000-mal größere Empfindlichkeit auf elektrische Felder aufweisen. Gleichzeitig wurden die Schaltzeiten der elektrischen Ionisationsfelder wesentlich verkürzt, da die technisch begrenzte Lebensdauer des Bose-Einstein-Kondensats nur relativ kurze Experimente erlaubt. Schließlich konnten Rydberg S-Zustände mit Hauptquantenzahlen bis $n = 202$ in einem BEC erzeugt werden. Da das bisher zur Detektion von Rydberg-Atomen verwendete Verfahren aus Feldionisation und Ionendetektion im bestehenden Aufbau jedoch keine Einzelatomdetektion ermöglicht, muss auf eine andere Messmethode zurückgegriffen werden, um einzelne Rydberg-Atome in einem Bose-Einstein-Kondensat nachzuweisen. Die Lösung stellt in diesem Fall die Beobachtung der Auswirkung der Rydberg-Anregung auf das BEC dar. Die Veränderungen des Kondensats, die durch einzelne Rydberg-Atome hervorgerufen werden, können mit Hilfe von Absorptionsaufnahmen der Atomwolke nach einer freien Expansion sichtbar gemacht werden.

Zunächst wird der Einfluss des Kondensats als dichtes Gas auf das Rydberg-Atom untersucht. Insbesondere wird die beobachtete Energieverschiebung der Rydberg-Zustände im Kondensat, basierend auf einem Modell von Enrico Fermi von 1934 [14], vollständig durch die Streuung des Rydberg-Elektrons an den einzelnen Atomen erklärt. Neben der Verschiebung wird auch die Verbreiterung der Spektrallinien und die Verkürzung der Lebensdauer von Rydberg-Zuständen im Kondensat untersucht. Die beobachtete Lebensdauer hängt von der Position des Rydberg-Atoms im BEC ab, die sich durch die Verstimmung des Anregungslasers kontrollieren lässt.

Nach allen bisherigen Beobachtungen ist die Wechselwirkung des positiv geladenen Atomrumpfs des Rydberg-Atoms mit dem Bose-Einstein-Kondensat vernachlässigbar. Demnach kann das System als ein einzelnes Elektron in einem Bose-Einstein-Kondensat betrachtet werden. So gesehen dient das Rydberg-Atom nur als eine Falle für ein einzelnes Elektron. Dieses befindet sich dabei bis zum Zerfall des Rydberg-Atoms in einem wohldefinierten Quantenzustand, wie weitere Untersuchungen ergeben. Diese Beobachtung bildet die Basis für das Verständnis der überraschend starken Wirkung eines einzelnen Rydberg-Elektrons auf ein Bose-Einstein-Kondensat. Neben einem Verlust von bis zu 50 Atomen aus dem

BEC je Rydberg-Atom, gemessen nach einer freien Expansion der Atomwolke, führt die Rydberg-Anregung auch zu einer kollektiven Schwingung des gesamten Kondensats.
In Zusammenarbeit mit David Peter und Hans Peter Büchler vom Institut für theoretische Physik III der Universität Stuttgart wurde ein Modell entwickelt, welches diese Messergebnisse weitgehend erklären kann. Es basiert auf der Beschreibung des homogenen Bose-Gases durch Nikolai N. Bogoliubov [15] und behandelt den Einfluss des Elektrons auf das Kondensat als eine kurze Störung, welche Anregungen im BEC erzeugt. In Abhängigkeit von dem Impuls der jeweiligen Anregungen kann es sich dabei um einzelne beschleunigte Teilchen oder um Schallwellen, so genannte Phononen, handeln. Beide führen, sobald das äußere Fallenpotenzial abgeschaltet wird, zu Verlusten von Atomen aus dem Kondensat. Bei sehr niedrigen Impulsen jedoch führen die Schallwellen zur Ausbildung kollektiver Oszillationen des gesamten Systems.

Diese erste Demonstration und das Verständnis dieses einfachen Modellsystems eines einzelnen Elektrons in einem Quantengas bilden den Ausgangspunkt für eine ganze Reihe weiterer Experimente. Diese reichen von der Untersuchung der Kopplung von Elektronen und Phononen, wie sie für einige Modelle der Supraleitung relevant sind, über Anwendungen in der Quantenoptik bis hin zur direkten Abbildung eines einzigen Elektronenorbitals. Das hier entwickelte Konzept lässt sich außerdem auch auf die Präparation eines einzelnen ultrakalten Ions in einem Bose-Einstein-Kondensat erweitern. Aufgrund der größeren Reichweite der Wechselwirkung zwischen Atomen und Ionen würde dies ein neues, bisher unerreichtes Regime starker Kopplung experimentell zugänglich machen.

Publications

In the framework of this thesis, the following articles have been published:

- J. B. Balewski and S. Hofferberth, *Riesenatom im Bose-Einstein-Kondensat*, Physik in unserer Zeit, **45**, 59–60 (2014)
- J. B. Balewski, A. T. Krupp, A. Gaj, S. Hofferberth, R. Löw and T. Pfau, *Rydberg dressing: Understanding of collective many-body effects and implications for experiments*, arXiv:1312.6346 (submitted 2013)
- J. B. Balewski, A. T. Krupp, A. Gaj, D. Peter, H. P. Büchler, R. Löw, S. Hofferberth and T. Pfau, *Coupling a single electron to a Bose-Einstein condensate*, Nature, **502**, 664–667 (2013)
- J. Nipper, J. B. Balewski, A. T. Krupp, S. Hofferberth, R. Löw and T. Pfau, *Atomic pair-state interferometer: Controlling and measuring an interaction-induced phase shift in Rydberg-atom pairs*, Physical Review X, **2**, 031011 (2012)
- J. Nipper, J. B. Balewski, A. T. Krupp, B. Butscher, R. Löw and T. Pfau, *Highly resolved measurements of Stark-tuned Förster resonances between Rydberg atoms*, Physical Review Letters, **108**, 113001 (2012)
- R. Löw, H. Weimer, J. Nipper, J. B. Balewski, B. Butscher, H. P. Büchler and T. Pfau, *An experimental and theoretical guide to strongly interacting Rydberg gases*, Journal of Physics B: Atomic, Molecular and Optical Physics, **45**, 113001 (2012)
- W. Li, T. Pohl, J. M. Rost, S. T. Rittenhouse, H. R. Sadeghpour, J. Nipper, B. Butscher, J. B. Balewski, V. Bendkowsky, R. Löw and T. Pfau, *A homonuclear molecule with a permanent electric dipole moment*, Science, **334**, 1110–1114 (2011)
- B. Butscher, V. Bendkowsky, J. Nipper, J. B. Balewski, L. Kukota, R. Löw, T. Pfau, W. Li, T. Pohl and J. M. Rost, *Lifetimes of ultralong-range Rydberg molecules in vibrational ground and excited states*, Journal of Physics B: Atomic, Molecular and Optical Physics, **44**, 184004 (2011)
- B. Butscher, J. Nipper, J. B. Balewski, L. Kukota, V. Bendkowsky, R. Löw and T. Pfau, *Atom-molecule coherence for ultralong-range Rydberg dimers*, Nature Physics, **9**, 970–974 (2010)

Contents

Introduction

The basic task of natural sciences is to seek simple laws governing the natural world. Finding such rules starts usually with an iterated cycle of systematic observations, formulation of hypotheses, and their testing and subsequent modification based on repeated experimental measurements. This process can often span over the course of decades.

Spectroscopy and Rydberg atoms

A prominent example is the understanding of atomic spectra. From the first systematic study of discrete absorption lines in the solar spectrum by Joseph von Fraunhofer in 1814 [16], it took almost a century until the formulation of Niels Bohr's model of the atom [17], for the first time, could provide at least a partial explanation for the occurrence of atomic spectra. This development was paved by systematic precise measurements of the solar spectrum by Anders Jonas Ångström, published in 1868, and subsequent efforts to identify patterns and their underlying fundamental principles. The spectrum of the hydrogen atom proved to be the first testing ground for the development of hypotheses, since its spectrum contained relatively few lines, grouped into different series. Early important work is seldom cited in literature, since it turned out to be completely wrong [18]. George J. Stoney, for example, pointed out in 1871, that the frequencies of lines, observed in the spectrum of hydrogen, coincide exactly with higher harmonics of a single fundamental vibration frequency [19]. This explanation was absolutely in line with knowledge from acoustics, and the higher harmonics not observed in the spectra could be simply explained as being to weak to be detected. Even though this approach provided excellent agreement, also for the spectra of other atomic and molecular species [18], it was proven to be bare coincidence by Arthur Schuster in 1881 [20]. After this major setback, which prompted many scientists to abandon the quest for patterns in absorption spectra, it was the school teacher Johann Jakob Balmer, whose attempt succeeded. In 1885, he found out that the wavelengths λ of the whole hydrogen series known at the time could be described by a simple formula, depending only on one integer number m [21]:

$$\lambda = const. \cdot \frac{m^2}{m^2 - 2^2} \tag{0.1}$$

However, one aspect of Stoney's theory was not all wrong. This was the notion to express the spectral lines in units of frequency. This idea, picked up again by Walter N. Hartley [22], led to the final breakthrough of Johannes Rydberg in 1890 [23]. Based mainly on spectroscopic data on alkali metals from George D. Liveing and Sir James Dewar [24], he developed a simple formula, that describes the observed spectra with only three parameters, besides one universal constant $Ryd = 3.2898 \cdot 10^{15}$ Hz, the so called Rydberg constant:

$$f = Ryd \left(\frac{1}{(n_1 - \delta_{l_1})^2} - \frac{1}{(n_2 - \delta_{l_2})^2} \right) \tag{0.2}$$

In Rydberg's original paper [23], $n_2 > n_1$ are integer numbers, where n_1 is kept constant. The parameter δ_{l_2} was called quantum defect later by Erwin Schrödinger [25]. Lines, described by the same first term in equation (0.2) and the same quantum defect, group into a series. In particular, Rydberg assigned the series S (sharp), P (principal), and D (diffuse). A forth series, called F (fundamental), was discovered later in 1907 by Arno Bergmann [18]. For hydrogen, the quantum defects δ_{l_i} vanish. Balmer's formula (0.1) then results from (0.2) by setting $n_1 = 2$. Series of lines with different values for n_1 could be identified later, starting with $n_1 = 1$, by Theodore Lyman in 1906 [26] and $n_1 = 3$ by Friedrich Paschen in 1908 [27].

In combination with work of Ernest Rutherford and others (see introduction to section 3.2), these observations paved the way for Niels Bohr's model of the atom [17], marking the begin of quantum theory, introduced by Max Planck in 1900 [28], in atomic physics. Admittedly, the principal idea of quantized states of electrons was published already three years earlier in 1910 by Arthur Erich Haas, considered as a carnival joke by his contemporaries [29]. The Bohr model already provides a good description of the hydrogen atom, describing circular electron orbits with energy $-h\,Ryd/n^2$, quantized with the principal quantum number n. The quantum defects δ_l, present in the spectra of the alkalis, however, could only be explained with the extension of Bohr's model by Arnold Sommerfeld in 1916 [30]. There, electrons are travelling on elliptical orbits around the nucleus. For atoms with more than one electron, the energy of the valence electron then also depends on its angular momentum, quantized as $\hbar l$, with the integer quantum number l of angular momentum ($0 \leq l \leq n-1$). The angular momentum determines the ellipticity of the orbits, which coincide with the circular Bohr orbits at the maximum value $l = n - 1$. Considering the outermost electron, the orbit at small values of l approaches the nucleus, which is only partly screened by the other electrons on lower energy levels. This screening is accounted for by the quantum defect δ_l. Within this model, the series S, P, and D can thus be understood as transitions between states with different principal quantum numbers n and angular momenta $l = 1 \rightarrow 0$, $l = 0 \rightarrow 1$, and $l = 1 \rightarrow 2$, respectively.

A proving ground for the new theories was provided by spectroscopy of hydrogen and, in particular, alkali atoms. The latter feature only a single valence electron and are much easier to study in the laboratory than atomic hydrogen H, which first has to be created from molecular H_2. Especially the states with high principal quantum numbers n, termed Rydberg atoms, turned out be particularly interesting. Absorption spectra of sodium up to $n = 50$ were already observed in 1909 by Robert W. Wood [31]. As a side note, these experiments were the first spectroscopic measurements performed in a laboratory, that could put astronomic observations of the solar spectrum in the rear, since those measurements were only reaching up to $n = 30$ at the time. Rydberg atoms, in the following, were not only used to benchmark the development of early quantum theory. Owing to their enormous size (see Figure 0.1), given by the radius $2a_0(n - \delta_l)^2$ (with Bohr radius $a_0 = 5.292 \cdot 10^{-11}$ m) of the classically allowed region, they turned out to be situated at the border between quantum physics and the realm of classical mechanics. Therefore, many of their properties, such as the Stark effect and the quantum defect, can be also explained using classical theories [34]. Consequently, Rydberg atoms form a prime example for the correspondence principle, formulated by Niels Bohr in 1920 [35].

Later on, Rydberg atoms became also important in other distinct fields, like astrophysics and plasmaphysics [36]. The development of the laser allowed for the efficient creation of Rydberg atoms, stimulating a resurrected interest in this field [37], which is lasting until today. The most interesting properties of Rydberg atoms are related to their enormous size, resulting in a strong

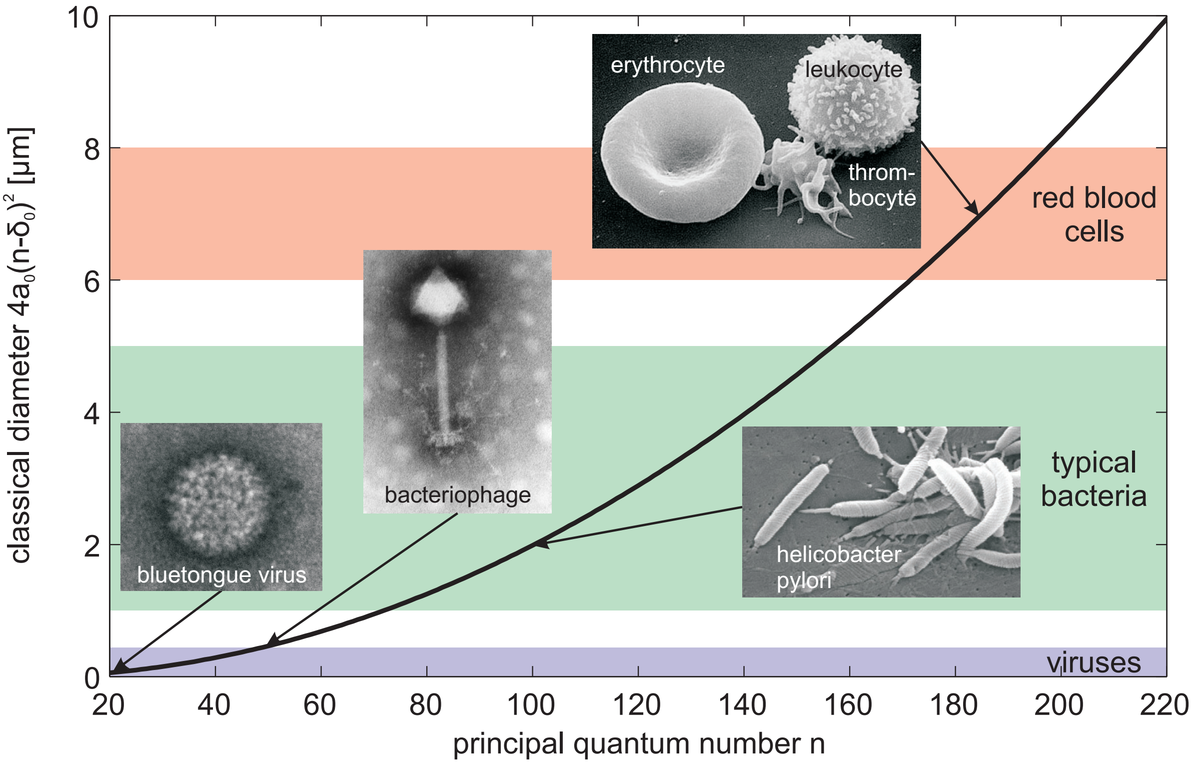

Figure 0.1: Size of Rydberg atoms compared to different biological objects. The diameter $4a_0(n - \delta_0)^2$ of the classical allowed region of the Rydberg electron is plotted depending on the principal quantum number for rubidium (quantum defect $\delta_0 = 3.135$ [32]). Scanning electron micrographs [33] of different biological objects are shown to illustrate the huge size of Rydberg atoms. They exceed the dimensions of large viruses already at $n \approx 50$. At principal quantum numbers around $n = 70$, the size of bacteria, the smallest living objects, is reached.

sensitivity to external fields and strong interactions among each other. Rydberg atoms, for example, have been already successfully used as nondestructive probes for weak fields, consisting of few photons [38] (Nobel Prize 2012 for Serge Haroche). Furthermore, they are discussed as a building block for gates in quantum information processing [39, 40]. The current state of the art in this field can be found e.g. in [7].

Bose-Einstein condensates

Also, the study of ultracold atomic gases has become an important test bench of physics in the past decades, allowing for the study of quantum phenomena in a regime qualitatively different from the classical world. Based on the work of Satyendra Nath Bose on the statistical distribution of photons, the quanta of light [41], Albert Einstein predicted a phase transition in a gas of non-interacting atoms [42]. As a consequence of quantum statistics, the particles in the gas are then condensed into the state of lowest energy. For a long time, this new phase, termed Bose-Einstein condensate (BEC), had no practical impact.

After the first observation of superfluidity in liquid helium [43, 44], Fritz London pointed out, that this phenomenon could be connected to Bose-Einstein condensation [45]. Although this approach, extended to a two-fluid model by László Tisza [46], turned out to be quite successful, the direct observation of a Bose-condensed phase in liquid helium is prevented by the strong interatomic interaction peculiar to helium. Estimates from neutron scattering experiments [47] suggest a condensate fraction of below 10% only; however, the analysis of this data is delicate [48]. The separate measurement of the superfluid and condensed fractions in liquid helium are thus an interesting topic until today [49]. On the theory side, the observation of superfluidity in liquid helium triggered significant progress. Among many others advances (see e.g. [50]), this was for example the development of the microscopic theory of a weakly interacting Bose gas by Nikolai N. Bogoliubov in 1947 [15]. While clearly not describing the strongly interacting limit, this model leads to good results for the superfluidity of liquid helium. The search for systems with weaker interaction, and thus higher condensate fraction, emerged. For a long time, spin-polarized hydrogen atoms, as suggested already in 1959 [51], were a promising candidate for achieving Bose-Einstein condensation of a weakly interacting gas. Indeed, a BEC of atomic hydrogen was reported in 1998 [52], after more than two decades of heroic experimental effort [53].

However, just as in the early days of atomic physics, it were again the alkali metals that, while being less ideal from a theoretical point of view, became more important, because of their easier handling in the laboratory. In contrast to spin-polarized hydrogen, the alkali metals are known to form solids at low temperatures. Moreover, due to their larger atomic mass, the critical temperature for the transition to the condensed state is more than one order of magnitude lower than for hydrogen. This reasoning [54], however, turned out to be irrelevant [55]. The development of laser cooling and trapping of neutral atoms, pioneered by Steven Chu, Claude N. Cohen-Tanoudji, and William D. Phillips ([56, 57, 58], Nobel Prize in 1997), compensated for the drawbacks of alkali atoms in realizing Bose-Einstein condensation. In combination with techniques for magnetic trapping of neutral atoms [59, 60] and evaporative cooling [61], which were also further developed during the quest for Bose-Einstein condensation of spin-polarized hydrogen [62, 63], this led to the final breakthrough in 1995, when the groups of Eric A. Cornell and Carl E. Wieman, and Wolfgang Ketterle announced the creation of Bose-Einstein condensates of rubidium ^{87}Rb [4] and sodium ^{23}Na [5], respectively (Nobel Prize in 2001).

Since then, the research in quantum degenerate gases has evolved dramatically. The applications range widely from the demonstration of basic physical phenomena, like wave-particle duality by interference experiments [64] and the creation of an atom laser [65, 66], to ambitious proposals for the construction of a gravimetric radar as a countermeasure against stealth technology [67]. Most notably, the theories for superfluidity were tested in a regime not accessible with liquid helium, in particular the weakly interacting and the non-uniform Bose gas [53, 68]. Moreover, current research aims at the simulation of quantum systems that are hard or impossible to model otherwise [6] (see also introduction to section 3.1).

Rydberg atoms in dense gases

The study of Rydberg atoms in a high density environment actually dates back almost exactly one century. In 1914[1], Robert W. Wood and René Fortrat extended Wood's first measurements of the absorption series in sodium from 1909 ([31], as mentioned above), en-

---

[1] Published only later, in 1916, delayed on account of the outbreak of World War I.

larging the number of observed lines by ten principal quantum numbers [69]. To this end, they studied the absorption of light, generated by a quartz mercury arc lamp, in an evacuated and heated tube, containing sodium. They used the, at the time, largest and most powerful quartz spectrograph in the world, located in Zurich. In addition, this measurements were performed at an increased vapour pressure, compared to previous measurements, in order to make smaller signals from the higher terms visible[2]. While noting in Wood's precedent paper [31], that the observed linewidth decreases for the transitions with higher principal quantum numbers, they found in their subsequent measurement that "one sacrifices the sharpness of the lines somewhat by this augmentation of density" at the higher terms. Furthermore, they compared the measured transition frequencies to Rydberg's formula (0.2) in its modified form by Walther Ritz [70]. For transitions at low principal quantum numbers, there is a systematic deviation from this formula, known already at the time and caused by the fact that the approximation of an hydrogenic atom becomes poor in that regime. In their measurements at high atomic densities, Wood and Fortrat now observed a systematic deviation of the line frequencies also at high principal quantum numbers, reaching up to $40\,\mathrm{GHz}$. Although noting that this "may result from slight errors of measurement", the effect seemed significant enough, that an attempt was made by William M. Hicks in 1916 to explain the results, using a refined scaling formula for the quantum defects [71]. However, while improving the consistency with Rydberg's formula for low principal quantum numbers, he also could not explain the line shift close to the end of the series. Although it is not possible to tell with absolute certainty today, it seems highly likely, considering their parameter regime, that the shift and the broadening of the high terms, observed by Wood and Fortrat, were indeed caused by the interaction of highly excited Rydberg states with ground state atoms. This phenomenon is one of the main topics of this thesis.

Twenty years later, in 1934, Edoardo Amaldi and Emilio Segrè [2, 3] and, independently, Christian Füchtbauer and coworkers [72, 73, 74] studied systematically the influence of different gases, in particular hydrogen, neon, helium, and argon, at variable density onto the high terms in the spectra of sodium and potassium. At densities reaching up to $10^{20}\,\mathrm{cm}^{-3}$, there are thousands of particles of the perturbing gas located inside one Rydberg atom. As they noted, it is a surprising fact, that the absorption lines can be observed at all in such a regime. They found a shift and a broadening of these lines, which both only depend on the type and the density of the perturbing foreign gas. Moreover, unexpected at the time, the line shift can be positive or negative, depending on the type of the foreign gas. This observation does not agree with a first simple guess, considering the gas as a dielectric medium, filling the space between the Rydberg electron and the Rydberg core.

A theoretical explanation of the line shift was given by Enrico Fermi in the same year [14]. He studied the interaction of the Rydberg electron and the positively charged Rydberg core with the foreign gas separately. He found that the impact of the positive ion is next to negligible. In order to describe the interaction of the Rydberg electron with the gas, he developed a model based on the scattering of the Rydberg electron from the neutral particles in the perturbing gas, introducing a new parameter, termed scattering length. The basic idea, in more modern terms [75], is that the slow incident particle has a large de Broglie wavelength, so that short-

---

[2] While no exact values are specified explicitly, they state that "to get the last members near the head of the bands a density corresponding to a red heat is necessary", while for the lower lines a temperature just above 100°C was sufficient. This corresponds to densities of sodium ranging from about $10^9\,\mathrm{cm}^{-3}$ up to some $10^{14}\,\mathrm{cm}^{-3}$, just reaching the regime of high density at the high terms (see Figure 0.2).

range properties of the interaction potential can not be resolved and are thus not important. To lowest order in the relative momentum of the collision, the effect of the scattering event can then be described by a single parameter, the scattering length. This concept turned out to be very successful in different branches of physics. In particular, it was used shortly after by Fermi to describe the scattering of slow neutrons from hydrogen atoms, introducing the so called Fermi pseudopotential (see section 3.2). This description of neutron scattering became very important shortly afterwards for the development of artificial nuclear fission.

Fermi's description of the interaction of Rydberg electrons with different neutral particles (atoms and molecules) was further refined in the following decades (see [76] and references therein). Much later, in 2000, Chris H. Greene and coworkers realized that this interaction can lead to an intriguing effect in a regime, that only became accessible at the advent of ultracold atoms (see above). For some alkali atoms, the electron-atom scattering length is negative, leading to an attractive interaction. At temperatures on the order of μK, the scattering of the Rydberg electron can thus bind another alkali atom inside its orbit, constituting a new class of chemical bond. These so called ultralong-range Rydberg molecules were created for the first time in 2009 [12, 13] by photoassociation from an ultracold gas of rubidium ^{87}Rb at densities on the order of $10^{13}\,\mathrm{cm}^{-3}$, using Rydberg S-states at principal quantum numbers around $n = 36$. In this regime, there is only rarely one additional atom located inside the volume of a Rydberg atom, making the formation of a molecule possible. Soon, it turned out that these molecules, besides their size, show interesting properties, opening up a new field of ultracold chemistry. After the creation of triatomic molecules [77], the coherent creation and dissociation [78, 79], and the existence of a permanent electric dipole moment [80, 11], remarkable for a homonuclear diatomic molecule, were demonstrated.

This thesis

Different parameter regimes for the study of Rydberg atoms in gases can be identified in the plane of principal quantum number n and density of the environment. These regimes are illustrated in Figure 0.2. If the gas contains on average more than one atom in the classical volume $4/3\pi(2a_0(n-\delta_0)^2)^3$ of one Rydberg atom, the system is considered as dense, since then a Rydberg electron is always interacting with at least one ground state atom (see Figure 0.2d). Most notably, the experiments of Amaldi and Segrè were performed under this condition.

Another length scale becomes important, if Rydberg atoms are excited with narrow bandwidth. Due to the strong interaction between two Rydberg atoms, Rydberg excitation is then only possible beyond a minimum distance, termed blockade radius r_B, around one Rydberg atom. If there is more than one atom inside a sphere with radius r_B, collective effects can arise (see paragraph 1.2.3). This regime has been subject of extensive ongoing studies for decades now. In particular, most applications of Rydberg atoms for quantum information so far are situated in this range of parameters [39, 40, 7]. The interaction with ground state atoms here would be rather detrimental, since it can lead to an additional source of decoherence (see section 7.3). However, even here the probability to find one or more additional atoms inside one Rydberg atom is small, but finite (see Figure 0.2a). This allows to create ultralong-range Rydberg molecules in this regime, as well.

Finally, at very low densities and principal quantum numbers, Rydberg atoms are quasi isolated (see Figure 0.2b). This regime is interesting for precision spectroscopy of Rydberg states.

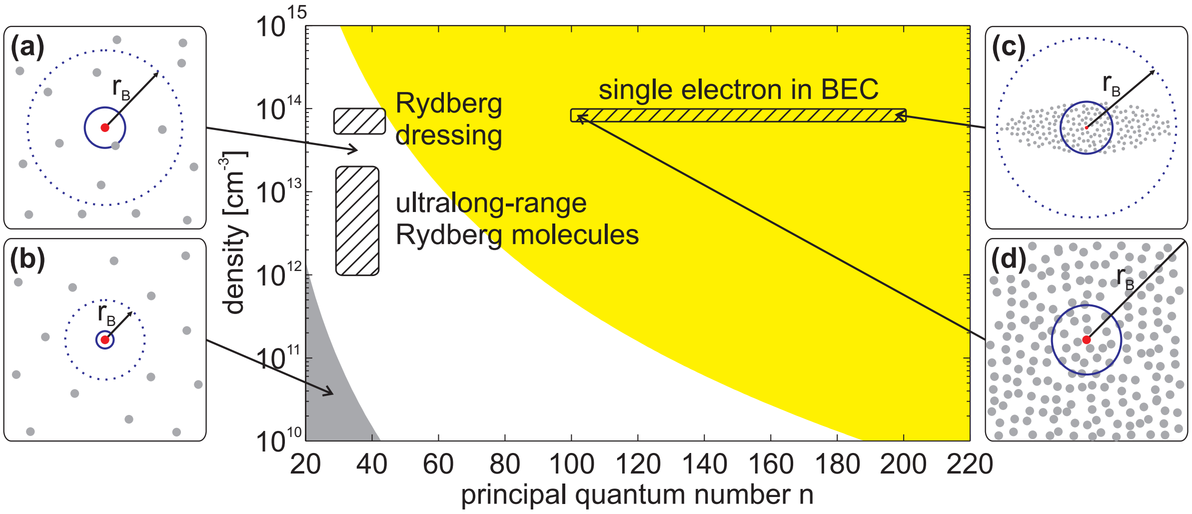

Figure 0.2: Different parameter regimes for Rydberg excitation [81]. At low principal quantum numbers n and samples at very low density, Rydberg atoms are quasi isolated (grey area and b). As soon as there is more than one atom inside the blockade sphere with radius r_B around one Rydberg atom, collective effects start to play a role (white area and a). In this regime, there is a small, but nonzero probability to nevertheless find a ground state atom inside a Rydberg atom, defined as the volume of the classically allowed region of the Rydberg electron $4/3\pi(2a_0(n-\delta_0)^2)^3$. This allows to observe ultralong-range Rydberg molecules. Furthermore, the measurements on Rydberg dressing are preformed here. At even larger densities and higher Rydberg states, there are, on average, always many atoms located inside one Rydberg atom (yellow area). This is the regime, where the experiments on coupling a single electron to a BEC take place. At very large principal quantum numbers $n \geq 110$, the blockade radius r_B becomes larger than the sample (c, d). For $n \approx 200$, the size of the Rydberg atom even reaches the radial extent of the BEC (c). The size of the ground state atoms (grey dots), Rydberg core (red dots) and the Rydberg electron wavefunction (blue circle), as well as the blockade volume (blue dotted circle) in the insets are not to scale. The blockade radius is calculated for Rydberg S-states assuming an excitation linewidth of 1 MHz and using the C_6-coefficients from [82] (see also section 1.2).

In this work, the topics of Rydberg atoms and Bose-Einstein condensates at densities up to $10^{14}\,\mathrm{cm}^{-3}$ are combined. In contrast to previous experiments [83, 84], now the focus lies on the atomic sample, from which Rydberg atoms are excited, rather than the population in the Rydberg state only. Explicitly, the goal is to observe the impact of few Rydberg excitations onto a large atomic sample. Two different approaches are studied in this work.

First, a regime of relatively low Rydberg states with principal quantum numbers right above $n = 30$ is considered. Theoretical proposals exist, where the strong interaction between Rydberg atoms is distributed over all atoms in a larger sample by weakly dressing them with a Rydberg state [85, 86]. The first part of this work is dedicated to the question, whether this effect is observable in the present experimental setup. This question is tackled both theoretically and experimentally. Simulations of realistic, experimentally relevant situations are presented, based on a theoretical model, developed in the framework of this thesis. The results are combined with experience gathered from experimental investigations, in order to identify practical challenges and provide possible solutions.

Then, the studies are extended to Rydberg states at higher principal quantum numbers reaching $n = 200$. This corresponds to more than 50-times larger Rydberg atoms, compared to previous work with this apparatus. Thus, an extreme regime is reached, where tens of thousands of atoms are located inside a single Rydberg atom, similar as in the measurements of Amaldi and Segrè. However, the regime investigated here differs also qualitatively from previous work, due to the properties of the Bose-Einstein condensate. The blockade radius r_B of these Rydberg states is larger than the size of the BEC (see Figure 0.2c). This offers the possibility to excite a single Rydberg atom in the condensate. The effect of the positively charged Rydberg core is negligible compared to the impact of the Rydberg electron, as already shown by Fermi [14]. Therefore, the system can be regarded as a single electron, trapped in a well-defined quantum state, inside a quantum gas. The Rydberg electron couples strongly to the BEC, creating excitations of single particles and phonons in the condensate. The experimental results can be understood using a model, based on Bogoliubov's microscopic theory of a weakly interacting Bose gas. This model has been developed in a close collaboration with the Institut für Theoretische Physik III of the university of Stuttgart, in particular with David Peter and Hans Peter Büchler. The main results of this thesis are the preparation of this intriguing system and first experiments studying the interaction of a single electron with a BEC. The demonstration of this fundamental system provides the basis for a wide range of further work. Some of the paths, opened up by the results presented here, are already followed by different groups.

This thesis is structured as follows:
First in part I, some basic properties of Rydberg atoms and Bose-Einstein condensates are reviewed in chapters 1 and 2. This facilitates the discussion in the following main theory chapter 3. This chapter starts with the derivation of a simple model of Rydberg dressing, that provides an intuitive understanding of the collective processes involved. Based on this model, simulations are presented, covering the parameter space, which is experimentally relevant. Afterwards, the direct interaction between a Rydberg atom and a dense surrounding gas is discussed. Both, the Rydberg core and the Rydberg electron are considered. In particular, the work of Fermi and its subsequent refinements are reviewed and later on applied to calculate the impact of a single Rydberg electron onto a BEC.
In part II, a short introduction to the experimental setup is given. It consists basically of a BEC apparatus for preparing ultracold samples of rubidium ^{87}Rb (chapter 4) and a laser system to excite Rydberg atoms (chapter 5). Here, the focus is on the requirements for exciting Rydberg atoms at high principal quantum numbers $n > 100$ in a BEC. This involves both substantial changes to the hardware and to the experimental sequence.
In part III, the experimental results are presented. First, the work on Rydberg dressing is summarized in chapter 6, listing both principal and practical challenges, that are impeding an experimental realization so far. In addition, possible solutions for this set of problems are proposed. Afterwards, the results on the coupling of a single Rydberg electron to a Bose-Einstein condensate, the main outcome of this work, are discussed. In chapter 7, the observations are treated focussing on the Rydberg atom, whereas in chapter 8, the impact of the Rydberg electron as an impurity on the BEC is considered.
Finally, a perspective of a wide range of further possible experiments and applications is given. This overview contains both ideas, that are already in the stage of being implemented, and other proposals, that are lying further ahead.

This thesis is accompanied by a comprehensive appendix, containing explicit calculations and further discussion, that allow to fully comprehend the content in minute detail.
All calculations and formulas are given on purpose in SI units. This might be at the expense of slightly more cumbersome expressions, but helps to avoid misconceptions caused by non-standard units [87].

Part I

Theoretical Basics

1 Rydberg atoms

Rydberg atoms are excited atoms with one or more electrons in a state with high principle quantum number n. Most physical properties of these atoms are dominated by the highly excited Rydberg electron, orbiting far away from the Rydberg core. Extensive literature is available reviewing general properties of Rydberg atoms [37] and e.g. their application for quantum information [7]. Therefore, in this chapter only some basic properties are shortly introduced, which are needed for further discussions in later chapters. This comprises also more general topics like atom-light interaction that are reviewed in the context of Rydberg atoms.

1.1 Atom-light interaction

All experiments discussed in this thesis are based on the optical excitation of Rydberg atoms using laser light. In order to describe the interaction with radiation, the internal structure of the atoms can be simplified to a three-level and finally to a two-level system for most problems within the framework of this thesis. Furthermore, the laser light contains always many photons so that it can be assumed as classical and the quantization of the light field can be neglected. In the following, the very basic equations governing the evolution of a two- and three-level system, coupled by a classical light field, are briefly reviewed. This discussion forms the basis for the theory developed in section 3.1.

1.1.1 Two-level atom

In the first approximation, an atom in a laser field can be described as a two-level system as depicted in Figure 1.1. The system then consists of a ground state $|g\rangle$ and an excited state $|e\rangle$, which are the eigenvalues of the unperturbed Hamiltonian $\hat{H}_0$, describing the system without the coupling light field. The evolution of the system is governed by the time-dependent Schrödinger equation:

$$i\hbar\frac{\partial\Psi(\vec{r},t)}{\partial t} = \hat{H}\Psi(\vec{r},t) \tag{1.1}$$

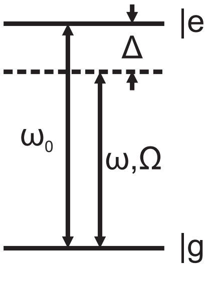

Figure 1.1: Sketch of the two-level system. The ground state $|g\rangle$ is coupled by a light field to the excited state $|e\rangle$. The frequency ω of the light is detuned by Δ from the energy separation $(E_e - E_g)/\hbar$ of the two states. The atom-light interaction results in a coupling with Rabi-frequency Ω.

The Hamiltonian $\hat{H} = \hat{H}_0 + \hat{H}_l$ is the sum of the Hamiltonian $\hat{H}_0$ describing the unperturbed system and terms $\hat{H}_l$ stemming from the interaction with monochromatic light. For a classical light field, the quantization can be neglected and $\hat{H}_l$ is given by the product of the dipole operator $\hat{\vec{d}} = e\hat{\vec{r}}$ and the electric field $\vec{E}(t) = \vec{E}_0 \cos(\vec{k}\vec{r} - \omega t)$ of a plane wave oscillating at frequency ω. In general, this frequency is detuned by $\Delta = \omega_0 - \omega$ from the energy separation $\hbar\omega_0 = E_e - E_g$ of the two states[1].

1.1.2 Rabi oscillations

The wavefunction $\Psi(\vec{r}, t)$ of the two-level system can be written as a linear combination with time-dependent coefficients $c_{g/e}(t)$:

$$\Psi(\vec{r}, t) = c_g(t) \left|g\right\rangle + c_e(t) \left|e\right\rangle e^{i\omega_0 t} \tag{1.2}$$

Inserting this ansatz into the Schrödinger equation (1.1) leads to a system of coupled differential equations

$$i\hbar\frac{\partial c_g}{\partial t} = c_e \hbar \tfrac{\Omega^*}{2}(e^{i\Delta t} + e^{-i(\omega+\omega_0)t}) \tag{1.3}$$

$$i\hbar\frac{\partial c_e}{\partial t} = c_g \hbar \tfrac{\Omega}{2}(e^{i(\omega+\omega_0)t} + e^{-i\Delta t}) \tag{1.4}$$

where the Rabi frequency Ω has been introduced as[1]:

$$\Omega = \vec{E}_0 \, e \left\langle e\right| \hat{\vec{r}} \left|g\right\rangle / \hbar \tag{1.5}$$

Here, the dipole approximation [88] has been applied, in which the electric field $\vec{E}(\vec{r}, t)$ is assumed as constant over the spatial extent of the two-level atom. This holds true for wavelengths $\lambda = 2\pi/|\vec{k}|$ smaller than the extent of the atom. The equations can be further simplified using the rotating-wave approximation, where the time evolution of the coefficients $c_{g/e}(t)$ is assumed to be much slower than the sum frequency $\omega + \omega_0$. Thus, terms oscillating at this frequency average to zero. This is a good approximation for weak driving fields with $\Omega \ll \omega$ and small detunings $\Delta \ll \omega$[2]. The system of first-order differential equations (1.3) and (1.4) in the simplified form

$$i\frac{\partial c_g}{\partial t} = c_e \tfrac{\Omega^*}{2} e^{i\Delta t} \tag{1.6}$$

$$i\frac{\partial c_e}{\partial t} = c_g \tfrac{\Omega}{2} e^{-i\Delta t} \tag{1.7}$$

can be converted into a decoupled second-order differential equation:

$$\frac{\partial^2 c_e}{\partial t^2} + i\Delta\frac{\partial c_e}{\partial t} + \frac{\Omega^2}{4} c_e = 0 \tag{1.8}$$

---

[1] In this chapter, both the detuning Δ and the Rabi frequency Ω are defined as angular frequencies in order to match textbook convention [88]. From chapter 3 on, ordinary frequencies are used, because they are more common for discussing experimental parameters.

[2] The standard counterexample is a far off-resonant dipole trap with infrared light, where $\omega_0 + \omega \approx \omega_0 - \omega$ and the counter-rotating terms have to be kept.

Solving this equation under the condition $c_e(0) = 0$ leads to $c_e(t) \propto e^{i\Delta/2t} \sin(\sqrt{\Omega^2 + \Delta^2}/2t)$. The probability $|c_e(t)|^2$ to find the system in the excited state can then be calculated from (1.7), accounting for the normalization $|c_g|^2 + |c_e|^2 = 1$. The system is found to undergo Rabi oscillations with an effective Rabi frequency $\sqrt{\Omega^2 + \Delta^2}$ and amplitude $\Omega^2/(\Omega^2 + \Delta^2)$:

$$|c_e(t)|^2 = \frac{\Omega^2}{\Omega^2 + \Delta^2} \sin^2(\sqrt{\Omega^2 + \Delta^2}/2\,t) \tag{1.9}$$

At short times t, the population $|c_e(t)|^2$ in the excited state rises to first order quadratically in $\sqrt{\Omega^2 + \Delta^2}t$.

1.1.3 AC Stark effect

In order to study steady state properties of a two-level system dressed with a light field [88], one can remove the explicit time dependence from equations (1.6) and (1.7) by substituting the coefficients $c_g'(t) = c_g(t)$, $c_e'(t) = c_e(t)\, e^{i\hbar\Delta t}$. In this basis, the Hamiltonian is of the form[3]:

$$\hat{H} = \hbar \begin{pmatrix} 0 & \Omega^*/2 \\ \Omega/2 & -\Delta \end{pmatrix} \tag{1.10}$$

Diagonalization of this Hamiltonian provides eigenenergies of the dressed two-level system:

$$E_{1/2} = \frac{\hbar}{2}\left(-\Delta \pm \sqrt{|\Omega|^2 + \Delta^2}\right) \tag{1.11}$$

The AC Stark effect shifts the two bare levels by $\mp\hbar\Delta/2\,(1 - \sqrt{|\Omega|^2/\Delta^2 + 1})$. For weak coupling laser fields $\Omega/\Delta \ll 1$, the expansion $\pm|\Omega|^2/(4\Delta)$ is commonly used [88]. However, for some effects higher order terms become important, even at weak dressing $\Omega/\Delta \ll 1$, as it is discussed in section 3.1. The excited state fraction of the new ground state can be calculated from the normalization condition of the eigenvectors to

$$f = \frac{|\Omega|^2}{2(|\Omega|^2 + \Delta^2 - \Delta\sqrt{|\Omega|^2 + \Delta^2})} \tag{1.12}$$

This expression simplifies to $f \approx |\Omega|^2/(4\Delta^2)$ for weak dressing $\Omega/\Delta \ll 1$.

1.1.4 Effective two-level atom

The concept of treating a three-level atom, coupled by two laser fields, is similar to the one of the two-level atom in the previous paragraph. Nevertheless, the additional level causes a wide range of further interesting effects. This comprises electromagnetically induced transparency (EIT), coherent population trapping, Autler-Townes splitting and Raman transitions [91, 92, 93]. In the framework of the experiments in this thesis, only a simple special case is relevant, that is discussed in the following. The excitation of a Rydberg state via a two-photon transition can

---

[3] There are different sign conventions [89]. Here, red detuning corresponds to $\Delta < 0$ [90].

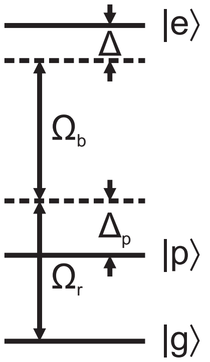

Figure 1.2: Sketch of the three-level atom. The ground state $|g\rangle$ is coupled by two light fields with Rabi frequencies Ω_r and Ω_b to the excited state $|e\rangle$. The light field driving the lower transition is detuned by Δ_p from an intermediate state $|p\rangle$. The detuning of the two-photon transition is Δ.

be described as a three-level atom with an intermediate state $|p\rangle$. Two laser fields with Rabi frequencies Ω_r and Ω_b are coupling the ground state $|g\rangle$ and the Rydberg level $|e\rangle$ with a total detuning Δ. In order to achieve coherent excitation, a large detuning Δ_p has to be chosen in order to avoid population of the intermediate state $|p\rangle$, which is typically short-lived (e.g. decay rate $\Gamma = 2\pi \cdot 6.067\,\mathrm{MHz}$ for $5P_{3/2}$ state of ^{87}Rb [94]). Within the same approximations as in paragraph 1.1.2, the Hamiltonian in the basis of ground state $|g\rangle$, intermediate state $|p\rangle$ and excited (Rydberg-)state $|e\rangle$ can be written as:

$$\hat{H} = \hbar \begin{pmatrix} 0 & \Omega_r/2 & 0 \\ \Omega_r/2 & -\Delta_p & \Omega_b/2 \\ 0 & \Omega_b/2 & -\Delta \end{pmatrix} \tag{1.13}$$

For simplicity, the Rabi frequencies are here assumed to be real. For large detunings $\Delta_p \gg \Omega_r$, the population of the intermediate state $|p\rangle$ according to equation (1.12) is small, scaling as $\Omega_r^2/(4\Delta_p^2)$. Furthermore, the time evolution in equation (1.9) at frequency $\sqrt{\Omega_p^2 + \Delta_p^2}/2$ becomes much faster than the time dependence expected for the other states. Thus, for calculating the populations in the ground and Rydberg state, one can assume a constant time averaged population of the intermediate state. Thereby, the state $|p\rangle$ can be virtually removed from the Schrödinger equation. The Hamiltonian in the remaining basis $|g\rangle$ and $|e\rangle$, resulting from this so called adiabatic elimination, then can be rewritten as [95]:

$$\hat{H} = \hbar \begin{pmatrix} \frac{\Omega_r^2}{4\Delta_p} & \frac{\Omega_r\Omega_b}{4\Delta_p} \\ \frac{\Omega_r\Omega_b}{4\Delta_p} & \frac{\Omega_b^2}{4\Delta_p} - \Delta \end{pmatrix} \tag{1.14}$$

A comparison of this result with the Hamiltonian of the two-level system in equation (1.10) shows that the resulting system behaves like a two-level atom, coupled by an effective Rabi frequency:

$$\Omega = \frac{\Omega_r\Omega_b}{2\Delta_p} \tag{1.15}$$

If the detuning Δ_p from the intermediate state is also much larger than the Rabi frequencies Ω_r and Ω_b, the additional Stark shift $\frac{\Omega_r^2}{4\Delta_p} - \frac{\Omega_b^2}{4\Delta_p}$ can be neglected and the effective detuning is equal to the detuning Δ of the two-photon transition. This assumption is fulfilled in good approximation in the experiments described in this thesis.

The values of the two Rabi frequencies Ω_p and Ω_r in the experiments are calculated [96] according to equation (1.5) from the measured intensities $I = c\epsilon_0/2|E_0|^2$, using the dipole matrix elements $\langle e|\,\hat{r}\,|g\rangle$ from [84].

1.2 Interaction between Rydberg atoms

Their strong binary interactions make Rydberg atoms appealing candidates for e.g. quantum information and simulation. In particular, these kind of interaction can exceed the interaction between neutral ground state atoms by much more than ten orders of magnitude [7]. After a basic introduction on binary interaction between Rydberg atoms, the impact on to the excitation dynamics is discussed, forming the basis for the theory developed in section 3.1 and the experiments presented in chapter 7.

1.2.1 Van-der-Waals interaction

The dominant term in the interaction of a pair of Rydberg atoms, separated by a vectorial distance $R\vec{n}$ ($|\vec{n}| = 1$), is the electric dipole interaction [97]:

$$U_{dd} = \frac{\vec{d_1}\vec{d_2} - 3(\vec{n}\vec{d_1})(\vec{n}\vec{d_2})}{4\pi\epsilon_0 R^3} \tag{1.16}$$

where $\hat{\vec{d}} = e\hat{\vec{r}}$ is the operator of the electric dipole moment. In the absence of external fields and possible resonances (see subsequent paragraph 1.2.2), Rydberg states do not have a permanent electric dipole moment. The first term is therefore the van-der-Waals interaction, caused by the interaction of induced dipole moments. In this case, the interaction energy can be calculated using second order perturbation theory:

$$V_{vdW} = -\sum_{j,k\neq i} \frac{\langle k| \langle l| U_{dd} |i\rangle |j\rangle}{E_k + E_l - (E_i + E_j)} = \frac{C_6(i)}{R^6} \tag{1.17}$$

For a pair of atoms in state $|i\rangle$, one has to sum over all possible couplings to other pair states $|j\rangle |k\rangle$, mediated by the dipole-dipole operator (1.16). Due to the weighting with the inverse energy difference to the initial pair state, only pair states close in energy to the initial state contribute significantly. Scaling formulas for the interaction coefficients describing the interaction between pairs of equal Rydberg S-, P- and D-states of alkali atoms can be found in [82].

1.2.2 Förster resonant interaction

Second order perturbation theory breaks down, if the denominator in equation (1.17), the so called Förster defect $\Delta_F = E_k + E_l - (E_i + E_j)$, vanishes for one pair state k, l. On such a Förster resonance, a pair of dipole coupled Rydberg states is degenerate with the initial pair of Rydberg atoms. In a simple model, one can neglect all other states with larger Förster defect and consider only a pair of two-level atoms, labelled $i = 1$ and 2 (see Figure 1.3). This single interaction channel model is a good approximation in the close vicinity of a single Förster resonance. The two levels e and g in the two atoms are in general not identical; their energy

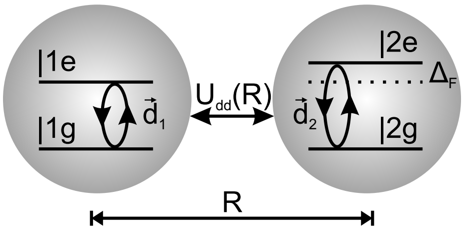

Figure 1.3: Sketch of single interaction channel model for Förster resonant interaction: A pair of two-level systems 1 and 2, where the transitions between the two levels is dipole allowed. The energy splittings differ by the Förster defect Δ_F. The transition dipole moments $\vec{d_1}$ and $\vec{d_2}$ interact via the dipole-dipole interaction operator $U_{dd}(R)$, which depends on the relative distance R between 1 and 2.

splittings differ by the Förster defect Δ_F. The only requirement is that the transition $|ig\rangle \leftrightarrow |ie\rangle$ is dipole allowed. In this basis, the Hamiltonian of the system is of the form (cf. equation 1.10):

$$\hat{H} = \hbar \begin{pmatrix} 0 & V_{dd} \\ V_{dd} & \Delta_F \end{pmatrix} \tag{1.18}$$

Here, $V_{dd} = \langle 1e, 2g| \, U_{dd} \, |1g, 2e\rangle = C_3/R^3$ describes the interaction of the two oscillating transition dipole moments $\vec{d_i}$ in the the two systems $i = 1, 2$. Diagonalizing this Hamiltonian leads to the energies

$$E_{1/2} = \frac{\Delta_F}{2} \pm \sqrt{\frac{\Delta_F^2}{4} + V_{dd}^2} \tag{1.19}$$

Close to the Förster resonance, where $\Delta_F \ll V_{dd}$, the interaction becomes dipolar:

$$E_{1/2}(\Delta_F \ll V_{dd}) \approx \pm V_{dd} = \pm \frac{C_3}{R^3} \tag{1.20}$$

The eigenstates in this limit are a linear combination $1/\sqrt{2}(|1g, 2e\rangle \pm |1e, 2g\rangle)$ of the unperturbed states. The sign of the Förster defect Δ_F then determines, whether the repulsive or the attractive branch is relevant.

Far from resonance, at large Förster defect $\Delta_F \gg V_{dd}$, the unperturbed states are nearly unaffected and the van-der-Waals interaction (equation 1.17) is recovered:

$$E_{1/2}(\Delta_F \gg V_{dd}) \approx \begin{cases} -\frac{V_{dd}^2}{\Delta_F} & = -\frac{C_3^2}{\Delta_F R^6} \\ \Delta_F + \frac{V_{dd}^2}{\Delta_F} & = \Delta_F + \frac{C_3^2}{\Delta_F R^6} \end{cases} \tag{1.21}$$

In Rydberg atoms, some states can be tuned into resonance by applying microwaves [95, 98] or small electric fields [99, 100, 101, 102, 103, 104]. By changing the Förster defect Δ_F, one can therefore easily change the character of the Rydberg-Rydberg interaction from van-der-Waals to dipolar and control the sign of the interaction close to resonance [10]. Furthermore, the dipole-dipole interaction V_{dd} typically shows an angular dependence [105, 106]. These effects and the relevance of Förster resonances in different physical and biological systems are discussed in depth in [11].

1.2.3 Rydberg blockade and collective excitation

The strong mutual interaction of Rydberg atoms has an important consequence for the excitation dynamics. A laser field couples a sample of identical atoms to the Rydberg state with Rabi frequency Ω as discussed in section 1.1, if the laser frequency is tuned to resonance. However, the strong interaction between two Rydberg atoms can shift states with more than one Rydberg excitation out of resonance. As a result, multiple Rydberg atoms can be excited only at distances where the interaction energy $V(\vec{r})$ does not exceed the excitation bandwidth $\hbar\Delta\omega$ of the driving laser field. Thus, without tuning the laser frequency, no further Rydberg excitation is possible in a region around one Rydberg atom, which is defined by the relation:

$$|V(\vec{r})| \leq \hbar\Delta\omega \tag{1.22}$$

In case of angular-dependent interaction, the shape of the blockaded volume becomes asymmetric. For isotropic van-der-Waals interaction $V(r) = C_6/r^6$, equation (1.22) defines a sphere with blockade radius

$$r_B = \sqrt[6]{\frac{C_6}{\hbar\Delta\omega}} \tag{1.23}$$

The excitation bandwidth can be given by power broadening ~Ω, technical sources of laser broadening or by the Fourier width in pulsed experiments. The C_6 coefficients for Rydberg S-states are scaling to first order with the principal quantum number $(n-\delta_0)^{11}$ [82]. The blockade radius is therefore increasing with $(n-\delta)^{11/6}$, assuming a constant excitation bandwidth $\Delta\omega$.
The mean interparticle distance in a gas of particle density ρ can be approximated as the Wigner-Seitz radius

$$r_m = \sqrt[3]{\frac{3}{4\pi\rho}} \tag{1.24}$$

If the density of an atomic sample is high enough and hence this length r_m is smaller than the blockade radius r_B, the Rydberg blockade manifests itself first of all as a reduced fraction of atoms in the Rydberg state. This aspect of Rydberg blockade is a crucial element in the application of Rydberg atoms in quantum optics and quantum information [7]. This comprises for example quantum logic gates [39, 40], single photon sources [107, 108] and single photon switches [109, 110].
Furthermore, there is an effect on the dynamics of the excitation process [111, 112]. If all N_c atoms inside a blockade volume are indistinguishable, the Rydberg excitation becomes delocalized and effectively shared among all atoms. Due to symmetry under permutation of atoms, the only state, that is coupled by the light field to the ground state $|N_c, 0\rangle = |g_1, g_2, ..., g_{N_c}\rangle$ of the system, is a linear combination of the form:

$$|N_c, 1\rangle = \frac{1}{\sqrt{N_c}} \sum_{i=1}^{N_c} |g_1, g_2, ..., r_i, ..., g_{N_c}\rangle \tag{1.25}$$

where g_i and r_i denote an atom in the ground and Rydberg state respectively. Here, the relative phases between the different states have been set to 1. This is a good approximation as long as the atoms are not separated by distances larger than the excitation wavelength. The coupling to the ground state is then given as the matrix element (see section 1.1):

$$\langle N_c, 1| \hat{H}_l |N_c, 0\rangle = \hbar\sqrt{N_c}\Omega/2 \tag{1.26}$$

The comparison with equation (1.10) shows that the coupling of the collective Rydberg state is increased by a factor $\sqrt{N_c}$, compared to the single atom matrix element. An ensemble consisting of N_c atoms inside one blockade sphere, coupled to the Rydberg state with Rabi frequency Ω, can therefore be treated as a single effective two-level atom, a so called super atom [113], that undergoes Rabi oscillations at the collectively enhanced Rabi frequency $\sqrt{N_c}\Omega$. Collectively enhanced Rabi oscillations have been demonstrated experimentally with a single super atom, consisting of two [114, 115] or multiple [116, 117] atoms. In larger many-body systems, inhomogeneities, both in the atomic density and in the coupling laser field, reduce the visibility of collective Rabi oscillations. In that case, saturation curves with an enhanced initial slope can be observed [118, 84]. Even though the super atom model has been very successful in describing the behaviour of strongly interacting Rydberg many-body systems (see e.g. [118, 119] and section 3.1), some care has to be taken in applying the concept of blockade. In principle, it is only applicable in the case of pure binary interaction. For example, already in the case of only three atoms and dipolar interaction, there are non-interacting and therefore non-blockaded configurations [120, 121]. Moreover, any effect that makes the atoms inside the blockade radius distinguishable, as for example inhomogeneous energy shifts on the same order as the Rydberg-Rydberg interaction energy, requires considerable modification of the simple concept of Rydberg blockade presented here. Such effects are faced later in section 7.3.

2 Bose-Einstein condensates

A system of weakly interacting bosons reaching a critical phase space density is undergoing a phase transition into a state, where all particles are in the ground state. At this point, the thermal de Broglie wavelength $\lambda_{\mathrm{dB}} = h/\sqrt{2\pi m k_B T}$ of the particles with mass m, density ρ and temperature T (k_B: Boltzmann constant) becomes comparable[1] to the interparticle distance ~$\rho^{-1/3}$. This phenomenon, the so called Bose-Einstein condensation, has been predicted by Einstein in 1924 [42] based on earlier work of Bose [41]. So far, Bose-Einstein condensates of cold atomic gases [4, 5], quasiparticles in solid state systems [122, 123, 124, 125, 126], and photons [127] have been observed.

The condensation of trapped, weakly interacting ultracold atomic gases is a crucial prerequisite for the experiments discussed in part III. Several review articles [128, 129] and textbooks (e.g. [53, 68, 88]) deal with this special case. Furthermore, there is a considerable overlap with the theory of superfluidity, developed in the context of liquid helium ^{4}He [50]. In this chapter, the most important results are recapitulated, allowing for convenient reference in the subsequent discussions.

2.1 Gross-Pitaevskii equation

A Bose-Einstein condensate under typical experimental conditions [129] can be described as a nonuniform dilute Bose gas. The many-body system consists of N bosons, that are interacting with a two-body interaction potential $V(\vec{r}-\vec{r}\,')$. The density ρ is low enough, such that the range of the interaction is much smaller than the mean interparticle distance $n^{-1/3}$. An external trapping potential $V_e(\vec{r})$ finally makes the gas nonuniform. In this treatment, three-body collisions are explicitly excluded. This kind of collisions would eventually make a real physical system crystallize into a solid configuration. The ground state of such a model therefore describes in reality only a metastable configuration. Then, the many-body Hamiltonian $\hat{H}$ in second quantization reads [128]:

$$\hat{H} = \int \hat{\Psi}^\dagger(\vec{r}) \left[-\frac{\hbar^2}{2m}\nabla^2 + V_e(\vec{r}) \right] \hat{\Psi}(\vec{r})\, d\vec{r} + \frac{1}{2} \iint \hat{\Psi}^\dagger(\vec{r})\hat{\Psi}^\dagger(\vec{r}\,')V(\vec{r}-\vec{r}\,')\hat{\Psi}(\vec{r}\,')\hat{\Psi}(\vec{r})\, d\vec{r} d\vec{r}\,' \tag{2.1}$$

Here, $\hat{\Psi}(\vec{r})$ and $\hat{\Psi}^\dagger(\vec{r})$ are the bosonic field operators, that annihilate and create a particle at position $\vec{r}$ respectively. They can be expressed in terms of single particle wavefunctions ϕ_i [68]:

$$\hat{\Psi}(\vec{r}) = \sum_i \phi_i \hat{a}_i \tag{2.2}$$

---

[1] The derivation of the more exact condition $\lambda_{\mathrm{dB}} \approx 1.38\, n^{-1/3}$ can be found e.g. in [88].

The corresponding creation and annihilation operators $\hat{a}_i^\dagger$ and $\hat{a}_i$ fulfil the usual bosonic commutation rules:

$$[\hat{a}_i, \hat{a}_j^\dagger] = \delta_{i,j}, \quad [\hat{a}_i, \hat{a}_j] = 0 \tag{2.3}$$

Furthermore, $\hat{a}_i^\dagger \hat{a}_i$ is the operator of the occupation number of state i. In the regime of Bose-Einstein condensation, there is a macroscopic occupation $N_0 \gg 1$ in the ground state ϕ_0. Thus, the eigenvalues of $\hat{a}_0^\dagger$ and $\hat{a}_0$, $\sqrt{N_0+1}$ and $\sqrt{N_0}$ can in good approximation be assumed as identical and the operators $\hat{a}_0^\dagger$ and $\hat{a}_0$ can be treated as complex numbers $\hat{a}_0^\dagger \approx \hat{a}_0 \approx \sqrt{N_0}$. In a generalization of the Bogoliubov approach [15], the bosonic field operator $\hat{\Psi}(\vec{r},t)$ can then be written in a decomposed form, where the Bose-condensed part is separated as a classical field $\psi(\vec{r},t) = \sqrt{N_0}\psi_0(\vec{r},t)$ [128, 68]:

$$\hat{\Psi}(\vec{r},t) = \psi(\vec{r},t) + \hat{\Psi}'(\vec{r},t) \tag{2.4}$$

The so called wavefunction of the condensate $\psi(\vec{r},t)$ has the meaning of an order parameter. Its modulus $|\psi(\vec{r},t)|^2 = N_0|\psi_0(\vec{r},t)|^2$ is the density distribution of the BEC. The operator $\hat{\Psi}'(\vec{r},t) = \sum_{i\neq 0} \phi_i \hat{a}_i$ accounts for population in states with higher momentum. This population can be caused by external perturbations (see also paragraph 3.2.4) or a short-range part of the interatomic interaction potential $V(\vec{r}-\vec{r}\,')$ [53]. Hence in interacting systems, there is a certain fraction of atoms in higher modes even at zero temperature (see paragraph 2.3.1).

In the regime, where only binary collisions play a role and at low temperatures, the interatomic interaction is fully characterized by the constant s-wave scattering length a [128]:

$$V(\vec{r}-\vec{r}\,') = g\delta(\vec{r}-\vec{r}\,'), \quad g = \frac{4\pi\hbar^2 a}{m} \tag{2.5}$$

For calculating the ground state of the system, the part $\hat{\Psi}'(\vec{r},t)$ can be neglected in equation (2.4) under the condition of diluteness $\rho a^3 \ll 1$. This condition assures that the depletion of the condensate mode due to the interatomic interaction is small. Inserting the s-wave scattering potential (2.5) into the Heisenberg equation for the Hamiltonian (2.1) leads to [128]:

$$i\hbar\frac{\partial}{\partial t}\psi(\vec{r},t) = \left(-\frac{\hbar^2}{2m}\nabla^2 + V_e(\vec{r}) + g|\psi(\vec{r},t)|^2\right)\psi(\vec{r},t) \tag{2.6}$$

This is the time-dependent Gross-Pitaevskii equation (GPE) [130, 131]. It has the form of a Schrödinger equation with the external potential $V_e(\vec{r})$ and a nonlinear term $g|\psi(\vec{r},t)|^2$. This term describes the mean-field acting on a single particle and produced by the interaction with the surrounding other bosons. The time-independent GPE is then obtained using the ansatz $\psi(\vec{r},t) = \psi(\vec{r})e^{-i\frac{\mu}{\hbar}t}$ in equation (2.6):

$$\left(-\frac{\hbar^2}{2m}\nabla^2 + V_e(\vec{r}) + g|\psi(\vec{r})|^2\right)\psi(\vec{r}) = \mu\psi(\vec{r}) \tag{2.7}$$

Here, μ denotes the chemical potential [128].

Alternatively, the time-independent GPE can be also obtained by minimizing the energy functional $E(\psi)$:

$$E(\psi) = \int \left[\frac{\hbar^2}{2m}|\vec{\nabla}\psi(\vec{r})|^2 + V_e(\vec{r})|\psi(\vec{r})|^2 + g/2|\psi(\vec{r})|^4\right] d\vec{r} \tag{2.8}$$

This is the expectation value of the N-particle state, neglecting terms of order $1/N$ under the normalization condition $\int |\psi(\vec{r})|^2 d\vec{r} = N$ [53].

2.2 Thomas-Fermi approximation

If the density $|\psi(\vec{r})|^2$ varies slowly in space, the quantum pressure [68] or kinetic energy term $-\frac{\hbar^2}{2m}\nabla^2\psi(\vec{r})$ in equation (2.7) can be neglected [129]. This is usually the case for a large number of particles and typical trapping potentials [53]. The density $\rho(\vec{r}) = |\psi(\vec{r})|^2$ can be calculated analytically as:

$$\rho(\vec{r}) = 1/g\,(\mu - V_e(\vec{r})) \tag{2.9}$$

The formation of this density profile can be depicted as the particles filling the trapping potential $V_e(\vec{r})$ up to the value μ [129]. The chemical potential μ is then determined by the particle number N and the normalization condition $\int d\vec{r}\,\rho(\vec{r}) = N$.

For the present experimental situations, a cylindrically symmetric harmonic potential with trapping frequencies ω_r and ω_z can be assumed [132]:

$$V_e(\vec{r}) = \frac{1}{2}m\left(\omega_r^2(x^2+y^2) + \omega_z^2 z^2\right) \tag{2.10}$$

The condensate then has a parabolic density profile

$$\rho(\vec{r}) = \rho_0\left(1 - \frac{x^2+y^2}{r_0^2} - \frac{z^2}{z_0^2}\right) \tag{2.11}$$

with peak density

$$\rho_0 = \frac{m}{4\pi\hbar^2 a}\mu \tag{2.12}$$

and Thomas-Fermi radii

$$r_0 = \sqrt{\frac{2\mu}{m\omega_r^2}}, \quad z_0 = \sqrt{\frac{2\mu}{m\omega_z^2}} \tag{2.13}$$

The chemical potential μ is determined from the normalization condition as:

$$\mu = \left(\frac{15\hbar^2\sqrt{m}}{2^{5/2}}\omega_r^2\omega_z aN\right)^{2/5} \tag{2.14}$$

The peak density therefore scales with the total atom number:

$$\rho_0 = \left(\frac{15m^3}{2^{15/2}\pi^{5/2}\hbar^3 a^{3/2}}\omega_r^2\omega_z N\right)^{2/5} \tag{2.15}$$

2.3 Excitations in Bose-Einstein condensates

In this section, excitations in Bose-Einstein condensates are described in two different regimes, that are both relevant to understand the experimental results in chapter 8. First, a homogeneous Bose gas is considered in paragraph 2.3.1. This provides a good description, if the wavelength of the excitation is much smaller than the spatial extent of the condensate. Afterwards in paragraph 2.3.2, excitations in the limit of very large wavelengths and thus small momenta are discussed. In this case, the wavelength is on the order of the size of the BEC, leading to collective excitations of the whole condensate.

2.3.1 Bogoliubov excitations

In order to study the properties of elementary excitations in Bose-Einstein condensates, it is instructive to consider the simple case of a uniform Bose gas without external potential $V_e = 0$ in a volume V. The Hamiltonian (2.1) can be rewritten using the following expression for the field operators [68]:

$$\hat{\Psi}(\vec{r}) = \sum_{\vec{p}} \hat{a}_{\vec{p}} \frac{1}{\sqrt{V}} e^{i\vec{p}\vec{r}/\hbar} \tag{2.16}$$

Expressing the interaction potential $V(\vec{r})$ in terms of Fourier components

$$V_{\vec{q}} = \int V(\vec{r}) e^{-i\vec{q}\vec{r}/\hbar} \, d\vec{r} \tag{2.17}$$

the Hamiltonian (2.1) then reads:

$$\hat{H} = \sum_{\vec{p}} \frac{\vec{p}^2}{2m} \, \hat{a}^\dagger_{\vec{p}} \hat{a}_{\vec{p}} + \frac{1}{2V} \sum_{\vec{p}_1, \vec{p}_2, \vec{q}} V_{\vec{q}} \, \hat{a}^\dagger_{\vec{p}_1+\vec{q}} \hat{a}^\dagger_{\vec{p}_2-\vec{q}} \hat{a}_{\vec{p}_1} \hat{a}_{\vec{p}_2} \tag{2.18}$$

The idea of the Bogoliubov approach [15] is now to separate the ground state with zero momentum $\vec{p} = 0$ as in the ansatz (2.4). Only the zero momentum component $V_0 = \int V(\vec{r}) \, d\vec{r}$ of the interaction potential $V(\vec{r})$ is considered. Retaining only terms up to quartic order in the particle operators with $\vec{p} \neq 0$ and respecting momentum conservation leads to:

$$\hat{H} = \frac{V_0}{2V} \hat{a}^\dagger_0 \hat{a}^\dagger_0 \hat{a}_0 \hat{a}_0 \sum_{\vec{p}} \frac{\vec{p}^2}{2m} \, \hat{a}^\dagger_{\vec{p}} \hat{a}_{\vec{p}} + \frac{V_0}{2V} \sum_{\vec{p} \neq 0} \left(4 \hat{a}^\dagger_0 \hat{a}^\dagger_{\vec{p}} \hat{a}_0 \hat{a}_{\vec{p}} + \hat{a}^\dagger_{\vec{p}} \hat{a}^\dagger_{-\vec{p}} \hat{a}_0 \hat{a}_0 + \hat{a}^\dagger_0 \hat{a}^\dagger_0 \hat{a}_{\vec{p}} \hat{a}_{-\vec{p}} \right) \tag{2.19}$$

For macroscopic particle numbers N, the particle creation and annihilation operators can be replaced by $\sqrt{N}$ as argued in section 2.1. For the first term, a higher order approximation resulting from the normalization condition

$$\hat{a}^\dagger_0 \hat{a}_0 + \sum_{\vec{p} \neq 0} \hat{a}^\dagger_{\vec{p}} \hat{a}_{\vec{p}} = N \tag{2.20}$$

is used, where again only terms up to quartic in particle operators are kept:

$$\hat{a}^\dagger_0 \hat{a}^\dagger_0 \hat{a}_0 \hat{a}_0 = N^2 - 2N \sum_{\vec{p} \neq 0} \hat{a}^\dagger_{\vec{p}} \hat{a}_{\vec{p}} \tag{2.21}$$

Furthermore, the zero momentum component V_0 of the interaction potential is expressed in terms of the scattering length a up to second order [68, 75]:

$$V_0 = g \left(1 + \frac{g}{V} \sum_{\vec{p} \neq 0} \frac{m}{\vec{p}^2} \right) \tag{2.22}$$

The Hamiltonian (2.19) can then be written as:

$$\hat{H} = \frac{gN^2}{2V} + \sum_{\vec{p}} \frac{\vec{p}^2}{2m} \, \hat{a}^\dagger_{\vec{p}} \hat{a}_{\vec{p}} + \frac{\rho}{2g} \sum_{\vec{p} \neq 0} \left(2 \hat{a}^\dagger_{\vec{p}} \hat{a}_{\vec{p}} + \hat{a}^\dagger_{\vec{p}} \hat{a}^\dagger_{-\vec{p}} + \hat{a}_{\vec{p}} \hat{a}_{-\vec{p}} + \frac{mg\rho}{\vec{p}^2} \right) \tag{2.23}$$

In order to diagonalize this Hamiltonian, a linear transformation, the so called Bogoliubov transformation[2], is used:

$$\hat{a}_{\vec{p}} = u_p^* \hat{b}_{\vec{p}} + v_p \hat{b}^\dagger_{-\vec{p}}, \quad \hat{a}^\dagger_{\vec{p}} = u_p \hat{b}^\dagger_{\vec{p}} + v_p^* \hat{b}_{-\vec{p}} \tag{2.24}$$

The new operators $\hat{b}_{\vec{p}}$, $\hat{b}^\dagger_{\vec{p}}$ fulfil the bosonic commutator relation $[\hat{b}_{\vec{p}}, \hat{b}^\dagger_{\vec{p}'}] = \delta_{\vec{p},\vec{p}'}$. This imposes the condition $|u_p|^2 - |v_p|^2 = 1$ for the coefficients and one immediately obtains:

$$\hat{b}_{\vec{p}} = u_p \hat{a}_{\vec{p}} - v_p \hat{a}^\dagger_{-\vec{p}}, \quad \hat{b}^\dagger_{\vec{p}} = u_p^* \hat{a}^\dagger_{\vec{p}} - v_p^* \hat{a}_{-\vec{p}} \tag{2.25}$$

If one choses [68]

$$u_p, v_p = \sqrt{\frac{\vec{p}^2/(2m) + g\rho}{2\epsilon(\vec{p})} \pm \frac{1}{2}} \tag{2.26}$$

the Hamiltonian (2.23) can finally be written in the diagonalized form:

$$\hat{H} = E_0 + \sum_{\vec{p}} \epsilon(\vec{p})\, \hat{b}^\dagger_{\vec{p}} \hat{b}_{\vec{p}} \tag{2.27}$$

with the ground state energy

$$E_0 = g\frac{N^2}{2V} + \frac{1}{2}\sum_{\vec{p}\neq 0} \left(\epsilon(\vec{p}) - g\rho - \frac{\vec{p}^2}{2m} + \frac{mg^2\rho^2}{\vec{p}^2} \right) \tag{2.28}$$

and the Bogoliubov dispersion relation

$$\epsilon(\vec{p}) = \sqrt{\left(\frac{\vec{p}^2}{2m}\right)^2 + \frac{g\rho}{m}\vec{p}^2} \tag{2.29}$$

The structure of the Hamiltonian (2.27) shows that the original system of interacting particles can be described as a set of independent quasiparticles with energy $\epsilon(\vec{p})$ and creation and annihilation operator $\hat{b}^\dagger$ and $\hat{b}$. The ground state or BEC-mode is then the vacuum of quasiparticles:

$$\hat{b}_{\vec{p}} |0\rangle = 0 \tag{2.30}$$

The same results can be obtained in a macroscopic theory using hydrodynamic equations [53]. The analogy to hydrodynamics also helps to understand the nature of the quasiparticles introduced above. The shape of the dispersion relation is shown later in Figure 3.13a. In the limit of low momenta, the dispersion relation (2.29) becomes linear in the momentum:

$$\epsilon(\vec{p}) \approx c_s |\vec{p}| \tag{2.31}$$

---

[2] Note that there are different notations for the Bogoliubov coefficients u and v. Here, a notation close to [68] is used. The coefficients u_p and v_p are chosen to depend only on the absolute value $p = |\vec{p}|$ of the momentum, which greatly simplifies the calculation [53]. Furthermore, both variables are chosen complex conjugate. The latter modification imposes no restriction to generality; the first is justified for the uniform Bose gas by equation (2.26).

This is the dispersion relation of a sound wave with the Bogoliubov speed of sound:

$$c_s = \sqrt{\frac{g\rho}{m}} \tag{2.32}$$

In the opposite limit of large momenta p, one obtains the dispersion law of a free particle with an offset energy $-g\rho$ due to the interaction:

$$\epsilon(\vec{p}) \approx \frac{\vec{p}^2}{2m} - g\rho \tag{2.33}$$

The transition between the two regimes is located at momenta around $|\vec{p}| = \hbar/\xi$, with the healing length:

$$\xi = \frac{\hbar}{\sqrt{2mg\rho}} = \frac{\hbar}{\sqrt{2}mc_s} \tag{2.34}$$

Excitations at this momentum carry an energy, which is equal to the mean-field interaction $g\rho$. In practice, the healing length ξ therefore provides an important length scale for the reaction of a BEC wavefunction on local perturbations. Modifications of the condensate density distribution take place only at wavelengths larger than the healing length ξ.

Another interesting insight can be obtained by rewriting the normalization condition (2.20) in terms of Bogoliubov operators. Using equation (2.24), the macroscopic total particle number N then reads:

$$N = N_0 + \sum_{\vec{p}\neq 0} |v_p|^2 + \sum_{\vec{p}\neq 0} \left(|u_p|^2 + |v_p|^2\right) \hat{b}^\dagger_{\vec{p}} \hat{b}_{\vec{p}} + \sum_{\vec{p}\neq 0} \left(u_p^* v_p^* \hat{b}^\dagger_{\vec{p}} \hat{b}^\dagger_{-\vec{p}} + u_p v_p \hat{b}_{-\vec{p}} \hat{b}_{\vec{p}} \right) \tag{2.35}$$

The last sum describes processes, where pairs of quasiparticles with opposite momentum are created or annihilated. In the expectation value of eigenstates of the Hamiltonian (2.27), this term obviously vanishes. The physical interpretation of the other terms is as follows. In the ground state of an interacting gas, not all particles are in the zero-momentum state. This means that, even in the absence of real excitations, the occupation number N_0 in the ground mode is reduced by the so called quantum depletion $\sum_{\vec{p}\neq 0} |v_p|^2$, caused by the interaction between the particles. Evaluating this term explicitly using the result (2.26), one can show that this number is proportional to $\sqrt{\rho a^3}$ [53].

If an excitation with momentum $\vec{p}$ is added to the condensate, the number of particles in the ground mode is further reduced by an amount

$$\Delta N_{\text{Bog}}(\vec{p}) = |u_p|^2 + |v_p|^2 = \left(\frac{\vec{p}^2}{2m} + g\rho \right) / \epsilon(\vec{p}) \tag{2.36}$$

where equation (2.26) has been inserted.

2.3.2 Collective excitations

In the previous paragraph 2.3.1, the excitation spectrum of a homogeneous Bose gas was derived. These results are used later in paragraph 3.2.4 to calculate the effect of a Rydberg electron onto a Bose-Einstein condensate. As the discussion there shows, the description becomes invalid for excitations at low momenta p, since the number of atoms associated with one quasiparticle excitations diverges (see Figure 3.13c). Here, the finite size of the system becomes important and the description as a homogeneous Bose gas is thus not appropriate any more. Therefore in this paragraph, the description of BEC excitations in the limit of low momenta p, where the whole condensate is affected, is reviewed. This discussion forms the basis to explain the experimental observations in section 8.2.

The evolution of the nonuniform Bose gas is governed by the time-dependent Gross-Pitaevskii equation (2.6). Instead of a microscopic description as in paragraph 2.3.1, now a macroscopic description is adequate, since the focus here is on collective excitations. The Gross-Pitaevskii equation (2.6) can be rewritten to provide equations for macroscopic observables, the atomic density $\rho(\vec{r},t) = |\psi(\vec{r},t)|^2$ and the velocity field:

$$\vec{v}(\vec{r},t) = \frac{\hbar}{2mi}\left(\psi(\vec{r},t)\vec{\nabla}\psi^*(\vec{r},t) - \vec{\nabla}\psi(\vec{r},t)\psi^*(\vec{r},t)\right)/\rho(\vec{r},t) \tag{2.37}$$

Then, one obtains [133]:

$$\frac{\partial}{\partial t}\rho + \vec{\nabla}(\vec{v}\rho) = 0 \tag{2.38}$$

$$m\frac{\partial}{\partial t}\vec{v} + \vec{\nabla}\left(\delta\mu + \frac{1}{2}m\vec{v}^2\right) = 0 \tag{2.39}$$

Here, $\delta\mu$ is the change of the chemical potential with respect to its value μ in the ground state of the system (see equation 2.7):

$$\delta\mu = V_e(\vec{r}) + g\rho - \frac{\hbar^2}{2m\sqrt{\rho}}\vec{\nabla}^2\sqrt{\rho} - \mu \tag{2.40}$$

In the next step, the kinetic energy pressure term $\frac{\hbar^2}{2m\sqrt{\rho}}\vec{\nabla}^2\sqrt{\rho}$ is neglected compared to the interaction energy $g\rho$. This corresponds to the Thomas-Fermi approximation in section 2.2, which is valid if the particle number is large and the density distribution $\rho(\vec{r},t)$ is smooth. Note that here these requirements have to be met not only in the ground state, but also during the dynamic evolution of the system. In particular, this means that only excitations at large wavelengths are covered. Setting $\vec{v} = 0$, one directly obtains the stationary solution $\rho_0\vec{r}$ (see equation 2.9). Linearising equation (2.38) and (2.39) with respect to small density changes $\delta\rho(\vec{r},t) = \rho(\vec{r},t) - \rho_0(\vec{r})$ and velocities $\vec{v}(\vec{r},t)$ directly leads to:

$$\frac{\partial^2}{\partial t^2}\delta\rho = \vec{\nabla}\left[c(\vec{r})\vec{\nabla}\delta\rho\right] \tag{2.41}$$

Here, the quantity $c(\vec{r}) = \sqrt{\rho_0(\vec{r})g/m} = \sqrt{(\mu - V_e(\vec{r}))/m}$ plays the role of a local sound velocity [68]. Without external trapping potential ($V_e = 0$), one obtains sound waves at the Bogoliubov speed of sound $c = c_s$ (see equation 2.32), which is the low momentum limit for a homogeneous Bose gas, as obtained from microscopic theory (see paragraph 2.3.1).

For the present experimental situations (see section 4.1), the special case of a cylindrically symmetric harmonic trapping potential $V_e(\vec{r})$ is considered (see paragraph 2.2). With the ratio $\lambda = \omega_z/\omega_r$ of trapping frequencies, the differential equation (2.41) then reads:

$$m\frac{\partial^2}{\partial t^2}\delta\rho = \vec{\nabla}\left[\mu - \frac{1}{2}m\omega_r^2(x^2 + y^2 + \lambda^2 z^2)\vec{\nabla}\delta\rho\right] \tag{2.42}$$

Looking for periodically oscillating solutions, one can set $\delta\rho(\vec{r},t) = \rho(\vec{r})e^{-i\omega t}$ and obtains:

$$\begin{aligned}\omega^2\delta\rho =& \omega_r^2\left[r\frac{\partial}{\partial r} + (\lambda^2-1)r\cos\theta\left(\cos\theta\frac{\partial}{\partial r} - \sin\theta\frac{1}{r}\frac{\partial}{\partial\theta}\right)\right]\delta\rho \\ &- \left[\frac{\mu}{m} - \frac{\omega_r^2}{2}\left(r^2 + (\lambda^2-1)z^2\right)\right]\Delta\delta\rho\end{aligned} \tag{2.43}$$

For a spherical trapping potential ($\lambda = 1$), the density modulation $\delta\rho$ is proportional to the spherical harmonics Y_{l,m_l} and equation (2.43) directly leads to a dispersion relation [133]. In a cylindrically symmetric potential, the solution is more involved. However, there exist explicit solutions in some special cases. Due to the symmetry of the problem, the projection of the angular momentum onto the symmetry axis m_l is still a good quantum number and one can choose an ansatz $\delta\rho(\vec{r}) = f(r)r^lY_{l,m_l}(\theta,\phi)$ [133]. This will not necessarily lead to eigenstates, since the angular momentum l is not a good quantum number any more [134], causing coupling between modes at different l. For the simplest choice $f(r) = 1$, this ansatz fulfils Laplace's equation and the second term in equation (2.43) vanishes:

$$\omega^2 = \omega_r^2\left[l + (\lambda^2-1)\cos\theta\left(l\cos\theta - \sin\theta\frac{\frac{\partial}{\partial\theta}Y_{l,m_l}}{Y_{l,m_l}}\right)\right] \tag{2.44}$$

Using the definition of the spherical harmonics Y_{l,m_l} and usual recurrence formulas for the associated Legendre polynomials P_{l,m_l} [135], one obtains:

$$\omega^2 = \omega_r^2\left[l + (\lambda^2-1)\left(\frac{l^2-m_l^2}{2l-1} + \frac{(l+m_l)(l+m_l-1)}{2l-1}\frac{P_{l-2,m_l}(\cos\theta)}{P_{l,m_l}(\cos\theta)}\right)\right] \tag{2.45}$$

It becomes obvious from this expression that the ansatz leads to a solution for $m_l = \pm l$:

$$\omega^2 = \omega_r^2 l \tag{2.46}$$

and for $m_l = \pm(l-1)$:

$$\omega^2 = \omega_r^2(l-1+\lambda^2) \tag{2.47}$$

These two dispersion relations can fully describe the dipole oscillations ($l = 1$). These modes are purely radial ($|m_l| = 1$) and axial ($m_l = 0$) and it is therefore not surprising that the corresponding eigenfrequencies coincide with the unperturbed harmonic oscillator values $\omega = \omega_r$ for $|m_l| = 1$ and $\omega = \omega_z$ for $m_l = 0$ of the trap. This type of oscillations can occur in combination with centre of mass oscillations of the condensate in the trap at the same frequencies [136].

For $l > 1$, the simple ansatz with $f(r) = 1$ in general does not lead to a solution. For the quadrupole modes $l = 2$, one obtains a result only in the cases with $|m_l| = 2$ ($\Rightarrow \omega = \sqrt{2}\omega_r$) and $|m_l| = 1$ ($\Rightarrow \omega = \sqrt{\omega_r^2 + \omega_z^2}$). For $m_l = 0$, however, equation (2.45) results in a coupling to a mode with $l = m_l = 0$, corresponding to a monopole oscillation or breathing mode. This motivates an ansatz [53] of a coupled quadrupole oscillation and monopole oscillation of the form $\delta\rho(\vec{r}) = (a + br^2)Y_{0,0}(\theta,\phi) + cY_{2,0}(\theta,\phi)$. Here, for the monopole mode, the simplest non-trivial radius dependence $f(r) \propto 1 + const. \cdot r^2$ is chosen. Inserting the equivalent expression $\delta\rho(r_\perp, z) = A + Br_\perp^2 + Cz^2$ in cylindrical coordinates into the differential equation (2.43) leads

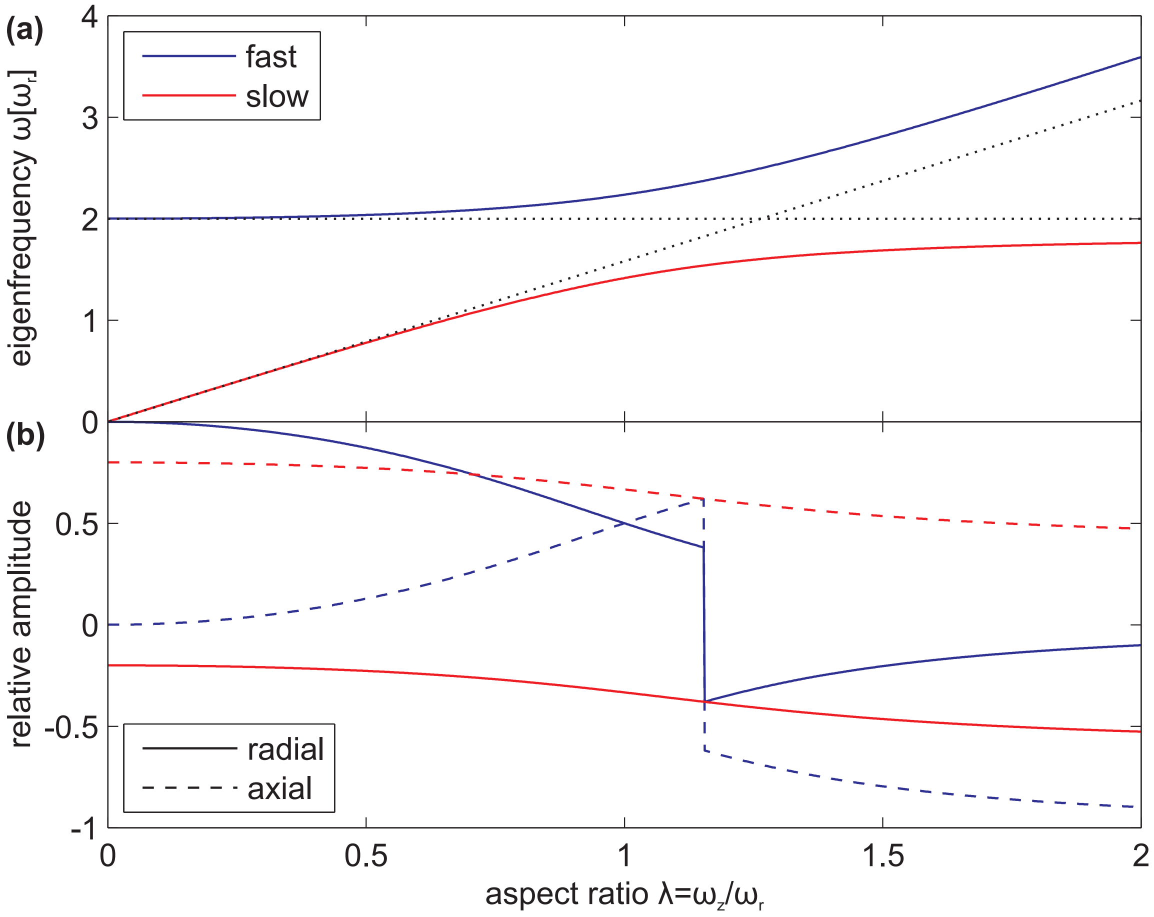

Figure 2.1: Eigenfrequencies and components of the coupled monopole and $m_l = 0$ quadrupole mode, depending on the BEC aspect ratio $\lambda = \omega_z/\omega_r$. In (a), the eigenfrequencies ω from equation (2.48) are shown in units of the radial trapping frequency ω_r. The asymptotic values for highly prolate condensates ($\lambda \ll 1$), $\omega = \sqrt{5/2}\omega_z$ for the slow and $\omega = 2\omega_r$ for the fast oscillation, are indicated as black dotted lines. In (b), the relative amplitudes $B/(|B| + |C|)$ and $C/(|B| + |C|)$ of the oscillation in radial (solid lines) and axial (dashed lines) direction for both the slow and the fast branch are plotted (same colour code as in a).

to a system of algebraic equations for the coefficients. One obtains two nontrivial $(B, C \neq 0)$ coupled modes with eigenfrequencies:

$$\omega^2 = \omega_r^2 \left(2 + \frac{3}{2}\lambda^2 \pm \sqrt{\frac{9}{4}\lambda^4 - 4\lambda^2 + 4} \right) \tag{2.48}$$

The dependence of these frequencies on the aspect ratio λ of the condensate is shown in Figure 2.1a. In the experimentally relevant limit of highly prolate condensates $\lambda \ll 1$, this leads to the two frequencies $\omega = \sqrt{5/2}\omega_z$ and $\omega = 2\omega_r$. For the current experimental parameters (see section 4.1), the correction of the exact expression (2.48) is less than half a percent compared to the limiting values. In Figure 2.1b, the relative amplitudes of the oscillation in radial and axial direction of the condensate are shown. In the limit of highly prolate BECs, the fast oscillation is purely radial, whereas the slow branch shows a four times larger amplitude in axial direction

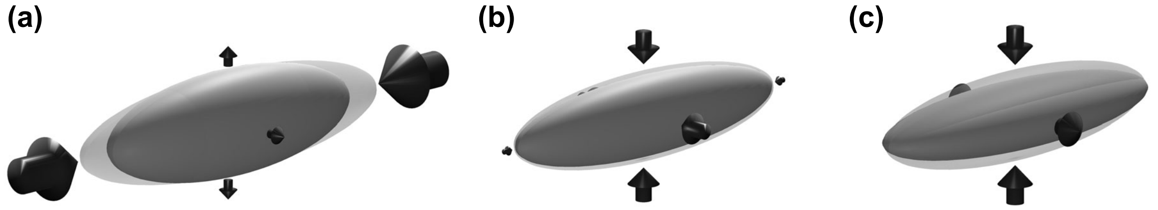

Figure 2.2: Shape of the three experimentally most relevant quadrupolar oscillations [129]. The slow quadrupolar $m_l = 0$ mode (a) at $\omega \approx \sqrt{5/2}\omega_z$ is out of phase in radial and axial direction. For the fast quadrupolar $m_l = 0$ mode (b) at $\omega \approx 2\omega_r$, the two directions are in phase, but the amplitude of the axial oscillation vanishes in the limit of highly prolate condensates ($\lambda \rightarrow 0$). The $|m_l| = 2$ quadrupole mode (c) at $\omega = \sqrt{2}\omega_r$ is purely radial.

than in radial direction. Furthermore, the two directions oscillate in phase for the fast quadrupolar mode and out of phase by π for the slow quadrupolar mode.

In Figure 2.2, the shape of the three experimentally most relevant modes are sketched for a prolate condensate ($\lambda < 1$). The first collective oscillations of Bose-Einstein condensates, observed in time of flight experiments, were the slow quadrupolar $m_l = 0$ mode and the $|m_l| = 2$ quadrupole mode [137]. Shortly afterwards, also the fast quadrupolar $m_l = 0$ mode was discovered [134] and studied in situ using nondestructive phase-contrast imaging [136]. For the present experiments, mainly the slow quadrupolar $m_l = 0$ oscillation is relevant. The excitation of the other modes is unlikely due to their asymmetry ($|m_l| = 2$) or higher frequency (fast $m_l = 0$). The good agreement of the eigenfrequency, calculated here, with the measured frequency (see section 8.2) shows that additional effects from finite temperature [138] and influence of the thermal cloud [136] can be neglected in the present case in good approximation.

3 Interaction of Rydberg atoms and ground state atoms

In this thesis, the interaction between Rydberg atoms and ground state atoms is investigated in two different approaches. First, in section 3.1, the possibility to imprint the strong binary interaction between Rydberg atoms (see section 1.2) onto all atoms in an atomic sample is discussed. Afterwards, in sections 3.2 and 3.3, the direct interaction between the constituents of the Rydberg atom, the Rydberg electron and the positively charged core, and multiple atoms in the ground state is studied.

3.1 Rydberg dressing

Rydberg atoms show a very strong van-der-Waals type interaction, typically more than ten orders stronger than the interaction between ground state atoms [7]. At short distances or close to a Förster resonance, there is a transition to a long range dipolar interaction, which can exhibit different kinds of angular dependence (see section 1.2). Furthermore, such a Förster resonance allows to easily tune the interaction strength [10]. As a result, Rydberg atoms show a large and tunable interaction, which makes them promising candidates for extending current schemes of quantum simulation with ultracold quantum gases [6].

The most obvious problem in using Rydberg excitation in quantum gases is the mismatch in timescales; the lifetime of Rydberg atoms in states with low angular momentum is on the order of tens of microseconds, whereas it typically takes three orders of magnitude longer for a many-body system to equilibrate in a typical experiment. This problem can be overcome by only weakly dressing [85, 86] the atomic ground state with a small fraction f of the Rydberg state, thereby enhancing the overall lifetime of the system by the factor $1/f$. As discussed in paragraph 1.2.3, the strong interaction between Rydberg atoms can result in collective effects in the excitation process, namely the suppression of further excitation in a volume around the first Rydberg atom, the so called Rydberg blockade effect. This effect has to be included in the calculation of the effective dressing potential, as has been already shown by a very simple two-atom model [9]. At typical densities in quantum degenerate atomic gases, the number of atoms inside a blockaded volume can become very large, which affects the dressing potential significantly. There is a transition from the pure two-body interaction to a collective N-body regime, with the effective interaction vanishing at large densities [8].

In this section, an analytical N-atom model for the dressing potential is described [139], that fully accounts for blockade effects. The analytical model, developed in the following, leads to the same results as the purely numerical approach in [8]. At the same time, it provides an intuitive picture for the processes involved and it furthermore allows significantly extended simulations closer to real experimental situations. In particular, the effect of Rydberg dressing on a three-dimensional asymmetric BEC and the role of Thomas-Fermi approximation in the Rydberg dressed condensate is studied. The implications for an experimental realization in the present setup are discussed in paragraph 3.1.4.

3.1.1 Binary interaction

Following the argumentation of [9], first the simple case of two atoms, dressed with a Rydberg state by a coupling field with Rabi frequency Ω and laser detuning Δ, is discussed. For simplicity, the interaction $V(R)$ between atoms in the particular Rydberg state are assumed to be of purely repulsive van-der-Waals type. In fact, it turns out that the actual shape of the Rydberg interaction plays a minor role, effectively reduced to the sign of the potential $V(R)$ and the value of the blockade radius r_B; one can incorporate attractive interaction by simply changing the sign of the detuning. Using the dressed states approach, that has been described in section 1.1 for a two-atomic system, the Hamiltonian in the basis $|gg\rangle$, $1/\sqrt{2}\,(|gr\rangle + |rg\rangle)$ and $|rr\rangle$ can be written as:

$$H = h \begin{pmatrix} 0 & \Omega/\sqrt{2} & 0 \\ \Omega/\sqrt{2} & -\Delta & \Omega/\sqrt{2} \\ 0 & \Omega/\sqrt{2} & -2\Delta + V(R) \end{pmatrix} \tag{3.1}$$

Here, the asymmetric singly excited state $1/\sqrt{2}\,(|gr\rangle - |rg\rangle)$ has been omitted, as it is not coupled by Ω. It is straightforward to obtain the new ground state of the system by diagonalizing (3.1), depending on the interatomic distance R. As can be seen in Figure 3.1a, this ground state shows a steep avoided crossing at around the blockade radius r_B for the combination of blue laser detuning and repulsive potentials, whereas for red detunings, there is a smooth step. The blockade radius r_B is defined as the interatomic distance, where the power broadening $\Omega_{\text{eff}} = \sqrt{\Omega^2 + (2\Delta)^2}$ equates to the absolute value of the Rydberg-Rydberg interaction $V(r_B)$ (cf. equation 1.22 in paragraph 1.2.3). For a repulsive van-der-Waals interaction $V(R) = C_6/R^6$, as it is present for most Rydberg states far from possible resonances (see section 1.2), one obtains:

$$r_B = \left(\frac{C_6}{h\sqrt{\Omega^2 + (2\Delta)^2}} \right)^{1/6} \approx \left(\frac{C_6}{h\,|2\Delta|} \right)^{1/6} \tag{3.2}$$

Here, the second part is the common approximation for weak dressing $\Omega^2/\Delta^2 \ll 1$. In the case of red detuning and repulsive potentials, the potential (up to an offset) is given as the Rydberg interaction potential, weighted with the probability f^2 to find both atoms in the Rydberg state. At large distances $R > r_B$, where the Rydberg blockade does not play a role, this factor is approximately (see equation (1.12) in paragraph 1.1.3):

$$f^2 = \frac{\Omega^4}{4(\Omega^2 + \Delta^2 + \Delta\sqrt{\Omega^2 + \Delta^2})^2} \approx \frac{\Omega^4}{16\Delta^4} \tag{3.3}$$

At interatomic distances $R \approx r_B$, the detuning of the doubly excited state $|rr\rangle$ increases due to the Rydberg-Rydberg interaction, tuning this state out of resonance. This is the well known

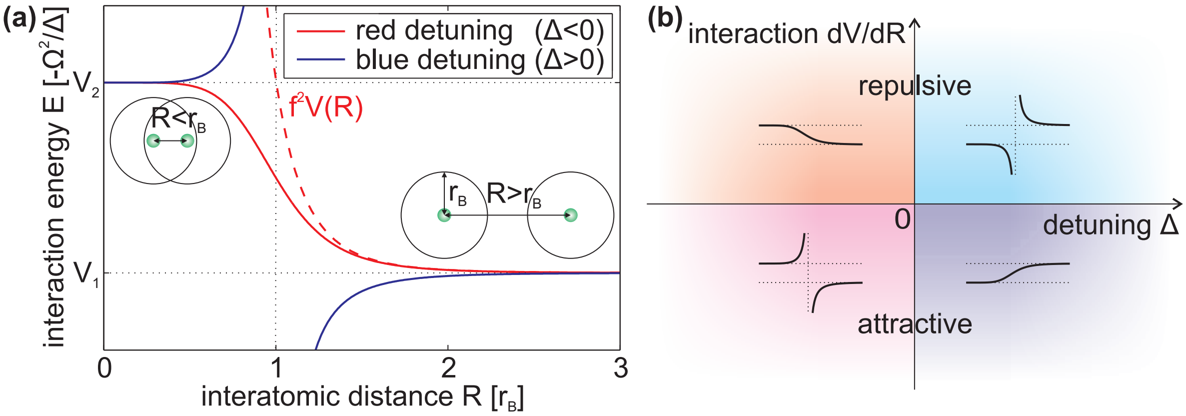

Figure 3.1: Sketch of binary Rydberg dressing potentials. In (a), the interaction potential of a pair of atoms, dressed with a repulsive Rydberg state $\left(\frac{dV}{dR} > 0\right)$ by a coupling laser field with Rabi frequency Ω and detuning Δ ($\Delta < 0$ red, $\Delta > 0$ blue), is shown. In both cases, the interaction potential saturates for very large and very small distances onto a constant value $V_{1/2}$, which depends only on the laser parameters Ω and Δ. In case of red detuning and repulsive interaction (or blue detuning and attractive interaction), the potential converges to the Rydberg-Rydberg interaction potential $V(R)$, weighted with the Rydberg fraction f squared (dashed line, corrected for offset V_1). Note the scaling of the energy axis with the sign of the detuning Δ. For blue detuning $\Delta > 0$, the potential effectively becomes repulsive. The parameter regimes, where the four possible potential shapes occur, are further illustrated in (b). For red detuning, the asymptotic form of the potential is repulsive; for blue detuning, it is attractive. Avoided crossings appear for the combination of repulsive interaction and blue detuning, as well as for attractive interaction and red detuning.

phenomenon of Rydberg blockade (see paragraph 1.2.3). Therefore, the probability to find both atoms in the Rydberg state decreases dramatically and the potential saturates at a constant value. In case of blue detuning, the interaction energy shows the same asymptotic behaviour, but with the saturation values for small and large interatomic distances R interchanged. It is important to note that the difference between the asymptotic values of the potential energy and therefore also the overall magnitude of the dressing effect is determined only by the laser parameters Ω and Δ [140, 141]. These values have been already given by Johnson et al. [9]:

$$V_1 = h\Delta\left(\sqrt{\frac{\Omega^2}{\Delta^2}+1}-1\right) \tag{3.4}$$

$$V_2 = h\frac{\Delta}{2}\left(\sqrt{\frac{2\Omega^2}{\Delta^2}+1}-1\right) \tag{3.5}$$

The overall energy scale is given by the difference of equations (3.4) and (3.5), which can be approximated as $-h\frac{\Omega^4}{8\Delta^3}$ for large detunings $|\Delta| \gg \Omega$. The actual shape and strength of the Rydberg interaction determines mainly the value r_B of the blockade radius and thus the transition between the two regimes. For attractive Rydberg interaction potentials, the same potential shapes appear (see Figure 3.1b). Only the sign of the laser detuning Δ has to be inverted in Figure 3.1a to account for attractive interaction potentials $V(R)$.

The two-atom result has a very simple explanation: If the two atoms are separated by a distance much larger than the blockade radius r_B, the system can be described as two independent atoms in a laser field with Rabi frequency Ω and detuning Δ with respect to the transition to the Rydberg level. Therefore, both atoms individually exhibit an AC Stark shift $V_1/2$ (see paragraph 1.1.3). If the two atoms approach each other, at the distance of the blockade radius r_B (equation 3.2), the Rydberg-Rydberg interaction potential becomes so strong that the state with both atoms excited is tuned out of resonance. The explanation for the behaviour of the system in the blockade regime becomes obvious from the following discussion of the N-atomic case.

3.1.2 N-atom model

Now, the density-dependent energy of a system consisting of N Rydberg dressed atoms is considered. At very low densities, the interatomic distances R are much larger than the blockade radius r_B. The atoms are therefore independent and the energy of the system is N-times the light shift $V_1/2$ of one single atom in equation (3.4):

$$V_1(N) = Nh\frac{\Delta}{2}\left(\sqrt{\frac{\Omega^2}{\Delta^2}+1}-1\right) \tag{3.6}$$

In the high density limit, all atoms are situated within one blockade sphere of volume $\frac{4}{3}\pi r_B^3$. In this case, the dimensionality of the Hilbert space can be dramatically reduced by the fact that all states with more than one Rydberg excitation are completely tuned out of resonance due to the Rydberg blockade. The resulting Hamiltonian in the $(N+1)$-dimensional basis $|gg...g\rangle$, $|rg...g\rangle$, $|gr...g\rangle$,... , $|gg...r\rangle$ reads:

$$H_N = h\begin{pmatrix} 0 & \frac{\Omega}{2} & \frac{\Omega}{2} & \cdots & \frac{\Omega}{2} \\ \frac{\Omega}{2} & -\Delta & 0 & \cdots & 0 \\ \frac{\Omega}{2} & 0 & \ddots & \ddots & \vdots \\ \vdots & \vdots & \ddots & -\Delta & 0 \\ \frac{\Omega}{2} & 0 & \cdots & 0 & -\Delta \end{pmatrix} \tag{3.7}$$

It can be shown, e.g. by mathematical induction (see appendix A.1.1), that the polynomial determining the eigenenergies E is given as:

$$\det\left(H_N - \mathbb{1}E\right) = \left[E^2 + h\Delta E - h^2\frac{N\Omega^2}{4}\right]\left(-h\Delta - E\right)^{N-1} \tag{3.8}$$

Therefore, the energy of the ground state of the fully blockaded N-atomic state is

$$V_2(N) = h\frac{\Delta}{2}\left(\sqrt{\frac{N\Omega^2}{\Delta^2}+1}-1\right) \tag{3.9}$$

Comparing this result to equations (3.4) and (3.5), the explanation of the energy in the limit of a fully blockaded system becomes obvious. Due to the Rydberg blockade, all N atoms share one Rydberg excitation, forming a collective state $\frac{1}{\sqrt{N}}\sum_{i=1}^{N}|g_1, g_2, ..., r_i, ..., g_N\rangle$. This state, a so called super atom [113], is coupled by the light field to the ground state with a collectively enhanced Rabi frequency $\sqrt{N}\Omega$ (see paragraph 1.2.3). The collective Rabi frequency then also has to be used in the calculation of the AC Stark effect. The energy of the fully blockaded N-atomic system (equation 3.9) is therefore the light shift of a single super atom with a collective Rabi frequency $\sqrt{N}\Omega$ and detuning Δ. In the special case $N = 2$, the result of equation (3.5) is recovered. The interaction potential induced by Rydberg dressing, shown in Figure 3.1a, can thus be viewed as the gradual transition from a collective light shift of one super atom to the individual light shift of two independent atoms in the vicinity of the blockade radius r_B.

To study the consequences of high densities for the effect of Rydberg dressing, the additional interaction energy E_{dress} per atom is now calculated. The number of atoms N within one blockade sphere of radius r_B is determined by the ground state atom density ρ:

$$N = \frac{4}{3}\pi r_B^3 \rho = \frac{\rho}{f\rho_B} \tag{3.10}$$

Here, ρ_B denotes the critical density, where according to [8] blockade phenomena start to play a role. This is the case, when the average number of Rydberg atoms in a blockade sphere $f\rho \cdot 4/3\pi r_B^3$ approaches unity:

$$\rho_B = \frac{3}{\pi r_B^3}\frac{\Delta^2}{\Omega^2} = \frac{3\sqrt{2h}}{\pi\sqrt{C_6}}\frac{|\Delta|^{5/2}}{\Omega^2} \tag{3.11}$$

The difference of light shifts between one super atom $V_2(N)$ (equation 3.9) and N independent atoms $V_1(N)$ (equation 3.6) is shared among all N atoms, so that the contribution per atom reads:

$$E_{\text{dress}}(\rho) = h\frac{\Delta}{2}\left(\frac{\Omega^2}{4\Delta^2}\frac{\rho_B}{\rho}\left(\sqrt{4\frac{\rho}{\rho_B}+1}-1\right) - \left(\sqrt{\frac{\Omega^2}{\Delta^2}+1}-1\right)\right) \tag{3.12}$$

Note that this expression is only valid for $\rho/\rho_B \geq \Omega^2/(4\Delta^2)$; at lower densities, the blockade does not play a role any more and the mean interaction energy per particle is given as $f^2V(\rho^{-1/3}) \ll 1$. The relevant quantity for calculating the impact on an ultracold sample (see following paragraph 3.1.3) is the variation of the energy density $E_{\text{eff}}(\rho) = \rho E_{\text{dress}}(\rho)$ with density:

$$\partial_\rho E_{\text{eff}}(\rho) = h\frac{\Delta}{2}\left(1 - \sqrt{\frac{\Omega^2}{\Delta^2}+1} + \frac{\Omega^2}{2\Delta^2}\frac{1}{\sqrt{4\frac{\rho}{\rho_B}+1}}\right) \tag{3.13}$$

The density dependence of this quantity is shown in Figure 3.2. For low densities ρ and weak dressing $\Omega^2/\Delta^2 \ll 1$, there is a linear increase with slope

$$g_{\text{eff}} = -h\frac{\pi}{6}r_B^3\frac{\Omega^4}{\Delta^3} \tag{3.14}$$

This slope deviates from the value in [8] only by a constant factor of $\pi/2$. At higher densities, the last part of equation (3.13) vanishes and the energy functional $\partial_\rho E_{\text{eff}}$ quickly saturates on a constant value

$$\mu_{\text{sat}} = h\frac{\Delta}{2}\left(1 - \sqrt{\frac{\Omega^2}{\Delta^2}+1}\right) \approx -h\frac{\Omega^4}{2\Delta^3} \tag{3.15}$$

This expression agrees exactly with the result in [8]. The energy $E_{\text{dress}}(\rho)$ from equation (3.12) saturates on the same value as the derivative $\partial_\rho E_{\text{eff}}(\rho)$. The saturation value is the AC Stark

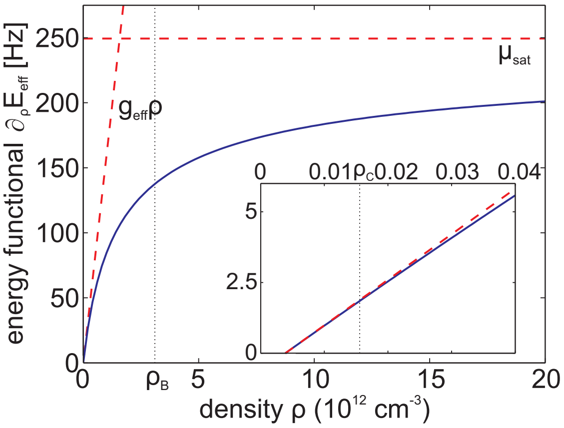

Figure 3.2: Rydberg dressing induced energy functional $\partial_\rho E_{\text{eff}}(\rho)$ versus ground state atom density ρ. The dashed lines indicate the asymptotic behaviour at high and low densities. The inset shows a zoom at very low densities. The values are calculated for a Rabi frequency of $\Omega = 10\,\text{kHz}$, a red detuning of $\Delta = 100\,\text{kHz}$ and a purely repulsive van-der-Waals interaction with $C_6/h = 1.89 \cdot 10^{-28}\,\text{Hzm}^6$, corresponding to the 35S Rydberg state [82] and resulting in a blockade radius of $r_B = 3.1\,\mu\text{m}$. The critical densities ρ_B and ρ_C are explained in the text.

shift of a single free Rydberg dressed atom, since the contribution of the dressed super atom to the energy of a single atom becomes negligible.

As can be seen in Figure 3.2, the energy functional $\partial_\rho E_{\text{eff}}$ deviates from the initial linear slope already at densities well below ρ_{B}. The simple explanation is that collective effects already start to play a role as soon as there are more than two atoms within one blockade volume. This is the case at densities above

$$\rho_C = \frac{3}{2\pi r_B^3} = \frac{3}{2\pi}\sqrt{\frac{2h|\Delta|}{C_6}} \tag{3.16}$$

As a consequence, collective effects beyond two-body interaction have to be considered also at relatively low densities, where they already start to reduce any influence of Rydberg dressing.

3.1.3 Rydberg dressing of Bose-Einstein condensates

The model, developed in the previous paragraph, allows now to calculate the modification of the wavefunction of a Bose-Einstein condensate under Rydberg dressing. It provides an analytical expression of the steady state density distribution of a BEC, dressed with a homogeneous coupling field Ω, even in case of a cylindrically symmetric harmonic trapping potential. Thus, not only effects in realistic experimental situations can be predicted, but also the scaling of the deformation with different parameters can be extracted.

A BEC in a three-dimensional harmonic trap is considered. The evolution of the condensate wavefunction $\psi(\vec{r}, t)$ is described by the Gross-Pitaevskii equation:

$$i\hbar\frac{\partial\psi}{\partial t} = \left[-\frac{\hbar^2\nabla^2}{2m} + \sum_{i=1}^{3}\frac{m\omega_i^2 x_i^2}{2} + g_s\,|\psi|^2 + \partial_\rho E_{\text{eff}}(|\psi|^2)\right]\psi \tag{3.17}$$

As introduced in section 2.1, the first two terms are the usual kinetic energy contribution and the harmonic trapping potential, characterized by the three trapping frequencies ω_i. The third term is the mean-field contribution of the contact interaction between the atoms, while the fourth term $\partial_\rho E_{\text{eff}}(\rho)$ from equation (3.13) describes the effect of Rydberg dressing on the BEC. Besides mean-field approximation, this incorporates two further approximations: First of all, local

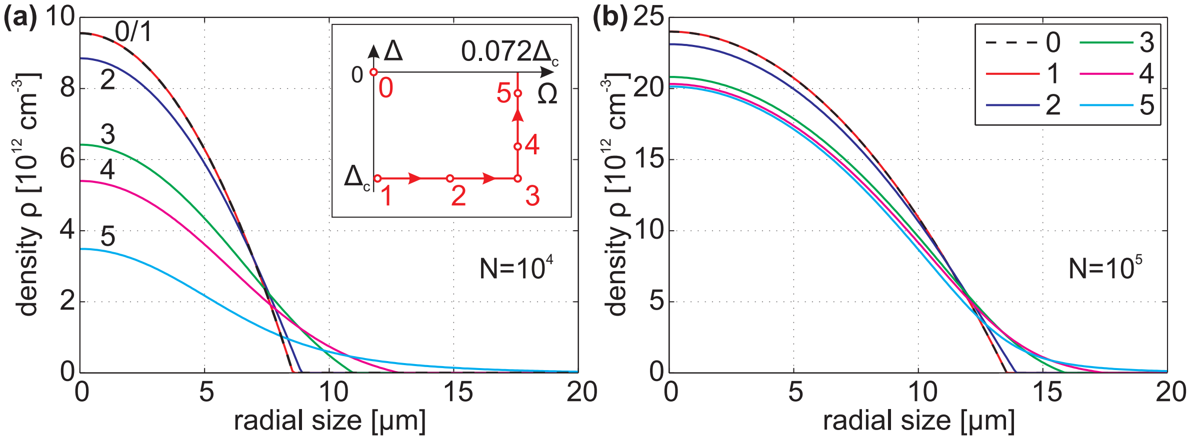

Figure 3.3: Reproduction of Figure 3 of [8] with the analytical model: Density profiles $\rho(r)$ of a Bose-Einstein condensate, consisting of $N = 10^4$ (a) and $N = 10^5$ (b) atoms, in a radially symmetric trap with trap frequency $\omega = 2\pi \cdot 15.9\,\mathrm{Hz}$. The inset in (a) shows the parameters of the laser field, coupling to the Rydberg level, in the plane of Rabi frequency Ω and detuning Δ in units of the critical detuning $\Delta_c = 107\,\mathrm{kHz}$. For larger condensates and hence higher densities ρ, the effect of Rydberg dressing is strongly reduced.

density approximation requires the sample to be much larger than the length scale of the interaction, given by the blockade radius r_B (equation 3.2). Secondly, the actual shape of the Rydberg interaction potential is neglected by assuming a step between the two asymptotic values of the dressing potential at the blockade radius r_B. Even without solving equation (3.17), some important conclusions can be drawn. In the very low density regime, the interaction energy is linear in the density $|\psi|^2$ and can therefore be described with an effective s-wave scattering length $\frac{m g_{\mathrm{eff}}}{4\pi\hbar^2}$ (see equation 3.14). For high densities, the energy functional $\partial_\rho E_{\mathrm{eff}}(\rho)$ becomes constant and thus only contributes as a constant offset to the chemical potential μ. In this case, no effect of Rydberg dressing on the density distribution can be expected.

The ground state stationary solution $\psi(\vec{r},t) = \psi(\vec{r})e^{-i\mu/ht}$ of equation (3.17) can be obtained numerically, e.g. using the split-step Fourier method [142]. For condensates with large atom numbers, the trapping potential and the interaction energy are large [129]. In Thomas-Fermi approximation, the kinetic energy term can be neglected, which is usually a good approximation, except for the low density wings of the condensate [143]. Without the additional energy functional $\partial_\rho E_{\mathrm{eff}}$, the stationary Gross-Pitaevskii equation becomes linear in $|\psi|^2$, making the analytical solution particularly simple. The well known result is a paraboloidal density distribution $\rho = |\psi|^2$, where the value of the chemical potential μ is determined by the normalization to the total atom number N (see section 2.2). With the contribution from Rydberg dressing (equation 3.13), the calculation of the modified ground state density ρ becomes only slightly more involved. For red detunings $\Delta < 0$, equation (3.17) can be rewritten as a cubic equation in the density ρ, that can be efficiently solved analytically. Only the chemical potential μ has to be calculated numerically under the constraint that the total BEC atom number remains constant. In Figure 3.3, the condensate density distributions, resulting from the same parameters

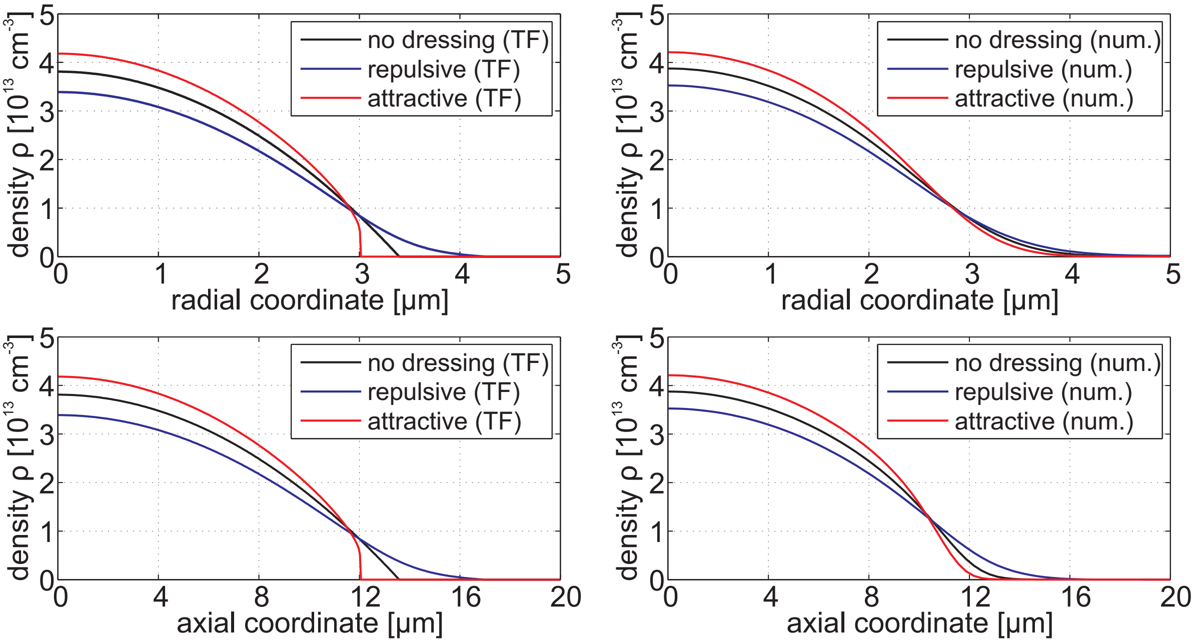

Figure 3.4: Radial and axial density profiles of a BEC, consisting of 10^4 ^{87}Rb atoms, in an axially symmetric trap with trap frequencies $\omega_r = 2\pi \cdot 80\,\text{Hz}$ and $\omega_z = 2\pi \cdot 20\,\text{Hz}$. The analytical result using Thomas-Fermi approximation (TF, left) is compared to the full numerical solution of the Gross-Pitaevskii equation in three dimensions (num., right). The unperturbed density distribution as well as two different Rydberg dressed situations are shown. The repulsive case has been calculated for the same parameters as Figure 3.2 (35S, $\Omega = 10\,\text{kHz}$, $\Delta = 100\,\text{kHz}$). For the attractive case, the sign of the detuning has been inverted.

as in [8], is shown[1]. The analytical model is in very good agreement with the numerical results of [8], which were also obtained within Thomas-Fermi approximation, but with a finite deviation. Nevertheless, the results should be more than enough precise to allow predictions about overall scaling and orders of magnitude. However, since the additional term $\partial_\rho E_\text{eff}$ of Rydberg dressing is expected to be small, it is not obvious that Thomas-Fermi approximation is valid here. As an exemplary check, the full Gross-Pitaevskii equation is solved, using the split-step Fourier method, and shown in comparison to the analytical result in Thomas-Fermi approximation in Figure 3.4. As expected, a repulsive dressing potential leads to an expansion of the condensate, whereas an attractive potential makes the cloud become smaller and denser. Furthermore, the full numerical solution and the result of Thomas-Fermi approximation agree very well in the centre of the condensate, while the deviation at the outer parts becomes significant. It turns out that, in these regions, the kinetic energy term is dominating the density distribution, so that here the effect of Rydberg dressing is even less visible than in the centre of the BEC. This is in contrast to what one could have expected from the scaling of the energy functional $\partial_\rho E_\text{eff}(\rho)$ with the density alone (see Figure 3.2). However, the fact that the impact of Rydberg dressing is vanishing at higher densities, can be seen comparing the attractive and repulsive dressing. The

---

[1] The atom number N in [8] is obviously misquoted one order to high. Moreover, creating a BEC of rubidium in an isotropic trap at a trap frequency as low as $\omega = 2\pi \cdot 15.9\,\text{Hz}$ is challenging at best.

effect of repulsive Rydberg dressing is slightly stronger, since it becomes self-amplifying.
Since the modification of the density distribution by the Rydberg dressing is the strongest in the centre of the condensate, the relative change of peak density is used in order to quantify the response of a three-dimensional asymmetric BEC in the following paragraph 3.1.4. As the behaviour of this quantity is well reproduced using Thomas-Fermi approximation, one can make use of the significant speed up provided by the analytical calculation within Thomas-Fermi approximation. Furthermore, the residual deviation from the more exact numerical simulation further decreases at higher atom numbers in the condensate. In the experimentally relevant parameter regime, the correction is therefore even smaller.

3.1.4 Systematic study of the parameter space

Based on the model developed in the previous paragraph 3.1.3, the deformation of a BEC can be calculated depending on different experimentally accessible parameters. These are essentially the laser parameters, characterized by the Rabi frequency Ω and the detuning to the Rydberg state Δ, the initial peak density ρ_0 of the condensate and the blockade radius r_B, which, within the model of equation (3.2), can be controlled via the C_6 coefficient of the Rydberg state.
From Figure 3.2, one can conclude that the effect of Rydberg dressing is vanishing at high atomic densities. Here, the Rydberg blockade limits the achievable interaction strength. In a not fully blockaded sample, at densities below ρ_B, a higher density increases the collective Rabi frequency $\sqrt{N}\Omega$, leading to more Rydberg excitation in the system. Above ρ_B, however, no further Rydberg excitation is possible. The total interaction energy, determined by the number of Rydberg excitations in the system, is then saturated on a constant value, that is shared among more and more atoms. The contribution for each individual atom is thus effectively vanishing at high densities. At very low densities, however, the interatomic distance increases, thereby also reducing the interaction strength. The maximum effect is therefore expected in the intermediate regime, where the energy difference per atom between the blockaded system and the non-blockaded system is the highest. One can estimate this region to be at the point, where the system just starts to become fully blockaded, at densities around $\rho = \rho_B$.
The laser parameters Ω and Δ mainly determine the fraction of Rydberg excitations $f \approx \Omega^2/(4\Delta^2)$. Large Rabi frequencies Ω and small detunings Δ to the Rydberg state are thus increasing the effect of Rydberg dressing. However, there is an upper bound of the tolerable Rydberg fraction f, given by the decay of the Rydberg state. Large Rydberg fractions f

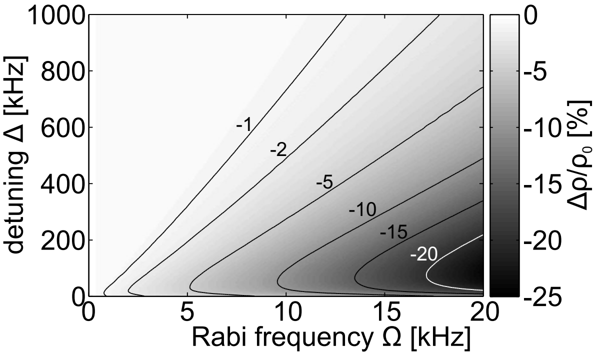

Figure 3.5: Dependence of Rydberg dressing of a BEC on the laser parameters Ω and Δ. The relative change of peak density $\Delta\rho/\rho_0$ in steady state is calculated for a condensate, consisting of $N = 2 \cdot 10^4$ atoms, in a cylindrically symmetric trap with trap frequencies $\omega_r = 2\pi \cdot 20\,\text{Hz}$ and $\omega_z = 2\pi \cdot 80\,\text{Hz}$. The condensate is dressed with a repulsive Rydberg state with $C_6/h = 6.10 \cdot 10^{-29}\,\text{Hzm}^6$, corresponding to the 32S Rydberg state.

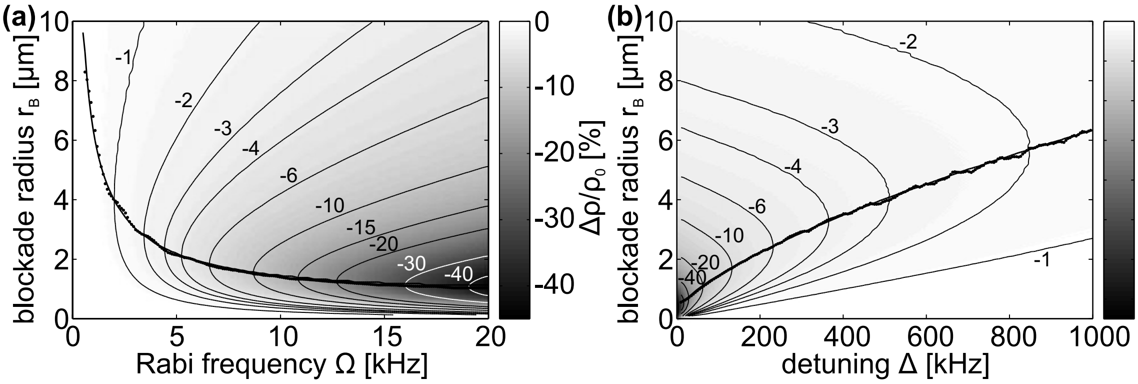

Figure 3.6: Dependence of Rydberg dressing of a BEC on the Rabi frequency Ω (a), laser detuning Δ (b) and the blockade radius r_B as an independent quantity. The relative change of peak density $\Delta\rho/\rho_0$ in steady state is calculated for a condensate, consisting of $N = 2 \cdot 10^4$ atoms, in a cylindrically symmetric trap with trap frequencies $\omega_r = 2\pi \cdot 20\,\mathrm{Hz}$ and $\omega_z = 2\pi \cdot 80\,\mathrm{Hz}$. The condensate is dressed detuned by $\Delta = 100\,\mathrm{kHz}$ (a) with Rabi frequency $\Omega = 10\,\mathrm{kHz}$ (b) to a repulsive Rydberg state with $C_6/h = 6.10 \cdot 10^{-29}\,\mathrm{Hzm}^6$, corresponding to the 32S Rydberg state. The black dots show the blockade radii with maximum effect at fixed Ω and Δ respectively. The black solid line shows the value of $r_{B,m}$ (equation 3.18), when the sample on average starts to become fully blockaded. This is where the maximum effect is expected (see text).

lead to a strongly reduced lifetime $\propto 1/f$ of the dressed state, that prevents the observation of any mechanical effect. This constraint is further discussed in chapter 6.

In order to quantify the effect of Rydberg dressing onto a BEC, the relative change $\Delta\rho/\rho_0$ of the peak density of the condensate is calculated. The dependence of this quantity on the Rabi frequency Ω and the laser detuning Δ to the Rydberg state are shown in Figure 3.5. The range of Rabi frequencies is given by technical constraints, that are discussed later in chapter 6. As expected, the effect increases towards higher Rabi frequencies Ω and lower detunings Δ. At very small detunings $\Delta \leq \Omega$, however, there is some deviation from this trend, since here the blockade radius r_B, according to equation (3.2), becomes large. Anyway, the approximation of weak dressing $f \ll 1$ is not fulfilled any more in this parameter region.

The calculations so far assumed that the finite blockade radius r_B is given by power broadening according to equation (3.2), neglecting technical sources of laser broadening. In Figure 3.6, the influence of the blockade radius r_B is studied as an independent quantity. The effect of Rydberg dressing increases monotonously with Rabi frequency Ω and decreases with detuning Δ. For each value of Ω and Δ, however, there is a clear maximum in the blockade radius r_B. This observation can be explained by the fact that the blockade radius r_B determines the length scale of the system. The density ρ is rescaled by the blockade radius r_B according to equation (3.10). As discussed before, the maximum effect of Rydberg dressing is expected, when the system becomes fully blockaded at $\rho = \rho_B$. Keeping the density ρ fixed, one can calculate the optimal blockade radius $r_{B,m}$ from equation (3.11):

$$r_{B,m} = \sqrt[3]{\frac{3}{\pi\rho}\frac{\Delta^2}{\Omega^2}} \qquad (3.18)$$

It turns out that this reproduces the dependence observed in Figure 3.6 even quantitatively, if $3/4$ times the mean density of the dressed condensate is used. In case of small deformations of the condensate, also the mean density $\overline{\rho} = 2/5\rho_0$ of the initial Thomas-Fermi density distribution with peak density ρ_0 is a good approximation.

3.1.5 Dipolar interaction

Within the model presented in this work, the shape of the interaction potential only determines the value of the blockade radius r_B and the sign of the Rydberg dressing. Therefore, one would not expect that a Rydberg-Rydberg interaction of dipolar type could lead to fundamentally new effects. However, it seems worthwhile to consider the dipolar interaction of Rydberg states close to a Förster resonance. Some Rydberg states can be tuned into resonance by applying microwaves [95, 98] or small electric fields [99, 100, 101, 102, 103, 104]. First of all, the interaction between two Rydberg atoms close to such a resonance shows an angular dependence [105, 106], that is expected to translate directly into the Rydberg dressed interaction. Secondly and more importantly, the strength and sign of the interaction close to the Förster resonance can be tuned via the Förster defect Δ_F [144]. This would not only allow to easily realize repulsive and attractive Rydberg dressing while keeping other parameters of the system, like e.g. the Rabi frequency Ω, constant, but also enable to control the blockade radius r_B of the system by changing the interaction strength. As the discussion above in paragraph 3.1.4 showed, this is a key parameter that rescales the important density scale of the problem.
Yet in case of a Förster resonance, the level scheme becomes slightly more involved. The two-atom Hamiltonian (3.1) has to be extended by the pair state $|r'r''\rangle$, which, on Förster resonance ($\Delta_F = 0$), becomes degenerate with the doubly excited Rydberg state $|rr\rangle$:

$$H = h \begin{pmatrix} 0 & \Omega/\sqrt{2} & 0 & 0 \\ \Omega/\sqrt{2} & -\Delta & \Omega/\sqrt{2} & 0 \\ 0 & \Omega/\sqrt{2} & -2\Delta & U_{dd}(R) \\ 0 & 0 & U_{dd}(R) & -2\Delta + \Delta_F \end{pmatrix} \tag{3.19}$$

where $U_{dd}(R)$~R^{-3} is the coupling of the two doubly excited Rydberg states (see equation (1.16) in section 1.2). Negative Förster defects $\Delta_F < 0$ lead to a repulsive interaction;

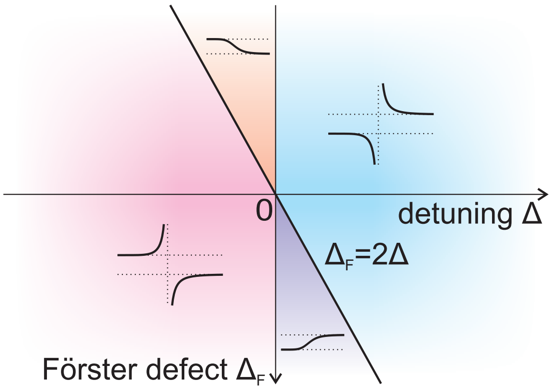

Figure 3.7: Sketch of different potentials of a pair of atoms, dressed with a Rydberg state close to a Förster resonance. In the plane of detuning Δ and Förster defect Δ_F, four different regimes are identified. The regime of a smooth potential is narrowed down compared to Figure 3.1b onto a range of small absolute detunings $|\Delta| < |\Delta_F|/2$.

an attractive interaction can be realized by choosing positive Förster defects. It turns out that similar potential curves as in Figure 3.1a can be obtained. In particular, the asymptotic values are the same as for the Hamiltonian (3.1). However, the smooth dressing potential (red curve in Figure 3.1a) is only present in the regime of small absolute detunings $|\Delta| < |\Delta_F|/2$. For larger detunings Δ, there is an additional avoided crossing occurring. The regimes of different two body potentials in the plane of detuning Δ and Förster defect Δ_F are sketched in Figure 3.7. One has to note that the avoided crossings are likely to play a role only in very cold atomic samples, since fast atoms follow the potential curves diabatically [145]. Then, only the asymptotic values of the potential and the blockade radius r_B are important. In this case, the sign of the Rydberg dressed potential can be fully controlled with the sign of the laser detuning Δ alone, also in the absence of a Förster resonance.

3.2 Electron-atom scattering

A large portion of today's knowledge in atomic and nuclear physics is stemming from scattering experiments, ranging from the early days of atomic physics to nowadays particle physics. The long tradition of scattering experiments started with the famous Geiger-Marsden experiment from 1909, the elastic scattering of α particles [146]. Together with results from electron scattering, their findings were interpreted by Rutherford later in 1911 as the discovery of the atomic nucleus [147]. Deep inelastic scattering [148, 149] of high energy electrons was later on used to clarify the structure of hadrons, leading to the discovery of quarks. The scattering of slow electrons also plays an important role in the history of physics. In the early 1920ies, Ramsauer and Townsend studied independently the collisions of low-energy electrons and atoms [150, 151]. The characteristic minimum of the scattering probability at a certain electron energy, the so called Ramsauer-Townsend minimum, is the first phenomenon observed, indicating that the electron can not be described by classical mechanics. Its later explanation in the framework of de Broglie's wave-particle duality [152] was an important step in the development of quantum mechanics.

The interaction of Rydberg atoms with gases at high densities is largely dominated by the scattering of the highly excited Rydberg electron from the neutral ground state atoms. As mentioned in the introduction, first studies in this direction where undertaken in 1934 by Amaldi and Segrè [2, 3] and independently by Füchtbauer and coworkers [74]. They investigated systematically the influence of admixtures of various gases such as hydrogen, nitrogen and different noble gases on absorption spectra of sodium and potassium. For high terms, the Rydberg states, they found a shift and broadening of absorption lines, which depend only on the type of perturbing foreign gas and its density. The explanation of the line shift in terms of low electron scattering was given by Fermi in 1934 [14], introducing the nowadays well known Fermi pseudopotential, reducing the complex interaction of the Rydberg electron and ground state atoms to a single parameter, the scattering length a. Within Fermi's model, the Rydberg electron in its orbital is assumed as a quasi-free particle, that is scattering with low momentum $\hbar k = \hbar|\vec{k}|$ at the ground state atoms. This approach was further refined by extending it to alkali metals perturbing gas [153] and higher momenta [154], recovering the original result if the impulse approximation [155] is applied. Considering a single particle incident upon a system of two or more scattering partners, this approximation in general consists of three main points [156]:

1. The range of interaction is small compared with the interparticle distance, leading to pure binary interaction between the incident particle and the target particles.
2. The target system is dilute, so that there is no sizeable attenuation of the incident particle by the target system. This means that, dealing with one single scattering event, the impact of the previous events can be largely neglected.
3. The single scattering event lasts short enough that binding forces during the collision may be neglected.

The experimental results presented in this thesis, considering Rydberg S-states with principal quantum numbers between $n = 110$ and $n = 202$, thermal clouds, and Bose-Einstein condensates of rubidium ^{87}Rb at densities up to $10^{14}\,\mathrm{cm}^{-3}$, can be largely explained by the original free electron model of Fermi. The absolute value of the relevant triplet electron-atom scattering length here is $16.1\,a_0$ [157], which is much smaller than the mean interparticle distance ranging from about $2500\,a_0$ to more than $10000\,a_0$. In the following and in section 7.1, it becomes clear that also the other requirements for impulse approximation are fulfilled in the present situation. A good review of the extensions of the Fermi model can be found in [76] and [13]. In the following section, Fermi's original derivation [14] is recapitulated, since it deals exactly with the situation discussed in this thesis. Later on, the influence of higher order scattering theory is shortly reviewed. Finally, the effects of the scattering on the Rydberg electron and the scattering atoms are discussed.

3.2.1 Fermi pseudopotential

Even though it does not fully comply with modern textbook nomenclature [75], the original derivation of Fermi's pseudopotential is very instructive, not only for historical reasons. Besides the original publication from 1934 [14], this part is based on the paper of Reinsberg [158] from the same year and the discussion in [159].

The starting point is the stationary Schrödinger equation for the Rydberg electron in the combined potential, created by the Rydberg core $U(\vec{r}) = -\frac{e^2}{4\pi\epsilon_0}\frac{1}{|\vec{r}|}$ and the surrounding neutral ground state atoms $\sum_i V_i$:

$$\left[-\frac{\hbar^2}{2m_e}\Delta + U(\vec{r}) + \sum_i V_i\right]\psi(\vec{r}) = E\psi(\vec{r}) \tag{3.20}$$

The interaction potential V_i is assumed to be short-range and isotropic. This is the case in the system under investigation. The interaction is given by the polarization of an atom at position $\vec{R}_i$ with polarizability α:

$$V_i = -\frac{1}{(4\pi\epsilon_0)^2}\frac{\alpha e^2}{2|\vec{R}_i - \vec{r}|^4} \tag{3.21}$$

The range of the polarization potential can be estimated by the characteristic radius r^*. This is the distance, at which the polarization potential equals the centrifugal potential $\hbar^2/(2m_{ae}r^2)$, with m_{ae} denoting the reduced mass of the electron and the atom [160]:

$$r^* = \frac{\sqrt{m_{ae}\alpha e^2}}{4\pi\epsilon_0\hbar} \tag{3.22}$$

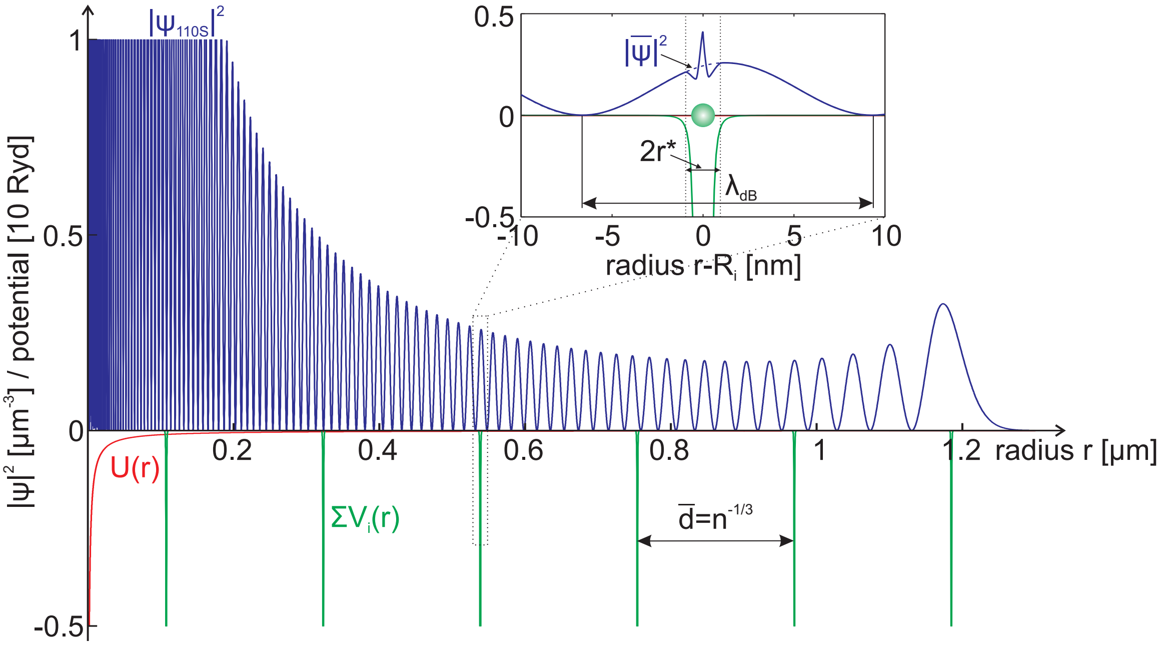

Figure 3.8: Semiquantitative sketch of length scales: Radial profile of probability density $|\psi_{110S}|^2$ for an electron in the $110S$ Rydberg state. The Coulomb potential $U(r)$, created by the positively charged Rydberg core (red) and the polarization potential $\sum_i V_i$ by neutral ^{87}Rb ground state atoms with polarizability $\alpha = 5.38 \cdot 10^{-39}\,\mathrm{J}\frac{\mathrm{m}^2}{\mathrm{V}^2}$ (green), are indicated. Locally, the wavefunction of the Rydberg electron is deformed by the polarization potential. Averaging over one interaction range, given as the characteristic radius $r^* \approx 0.96\,\mathrm{nm}$, leads to the dashed probability density $|\overline{\psi}|^2$ of the Rydberg electron, as indicated in the inset. The mean interparticle distance $\overline{d} = 220\,\mathrm{nm}$ corresponds to an atomic density of $10^{14}\,\mathrm{cm}^{-3}$. The indicated value of the de Broglie wavelength λ_{dB} is just providing an order of magnitude, since it varies with position.

For rubidium ^{87}Rb, this characteristic radius is $r^* = 0.96\,\mathrm{nm}$, which is much smaller than the mean interparticle distance of $\overline{d} = 220\,\mathrm{nm}$ at a density of $10^{14}\,\mathrm{cm}^{-3}$.
Furthermore, the Rydberg electron is assumed to be slow; in particular, the de Broglie wavelength λ_{dB} is required to be much larger than the interaction range ~r^*. In Figure 3.8, the relevant length scales are sketched for the $110S$ Rydberg state. The assumptions are well justified, except for regions very close to the Rydberg core, where the de Broglie wavelength λ_{dB} becomes small. However, this region has only little significance for the calculations in this thesis. In particular, the contribution to the mean energy shift of the Rydberg atom, averaged over the whole volume, is negligible due to the scaling of the volume element with the radius squared (see paragraph 3.2.3). The Schrödinger equation (3.20) is then averaged over a small volume. This volume is chosen smaller than the de Broglie wavelength λ_{dB}, but larger than the range ~r^* of the polarization potential and the mean interparticle distance $\overline{d}$. The averaged wavefunction $\overline{\psi}(\vec{r})$ outside the interaction region resembles then the wavefunction $\psi(\vec{r})$. This way, the local impact of perturbing neutral atoms is removed (see inset of Figure 3.8). Under this conditions, the mean of the derivative of the wavefunction can be replaced by the derivative

of the averaged wavefunction ($\overline{\Delta\psi} = \Delta\overline{\psi}$) and one obtains:

$$-\frac{\hbar^2}{2m_e}\Delta\overline{\psi}(\vec{r}) - (E - U(\vec{r}))\,\overline{\psi}(\vec{r}) + \overline{\sum_i V_i\psi(\vec{r})} = 0 \tag{3.23}$$

Now, the region with distance $r = |\vec{r} - \vec{R}_i|$, $0 < r < \lambda_{\mathrm{dB}}$, closely around a single perturbing neutral atom is considered. This environment is extending over regions with vanishing and non-vanishing interaction $V(r)$ with the perturber. Outside the interaction zone ($r > r^*$), the wavefunction $\psi(\vec{r})$ is equal to the averaged wavefunction $\overline{\psi}(\vec{r})$ and to first order constant, since r is smaller than the de Broglie wavelength λ_{dB}. Inside the interaction zone ($r \leq r^*$), the energy $E - U(\vec{r})$ is much smaller than the interaction with the perturbing atom $V(r)$ and can be neglected. Therefore, the wavefunction $\psi(\vec{r})$ in the considered region becomes radially symmetric around the perturbing ground state atom and reads (see Figure 3.9a):

$$\psi(\vec{r}) = \begin{cases} \overline{\psi} = const. & \text{for } r > r^* \\ \psi(r) & \text{for } r \leq r^* \end{cases} \tag{3.24}$$

The Schrödinger equation (3.20) inside the interaction zone $r \leq r^*$ then simplifies to:

$$\frac{1}{r^2}\frac{\partial}{\partial r}\left(r^2\frac{\partial\psi}{\partial r}\right) = \frac{2m_e}{\hbar^2}V(r)\psi(r) \tag{3.25}$$

Considering the Laplace operator in spherical coordinates, a more suitable form can be obtained using the substitution

$$\psi(r) = u(r)/r \tag{3.26}$$

which then leads to:

$$\frac{\partial^2 u}{\partial r^2} = \frac{2m_e}{\hbar^2}V(r)u(r) \tag{3.27}$$

For large distances r, the interaction potential $V(r)$ vanishes and $u(r)$ thus becomes linear, as r is approaching r^*. The slope of $u(r)$ is fixed by equation (3.24) to $\overline{\psi}$, so that $u(r)$ reads:

$$u(r) = \overline{\psi}\cdot(r - a) \ \text{ for } r > r^* \tag{3.28}$$

Here, a is the intercept of the asymptotic wavefunction (3.28) with the abscissa (see Figure 3.9b). This quantity is nowadays called s-wave scattering length[2]. Now, the averaged interaction energy stemming from one single perturber i can be calculated using the substitution (3.26) and equation (3.27). Under the condition that there is exactly one perturbing atom inside the volume V_0 over which the wavefunction is averaged, one obtains:

$$\overline{V_i\psi(\vec{r})} = \frac{4\pi}{V_0}\int V(r)u(r)r\,dr = \frac{4\pi}{V_0}\int\frac{\hbar^2}{2m_e}\frac{d^2u}{dr^2}r\,dr = \frac{2\pi\hbar^2 a}{m_e V_0}\overline{\psi} \tag{3.29}$$

The last integral can be solved using integration by parts, under the condition that the wavefunction ψ is differentiable at the position of the perturbing atom[3]. If there is no perturbing

---

[2] The sign here is chosen different to Fermi [14] in order to match nowadays textbook convention [75].

[3] This implies that $\left(\frac{du}{dr}r - u\right)_{r=0} = \left(\frac{\partial\psi}{\partial r}r^2\right)_{r=0} = 0$.

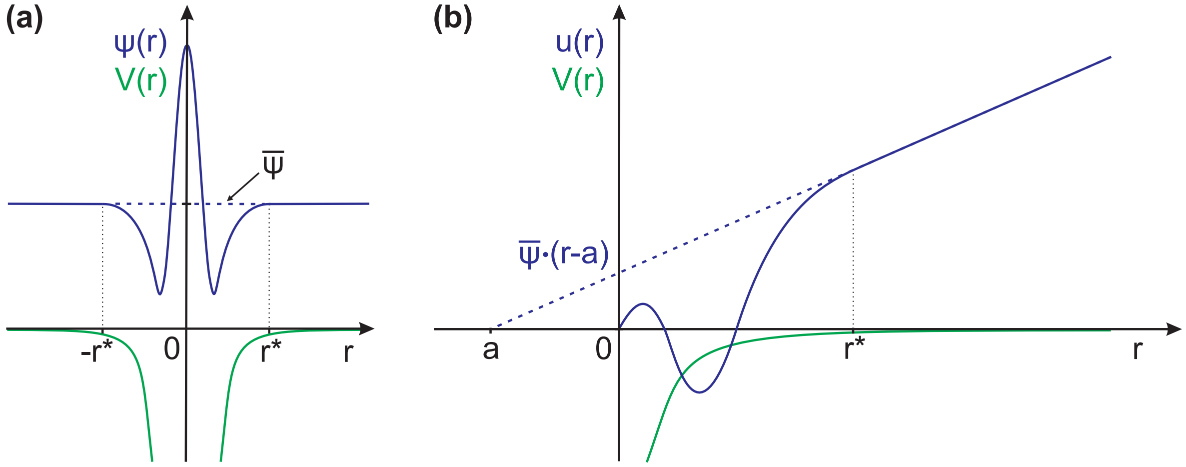

Figure 3.9: Sketched behaviour of the Rydberg electron wavefunction ψ (a) and $r\psi(r)$ (b) close to a perturbing atom. The region of interest is much smaller than the de Broglie wavelength λ_{dB}, so that outside the interaction zone ($r > r^*$) the wavefunction becomes constant $\psi(r) = \overline{\psi}$.

atom within the volume of interest, the interaction is vanishing. The general expression of equation (3.29) therefore reads:

$$\overline{V_i\psi(\vec{r})} = \frac{2\pi\hbar^2 a}{m_e}\,\frac{\delta_{r^*}(r)}{V_0}\,\overline{\psi} \tag{3.30}$$

Here, $\delta_{r^*}(r)$ is a function that vanishes if $r > r^*$ and is one otherwise. For short-range interaction, r^* vanishes and the function $\delta_{r^*}(r)/V_0$ converges to the Dirac delta function, so that the interaction potential in the Schrödinger equation (3.20) can be written as:

$$\sum_i V_i(\vec{r}) = \int \sum_i V_{\text{pseudo}}(\vec{r} - \vec{R}_i)\,|\psi(\vec{r})|^2\ d\vec{r} \tag{3.31}$$

with the well-known Fermi pseudopotential

$$V_{\text{pseudo}}(\vec{r}) = \frac{2\pi\hbar^2 a}{m_e}\,\delta(\vec{r}) \tag{3.32}$$

This very last step was introduced by Fermi only later in 1936, when treating the scattering of slow neutrons from hydrogen atoms [161]. This is the reason why, in the literature, the pseudopotential is mostly connected to nuclear physics. However, the main steps of the derivation were already formulated in 1934 [14]. Here, Fermi was only interested in the total effect of a large number of perturbing atoms inside the wavefunction $\psi(\vec{r})$ of the Rydberg electron. By summing up equation (3.29) over all atoms inside a Rydberg atom, he directly obtained the shift of the Rydberg absorption line, measured by Amaldi and Segrè [2, 3]:

$$\Delta E(\rho) = \frac{2\pi\hbar^2 a}{m_e}\rho \tag{3.33}$$

where ρ is the density of ground state atoms. This equation can be also obtained by integrating the pseudopotential (3.32) over the density distribution of the Rydberg electron $|\psi(\vec{r})|^2$ and the constant particle density $\rho(\vec{R}) = \rho$. This approach and therefore also the expression for the shift in equation (3.33) are only valid if there are many atoms inside the volume of the Rydberg atom. If there are only one or few atoms inside the Rydberg atom, it is more appropriate to calculate the potential energy of a single ground state atom at distance $\vec{R}$ from the centre of the Rydberg electron wavefunction $\psi(\vec{r})$ by integrating only over the electron density $|\psi(\vec{r})|^2$:

$$V_{\text{scat}}(\vec{R}) = \int V_{\text{pseudo}}(\vec{r} - \vec{R})|\psi(\vec{r})|^2 \, d\vec{r} = \frac{2\pi\hbar^2 a}{m_e}|\psi(\vec{R})|^2 \tag{3.34}$$

For Rydberg S-states with principal quantum numbers in the range of about $n = 30$ to $n = 70$, this allows a bound state of a Rydberg atom and one or more ground state atoms, so called ultralong-range Rydberg molecules, that have been predicted by Greene in 2000 [162] and first experimentally observed in 2009 [12, 77]. However, it has to be noted that the molecular potential (3.34) describes only the contribution to zeroth order in the electron momentum $\hbar k$ (see paragraph 3.2.2). Furthermore, it neglects any retroaction of the ground state atoms onto the Rydberg electron wavefunction $\psi(\vec{r})$. This effect is small, but, in the case of diatomic molecules, it can lead to a permanent electric dipole moment [80].

Finally, obtaining the value of the electron-atom scattering length a requires a more involved calculation [157]. Depending on the species of the perturbing atom and the relative orientation of the electron spin and atomic spin, the value can be positive and negative, as pointed out by Fermi [14] and concluded by Reinsberg [158], based on Holtsmark's calculations of the Ramsauer effect in argon and krypton [163, 164]. This fact is explaining the blue and red shifts observed in [2, 3, 74]. For rubidium ^{87}Rb, the triplet scattering length relevant for the present experiments is $a_{\uparrow\uparrow} = -16.1\, a_0$, whereas the singlet scattering length $a_{\uparrow\downarrow} = 0.627\, a_0$ is much smaller and has a different sign [157].

3.2.2 Higher order contributions

So far, the scattering of the Rydberg electron from ground state atoms inside its wavefunction has only been treated in zeroth order of the electron momentum $\hbar k$. Higher order contributions have been calculated by A. Omont [76] by expanding the electron wavefunction in terms of Fourier transformed plain waves ψ_i. The matrix elements of the interaction energy $V(\vec{R})$ with the perturbing ground state atom (equation 3.21) read:

$$\langle j|\, V(\vec{R})\, |i\rangle = 4\pi a_0^3 \sum_l (2l+1) \cdot R_l \left[P_l \left(\vec{\nabla}'\vec{\nabla}/k^2 \right) \psi_j^*(\vec{r}\,')\psi_i(\vec{r}) \right]_{\vec{r}=\vec{r}\,'=\vec{R}} \tag{3.35}$$

where P_l are the Legendre polynomials and the reaction matrix elements R_l are connected to the scattering phase shifts η_l by:

$$R_l = -2Ryd \cdot \tan \frac{\eta_l}{2a_0 k} \tag{3.36}$$

The first term with $l = 0$ of the expansion (3.35) leads to the expectation value

$$V_s(\vec{R}) = 4\pi a_0^3 R_0 |\psi(\vec{R})|^2 \tag{3.37}$$

With the scattering phase shift η_0 from [165], one obtains

$$R_0 = \frac{2Ryd}{a_0}\left(\frac{a}{2} + \frac{\hbar^2}{m_e e^2 a_0^2} \cdot \frac{\pi}{6}\alpha k\right) \tag{3.38}$$

This results in a potential, which is of the form of the molecular potential (3.34), calculated from Fermi's pseudopotential (3.32):

$$V_s(\vec{R}) = \frac{2\pi\hbar^2}{m_e} a(k) |\psi(\vec{R})|^2 \tag{3.39}$$

This term is describing s-wave scattering with a momentum-dependent s-wave scattering length:

$$a(k) = a + \frac{\hbar^2}{m_e e^2 a_0^2} \cdot \frac{\pi}{6}\alpha k + O(k^2) \tag{3.40}$$

To the same order in the electron momentum $\hbar k$, the second term with $l = 1$ leads to a p-wave contribution:

$$V_p(\vec{R}) = \frac{12\pi a_0^3}{k^2} R_1 |\vec{\nabla}\psi(\vec{R})|^2 \tag{3.41}$$

Using the scattering phase shift η_1 from [165], one obtains

$$R_1 = -\frac{e^2}{(4\pi\epsilon_0)^2 a_0^3} \cdot \frac{\pi}{30}\alpha k \tag{3.42}$$

This resulting finally in:

$$V_p(\vec{R}) = -\frac{e^2}{(4\pi\epsilon_0)^2} \frac{2\pi^2}{5} \frac{\alpha}{k} |\vec{\nabla}\psi(\vec{R})|^2 \tag{3.43}$$

It is important to note here, that this description breaks down in the vicinity of possible resonances. For the scattering of alkali metal atoms and electrons, there is a typical p-wave shape resonance [76], that for rubidium appears at an electron energy of 23 meV [166]. The scattering potential is affected in the range of approximately 10 meV around the resonance [167, 168, 169]. The kinetic energy $E_{\text{kin}}(R) = \hbar^2(k(R))^2/(2m_e)$ can be estimated, depending on the radial distance R to the Rydberg core, using a semiclassical approximation [76, 12]:

$$E_{\text{kin}}(R) = -\frac{Ryd}{(n-\delta_0)^2} + \frac{1}{4\pi\epsilon_0}\frac{e^2}{R} \tag{3.44}$$

With increasing principal quantum number n, the radial position of the shape resonance thus increases up to an asymptotic value of 63 nm, as shown in the inset of Figure 3.10. For low Rydberg states at around $n = 30$ to $n = 40$, the p-wave shape resonance therefore leads to a significant contribution to the scattering potential. This becomes manifest for example in the existence of excited states of ultra long-range Rydberg molecules, which are bound by internal quantum reflection at the p-wave shape resonance [77]. However, in order to estimate the relevance of the effect, one has to compare the region, in which the shape resonance plays a role, to the total extent of the Rydberg electron wavefunction. In Figure 3.10, the radial position of the shape resonance is shown, normalized to the limit of the classically allowed region at $2a_0(n - \delta_0)^2$, for different principal quantum numbers n. Considering the spherical symmetry and the scaling of the volume element with r^2, it becomes obvious that the actual relative

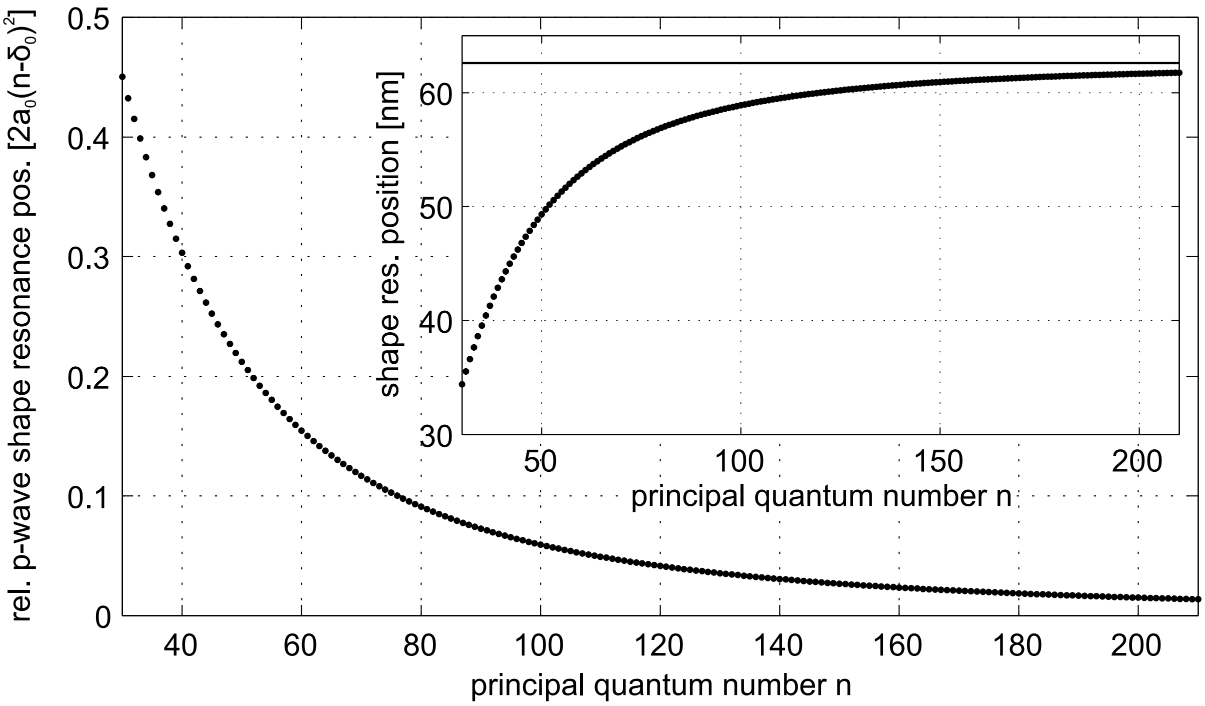

Figure 3.10: Estimated radial position of the triplet p-wave shape resonance in Rubidium Rydberg states with principal quantum number n. The position, where the Rydberg electron reaches the resonance energy 23 meV [166], according to the semiclassical approximation (3.44), is normalized to the extent of the Rydberg state, given by the limit of the classically allowed region $2a_0(n-\delta_0)^2$. In the inset, the saturation of the unnormalized quantity to the asymptotic value 63 nm (solid black line) is shown.

volume, in which the shape resonance modifies the scattering potential, becomes very small already at principal quantum numbers just above $n = 100$. In the framework of this thesis, the influence of the p-wave shape resonance hence can be neglected in very good approximation.

In Figure 3.11, the different relevant contributions to the scattering potential for Rydberg S-states and rubidium ^{87}Rb atoms are shown for the case of triplet scattering, where the spins of the Rydberg electron and the colliding atoms are parallel. The radial Rydberg wavefunctions are taken from numerical calculations [79] and the electron momentum $\hbar k(r)$ is approximated semiclassically according to equation (3.44). As can be seen in Figure 3.11a, the main contribution stems from the zero energy s-wave scattering. This part leads to an attractive potential, which is proportional to the probability density of the Rydberg electron. The momentum dependence of the s-wave scattering length (equation 3.40) is always positive and therefore reduces the potential depth. The p-wave contribution is negative, but out of phase by π in the oscillatory behaviour of the Rydberg electron wavefunction, and leads to a small correction, leading to a slightly deeper and smoother potential.

In Figure 3.11b and (c), the mean $\overline{V} = \int V(\vec{r})\,d\vec{r} / \int d\vec{r}$ and the standard deviation $\Delta V = (\int V(\vec{r})^2\,d\vec{r} / \int d\vec{r} - \overline{V}^2)^{1/2}$ of the scattering potential in different approximations, calculated over the whole extend of the Rydberg electron wavefunction, are shown. As discussed above, the perturbative description of the scattering potential fails at low distances to the Ryd-

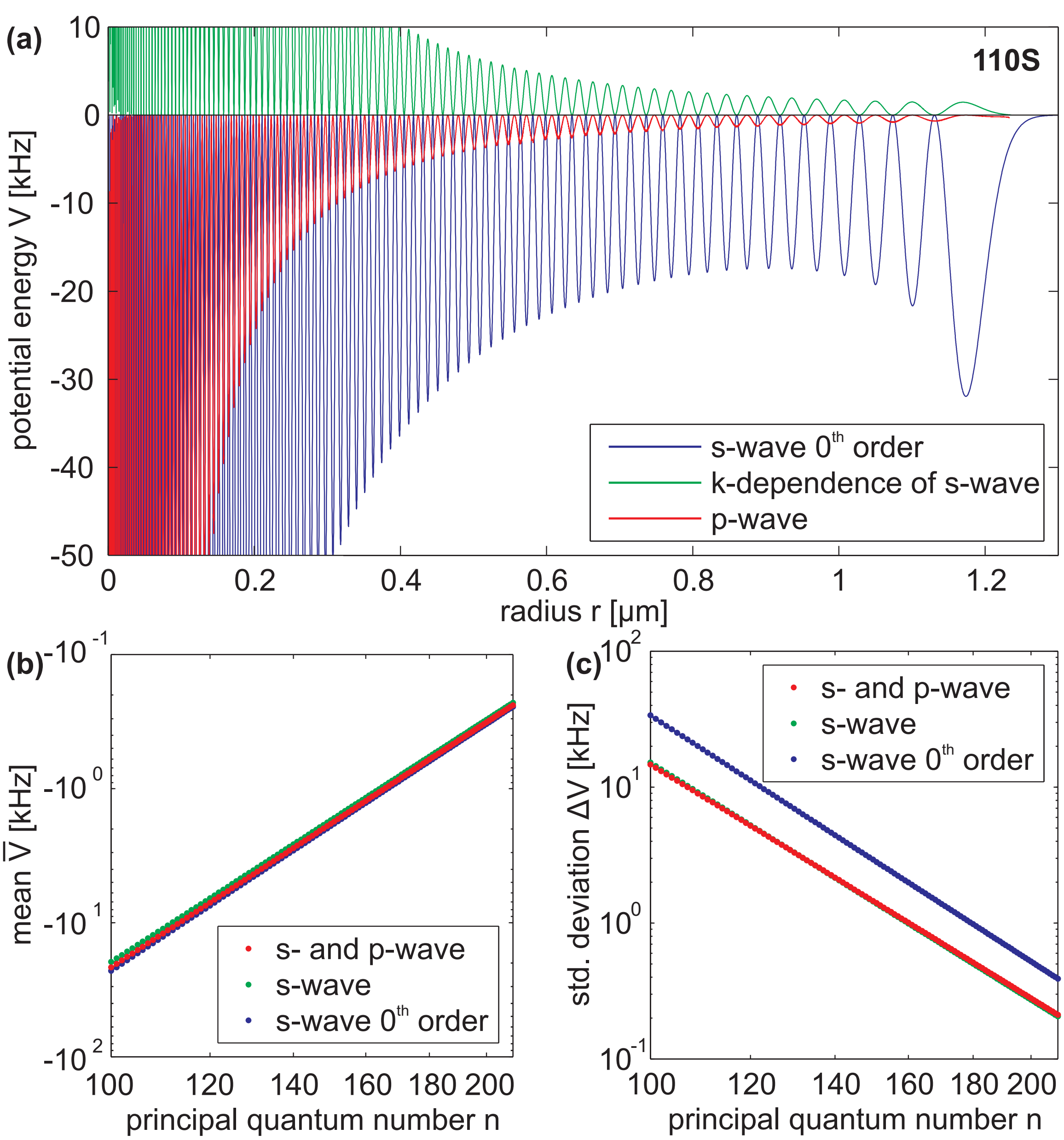

Figure 3.11: Different contributions to the scattering potential: (a) s-wave scattering potential $V(r)$ of the $110S$ Rydberg state, assuming a constant zero energy electron-atom scattering length of $a = -16.1\,a_0$ [157] and corrections due to the momentum dependence of the scattering length $a(k)$, according to equation (3.40), and p-wave scattering (equation 3.43). Note that the semi-classical approximation (3.44) is only valid inside the classically allowed region $r \leq 2a_0(n-\delta_0)^2$. Below, the dependence of the mean $\overline{V}$ (b) and standard deviation ΔV (b) of the total scattering potential on the principal quantum number n is shown. The average is conducted over the whole volume of the Rydberg atom. For the standard deviation, the inner region $r < 0.1\,\text{nm}$ has to be excluded.

berg core. Anyway, in this region the influence of the positively charged Rydberg core has to be included (see also section 3.3). It turns out that this is negligible for the calculation of the mean potential $\overline{V}$. However, for the calculation of the standard deviation, the inner part of the potential has to be excluded, since it contains unphysical large amplitude oscillations at very small wavelengths. The result depends only weakly on the exact choice of the cut-off radius above a certain value. Therefore, a constant cut-off of $0.1\,\mathrm{nm}$ is used for all principal quantum numbers.

Due to the normalization of the electron wavefunction $\psi(\vec{r})$, the mean of the s-wave scattering potential (3.39) with constant scattering length $a(k) = a$ is inversely proportional to the volume of the Rydberg atom and thus scaling as $(n - \delta_0)^{-6}$. Taking higher order terms into account leads to a slightly different scaling and amplitude. The momentum-dependent correction in the scattering length is positive (see equation 3.40), therefore reducing the attractive scattering potential. The p-wave contribution to the same order in k leads to a slight correction in the other direction. However, for higher principal quantum numbers, both corrections to the approximation in zeroth order of the electron momentum $\hbar k$ vanish. This can be explained by the fact that the mean momentum of the Rydberg electron, which is proportional to the Kepler frequency, decreases with $(n - \delta_0)^{-3}$. The standard deviation ΔV of the potential also shows a scaling roughly proportional to $(n - \delta_0)^{-6}$. The oscillatory behaviour of the zeroth order s-wave potential is damped by the corrections linear in the electron momentum $\hbar k$, since both the momentum-dependent scattering length (3.40) and the p-wave potential (3.43) lead to contributions which are out of phase by π (see also Figure 3.11a).

3.2.3 Influence on the Rydberg line

Based on the discussion in the previous paragraph, now the impact of the scattering of the Rydberg electron from many atoms inside its wavefunction can be calculated. The relevant properties are the mean $\overline{V}$ and the standard deviation ΔV of the scattering potential, shown in Figure 3.11. These two quantities fully characterize the problem in the limit of a large number N of atoms, positioned randomly inside the Rydberg electron wavefunction. According to the central limit theorem [170], the total energy shift of the Rydberg atom converges then to a Gaussian distribution with mean $N\overline{V}$ and standard deviation $\sqrt{N}\Delta V$. If the density ρ of ground state atoms is constant over the size of the Rydberg atom, the number N of ground state atoms inside the Rydberg atom is the product of the density ρ and the volume of the Rydberg electron wavefunction ~$(n - \delta_0)^6$. This means that the dependence on the volume of the Rydberg atom in the total energy shift $\Delta E = N\overline{V}$ cancels out. Therefore, one obtains to zeroth order in the electron momentum an energy shift, which is only proportional to the density ρ. This is exactly the expression (3.33), given by Fermi already in 1934 [14]. If higher order terms are taken into account, there is a residual dependence on the principal quantum number n, as can be seen in Figure 3.12. Again, these corrections become smaller at higher principal quantum numbers. In the range of $n = 100$ to $n = 200$, the modification by all terms linear in the electron momentum $\hbar k$ decreases from about 5% to 2%. The statistical distribution of the energy shifts, according to the central limit theorem, becomes more narrow for higher numbers N~$(n - \delta_0)^6$ of atoms inside the Rydberg electron wavefunction. Therefore, the full width at half maximum (FWHM) $\Delta(\Delta E) = 2\sqrt{2\ln 2}\cdot\sqrt{N}\Delta V$ depends on the principal quantum number n, even in the lowest order approximation.

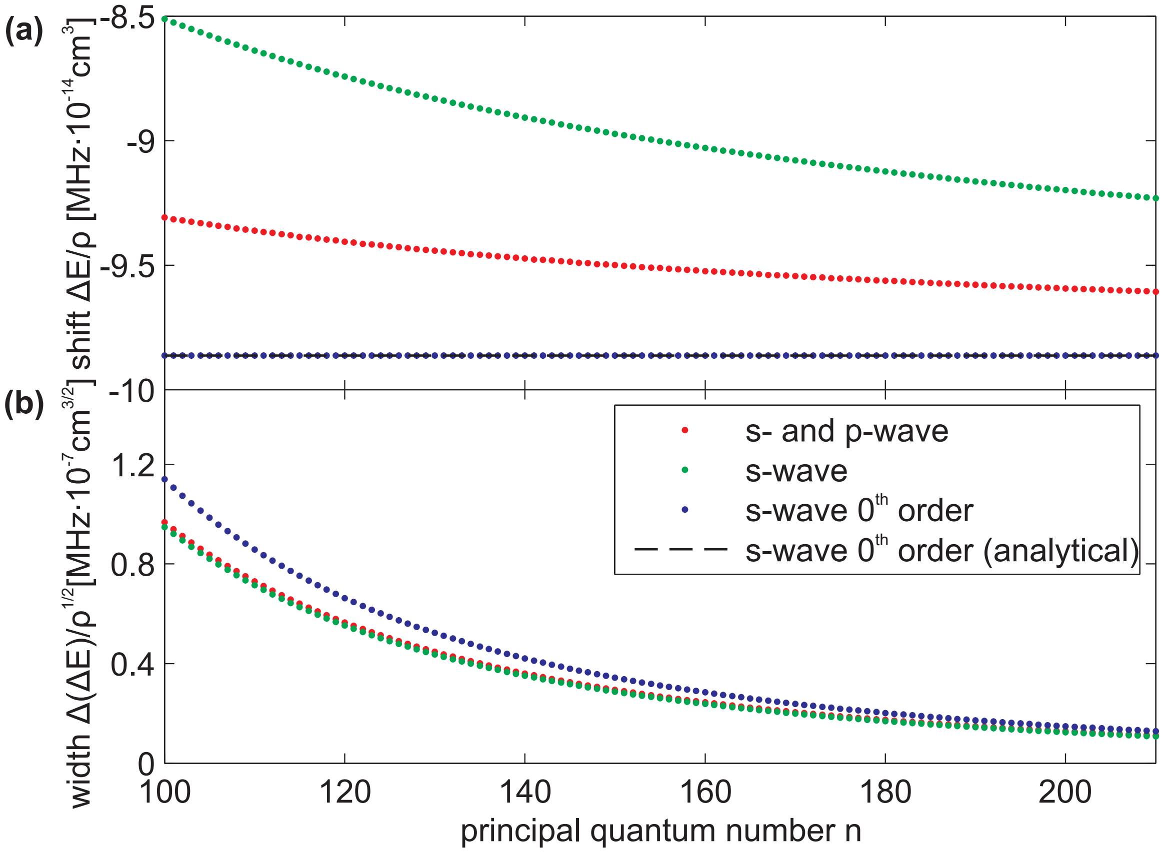

Figure 3.12: Mean energy shift $\Delta E = N\overline{V}$ (a) and broadening $\Delta(\Delta E) = 2\sqrt{2\ln 2}\cdot\sqrt{N}\Delta V$ (FWHM, b) of Rydberg S-states as expected from the central limit theorem. Different orders of approximation have been calculated numerically. The analytical result for the total energy shift (equation 3.33) to zeroth order in the electron momentum $\hbar k$ (black dashed line in a) matches exactly the numerical result (blue dots).

3.2.4 Creation of excitations in a BEC

In the last paragraph 3.2.3, the scattering of a highly excited Rydberg electron at a large number of ground state atoms inside its wavefunction has been discussed from the perspective of the Rydberg atom. Now, the impact onto the scattering atoms in a Bose-condensed sample is considered. A first guess could be based on classical scattering with a geometric cross section $4\pi a^2$, similar to the treatment of single ion impurities [160]. This approach and its results for the parameters of the experiments in this thesis are discussed in appendix B.2.2. It turns out that this description reproduces the observed trend and gives rough orders of magnitude; however, this treatment clearly does not explain the experimental observations. Instead, now a different approach is discussed, which has been developed in a collaboration with David Peter and Hans Peter Büchler [171]. This theory includes the properties of the Bose-Einstein condensate as a quantum liquid. In particular, the spectrum of Bogoliubov excitations, discussed in paragraph 2.3.1, is taken into account.

3.2.4.1 Interaction operator

The basic idea is to treat the scattering potential V_{scat}, created by the Rydberg electron, as a short perturbation:

$$\hat{H}_{\text{int}} = \int \rho(\vec{r}) V_{\text{scat}}(\vec{r}) s(t)\, d\vec{r} \tag{3.45}$$

The time dependence $s(t)$ is caused by the finite lifetime of the Rydberg atom (see section 7.2) and the experimental sequence (see paragraph 5.3.2), that limits the interaction time to at most $10\,\mu\text{s}$. The shape and impact of this factor are discussed on page 56. The BEC density ρ is assumed to be constant over the Rydberg atom and hence the basic equations of a uniform Bose gas, as discussed in paragraph 2.3.1, can be applied. Using the bosonic field operator (2.16), the Fourier components $\rho_{\vec{k}}$ of the atomic density $\rho(\vec{r})$ can be expressed in terms of particle creation and annihilation operators:

$$\rho_{\vec{k}} = \int \rho(\vec{r}) e^{-i\vec{k}\vec{r}/\hbar} d\vec{r} = \sum_{\vec{p}} \hat{a}^{\dagger}_{\vec{p}-\vec{k}} \hat{a}_{\vec{p}} \tag{3.46}$$

Expressing also the scattering potential $V_{\text{scat}}(\vec{r})$ in the Hamiltonian (3.45) of the interaction by its Fourier transform $V_{\text{scat}}(\vec{k}) = \int V_{\text{scat}}(\vec{r}) e^{-i\vec{k}\vec{r}/\hbar} d\vec{r}$, one can identify the Fourier components $\rho_{\vec{k}}$ in the interaction Hamiltonian (3.45) and obtains (see appendix A.2.1):

$$\hat{H}_{\text{int}} = \frac{1}{V} \sum_{\vec{k},\vec{p}} \hat{a}^{\dagger}_{\vec{p}-\vec{k}} \hat{a}_{\vec{p}}\, V_{\text{scat}}(\vec{k}) s(t) \tag{3.47}$$

This result can be alternatively expressed in terms of creation and annihilation operators of Bogoliubov excitations (see appendix A.2.2).

3.2.4.2 Excitation probability

However, one can directly proceed with expression (3.47) and calculate the probability $P(\vec{q})$ to create a Bogoliubov-type excitation (see paragraph 2.3.1) at quasimomentum $\vec{q}$. Starting from the ground state $|0\rangle$, the transition probability into the final state $|\vec{q}\rangle = \hat{b}^{\dagger}_{\vec{q}} |0\rangle$ with one excitation at momentum $\vec{q}$ can be calculated to lowest order using perturbation theory, similar as in [172, 173]:

$$P(\vec{q}) = \left| -\frac{i}{\hbar} \int_0^{\infty} e^{i\epsilon(\vec{q})t/\hbar} \langle \vec{q}|\, \hat{H}_{\text{int}}\, |0\rangle\, dt \right|^2 \tag{3.48}$$

Here, $\epsilon(\vec{q})$ is the energy of a quasiparticle excitation at momentum $\vec{q}$. The evaluation of this expression, inserting the perturbation (3.47) and the definition of $\hat{b}_{\vec{q}}$ (equation 2.25), is straightforward and leads to:

$$P(\vec{q}) = \frac{N_0}{\hbar^2 V^2} |u_q - v_q|^2 \, |V_{\text{scat}}(\vec{q})|^2 \, |s\left(\epsilon(\vec{q})/\hbar\right)|^2 \tag{3.49}$$

Here, the Fourier transform $s(\omega)$ of the time dependence $s(t)$ of the perturbation has been introduced. Now, the results for the uniform Bose gas from paragraph 2.3.1 (equations 2.26

and 2.29) can be applied. The final result then reads:

$$P(\vec{q}) = \frac{N_0}{\hbar^2 V^2} \left|V_{\text{scat}}(\vec{q})\right|^2 \frac{\vec{q}^2}{2m\epsilon(\vec{q})} \left|s\left(\epsilon(\vec{q})/\hbar\right)\right|^2 \tag{3.50}$$

The quantity

$$S(\vec{q}) = \frac{\vec{q}^2}{2m\epsilon(\vec{q})} \tag{3.51}$$

is referred to in literature as the static structure or form factor of the homogeneous Bose gas, which is the dynamic structure factor $S(\vec{q},\omega) = S(\vec{q})\delta(\omega - \epsilon(\vec{q})/\hbar)$, integrated over frequency space. This quantity was first introduced in the description of the scattering of a particle from a quantum liquid [173]. It is the Fourier transform of density correlations in the ground state of the liquid [172]. In its present form, it was first derived for the description of light scattering from a Bose-Einstein condensate [174, 175]. The consequences of this function, discussed in that context [172], apply here as well. At small momenta $|\vec{q}| < \hbar/\xi$, the quasiparticle excitations are of phonon-type (see paragraph 2.3.1). In this case, the excitation probability $P(\vec{q})$ is suppressed linearly in $|\vec{q}| = q$ with $S(\vec{q}) \approx \frac{\xi q}{2\hbar}$ (see Figure 3.13b). However, free particle excitations at large momenta $q > \hbar/\xi$ remain unaffected, since then the static structure factor $S(\vec{q}) \to 1$.

By summing (3.50) over all momenta $\vec{q}$, one can now calculate the total number N_{Bog} of quasiparticle excitations created by one Rydberg atom until it decays. In paragraph 2.3.1, a uniform Bose gas in a volume V with periodic boundary conditions was considered. In contrast to that, in the real experimental situation the momenta $\vec{q}$ are not quantized. Therefore, the sum is replaced by the integral $\sum_{\vec{q}} \to \frac{V}{(2\pi\hbar)^2} \int d\vec{q}$, leading to:

$$N_{\text{Bog}} = \sum_{\vec{q}} P(\vec{q}) = \frac{\rho}{\hbar^2} \frac{1}{(2\pi\hbar)^3} \int \left|V_{\text{scat}}(\vec{q})\right|^2 \frac{q^2}{2m\epsilon(\vec{q})} \left|s\left(\epsilon(\vec{q})/\hbar\right)\right|^2 \, d\vec{q} \tag{3.52}$$

3.2.4.3 Number of affected particles

In order to estimate the effect of these excitations onto the Bose-Einstein condensate, one has to consider the number of real particles, which are associated to a quasiparticle excitation at momentum $\vec{q}$. As shown in paragraph 2.3.1, this number is given as (cf. equation 2.36):

$$\Delta N_{\text{Bog}}(\vec{q}) = \left(\frac{\vec{q}^2}{2m} + g\rho\right) / \epsilon(\vec{q}) \tag{3.53}$$

The dependence of this quantity on the absolute value of the quasimomentum $q = |\vec{q}|$ is shown in Figure 3.13c. As expected in the free particle regime, at large momenta $q > \hbar/\xi$, it converges to one. Here, one quasiparticle corresponds to a real single atom being excited out of the condensate mode. At low momenta $q < \hbar/\xi$, the number of associated particles diverges as $\Delta N_{\text{Bog}}(q) \approx \frac{\hbar}{\sqrt{2}q\xi}$. The physical interpretation is that the quasiparticles at low momentum are sound waves, which can impact a large number of atoms. In the limit of very low momenta, this can lead to collective oscillations of the whole condensate (see paragraph 2.3.2).

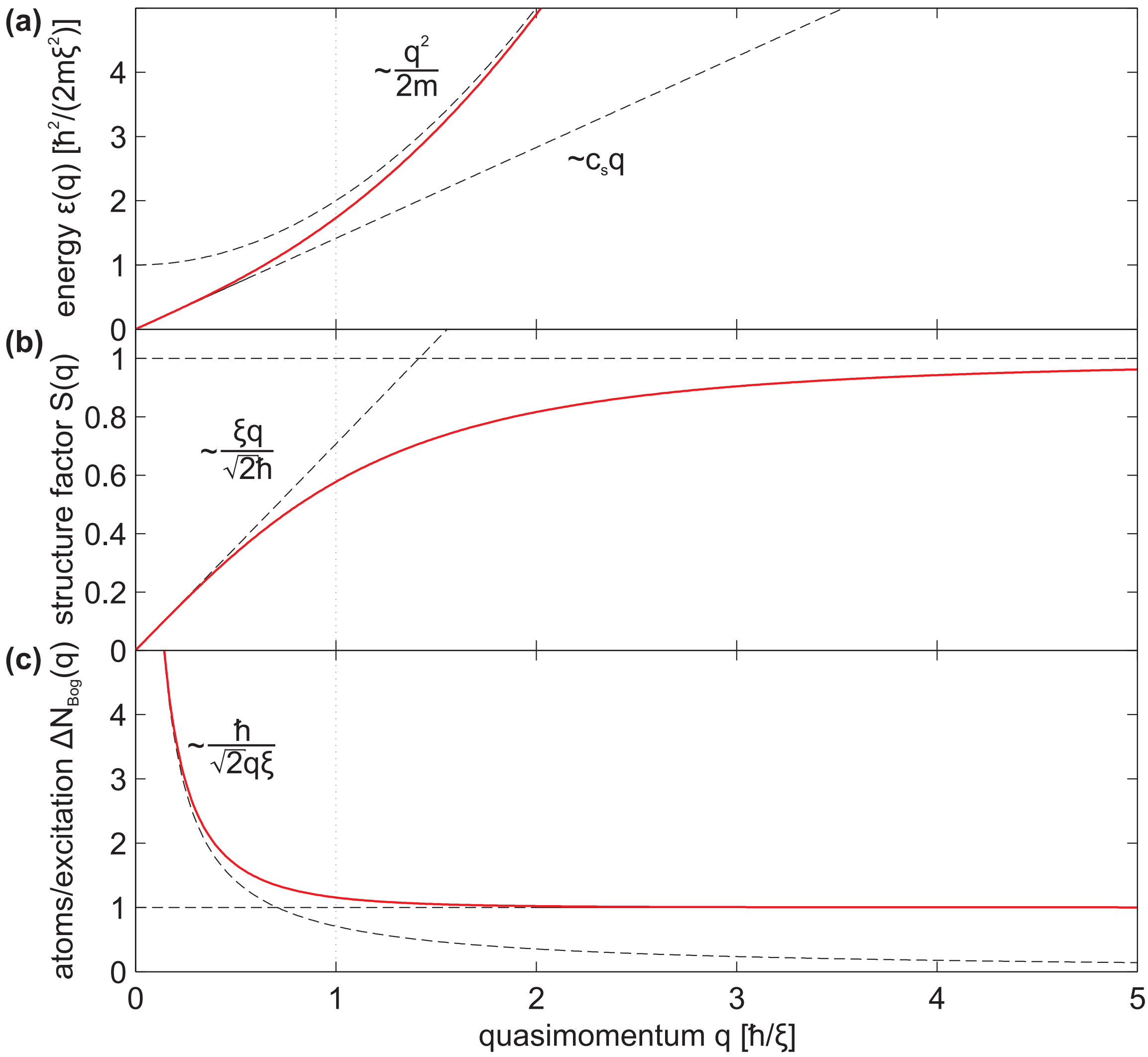

Figure 3.13: Properties of Bogoliubov quasiparticle excitations. (a) The dispersion relation $\epsilon(q)$ (equation 2.29), (b) the static structure factor $S(q)$ in the uniform Bose gas (equation 3.51), and (c) the number of individual atoms affected by one quasiparticle excitation are shown, depending on the quasiparticle momentum q (solid red lines). The asymptotic behaviour for low (phonons) and high (free particles) momenta q are indicated as dashed lines. The transition between the two regimes takes place at $q \approx \hbar/\xi$ (see paragraph 2.3.1), indicated as a vertical dotted line.

The total number of affected atoms in the condensate is obtained by summing over the product of equations (3.50) and (3.53):

$$\Delta N = \sum_{\vec{q}} P(\vec{q}) \cdot \Delta N_{\text{Bog}}(\vec{q}) = \frac{\rho}{\hbar^2} \frac{1}{(2\pi\hbar)^3} \int |V_{\text{scat}}(\vec{q})|^2 \, \frac{1+\xi^2 q^2/\hbar^2}{2+\xi^2 q^2/\hbar^2} \, |s(\epsilon(\vec{q})/\hbar)|^2 \, d\vec{q} \quad (3.54)$$

The product of the number of atoms $\Delta N_{\text{Bog}}(\vec{q})$ per quasiparticle excitation and the static structure factor $S(\vec{q})$ is a numerical weighting factor for Bogoliubov excitations. As shown in Figure 3.15b, the value of this factor shows a transition between $1/2$ at very low and 1 at very high momenta q, centred right at the transition between phonon and free particle regime.

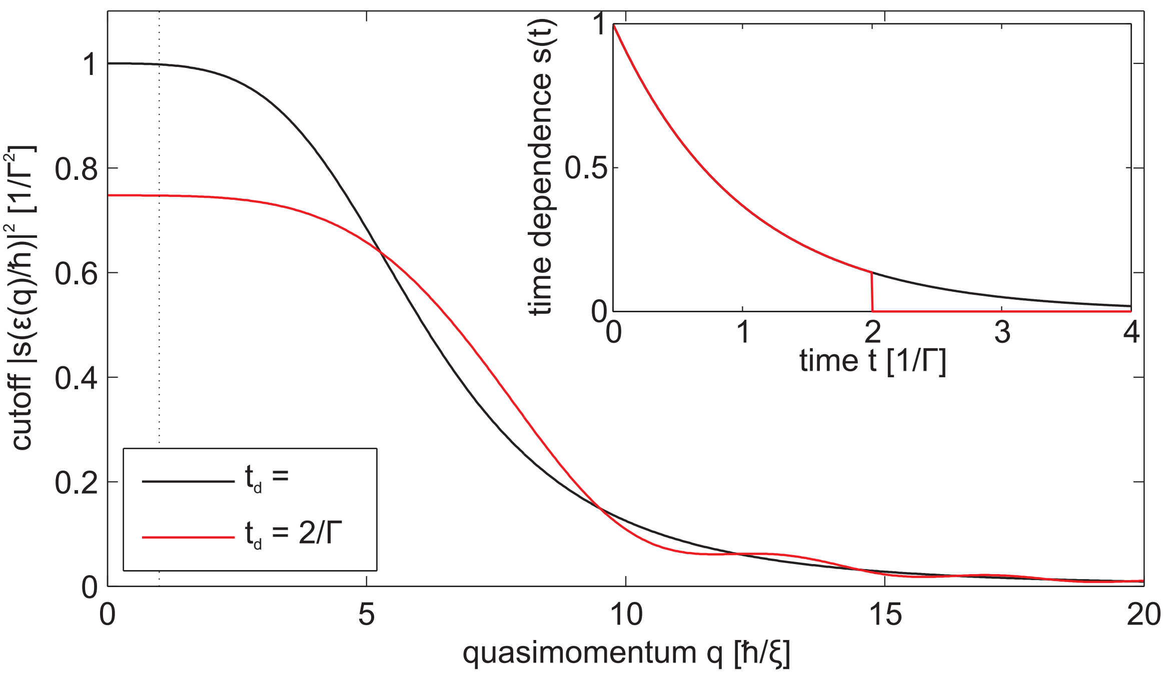

Figure 3.14: Influence of the time dependence of the interaction. The dependence of the additional factor $|s(\omega(\epsilon(q)/\hbar))|^2$ on the quasimomentum q is shown for two different time dependencies $s(t)$, depicted in the inset. In the experiment, the free exponential decay ($t_d = \infty$) is truncated at a certain time t_d. The example here shows $t_d = 2/\Gamma$, which corresponds to experiments with the $110S$ Rydberg state ($\Gamma \approx 5\,\mu\text{s}$ and $t_d = 10\,\mu\text{s}$). The transition between the phonon and the free particle regime is indicated as a vertical dotted line.

3.2.4.4 Time dependence of the interaction

The time dependence of the interaction of the Rydberg electron and the BEC enters into the total number ΔN of affected atoms as the Fourier transform $s(\omega)$. The probability to find an atom in the Rydberg state is decaying exponentially at rate Γ, leading to:

$$|s_\infty(\omega)|^2 = \frac{1}{\omega^2 + \Gamma^2} \tag{3.55}$$

This function provides a cutoff of excitations at large energies $\omega > \Gamma$. The physical interpretation is that the finite interaction time ~$1/\Gamma$ leads to a finite Fourier width of the excitation. Therefore, all quasiparticle excitations at energies below $1/\Gamma$ can in principle be excited. Via the Bogoliubov dispersion relation (2.29), this then also defines a range of accessible momenta $\vec{q}$. For short Rydberg lifetimes $\tau = 1/\Gamma$, the total number of atoms affected by one Rydberg electron is roughly scaling as τ^2. Note that this scaling corresponds to the result of lattice diffraction in the Raman-Nath regime [176]. This analogy is discussed in more detail in section 8.1. In the experimental sequence, any possibly existing Rydberg atom is ionized after $t_d = 10\,\mu\text{s}$. Therefore, the exponential decay is truncated, leading to a slightly modified expression:

$$|s_{t_d}(\omega)|^2 = \frac{1 + e^{-2\Gamma t_d} - 2\cos(\omega t_d)\, e^{-\Gamma t_d}}{\omega^2 + \Gamma^2} \tag{3.56}$$

For $t_d \gg 1/\Gamma$, this formula obviously converges to equation (3.55). The resulting factor in equation (3.53) is shown in Figure 3.14, both for a freely decaying Rydberg atom and for a finite time t_d. In both cases, $|s(\omega)|^2$ is largely constant at low momenta, in particular spanning over the full range of the phonon regime. The value of this level depends slightly on the value of t_d. The cutoff at high momenta, however, is only little affected.

3.2.4.5 Fourier transform of the interaction potential

The last term missing yet in order to evaluate the total number ΔN of atoms affected by one Rydberg excitation is the Fourier transformed potential from section 3.2. It describes the impact of the shape of the scattering potential. Due to the spherical symmetry of Rydberg S-states one obtains:

$$V_{\text{scat}}(q) = \frac{4\pi\hbar}{q} \int_0^\infty \sin\left(\frac{qr}{\hbar}\right) V_{\text{scat}}(r)\, r\, dr \tag{3.57}$$

If only the lowest order of the electron momentum is considered, the scattering potential $V_{\text{scat}}(r)$ is directly proportional to the probability density of the Rydberg electron. In the limit of high principal quantum numbers n, the integral in equation (3.57) can then be calculated analytically [177]. In order to be able to also account for a momentum dependent electron-atom scattering length $a(k)$ and p-wave scattering (see section 3.2.2), here, the integral is evaluated numerically using Rydberg wavefunctions from [79]. As a cross check, the results of the numerical and analytical calculations are compared in appendix A.2.3.

For calculating the number of quasiparticle excitations N_{Bog} and the total number $\Delta N(q)$ of atoms, the modulus squared of the Fourier transformed perturbing potential has to be considered. Fourier components at large momenta q, due to the spherical symmetry of the potential, count as q^2. The resulting weight $q^2|V_{\text{scat}}(q)|^2$ is shown in Figure 3.15c for two different Rydberg states. It shows equally spaced peaks, with an amplitude decaying to higher momenta q. This structure is mainly caused by the potential drop at the border of the classically allowed region at $r_{\text{class}} = 2a_0(n-\delta_0)^2$. Approximating the scattering potential as a spherically symmetric box potential $V_{\text{box}}(r) = \overline{V} \cdot \Theta(r_{\text{class}} - r)$, with the Heaviside step function $\Theta(r)$, leads to a first maximum at $q_m = 2\pi/3r_{\text{class}}$ and further maxima, spaced equidistantly at $2\pi/r_{\text{class}}$. This is consistent with the numerical result for the actual potential shape, shown in Figure 3.15c. Also the scaling of the amplitude can be explained by the approximation with a box potential. From equation (3.57), one directly obtains $V_{\text{box}}(q) \sim r_{\text{class}}^2 \overline{V}/q$. This leads to $q^2|V_{\text{box}}(q)|^2 \sim r_{\text{class}}^4 \overline{V}^2 \sim (n-\delta_0)^{-4}$, where the scaling of the mean potential $\overline{V} \sim (n-\delta_0)^{-6}$ from paragraph 3.2.2 has been used.

For comparison, the other contributions to the integral in equation (3.54) are shown. The time dependence of the interaction, plotted in Figure 3.15a, allows excitations within a relatively large range of energies. Furthermore, the increase of the number of atoms connected to one Bogoliubov quasiparticle at smaller quasimomenta q is largely compensated by the excitation probability, suppressed by the static structure factor $S(q)$ of the condensate. This leads only to a minor modification by the factor $\Delta N_{\text{Bog}}(q)$ between $1/2$ and 1 (see Figure 3.15b). Thus, it is the shape of the perturbing potential that determines which excitations dominate the impact onto the condensate. For the Rydberg states investigated in this thesis, at principal quantum numbers in the range of $n = 110$ to $n = 202$, the first peak of the weight $q^2|V_{\text{scat}}(q)|^2$ is always situated

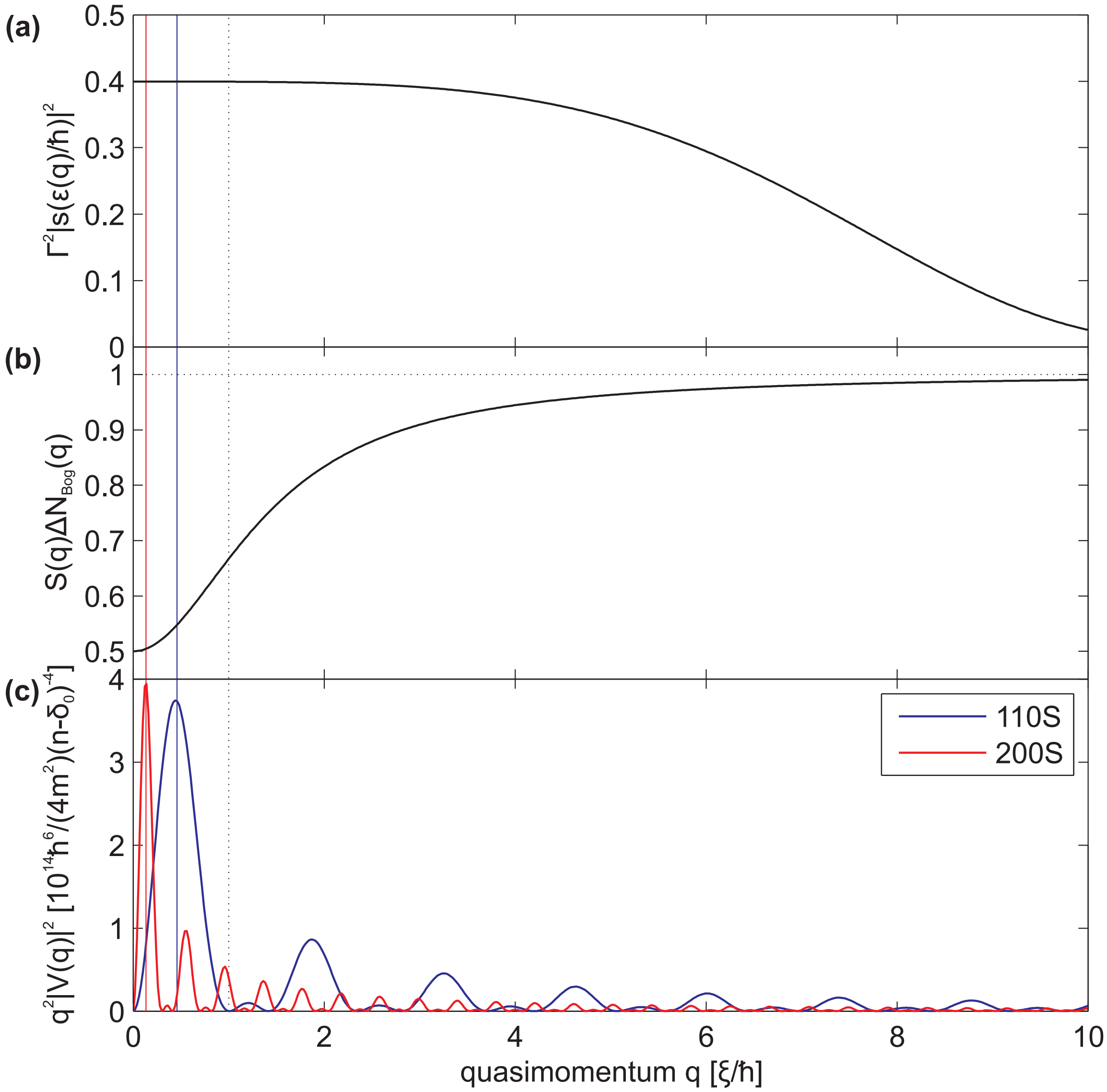

Figure 3.15: Different contributions to the total number of atoms affected by one Rydberg excitation depending on quasimomentum q. (a) Influence of the time dependence $|s_{t_d}(\omega(\epsilon(q)/\hbar))|^2$ (see equation (3.56) and Figure 3.14) for $t_d = 1/\Gamma$, which corresponds roughly to the mean lifetime of all Rydberg states investigated experimentally in chapter 8 ($1/\Gamma \approx t_d = 10\,\mu\text{s}$). (b) Weight $S(q)\Delta N_{\text{Bog}}(q)$ of Bogoliubov excitations. (c) Absolute square of the Fourier transformed electron-atom scattering potential $|V_{\text{scat}}|^2$ for two Rydberg S-states, weighted with q^2. Terms up to linear in the electron momentum are considered (see paragraph 3.2.2). Note the scaling of this ordinate in (c) with the principal quantum number n. The transition between the regimes of phonons and free particle excitations is shown as a dotted vertical line. The solid vertical lines indicate the maximum Fourier components of the scattering potentials at $q_m = \frac{\pi}{3a_0(n-\delta_0)^2}$.

in the regime of phonon excitations, since the size of the potential $2a_0(n-\delta_0)^2$ is always larger than typical values of the BEC healing length ξ. However, from Figure 3.15, it becomes clear that the integrated contributions at higher momenta q also play a role.

3.2.4.6 Different approximations of the electron-atom scattering potential

The influence of corrections to higher order in the electron momentum $\hbar k$ onto the line shift of Rydberg states is discussed in paragraph 3.2.2. The same comparison for the total number ΔN of atoms affected by one Rydberg excitation is shown in Figure 3.16a. As with the line shift, the k-dependent reduction of the scattering length leads to a smaller effect, that is corrected

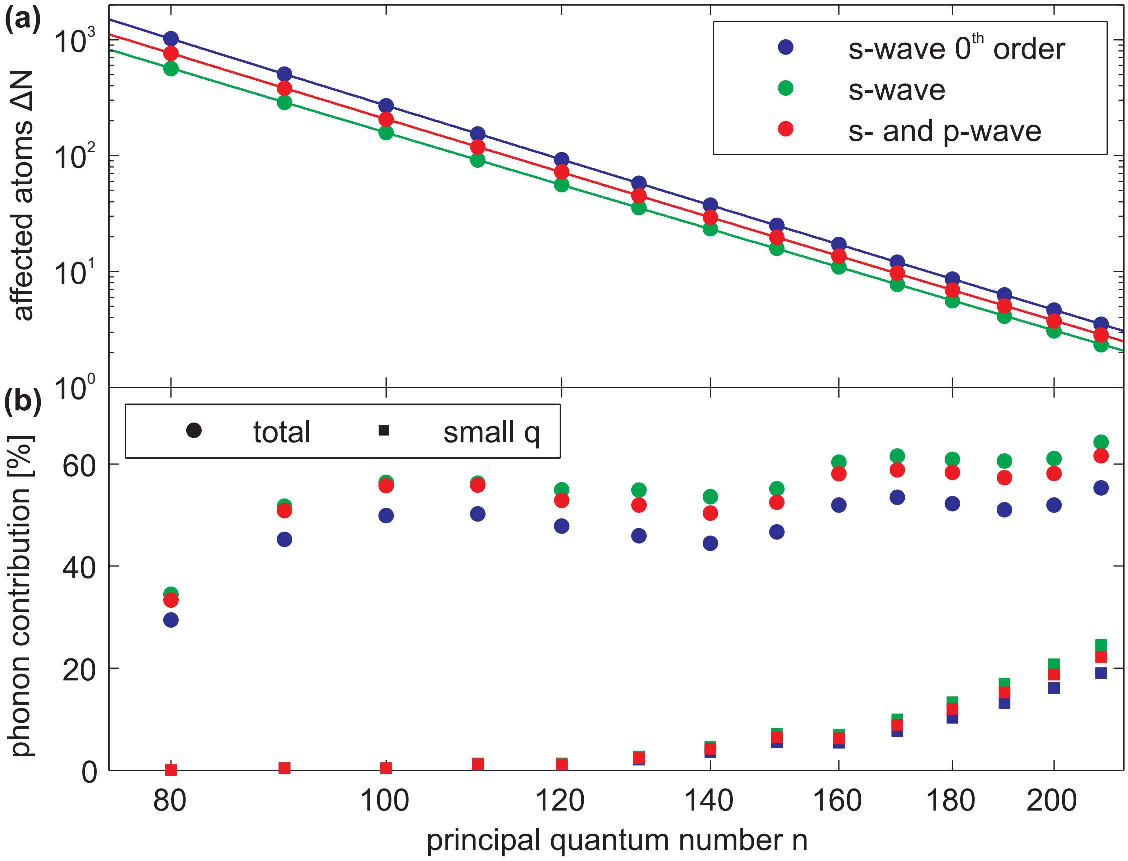

Figure 3.16: Number ΔN of atoms affected by one Rydberg excitation for different Rydberg S-states. In (a), the dependence on the principal quantum number n is shown for different orders of approximation of the electron atom scattering potential (see paragraph 3.2.2). A homogeneous condensate density of $\rho = 8.6 \cdot 10^{13}\,\mathrm{cm}^{-3}$ over the size of the Rydberg atom is assumed. This corresponds to the typical mean peak density over one experimental sequence, see section 8.1. The lifetime of the Rydberg state here is kept fixed at a constant value of $\tau = 10\,\mu\mathrm{s}$, corresponding roughly to the mean lifetime of all Rydberg states investigated experimentally in the condensate (see section 7.2). The solid lines are fitted power laws. In (b), the relative contribution of phonons ($q < \hbar/\xi$, circles) and phonons at very low momentum $q < 4.9 \cdot 10^5\,\hbar/m \approx 0.13\,\hbar/\xi$ (squares) is shown.

again to slightly higher values by the p-wave contribution; although here, the deviation is more pronounced. The correction to first order in k decreases from 23% to 19% between $n = 110$ and $n = 200$. All three curves, however, follow a power law with exponent -5.5 ± 0.1 in the principal quantum number $n - \delta_0$. This is close to the value of -6, expected from the simple following consideration. As discussed above, the integrand in equation (3.54) scales as the weight $q^2|V_{\text{scat}}(q)|^2 \sim (n - \delta_0)^{-4}$. Since the momentum dependence of this factor is rescaled proportional to $(n - \delta_0)^{-2}$, the integration over all q leads to $\Delta N \sim (n - \delta_0)^{-6}$.

Figure 3.16b shows the relative contribution of excitations in the phonon regime to the total number of atoms affected by the Rydberg excitation. As expected, the low momentum components play a more important role at higher principal quantum numbers, since the position of the dominant Fourier component is inversely proportional to the size of the Rydberg electron wavefunction $\sim (n - \delta_0)^{-2}$. The oscillatory behaviour is caused by the peaked structure of the Fourier transformed scattering potential (see Figure 3.15c). When the momentum scale is decreased at higher n, more and more maxima of $q^2|V_{\text{scat}}(q)|^2$ are located within the phonon regime, defined as $q < \hbar/\xi$.

As another important quantity, in Figure 3.16b, the relative contribution of excitations at momenta lower than $q_{\text{min}} = 4.9 \cdot 10^5\,\hbar/m \approx 0.13\,\hbar/\xi$ is shown. In the experiments discussed in section 8.1, excitations at momenta above this approximate threshold are detected as atom losses in time of flight imaging. It turns out that, at low principal quantum numbers n, next to all excitations lead to atom losses, whereas at higher n a significant part of the excitations remains undetected. In the parameter space studied experimentally in the framework of this thesis, ranging from principal quantum numbers $n = 110$ up to $n = 202$, the contribution of phonons and free particles to the atom loss signal is therefore roughly equal.

3.3 Ion-atom interaction

Rydberg atoms of course not only consist of an electron, but also contain a positively charged nucleus, that can also interact with atoms in its vicinity. Systems with ionic impurities in Bose-Einstein condensates have first been experimentally realized by Penning ionization of metastable atoms [178] and photoionization [179]. The impact of a single ion on a condensate has been studied combining a Paul trap and a cold atom apparatus [160, 180]. Various theoretical proposals exist for ion impurities in Bose-Einstein condensates. This ranges from the creation of mesoscopic molecular ions [181] and polarons [182, 183] to bosenova type collapse of the BEC [184]. However, the theoretical description dates back to the studies of impurities in liquid helium [185, 186, 187, 188]. A simple estimate of the total energy shift of a single ion, interacting with a gas of neutral ground state atoms, has been already given by Fermi [14] in the context of Rydberg atoms in high density gases (see introduction to section 3.2).

The discussion in this section shows that the effects arising from the ion-atom interaction are negligible compared to the electron-atom scattering, described previously in section 3.2.

3.3.1 Line shift of the Rydberg state

The interaction of the positively charged Rydberg core with the surrounding neutral ground state atoms is now considered first from the perspective of the Rydberg atom. There is an energy shift of the Rydberg state from the polarization of the surrounding particles by the ionic charge, that can be easily estimated [14]. If the relative motion of the Rydberg atom and the surrounding atoms can be neglected, the total energy shift is the sum of the polarization (3.21) of all atoms surrounding the nucleus at distances r_i:

$$\Delta E_{\text{pol}} = \frac{\alpha e^2}{2(4\pi\epsilon_0)^2} \sum_i \frac{1}{r_i^4} \tag{3.58}$$

The mean over the sum in (3.58) diverges, if the finite sizes of the Rydberg core and atoms are neglected, however, the expression of the most probable value in a homogeneous gas of density ρ is finite:

$$\sum_i \frac{1}{r_i^4} = -s \left(\frac{4\pi\rho}{3}\right)^{4/3} \tag{3.59}$$

The intuitive explanation is that the strongest contribution comes from the next neighbour at the mean interparticle distance $\overline{r} = \sqrt[3]{3/(4\pi\rho)}$ and the numerical factor $s \approx 2.6$ [14] accounts for the contribution of all particles further apart. This leads then to a red shift, which is proportional to the density ρ of perturbing atoms to the power of $4/3$:

$$\Delta E_{\text{pol}} = -\frac{\alpha e^2}{2(4\pi\epsilon_0)^2} \; s \left(\frac{4\pi}{3}\right)^{4/3} \rho^{4/3} \tag{3.60}$$

For $\rho = 10^{14}\,\text{cm}^{-3}$, which is a typical BEC density in this work, this leads to a line shift of $-26\,\text{kHz}$. This shift is largely negligible compared to the impact of the Rydberg electron, which is next to three orders of magnitudes larger (see Figure 3.12a). However, the exponent of the scaling with the atomic density is slightly larger than for the impact of the electron (equation 3.33). This means that the effect of the ion-atom interaction can become important at higher densities. Indeed, it leads to a sizeable contribution in the measurements of Amaldi and Segrè [2, 3], that where performed at densities up to $10^{20}\,\text{cm}^{-3}$.

3.3.2 Rydberg core as an ion impurity

As shown before, the influence of a high density environment onto a Rydberg atom is dominated by the interaction of the Rydberg electron with the atoms inside its wavefunction. Now, the impact of the Rydberg core as a positively charged ion onto the surrounding atoms is discussed. A static positively charged ion in a Bose-Einstein condensate is expected to attract atoms by the attractive polarization potential (3.21). An estimate for the steady state number ΔN of accumulated atoms around the impurity from thermodynamic considerations is given in [189], based on earlier work on ^{3}He impurities in liquid ^{4}He [190, 191]. In the case that the scattering between BEC atoms among each other and from the impurity can be treated as individual binary events, the energy density $\mathcal{E}$ of the system reads, depending on the densities ρ of atoms (a) and impurities (i):

$$\mathcal{E}(\rho_a, \rho_i) = \frac{1}{2} U_{aa} \rho_a^2 + U_{ai} \rho_a \rho_i \tag{3.61}$$

Here, U_x ($x = aa,\, ai$) denotes the mean field interaction constant $U_x = 2\pi\hbar^2 a_x / m_x$. The quantity ΔN is defined as the number of atoms, that has to be added in order to keep the chemical potential $\mu_a = \partial\mathcal{E}/\partial\rho_a$ of the BEC constant, when one impurity is added:

$$\frac{\partial\mu_a}{\partial\rho_i} + \frac{\partial\mu_a}{\partial\rho_a}\Delta N = 0 \tag{3.62}$$

Inserting equation (3.61) into (3.62) immediately leads to the result:

$$\Delta N = -\frac{U_{ai}}{U_{aa}} = -\frac{m_{aa}}{m_{ai}}\frac{a_{ai}}{a_{aa}} \tag{3.63}$$

For a charged impurity, the atom-impurity scattering length a_{ai} itself is also a function of the reduced mass m_{ai}. In contrast to the electron-atom scattering (see section 3.2), there are no predictions for the Rb$^+$-Rb scattering length so far. However, the order of magnitude for a singly charged impurity interacting with atoms with polarizability α can be estimated as the characteristic radius r_{ai} of the polarization potential [160]. This radius is defined as the distance, at which the p-wave centrifugal barrier $V_z = \hbar^2/(2 m_{ai} r^2)$ is equating the polarization potential (3.21):

$$r_{ai} = \sqrt{\frac{m_{ai}\alpha e^2}{(4\pi\epsilon_0\hbar)^2}} \tag{3.64}$$

In order to check the validity of this approximation, one can compare the resulting value of $r_{ai} = 18.1\, a_0$ for the electron-atom scattering length to the known e^--^{87}Rb scattering length a. The absolute value agrees quite well with the value $a_{ai} = -16.1\, a_0$ for the triplet scattering most relevant in this work, whereas the singlet scattering length $a_{ai} = 0.627\, a_0$ differs considerably [157].

For the ^{87}Rb$^+$ Rydberg core, this leads to a characteristic radius of $r_{ai} = 5000\, a_0$. Using this value as an estimate for the scattering length $a_{ai} \approx -r_{ai}$ leads to an accumulation of about $\Delta N = 46$ atoms. In order to judge whether this can cause a sizeable effect in a Rydberg atom, one has to compare this to the effect of the Rydberg electron. In case of a charged impurity, one obtains a scaling of $\Delta N \propto 1/\sqrt{m_{ai}}$. This means that for ^{87}Rb, the interaction strength of an electron is two orders of magnitude stronger than the interaction strength expected for a positively charged ion. Here, ΔN exceeds 10^4 atoms, clearly reaching the limits of weak perturbation assumed in the derivation of expression (3.63). Even though this estimate is not valid in the case of the electron any more, it clearly shows that, in the present case, any effect of the Rydberg core can be largely neglected compared to the impact of the Rydberg electron.

Part II

Experimental Setup

In this part, the experimental setup and the methods used to obtain the results presented in part III are described. The basic idea of the present experimental apparatus is to combine ultracold dense atomic samples with highly excited Rydberg states. This concept proved to be quite successful; although the apparatus has been continuously extended and modernized by the preceding six generations of PhD students [192, 84, 96, 13, 79, 11], the core is now almost ten years old. Even though some parts seem to be or are indeed outdated, there are some persistent advantages, that enabled interesting discoveries during the past few years.

The previous work at this apparatus was mainly focused on the spectroscopy of Rydberg states at relatively low principal quantum numbers, between $n = 34$ and $n = 46$, in dense but still thermal samples of cold atoms. Some initial experiments have been also performed on the combination of Rydberg atoms and Bose-condensed samples [84, 83]. However, in that work, the diagnostics were still based on Rydberg spectroscopy by field ionization and subsequent ion detection. Due to the limitations of this technique in the present configuration (see paragraph 5.3.1), the information obtained about Rydberg excitation in the condensate was rather indirect. The main advance of the work presented in this thesis is the extension to much higher principal quantum numbers $n > 100$ and direct studies of their impact onto a Bose-Einstein condensate. Performing experiments in this regime imposes some demanding requirements on the experimental setup. These points are discussed in more detail alongside a short overview of the whole apparatus.

The description of the experimental setup is grouped into two chapters: Chapter 4 deals with the methods, which are used to prepare and probe a sample of ultracold atoms. After a technical description, the free expansion of a BEC is discussed, since this is crucial for the interpretation of absorption images, taken after a time of flight. Chapter 5 is dedicated to the excitation and the detection of Rydberg atoms. Besides a description of the laser system used for Rydberg excitation, the focus here lies on the control of electric fields, required to study Rydberg atoms at high principal quantum numbers, and the different experimental sequences applied in the BEC and thermal samples, respectively. Within the framework of this thesis, some overlap between the two initially separate parts of the setup, described in chapters 4 and 5, emerged. For example, effects of the Rydberg excitation lasers have to be considered already during the preparation of the atomic sample and the Rydberg excitation in the condensate, in turn, can be studied using the imaging of the atomic sample.

In the following, the most important parts of the experimental setup are described. References to previous PhD theses are added for more detailed information. Only those parts, which underwent significant changes or which are essential to understand the experiments described in this thesis, are discussed more thoroughly.

4 Ultracold atoms

4.1 Preparation

The core of the experimental setup is a rubidium ^{87}Rb BEC apparatus, based on the design from [193], with some modifications required for experiments with Rydberg atoms as discussed later in chapter 5. It consists of a cloverleaf type magnetic trap [194] in an ultra-high vacuum steel chamber, operated at pressures below 10^{-11} mbar. The atoms are loaded via a magneto-optical trap (MOT) and a Zeeman slower from an effusive oven. Even though this imposes some stringent limitations, especially on the repetition rate of the experiment and the optical access to the atomic sample, the benefits of this concept for Rydberg spectroscopy should not be underestimated (see chapter 5). Its main purpose is to trap and cool a sample of atoms down to quantum degeneracy. Starting from a hot rubidium vapour, the apparatus increases the phase space density by about 14 orders of magnitude. The key figures of merit are the repetition rate, the rate at which a cold atomic sample is produced, and the reproducibility and stability of shape, size and temperature of the resulting atomic cloud. Both are principal prerequisites for systematic studies with decent statistics.

The starting point is a beam of rubidium atoms emerging from an effusive oven, which is heated to $150°$C. This part is operated at pressures of around 10^{-7} mbar. The hot atomic beam is directed through a differential pumping stage and a mechanical shutter into a Zeeman slower [195]. This consists of a 85 cm long tube with magnetic field coils, providing an increasing magnetic field strength towards the chamber. The atomic beam is slowed down by absorbing light from a counterpropagating laser beam, resonant to the cooling transition $5S_{1/2}(F = 2) \rightarrow 5P_{3/2}(F = 3)$. The magnetic field induces a Zeeman effect, that compensates for the decreasing Doppler shift of the decelerating atoms.

The slowed down atoms are loaded into a MOT, that consists of a quadrupole magnetic field and six counterpropagating laser beams near-resonant to the cooling transition. Since the transition is not closed, one has to apply a repumping laser, acting on the transition $5S_{1/2}(F = 1) \rightarrow 5P_{3/2}(F = 2)$. The cooling light for both the MOT and the Zeeman slower is derived from a single titanium-sapphire laser (see e.g. [11]), whereas the repumping light is created with a separate diode laser. During a larger period of maintenance work on the oven part and a realignment of the Zeeman slower tube, the loading time of the MOT could be reduced to 2 s compared to previously 8 s [11] and 5 s [79]. This way, a precooled trapped sample of several 10^9 atoms at a few mK is prepared. To further the increase density, a dark MOT phase of 20 ms was introduced in [11].

The magnetic quadrupole field is then switched off for a 15 ms long phase of molasses cooling, while the cooling light is further detuned [192]. This decreases the temperature to around 20 µK, while loosing around half of the atoms. At the same time, due to the absence of a well defined quantization axis by the magnetic field, the atoms depolarize and are then equally distributed

over all m_F levels. Therefore, the atoms are pumped into the $F = 2$, $m_F = 2$ state, using a circularly polarized laser beam on the cooling transition at a small axial offset field.
The atoms are then loaded into the magnetic trap by ramping up the magnetic fields in 5 ms. The mode of the initial catch trap is matched to the size and shape to the MOT. This allows to transfer more than half of the atoms from the MOT into the magnetic trap. The atoms are then compressed to a cigar-shaped sample by first ramping up the current in the cloverleaf coils in 100 ms and subsequently increasing the current in the pinch and bias coils to the final value of 400 A within 150 ms. The system of power supplies for the magnetic trap is described in [96]; only the power supply of the pinch and bias coils has been replaced with a pair of more stable devices[1] connected in parallel. The magnetic field coils (depicted in Figure 5.2a and in [192]) generate a to first order harmonic, axially symmetric trap with trap frequencies:

$$\omega_r = \sqrt{\frac{g_F m_F \mu_B}{m}\left(\frac{B'^2}{B_0} - \frac{B''^2}{2}\right)} \tag{4.1}$$

$$\omega_z = \sqrt{\frac{g_F m_F \mu_B}{m} B''} \tag{4.2}$$

Here, μ_B denotes the Bohr magneton and the Landé factor is $g_F = 2$ in the present case with atoms in the $F = 2$ state. The magnetic field gradient $B' = 5.98 \cdot I_{CL}$ mT/(Am) is proportional to the current I_{CL} through the cloverleaf coils. The axial curvature $B'' = 0.83 \cdot I_{PB}/\mathrm{A\,T/m^2}$ depends on the current I_{PB}, which runs simultaneously through the pinch and bias coils. Both prefactors were determined for the present situation by measuring centre of mass oscillations of a BEC in the trap. Additionally, the offset field B_0 at the centre of the trap can be controlled independently by running an additional current through the bias coils. Without this additional current, the trap offset is $B_0 = 1.355$ mT, as determined by spectroscopy of Rydberg S-states. In the present experiments, an offset field of around $B_0 = 0.08$ mT was chosen, corresponding to trap frequencies of about $\omega_z = 2\pi \cdot 22$ Hz and $\omega_r = 2\pi \cdot 340$ Hz respectively. In principle, slightly higher values for the radial trapping frequency ω_r are possible at lower offset fields. This is favourable for evaporative cooling, since it increases the density and therefore the collision rate, leading to faster thermalization. However, this magnetic offset field has proven to be a good compromise if the field is subsequently ramped to higher values.
The longest step in the preparation of a cloud of ultracold atoms is the evaporative cooling. Here, the transitions between different m_F magnetic sublevels are driven by off-resonant radio frequency (RF) radiation. On resonance, atoms are transferred from the trapped $m_F = 2$ state into untrapped states with $m_F < 1$. The RF is detuned, such that transitions are only induced in those regions of the trap, where the Zeeman effect tunes the atoms in resonance. Since the atoms are trapped in the local minimum of a magnetic field, the RF detuning can be chosen in a way that only the hottest atoms, which can reach the outer border of the magnetic trap, are affected. By slowly ramping the frequency, starting from about 45 MHz down to less than 1 MHz over about 40 s, the cloud can partly rethermalize, leading to a cooling of the remaining atoms. By choosing the end frequency of the RF ramp accordingly, one can obtain either ultracold thermal clouds or Bose-Einstein condensates.
In order to realize a Bose-Einstein condensate at low density, as required for example for Rydberg dressing (see section 3.1), the offset field B_0 is then increased up to a value of

---

[1] Agilent 6682A, 5000 W power supply, 21 V, 240 A

$B_0 = 1.355\,\mathrm{mT}$ by adiabatically turning off the additional compensation currents, which are running through the bias coils [192]. This reduces the radial trapping frequency to about $\omega_r = 2\pi \cdot 82\,\mathrm{Hz}$. At the same time, the high magnetic field separates the different Zeeman components of Rydberg states, enabling to resolve a single quantum state. However, great care has to be taken, so that the Bose-Einstein condensate survives the ramping and in particular that no shape oscillations are excited (see paragraph 2.3.2). Therefore, a smooth S-shaped magnetic field ramp lasting over $400\,\mathrm{ms}$, much longer than the inverse trap frequencies, is chosen. In order to avoid heating during this time, the RF source used for evaporative cooling is left on during this step. The RF has to be changed simultaneous with the magnetic field, such that only hot atoms are removed.

The focused blue Rydberg excitation light generates a potential for the ground state atom (see Figure 5.3). Fast switching of this laser can therefore also excite shape oscillations of the BEC and even the thermal cloud. Therefore, this light is already switched on adiabatically over $400\,\mathrm{ms}$ during the ramping of the offset field.

4.2 Detection

At the end of each experimental cycle, the magnetic trap is switched off and the atoms are released. After a variable time of flight, an absorption image is taken from top. For this purpose, a circularly polarized laser beam near-resonant to the $5S_{1/2}(F = 2, m_F = 2) \rightarrow 5P_{3/2}(F = 3, m_F = 3)$ transition is applied from below for $100\,\mu\mathrm{s}$. This laser beam is derived from the same laser system, which is used to create the MOT light. In order to adapt the quantization axis of the atoms to the imaging axis, a small magnetic offset field is applied along the y-axis (see Figure 5.2) $20\,\mu\mathrm{s}$ before the currents through the cloverleaf and pinch-bias coils are switched off. The amplitude and timing of this offset field are crucial. If it is too low or switched on too late, the atoms are depolarized and therefore only partly detected. If, on the contrary, the offset field is switched on too early, the atomic cloud is accelerated by the additional magnetic field pulse. In the worst case, both can happen simultaneously. Experimentally, both amplitude and timing of the bias field were adjusted in a way that the atomic cloud falls down perfectly vertically and there is no transfer of atoms into other states. This can be controlled in a Stern-Gerlach-type experiment.

At the end, the number of atoms can be extracted directly from the absorption profile. The further interpretation of time of flight images is a little bit more involved. The evolution of a Bose-Einstein condensate during time of flight is thus discussed in more detail in the following. As the atomic cloud falls down in gravity, it also expands, driven by the thermal energy and the mean-field interaction of the particles. In a thermal sample, the atoms detach ballistically from the centre of mass of the cloud, according to their thermal energy. For long time of flights, the density distribution of the sample therefore approaches a spherically symmetric Gaussian distribution. From the measured width of this distribution, then the temperature of the sample can be determined. The corresponding equation can be found e.g. in [129] or [192]. The fitting routines, used to extract parameters like density and temperature, are described in [84].

4.2.1 Time of flight expansion of a BEC

For a condensate in Thomas-Fermi approximation (see section 2.2), the thermal energy of the atoms is neglected and the expansion is therefore driven by the mean-field interaction. The expansion can be calculated using a simple and instructive classical model, that leads to the same result as a quantum mechanical calculation based on the Gross-Pitaevskii equation [196]. Each particle in the BEC individually experiences a force, created by the trapping potential and the mean-field interaction (see section 2.1):

$$\vec{F}(\vec{r},t) = -\vec{\nabla}\left[V(\vec{r},t) + g\rho(\vec{r},t)\right] \tag{4.3}$$

The trapping potential $V(\vec{r},t)$ is off at times $t > 0$. For harmonic potentials, the shape of the condensate is only dilated [196]. This means that any infinitesimal small fraction of the condensate moves along a trajectory:

$$R_i(t) = \lambda_i(t)R_i(0), \quad i = x,y,z \tag{4.4}$$

Here, $R_i(0)$ $(i = x,y,z)$ denote the initial equilibrium Thomas-Fermi radii, that are fixed by the condition $\vec{F}(\vec{r},0) = 0$:

$$\vec{\nabla}\left[g\rho(\vec{r},0)\right] = -\vec{\nabla}V(\vec{r},0) \tag{4.5}$$

This is equivalent to the treatment in section 2.2. The density distribution of the condensate is then rescaled as:

$$\rho(\vec{r},t) = \frac{1}{\lambda_x(t)\lambda_y(t)\lambda_z(t)}\,\rho\left(\left\{\frac{r_i}{\lambda_i(t)}\right\}_{i=x,y,z},0\right) \tag{4.6}$$

Applying Newton's law $m\ddot{\vec{R}} = \vec{F}(\vec{R}(t),t)$ on the trajectories (4.4), one can substitute the density gradient $\vec{\nabla}\rho(\vec{r},t) = 1/[\lambda_x(t)\lambda_y(t)\lambda_z(t)]\vec{\nabla}\rho(\{R_i/\lambda_i(t)\}_{i=x,y,z}\,,0)$ in the expression of the force (4.3) by using equation (4.5). This immediately leads to:

$$m\ddot{R}_i(t) = -\partial_{r_i}V(\vec{R}(t),t) + \frac{1}{\lambda_x(t)\lambda_y(t)\lambda_z(t)\lambda_i(t)}\partial_{r_i}V(\vec{R}(0),0) \tag{4.7}$$

For harmonic trapping potentials $V(\vec{r})$, the initial Thomas-Fermi radii $R_i(0)$ cancel out, thereby justifying the self-similar ansatz (4.4). For an axially symmetric trapping potential as in the present experiment, one obtains a system of coupled differential equations for the scaling factors $\lambda_r(t)$ and $\lambda_z(t)$ in cylindrical coordinates:

$$\begin{aligned}\ddot{\lambda}_r &= \frac{\omega_r^2(0)}{\lambda_r^3\lambda_z} - \omega_r^2(t)\lambda_r\\ \ddot{\lambda}_z &= \frac{\omega_z^2(0)}{\lambda_r^2\lambda_z^2} - \omega_z^2(t)\lambda_z\end{aligned} \tag{4.8}$$

It is equally straightforward to solve this set of equations numerically or expand it for highly prolate traps $\omega_r(0)/\omega_z(0) \ll 1$ in order to obtain an explicit result for the time of flight expansion, as stated in [129]. Introducing time-dependent modulations of the trapping potential, the differential equations (4.8) even allow to simulate shape oscillations, that were discussed analytically in paragraph 2.3.2.

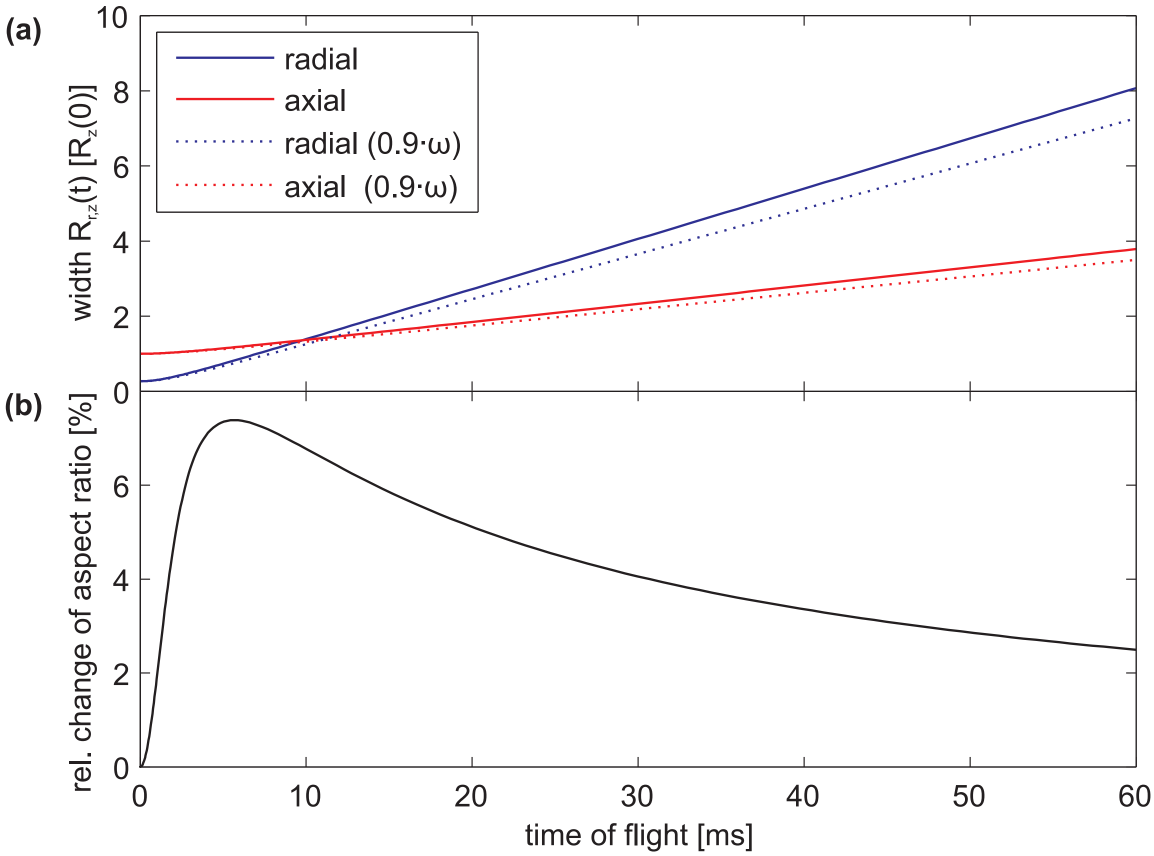

Figure 4.1: Simulated time of flight expansion of a Bose-Einstein condensate. In (a), the radial (blue) and the axial (red) expansion in units of the axial Thomas-Fermi radius $R_z(0)$ are shown versus the duration of the time of flight. The calculations were done by numerically solving the system of differential equations (4.8) for the trap frequencies $\omega_z = 2\pi \cdot 22\,\mathrm{Hz}$ and $\omega_r = 2\pi \cdot 82\,\mathrm{Hz}$, corresponding to the experimental situation at a high offset field of $B_0 = 1.355\,\mathrm{mT}$ (solid lines), as well as for both trap frequencies lowered by $10\,\%$. In (b), the relative change of aspect ratio $R_z(t)/R_r(t)$, induced by the weaker trapping, is shown.

In Figure 4.1a, the expansion for two different pairs of trapping frequencies is shown. Since the density gradient is larger in radial direction, the expansion in this direction is faster than the axial expansion. Therefore, the aspect ratio of the condensate is inverted at time of flights above $10\,\mathrm{ms}$. In the limit of very long expansion times, the aspect ratio converges to exactly the inverse value of the aspect ratio in the trap. Furthermore, after an initially linear acceleration, visible as a quadratic increase in radii, the mean-field energy is completely turned into kinetic energy and the further expansion is linear in time. The timescale of this energy conversion is inversely proportional to the trap frequency, leading to an interesting effect shown in Figure 4.1b. Here, the relative change of the aspect ratio is plotted, which is caused by lowering both trap frequencies by $10\,\%$. Although the modified trapping frequencies lead to the same aspect ratio, both in the trap as well as in the limit of long time of flights, there is a significant deviation for experimentally relevant finite durations of the time of flight. This allows in principle to observe also isotropic deformations of a Bose-Einstein condensate as a modification of the aspect ratio in time of flight.

5 Rydberg excitation

For experiments with Rydberg atoms, basically three components are required: A narrow band laser system to excite Rydberg atoms, good electric field control, and a method to detect atoms in the Rydberg state. These three components are described in the following sections.

5.1 Laser system

In order to excite Rydberg states of rubidium with principal quantum numbers $n > 30$ in a single step directly from the ground state $5S_{1/2}$, a laser at a wavelength below $300\,\text{nm}$ is required. Such laser systems exist and can be used to excite Rydberg P-states. Alternatively, these states can be excited using three laser beams in a specific geometry, such that the Doppler effect is completely eliminated [197]. However, the most common schemes for Rydberg excitation rely on a two-photon transition. This enables the excitation of Rydberg S- and D-states at reduced Doppler effect, if a geometry with counterpropagating laser beams is chosen. To obtain higher two-photon Rabi frequencies, the lower transition can be chosen near-resonant either to the $5S_{1/2} \rightarrow 5P_{3/2}$ [198] or to the $5S_{1/2} \rightarrow 6P_{3/2}$ [199] transition, which requires lasers at wavelengths $780\,\text{nm}/480\,\text{nm}$ and $420\,\text{nm}/1020\,\text{nm}$ respectively. The laser driving the lower transition usually is detuned by several $100\,\text{MHz}$ to the intermediate state, which turns the actual three level atom into an effective two-level system with a coherent coupling of the ground and the Rydberg state (see paragraph 1.1.4). In both excitation schemes, the Rabi frequency of the lower transition is limited by off-resonant scattering from the intermediate P-state (see section 7.3), which depends on the ratio of Rabi frequency Ω_r of the lower transition and intermediate detuning Δ_p, as well as on the decay rate Γ_p of the P-state [200]:

$$\Gamma_{\text{scat}} = \frac{\Omega_r^2}{4\Delta_p^2}\Gamma_p \tag{5.1}$$

For the transition via the $6P_{3/2}$ state, the dipole matrix element of the upper transition is larger [199]. Furthermore, high power lasers are more readily available at infrared wavelengths than for blue light. However, in this scheme another limitation occurs. Two photons of the light at $420\,\text{nm}$ can ionize an atom in a two-photon transition, leading to additional atom losses and electric fields caused by the created ions [201, 202]. Considering also the higher decay rate of the $6P_{3/2}$ state and the smaller dipole matrix element of the lower transition, still a factor two to three in the two-photon Rabi frequency can be gained, compared to the transition via the $5P_{3/2}$ state with current laser technology.

The experiments, presented in this thesis, were conducted with a laser system consisting of a red ($780\,\text{nm}$) and an infrared ($960\,\text{nm}$) extended cavity diode laser. The infrared light is frequency converted into blue light at $480\,\text{nm}$ by frequency-doubling. The red laser is blue detuned by $\Delta_p = 500\,\text{MHz}$ to the intermediate $5P_{3/2}\,(F = 3, m_F = 3)$ state.

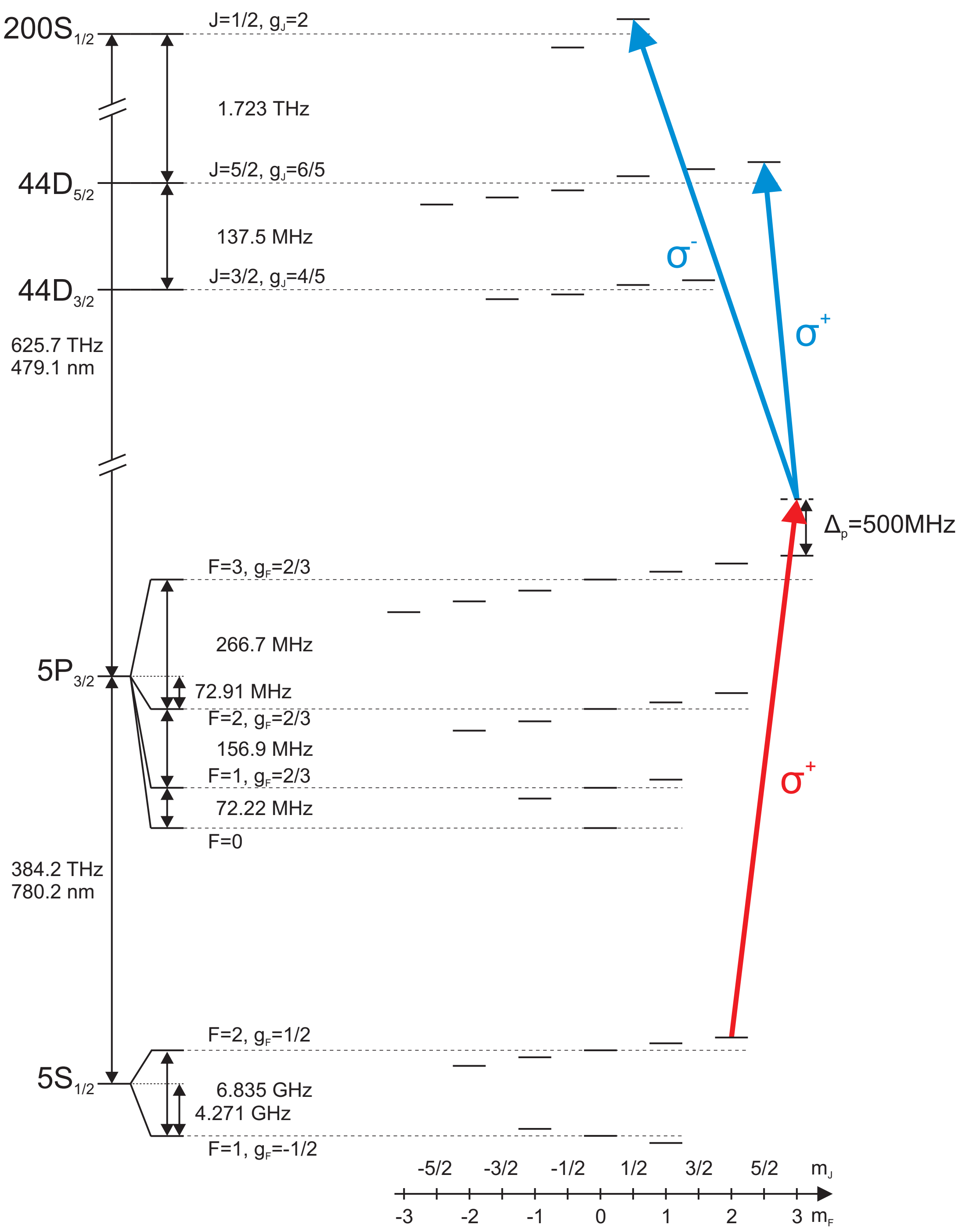

Figure 5.1: Level scheme for the Rydberg excitation of ^{87}Rb. Exemplarily the $200S_{1/2}$ and the $44D_{5/2,\,3/2}$ states are shown. On the left, the splitting by the fine structure and hyperfine structure is indicated. The hyperfine structure for the Rydberg states is negligible. In a magnetic field, the states are split further up according to the magnetic quantum number m_F (low states) and m_J (Rydberg states), as can be seen on the right. The Rydberg excitation is performed via a two-photon transition, blue detuned by $\Delta_p = 500\,\text{MHz}$ from the $5P_{3/2}\,(F = 3, m_F = 3)$ state; here, only the strongest excitation path is highlighted (see text). The fine structure splittings are taken from [94].

The excitation path and the splitting of the relevant states in a magnetic field are shown in Figure 5.1. Different Rydberg S- and Rydberg D-states can be excited by changing the polarization of the blue excitation light. Note that the excitation frequencies of Rydberg $nS_{1/2}\,, m_S = 1/2$ states do not depend on the magnetic field. However, neither the polarization of the light nor the spin polarization of the atomic sample are perfect. Due to the inhomogeneous field of the magnetic trap, there are always atoms that experience unwanted polarization components. At high laser powers, hence all magnetic substates of Rydberg S- and D-levels can be excited. Furthermore, evaporative cooling (see section 4.1) creates a small population of the weakly trapped $m_F = 1$ magnetic sublevel of the ground state. Therefore, all lines in the spectrum have a tiny mirror image, located at $1/2\mu_B B/h$ on the blue side. The splitting between these lines can for example be used to precisely measure the magnetic offset field of the trap.

The first measurements presented in this work were performed with a laser system locked to the modes of two home-built cavities, constructed with a single spacer. The excitation frequency in this setup is controlled using a double-pass acousto-optic modulator (AOM) and a master-slave configuration. This setup is described and characterized in detail in [159, 79]. Most of the results discussed in part III have been obtained with a new laser system, described in [203]. This next generation setup provides up to $150\,\text{mW}$ of blue laser power at the experimental chamber, about 50% more than the old system. For the frequency stabilization, here a commercial cavity[1] is used. The spacer of this cavity is made from premium grade ultralow expansion (ULE) glass. The thermal expansion coefficient of this material is below 2 ppb/K, much smaller than the one of low quality Zerodur glass (up to 100 ppb/K), which is used in the home-made cavity. Therefore, thermal drifts of the resonance frequency [11] are completely negligible even on the kHz-scale with this system. The cavity mirrors have a dual band coating allowing to stabilize both diode lasers at $780\,\text{nm}$ and $960\,\text{nm}$ simultaneously onto the same cavity at a designed finesse[2] of 1800. The frequency of the excitation lasers in the new setup is controlled by locking sidebands at variable frequency to a mode of the cavity. These sidebands and the modulation for the Pound-Drever-Hall technique are created with a fiber coupled electro-optic modulator (EOM). Both in the new and the old setup, the frequencies needed for scanning the laser frequency are generated using a system of direct digital synthesizers (DDS), developed in collaboration with the electronics workshop. This system is controlled using a combination of USB and digital (TTL) signals, allowing precise and fast scans of frequencies.

The red and the blue Rydberg excitation light of both laser systems are shone in from opposite directions into the experimental chamber (see Figure 5.2a). The counterpropagating geometry significantly reduces the Doppler effect [159] to around $18.5\,\text{kHz}$ at temperatures of $1\,\mu\text{K}$, compared to $77.5\,\text{kHz}$ for a collinear configuration. A flipping mirror and a dichroic mirror allow for fast interchange between the two laser systems, which can be easily extended to a simultaneous use. Both red laser beams are only slightly focused to a beam waist of $500\,\mu\text{m}$, while the blue laser beam from the old laser setup (system 1 in Figure 5.2a) is focused to a $30\,\mu\text{m}$ waist. An additional telescope in the path of the new blue laser (system 2 in Figure 5.2a) was used to initially obtain a waist of $10\,\mu\text{m}$. However, it was found that this strongly focused configuration leads to a significant deformation of the trap by the additional potential generated by the $480\,\mu\text{m}$

---

[1] Stable Laser Systems ATF 6020-4 notched cavity

[2] After finishing the experiments described in this thesis, the cavity has been replaced with a quad-band coated cavity for simultaneous use with wavelengths at 780 nm/960 nm and 840 nm/1020 nm and a finesse > 10000. This allows to stabilize another Rydberg laser system near-resonant to the $6P_{3/2}$ state at the same time.

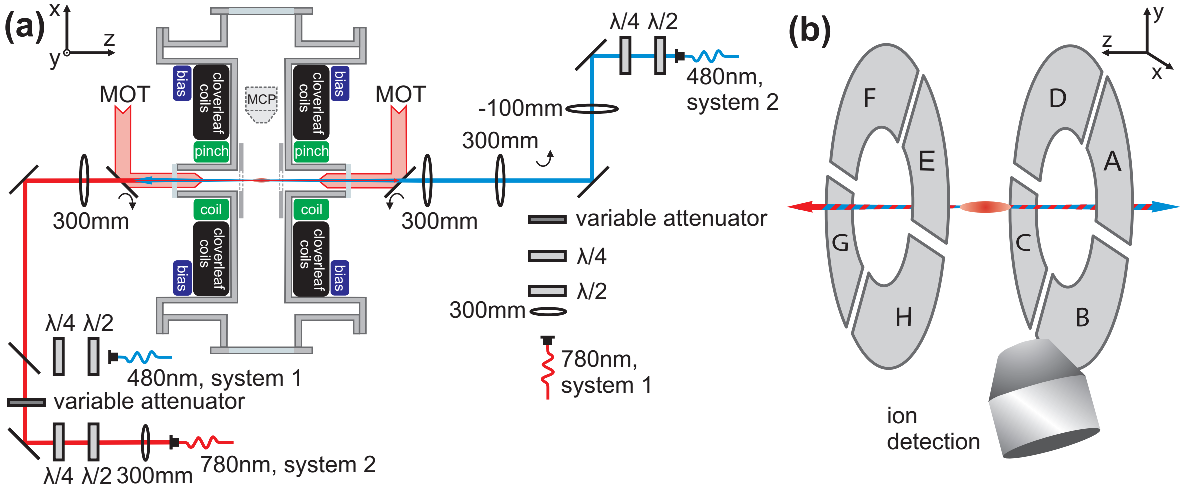

Figure 5.2: Schematic representation of the setup. In (a), the chamber with the field coils and the light path for Rydberg excitation is drawn from above. The axial MOT beams enter the chamber by motorized flipping mirrors at the beginning of each sequence. One can switch between two laser systems by flipping only one mirror, since the blue laser 1 is already overlapped with the red laser 2 using a dichroic mirror. In (b), the geometry of the field plates to control the electric field around the atomic cloud and the microchannel plate detector for ion detection is sketched.

laser. Therefore, the focus position was slightly changed by moving the last lens in front of the vacuum chamber until the combined potential of the trap and the blue laser was approximately harmonic. The defocused geometry leads to a calculated radial width of $60\,\mu\mathrm{m}$ at the position of the atomic cloud.

The alignment of the focused laser at $\lambda_b = 480\,\mathrm{nm}$ onto the BEC is crucial for all experiments with Rydberg excitation in a BEC. Due to the Rydberg blockade, the configuration of the maximum Rydberg signal, measured by field ionization, not necessarily corresponds to the position, where the focal position of the blue laser beam is in the centre of the condensate. To overlap the position, the blue laser beam is retroreflected with an additional mirror back into the optical fibre. The resulting optical lattice is pulsed for typically $0.2\,\mu\mathrm{s}$ to $10\,\mu\mathrm{s}$, which results in a diffraction pattern, visible in absorption images taken after a time of flight of duration t_{TOF}. For alignment of the blue laser beam, pulse lengths are always kept short enough, so that only the first diffraction order is populated. In this case, the population in the first order is proportional to the lattice depth [176, 205]. Using this signal, it is tedious but straightforward to align the angle of the incident beam and the position of the last lens in front of the vacuum chamber to the maximum lattice depth at the position of the BEC. Furthermore, since the diffraction orders are equally spaced at $2h/\lambda_b/m \cdot t_{\mathrm{TOF}}$, the lattice diffraction can be used to relate the position in time of flight images with corresponding atomic momenta, as required for the estimates in paragraph 3.2.4.

Both laser systems have been characterized to have a combined excitation linewidth below $60\,\mathrm{kHz}$ [159, 203]. At very low Rabi frequencies, spectral lines of Rydberg S-states at linewidths down to $30\,\mathrm{kHz}$, close to the Doppler limit and the natural linewidth (below $16\,\mathrm{kHz}$, depending on the Rydberg state) have been observed.

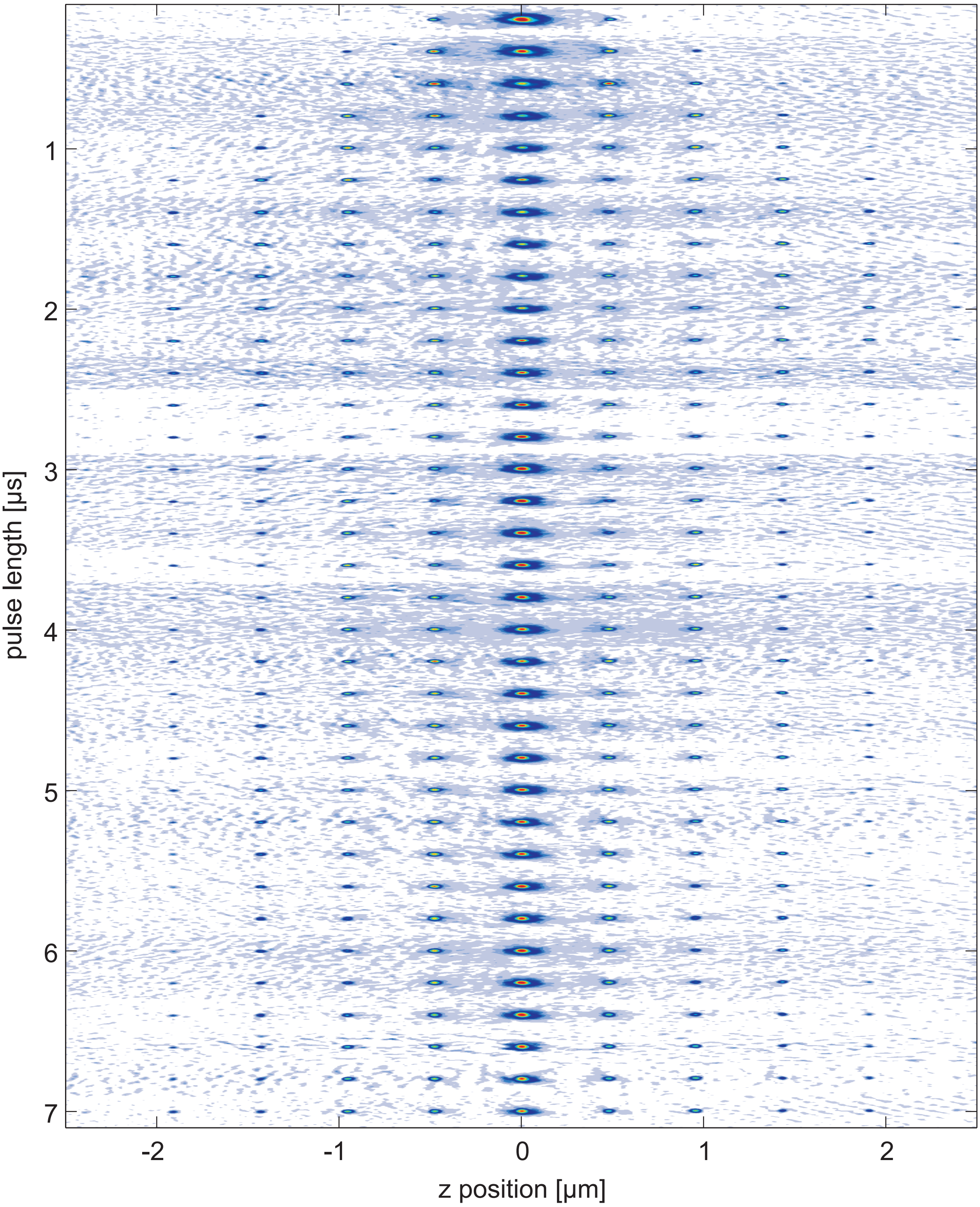

Figure 5.3: Time of flight images of a BEC, diffracted from a standing wave pulse, which is created by the retroreflected $480\,\mathrm{nm}$ laser. The time, which the optical lattice is on, was varied in steps of $0.2\,\mu\mathrm{s}$ from $0.2\,\mu\mathrm{s}$ to $7\,\mu\mathrm{s}$, while the time of flight was kept fixed at $t_{\mathrm{TOF}} = 20\,\mathrm{ms}$. This measurement was taken with the smallest focus (around $10\,\mu\mathrm{m}$ waist) and a laser power of $130\,\mathrm{mW}$. In the Raman-Nath regime, at short pulse length (here up to about $1\,\mu\mathrm{s}$), the number of observed diffraction orders increases monotonously [204, 205]. For longer pulse lengths, there is a revival of the zeroth order [176, 204] that is not visible in the data shown.

5.2 Electric field control

The polarizability of high Rydberg S-states is scaling with the principal quantum number as $(n - \delta_0)^7$ [206]. Furthermore, the classical ionization field decreases from $312\,\mathrm{V/cm}$ at $n = 35$ to $2.46\,\mathrm{V/cm}$ at $n = 110$ and even $0.21\,\mathrm{V/cm}$ at $n = 200$, proportional to $(n - \delta_0)^{-4}$ (see equation 5.2). Therefore, an excellent control of electric fields is a crucial prerequisite to be able to investigate Rydberg states at principal quantum numbers above $n = 100$. The experimental chamber of the present setup is very well suited for this task. All dielectric surfaces like windows, that could pick up charges and possibly create stray fields, are centimetres away from the position of the atomic cloud. Eight individually addressable electric field plates are positioned around the atomic cloud, as depicted in Figure 5.2b. A typical Stark map, measured by spectroscopy in a thermal sample, is shown in Figure 5.4a for the $160S$ Rydberg state. The overlaid theory curves were calculated using the database from [79]. Already at tiny electric fields on the order of $1\,\mathrm{mV/cm}$, the hydrogenic manifold [37] at principal quantum number $n = 157$ is crossing the $160S$ state. The coupling to these states leads to a significant modification of the observed quadratic Stark effect, also at smaller electric fields. The experimental signal follows the exact theory curve until it starts to vanish at field strengths above around $12\,\mathrm{mV/cm}$. This field strength is still well below the classical ionization threshold at $530\,\mathrm{mV/cm}$. The reason for the vanishing signal is a large broadening, which is caused by the coupling to the manifold states and by the inhomogeneity of the electric field. During the iterations of field compensation, the progress can therefore be determined from both the line position and width. In a well compensated situation, the configurations with highest spectral position and minimum width

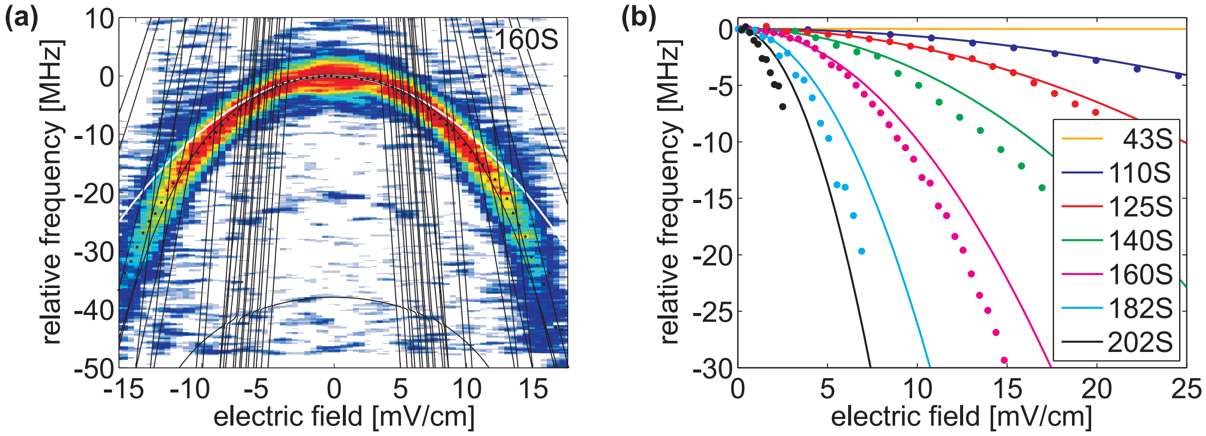

Figure 5.4: Stark maps of high Rydberg S-states. In (a), the calculated energies of Rydberg states in the vicinity of the $160S$ state are shown as black lines on top of the colour-coded ion signal for different electric fields. The black dots are line positions, extracted from Gaussian fits to the experimental data. The white line is a parabolic fit to the theory at low electric fields, where the Stark effect is purely quadratic. From this fit, the value of the polarizability for the theory curve in (b) is extracted. In (b), measured line positions (dots) for different Rydberg states are compared to the theoretically expected quadratic Stark effect. The polarizabilities are extracted from theoretical Stark maps [79], as shown in (a). Note that the first data point of the $43S$ state is already far above the range of electric fields relevant for the higher Rydberg states.

of the Rydberg line coincide. Another indication is provided by the measured polarizability. The white line in Figure 5.4a indicates the polarizability, extracted from the theory data at low electric fields and far from crossings with other states. Only close to absolute zero electric field, the curvature of the measured Stark map matches this theoretical polarizability. An insufficient field compensation in the other directions thus leads to a higher curvature, even at the centre of the measured Stark parabola. Comparing the experimental data to the calculated polarizability for measurements at different Rydberg states (see Figure 5.4b), one can estimate the quality of the current electric field control to be on the order of $1\,\mathrm{mV/cm}$. On this level, the electric field compensation is stable for about one week in the present setup. It allows to perform spectroscopy on Rydberg S-states at linewidths below $1\,\mathrm{MHz}$ up to principal quantum numbers of about $n = 125$. Even at $n = 202$, the measured linewidth does not exceed $4.5\,\mathrm{MHz}$ (see Figure 7.2). Due to residual field gradients, these ultimately narrow linewidths are only achievable in cold thermal samples at temperatures around $1\,\mu\mathrm{K}$ and low laser powers. Any heating leads to an additional broadening due to atoms, that are excited in regions apart from the zero position.

5.3 Detection

5.3.1 Rydberg spectroscopy in thermal samples

Previously, the detection of Rydberg atoms in the present setup was exclusively done by field ionization and subsequent ion detection. As discussed in the following, this technique is well-suited for studies of Rydberg excitation in large thermal samples, but limited for the investigation of Rydberg atoms in Bose-Einstein condensates, at least in the present setup.

After the laser excitation pulse, a voltage is applied to the field plates B&H (see Figure 5.2b). The electric field ionizes the Rydberg atoms and accelerates the ions towards a microchannel plate detector (MCP). The classical threshold E_{ion} for field ionization of Rydberg states can be estimated from the saddle point of the combined Coulomb potential created by the Rydberg core and the Stark potential from the external field. Identifying the energy of the saddle point and the energy of the Rydberg state [37], one obtains:

$$E_{\text{ion}}(n) = \frac{1}{16}\frac{e}{4\pi\epsilon_0 a_0^2}\,(n-\delta_0)^{-4} \tag{5.2}$$

For $n = 35$, this formula leads to fields above $310\,\mathrm{V/cm}$, which requires the use of high voltages around $2\,\mathrm{kV}$. Above $n = 110$, however, the ionization field reaches values of few V/cm and just some tens of Volts have to be applied. For low Rydberg states, a pair of independent high voltage power supplies and switches[3] is used. A small voltage difference between the two plates has to be chosen in order to direct the pulse of ions onto the microchannel plate detector. The rise time of the field pulse is about $400\,\mathrm{ns}$, whereas zero electric field is only reached after $15\,\mu\mathrm{s}$ due to pronounced ringing. For high principal quantum numbers $n > 100$, a low voltage switch[4] was implemented. Together with the lower voltages applied (up to $500\,\mathrm{V}$, typically

---

[3] Behlke HTS 61-03-GSM high voltage push pull switch with circuit for positive voltage pulses according to datasheet in order to reduce ringing.

[4] CGC instruments NIM-AMX500-3F digital threefold analogue switch.

around $50\,\mathrm{V}$), this device allows for significantly faster switching. With a matched ringdown resistor ($3\,\Omega$), absolute zero field in the chamber is reached in less than $1.6\,\mu\mathrm{s}$, as determined by Rydberg spectroscopy on the $110S$ state.

Depending on the electric field strength, the ions reach the detector about $2\,\mu\mathrm{s}$ to $260\,\mu\mathrm{s}$ after the ionizing field is switched on. The ions enter the detector through a grid in a grounded Faraday cage (see Figure 5.2), which shields the voltage of $-2\,\mathrm{kV}$ applied to the front of the microchannel plate in chevron configuration. This voltage is used to attract the incident ions and accelerate the electrons, which are generated by secondary emission towards an anode on ground potential. Via a simple home-made amplifying circuit, the charge on the anode is converted into a voltage signal, that is recorded with a PCI digitizer card[5]. The length of the field ionizing pulse is chosen to $60\,\mu\mathrm{s}$, such that crosstalks during switching do not affect the measured signal. The characterization of the MCP and the data processing is described in [159]. The overall detection efficiency for Rydberg atoms was determined to about only 2%. This means that single or even few Rydberg atoms are practically not detectable in the present setup. Due to the Rydberg blockade, only few Rydberg excitations are possible in the volume of a typical BEC, even at low principal quantum numbers. Thus, it is impossible to detect any isolated Rydberg signal from a condensate using field ionization and ion detection in the present setup.

For Rydberg spectroscopy in Bose-Einstein condensates, therefore a different approach was taken, that is described in the next paragraph. For spectroscopy in large thermal samples, however, where at least several hundreds of Rydberg atoms are created at once, the field ionization technique is still advantageous. Since the fraction of atoms excited with one laser pulse is typically small, a sequence of Rydberg excitation and ion detection can be repeated up to several hundred times (see Figure 5.5a) with one atomic cloud before the sample is significantly depleted. Scanning the excitation frequency at each pulse, a whole spectral line as shown in Figure 7.2 can be obtained in a single experimental run. In the present setup, the time between two subsequent Rydberg excitations is $6\,\mathrm{ms}$, leading to an overall sequence length of $2.4\,\mathrm{s}$. The lower limit is given at the moment by the minimum rearm time of $3\,\mathrm{ms}$ of the digitizer card, which is triggered on the individual excitation pulses. Of course, this limit can in principle be easily overcome by taking data during the whole sequence. However, this time does not play a role here, since the lifetime of the thermal cloud is on the order of several seconds. The possible speed up does not outweigh the additional resources required to deal with a larger amount of idle data.

The lifetime of Rydberg states in thermal samples is measured in section 7.2 by introducing a variable wait time between excitation and detection. Atoms decaying by spontaneous emission most probably end up in low states, close to the ground state [37]. Since the field ionization in the present setup is not state selective, the measured decay of the Rydberg population does not include the contribution of blackbody radiation or other decay processes, that mostly populate neighbouring Rydberg states (see [159] and further discussion in section 7.2).

5.3.2 Rydberg spectroscopy in Bose-Einstein condensates

Even at low principal quantum numbers around $n = 35$, the Rydberg blockade allows only much less than ten Rydberg excitations at a time in a Bose-Einstein condensate at the current

---

[5] ADLINK Technology PCI-9812

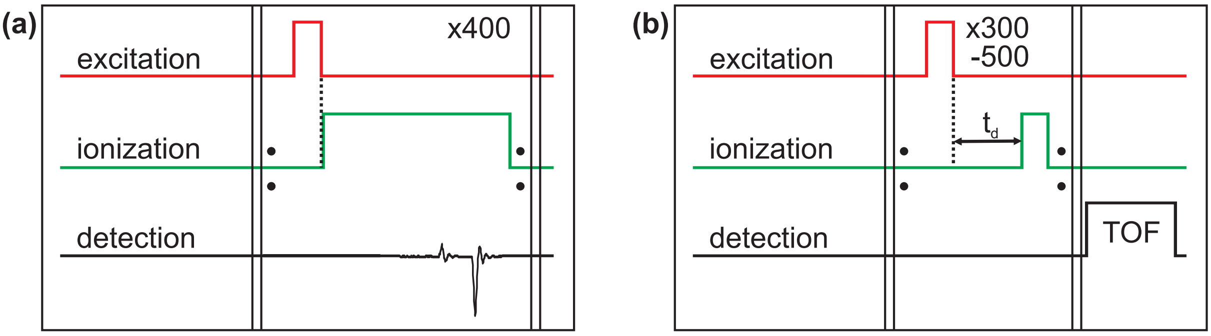

Figure 5.5: Sketch of different experimental sequences to excite and detect Rydberg atoms. (a) In a thermal sample, the cycle of excitation and field ionization is repeated several hundred times in one atomic cloud, while scanning the excitation frequency. The ions are detected as a negative peak in the current from the anode of the multichannel plate. (b) In a BEC, the cycle of excitation and field ionization is repeated also several hundred times, however, with a fixed wait time t_d between excitation and ionization. The Rydberg signal is then extracted from the atom loss of the BEC, measured by absorption imaging after a long time of flight (TOF).

parameters (see section 4.1). As discussed in the previous paragraph, the current setup for field ionization and ion detection is not suited to detect such low numbers of Rydberg atoms. Furthermore, the BEC is always surrounded by a thermal cloud. Even though the density of this cloud is very low, the infinite wings of its Gaussian density distribution cause a large contribution to the Rydberg population and therefore to the ion signal. As a matter of principle, it is not possible to separate the ion signal, stemming from the condensate, from ions emerging from the thermal cloud[6]. In order to isolate the effect of Rydberg excitation in a BEC, a different approach was developed in the framework of this thesis, that is described in the following.

The basic idea is to accumulate atom losses by repeatedly exciting and field ionizing Rydberg atoms. A sufficiently large depletion of the condensate can then be detected by absorption imaging after a time of flight (see section 4.2). If the atom losses would be only caused by field ionizing and extracting the Rydberg atoms, about 10000 subsequent Rydberg excitations would be required for a sizeable signal. However, as the discussion in paragraph 3.2.4 showed, the interaction between the Rydberg electron and the Bose-Einstein condensate can create elementary excitations, that carry a sufficient momentum to leave the condensate during a long time of flight, typically $50\,\text{ms}$. For the current parameters, Rydberg S-states at principal quantum numbers between $n = 110$ and $n = 202$ and BECs at peak densities up to $10^{14}\,\text{cm}^{-3}$, this additional effect is the dominant source of atom losses during time of flight (see appendix B.2.4). This significant amplification allows to accumulate a sizeable atom loss from the condensate, caused by as few as $300 - 500$ Rydberg excitations. Therefore, an additional wait time t_d is introduced between excitation and field ionization to allow the Rydberg electron to interact with the condensate. If the value of t_d is increased, the BEC atom losses, observed in time of flight imaging, saturate at a constant value. This way, the lifetime of the Rydberg atoms in the condensate is determined (see section 7.2). For the other measurements, a value of $t_d = 10\,\mu\text{s}$ is chosen, which is adapted to the mean lifetime of all Rydberg states investigated in this work.

---

[6] However, it turns out in section 7.1 that it is indeed possible to selectively excite Rydberg atoms only in regions with a certain atomic density.

After this interaction time, a short electric field pulse is applied in order to remove residual population in the Rydberg state or possibly existing ions. This clearing pulse provides well defined initial conditions for the next laser pulse. An ionization voltage increased by one order of magnitude[7] showed no detectable influence on the results. Together with the results presented in paragraph 7.2.2, this shows that population of lower Rydberg states does not play any role in the experiments described in chapters 7 and 8.

Since the lifetime of a Bose-condensed sample in the present setup is only on the order of $100\,\mathrm{ms}$, the whole sequence has to be orders of magnitude faster, compared to the measurements in the thermal cloud. Using low electric fields of $5.7\,\mathrm{V/cm}$, a $2\,\mu\mathrm{s}$ long field pulse is sufficient to ionize Rydberg atoms at principal quantum numbers $n \geq 110$ and safely extract the resulting ions from the atomic cloud. Taking the ring-down time of the electric fields into account, an experiment consisting of a $1\,\mu\mathrm{s}$ long Rydberg laser pulse, a delay time of $t_d = 10\,\mu\mathrm{s}$, and a clearing electric field pulse of $2\,\mu\mathrm{s}$ can be applied at a rate of $62.5\,\mathrm{kHz}$. An overall sequence, as depicted in Figure 5.5b, then takes $18.75\,\mathrm{ms}$ to $31.25\,\mathrm{ms}$.

At the end of the sequence, the atoms are released from the trap and imaged after a time of flight of $50\,\mathrm{ms}$ (see section 4.2). From the absorption images, the absolute atom number and aspect ratio of the condensate are extracted. Absolute values of the BEC atom number are obtained using the fitting routines described in [84]. Since the Rydberg excitation leads to a significant deformation of the condensate, the data presented in chapters 7 and 8 is evaluated differently. In particular, the atom number is determined by summing all pixels in a rectangle around the condensate and correcting the number for the average background signal in a region without atoms in each picture. The aspect ratio is extracted from a one-dimensional Thomas-Fermi fit to profiles, which are generated by integrating over 11 pixel wide slices (pixelsize $6.45\,\mu\mathrm{m}$) along the long and short axis of the condensate respectively.

During a typical sequence, the number of atoms in the condensate decreases from around $8 \cdot 10^4$ to around $5 \cdot 10^4$ atoms, even in the absence of Rydberg excitations, mainly due to off-resonant scattering from the intermediate $5P_{3/2}$ state (see section 5.1) and heating from the trap. Furthermore, the switching of the red Rydberg laser alone induces a shape oscillation of the condensate (see section 8.2). To eliminate both effects from the data, as well as to reduce the influence of drifts in the atom number and deformation during time of flight, originating from residual magnetic field gradients, the data from each absorption image is related to a reference measurement, where the blue Rydberg laser is detuned by more than $40\,\mathrm{MHz}$ and which is taken immediately before or after. Therefore, any Rydberg excitation is avoided, while keeping the atom loss and deformation due to the excitation lasers constant. For each data point in chapters 7 and 8, ten measurements where averaged to obtain sufficient statistics. Since each laser detuning and each reference measurement requires a new atomic sample, at least ten hours of uninterrupted measurement time are required to take one Rydberg spectrum, as shown in Figure 7.2, in the BEC. This does not include the time for warming up the apparatus, which typically takes additional two to three hours. In contrast to that, an averaged spectrum in the thermal cloud, measured by field ionization and ion detection as described in paragraph 5.3.1, can be obtained easily within ten minutes at much better resolution.

---

[7] Here, additional capacitor banks at $40\,\mu\mathrm{F}$ per field plate had to be used in order to provide sufficient current at the high voltage of $500\,\mathrm{V}$.

Part III

Interaction between Rydberg atoms and a BEC

6 Dressing a BEC with low Rydberg states

A common application for ultracold atoms is the simulation of complex many-body systems, encountered for example in condensed matter physics [6]. Prime examples are the superfluid to Mott insulator transition [207], studies of the BEC-BCS crossover [208] or the Ising model [209]. So far, in such approaches the atoms have mostly been used as hard spheres in various trapping potentials. Long-range interactions [210] have been realized by dipolar atomic species [211] and cold polar molecules [212, 213]. A controllable interatomic interaction beyond short-range isotropic character would greatly enrich the available toolbox for quantum simulation and quantum computation. For some atomic species, the isotropic s-wave interaction potential can be tuned using Feshbach resonances [214]. Atomic species with a magnetic dipole moment show an interaction, which contains an isotropic s-wave part and a long-range dipolar part [215]. Combining both, the dipolar interaction and a Feshbach resonance, the overall character of the interaction can be tuned by changing the strength of the s-wave part to a certain degree [216].

The interaction between Rydberg atoms is strong and tunable (see section 1.2). In section 3.1, the idea of distributing this interaction over all atoms in an ultracold sample by weakly dressing them with a Rydberg state was discussed theoretically. Based on this principle, Rydberg dressing has been proposed for the realization of a number of interesting phases in ultracold gases, such as rotons, solitons or supersolids [85, 86, 217, 218, 219, 220, 221, 141, 222]. An experimental observation of an ultracold atomic cloud, being deformed under Rydberg dressing, would mark a first step into this direction. However, this proof of principle has not been achieved yet. In paragraph 3.1.3, the modification of the peak density of a Bose-Einstein condensate, dressed with a Rydberg state, has been calculated for parameters that are in principle experimentally accessible. Even though a small, but still sizeable effect seems possible, there are further practical and principal constraints, that have not been considered in the calculations yet. These are currently restricting the parameter space to ranges, where only negligible effects can be expected. These challenges are discussed now on the basis of experimental results on dressing a Bose-Einstein condensate with different Rydberg S-states and a Rydberg D-state close to a Förster resonance.

6.1 Rydberg dressing with S-states

The first approach to Rydberg dressing is based on Rydberg S-states. For these states, the interatomic interaction is isotropic and purely repulsive; thus, the theoretical model developed in section 3.1 can be directly applied. In the present experimental apparatus, Bose-Einstein condensates of rubidium ^{87}Rb can be realized in a cylindrically symmetric trap (see chapter 4). Typical atom numbers vary around $N = 10^5$, corresponding to a peak density of $\rho_0 = 10^{14}\,\text{cm}^{-3}$. Atom numbers down to $N = 2 \cdot 10^4$ can be realized in order to reduce the peak density to $\rho_0 = 5 \cdot 10^{13}\,\text{cm}^{-3}$. This is favourable, since the effect of Rydberg dressing increases at lower atomic densities, as discussed in paragraph 3.1.3. However, this gain is at the expense of larger atom number fluctuations, which are observed for small condensates. For the measurements presented in this section, low Rydberg states at principal quantum numbers between $n = 30$ and $n = 40$ were chosen in order to obtain a relatively small blockade radius r_B (see paragraph 1.2.3). This is important for two reasons. First of all, an effect of Rydberg dressing can only be expected, if the sample is larger than the blockade radius r_B. Otherwise, all atoms are located in a region, where the dressing potential is flat (see Figure 3.1a) and no effect can be expected. Second, the optimal blockade radius $r_{B,m}$, according to equation (3.18), decreases at high atomic densities as ~$\rho^{-1/3}$; counterintuitively, Rydberg states with lower principal quantum number and thus weaker binary interaction are expected to cause a stronger Rydberg dressed interaction at high atomic densities. This property, leading to a common misconception, is caused by the fact that the overall energy scale of Rydberg dressing is only depending on the AC Stark effect and thus on the laser parameters Ω and Δ, as already pointed out in section 3.1.
The experimental sequence, used throughout this chapter, is designed to allow for the BEC density distribution to reach its equilibrium. The condensate is dressed for $100\,\text{ms}$, during which the coupling lasers are switched on adiabatically. This time corresponds to about twice the inverse axial trap frequency. The remaining part of the sequence and the evaluation of the data are very similar to the one described in paragraph 5.3.2, with the only difference that the reference measurements without Rydberg excitation were performed by keeping the red Rydberg laser off. Although the additional potential created by Rydberg dressing is radially symmetric, an asymmetric deformation of the condensate can be expected after a finite time of flight (see discussion in section 4.2).
A first practical limitation is caused by the scheme for Rydberg excitation based on a two-photon transition. Atom losses, caused by off-resonant scattering from the intermediate state (see section 5.1), limit the affordable Rabi frequency depending on the time, during which the red Rydberg laser is incident onto the atoms. In the experiment, the red laser power, driving the lower transition, is chosen such that the total atom loss over the whole sequence is largely negligible. For experiments lasting $100\,\text{ms}$, this results in effective Rabi frequencies on the order of few kHz.
The results for two different Rydberg S-states are shown in Figure 6.1 in comparison to reference Rydberg spectra, measured by field ionization and ion detection in a thermal sample as described in paragraph 5.3.1. For the Rabi frequencies given in Figure 6.1, the onset of full blockade according to equations (3.2) and (3.18), using the mean density $\overline{\rho} = 2/5\rho_0$, is taking place at detunings Δ just below $100\,\text{kHz}$. This is the regime, where the largest effect can be expected according to paragraph 3.1.4. Here, obviously the decay from the Rydberg state, visible as a loss feature in Figure 6.1b, is the limiting factor; the decay leads to strong heating that de-

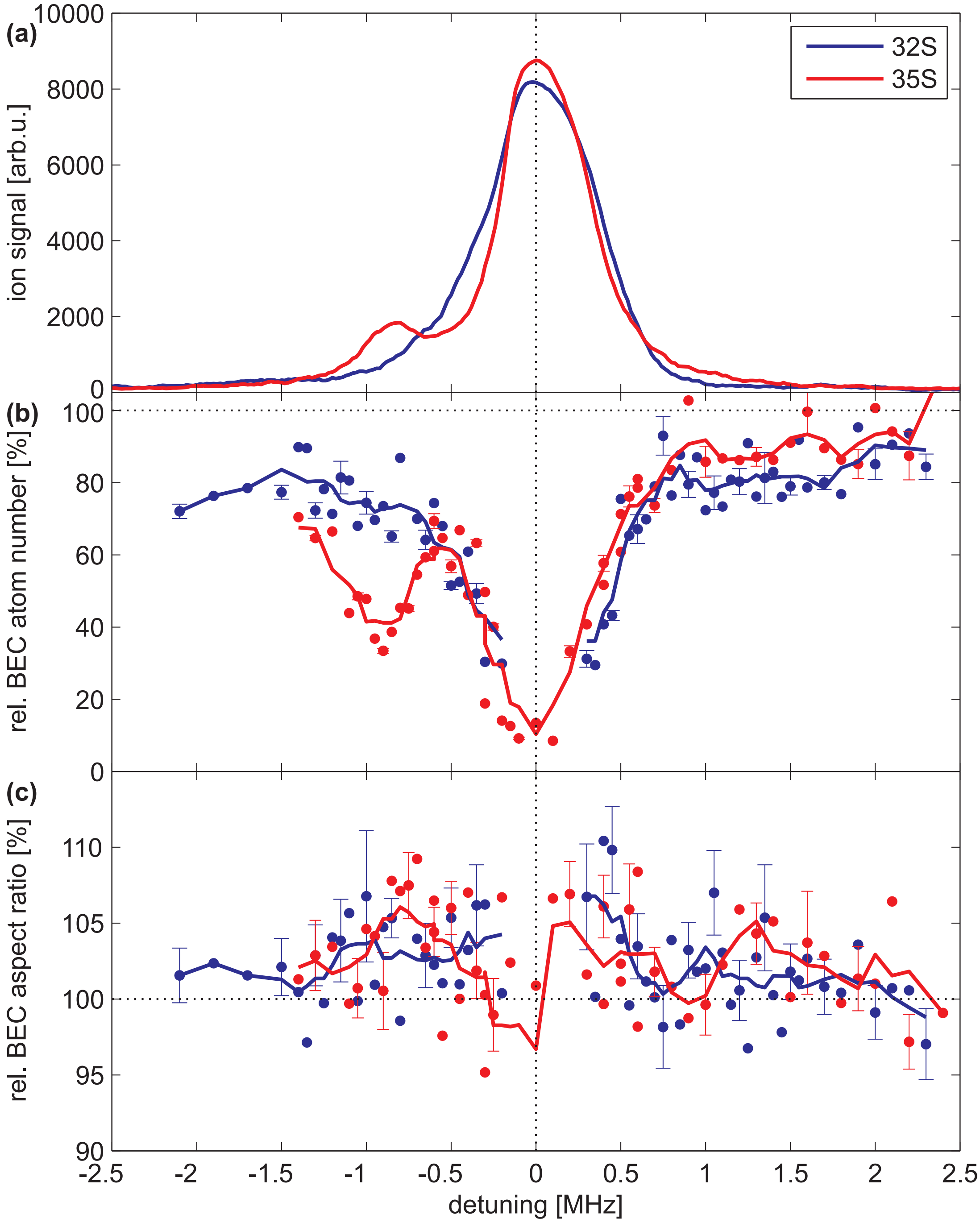

Figure 6.1: Dressing repulsive Rydberg S-states to a Bose-Einstein condensate. The condensate, consisting of $2 \cdot 10^4$ atoms, is dressed for 100 ms at fixed Rabi frequencies $\Omega = 3.4\,\mathrm{kHz}/2.3\,\mathrm{kHz}$ and variable detuning Δ to the $32S$ and $35S$ Rydberg state respectively. In the lower panels, the relative change of BEC atom number (b) and aspect ratio (c) are shown. The reference spectrum in a thermal sample (a) was measured by field ionization. The parameters (excitation pulse length 100 µs, Rabi frequencies $\Omega = 17.5\,\mathrm{kHz}/2.3\,\mathrm{kHz}$) were chosen in order to make tiny signals from molecular states (as present for the $35S$ state) visible. The signal on resonance is thus highly saturated. The solid lines in (b) and (c) are a moving average (spectral resolution ~0.3 MHz) as a guide to the eye.

stroys nearly the whole condensate at small detunings $|\Delta| < 200\,\text{kHz}$. Outside this regime, the expected effect of Rydberg dressing is very small, as can be seen in Figure 3.5. Consequently, there is no significant deformation of the condensate detected within the experimental error (see Figure 6.1c). For long pulse lengths, it is obviously the decay of the Rydberg state that limits the maximum Rydberg fraction $f \approx \frac{\Omega^2}{4\Delta^2}$ and thus the Rabi frequency. Measurements with shorter pulse lengths, where the scattering from the intermediate state is the dominating loss mechanism, are discussed in appendix B.1.1. Furthermore, another problem becomes obvious from the measurement on the $35S$ state. In the reference spectrum taken in a thermal sample at $10^{12}\,\text{cm}^{-3}$, there is a small additional line, red detuned by about $0.85\,\text{MHz}$ to the atomic line (see Figure 6.1a). This line can be assigned to a molecular bound state of a Rydberg atom and a ground state atom, so called ultralong-range Rydberg molecules [12, 77]. In the BEC, this leads to loss features, that are more pronounced for two reasons. First, the scaling of the Franck-Condon factor for the photoassociation of molecules with the density of ground state atoms leads to an increased excitation probability in the BEC. And second, these bound states show a reduced lifetime at higher densities [223], thereby causing stronger atom losses.

6.2 Rydberg dressing close to a Förster resonance

In paragraph 3.1.5, the possibility of dressing an atomic sample with a Rydberg state close to a Förster resonance (see paragraph 1.2.2) has been discussed theoretically. Although there is no full many-body model describing this situation available yet, it seems worthwhile to investigate this regime experimentally. In this section, measurements on the $44D_{5/2}$, $m_J = 5/2$ state are presented. The dipole matrix element, coupling the intermediate $5P_{3/2}$ state to the Rydberg state, is about a factor of two larger for Rydberg D-states than for S-states at the same principal quantum number n [84]. Thus, larger Rabi frequencies can in principle be achieved. Furthermore, the particular state chosen here can be tuned into resonance with a pair state, consisting of the $46P_{3/2}$, $m_J = 3/2$ and different $42F_{7/2}$ Rydberg states, by applying moderate electric fields [144]. The experiments discussed in this section have been conducted close to the resonance with the $42F_{7/2}$, $m_J = 7/2$ state. This magnetic sublevel leads to a resonance, which is relatively strong and, in addition, does not depend on the magnetic field [11].

In Figure 6.2, the results for two different Förster defects Δ_F are shown. Since the sign of the Förster defect determines the sign of the interaction potential (see paragraph 1.2.2 and [10]), an effect of Rydberg dressing should be visible as a qualitative difference between the two measurements. The experiments in this section were performed with condensates at a four times higher atom number and thus next to twice the peak density compared to the ones on the S-states in section 6.1. The better stability of the experiment at these parameters leads to a lower noise level; however, the expected effect of Rydberg dressing is even further decreased, because of the higher atomic density and therefore again below the experimental noise level. In particular, there is no significant difference between the measurements at different Förster defects (see also appendix B.1.2). Instead, for both measurements on a Rydberg D-state, a band of molecular states emerges in the spectrum (see Figure 6.2a). In the same range of detunings, there is a strong and several MHz broad loss feature in the measurements with the BEC, as can be seen from Figure 6.2b. Furthermore, this loss seems to be connected to a change in aspect ratio (Figure 6.2c). This observation in time of flight images does not necessarily im-

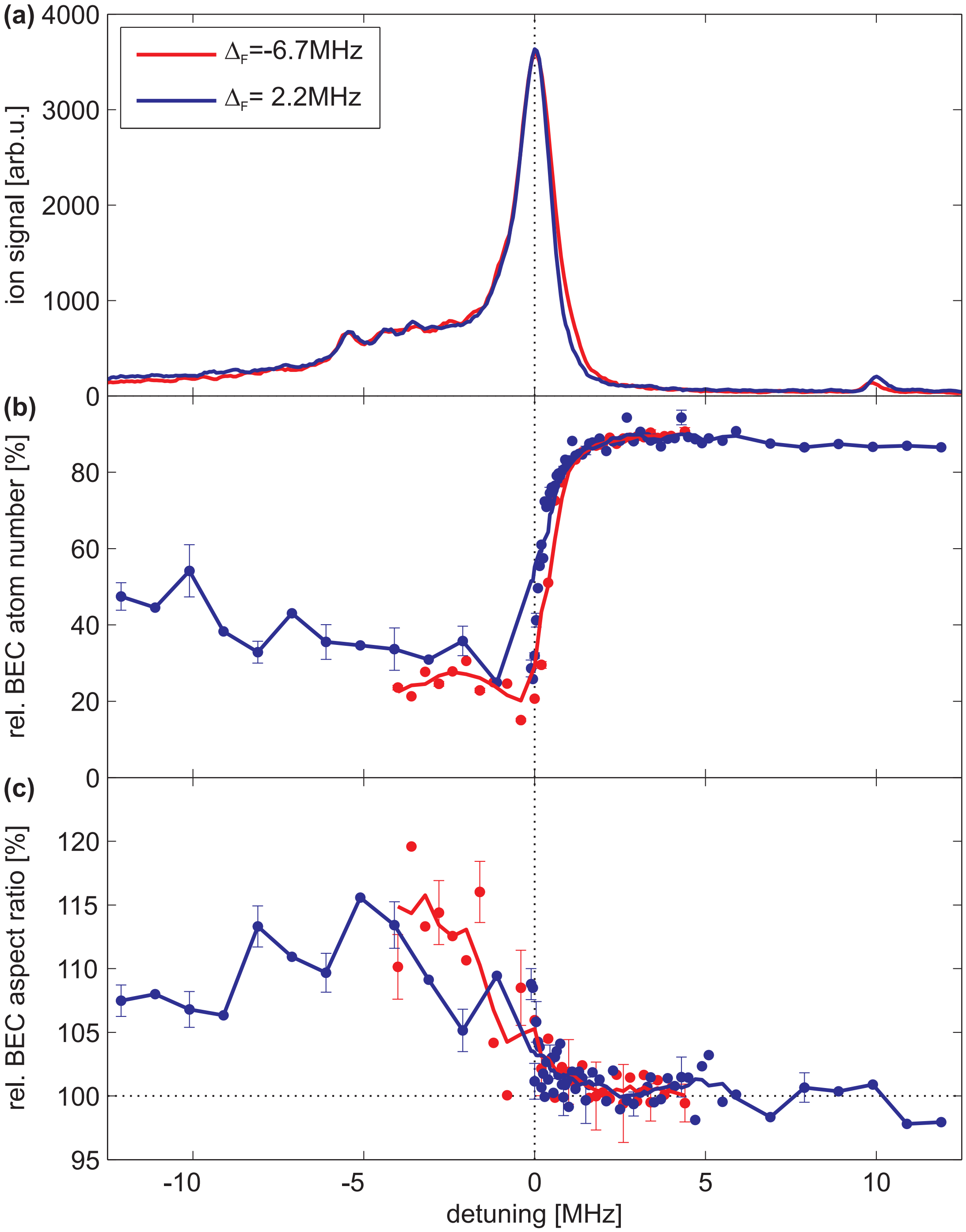

Figure 6.2: Dressing of a Rydberg D-state to a Bose-Einstein condensate. The condensate, consisting of $8 \cdot 10^4$ atoms, is dressed for 100 ms at fixed Rabi frequency $\Omega = 2.6\,\text{kHz}$ and variable detuning Δ to the $44D_{5/2}$, $m_J = 5/2$ Rydberg state for different Förster defects Δ_F. In the lower panels, the relative change of BEC atom number (b) and aspect ratio (c) are shown. The reference spectrum in a thermal sample (a) was measured by field ionization. The parameters (excitation pulse length 5 µs, Rabi frequency $\Omega = 8.5\,\text{kHz}$) were chosen to make tiny signals from molecular states visible. Therefore, the signal on resonance is highly saturated. The solid lines in (b) and (c) are a moving average (spectral resolution ~1 MHz) as a guide to the eye.

ply an isotropic deformation of the BEC in the trap, as discussed in section 4.2. However, it also seems unlikely that this deformation is caused by uniform losses alone, since it does not fully coincide with the observed BEC atom losses. In particular, there is no such pronounced effect observed in the measurements of the Rydberg S-states (see Figure 6.1b), although there are equally strong atom losses present close to resonance. Instead, the observed deformation of the condensate could possibly originate from an anisotropic loss of atoms, which then would be specific for ultralong-range Rydberg molecules created from D-states. Due to the toroidal shape of the Rydberg electron wavefunction of the $D_{5/2}$, $m_J = 5/2$ state, only pairs of atoms, whose internuclear axis is aligned almost perpendicular to the magnetic field axis, can be photoassociated. This leads to a depletion of atom pairs, that lie close together in radial direction of the condensate. In any case, ultralong-range Rydberg molecules cause a serious problem for the observation of Rydberg dressing at red detuning, especially at Rydberg D-states, where the molecular spectrum is not restricted to single, well resolved lines.

6.3 Conclusion on Rydberg dressing

Several technical and principle constraints impede an experimental observation of Rydberg dressing in the current setup. Some of them, like the limitation of accessible Rabi frequencies and the presence of ultralong-range Rydberg molecules, have already been discussed in the previous sections 6.1 and 6.2. The latter effect becomes even more important at Rydberg states with higher principal quantum number n. As the depth of the molecular potential is decreasing proportional to $(n - \delta_0)^{-6}$ (see paragraph 3.2.3), the molecular states come closer to the atomic Rydberg state in the spectrum. Then, polyatomic bound states [77] start to play a role, eventually leading to a density-dependent shift of the Rydberg line [2, 171].

Another problem is the unfavourable scaling of the effect with the density of ground state atoms. A low temperature sample is required to observe the small effects expected. Such samples, like Bose-Einstein condensates, typically feature a high atomic density. As discussed in section 3.1, the impact of Rydberg dressing is greatly reduced in strongly blockaded samples. Elements with larger background s-wave scattering length, such as cesium, allow for the preparation of condensates at lower peak density [224]. In this case, the modification of the density distribution, however, would be even smaller due to the large mean-field interaction between the atoms. Furthermore, ultracold samples of cesium can only be prepared in optical dipole traps. Common red detuned dipole traps create differential light shifts between the ground and Rydberg state, that can lead to an inhomogeneous laser detuning Δ to the Rydberg state. Therefore, a magic wavelength trap [225] is required. Instead of reducing the atomic density, one possibility is to reduce the blockade radius r_B of the sample, in order to tune the system just to the onset of saturation. To this end, a Rydberg state at even lower principal quantum numbers n can be chosen, since the C_6-coefficient is scaling as $(n - \delta_0)^{11}$ [82]. Alternatively, the excitation linewidth Δf can in principle be increased artificially. The drawback of the first possibility is that the lifetime of the Rydberg state at the same time decreases $\propto (n - \delta_0)^3$, thereby reducing the tolerable Rydberg fraction. The latter is not practicable due to the unfavourable scaling $r_B \propto (\Delta f)^{1/6}$ and the fact that large excitation linewidths preclude the realization of small laser detunings Δ. Another possibility involves a Förster resonance to tune the Rydberg interaction strength, as discussed in paragraph 3.1.5.

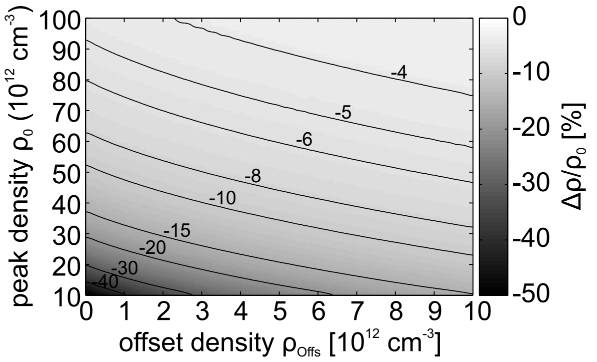

Figure 6.3: Dependence of Rydberg dressing of a BEC on the initial peak density ρ_0 and an offset density ρ_{Offs}, simulating a residual thermal cloud. The relative change of peak density $\Delta\rho/\rho_0$ in steady state is calculated for a condensate in a cylindrically symmetric trap with trap frequencies $\omega_r = 2\pi \cdot 20\,\text{Hz}$ and $\omega_z = 2\pi \cdot 80\,\text{Hz}$. The condensate is dressed at a detuning of $\Delta = 100\,\text{kHz}$ with Rabi frequency $\Omega = 10\,\text{kHz}$ to the $32S$ Rydberg state.

A further principal challenge is the long timescale, that is required for experiments studying mechanical effects on the whole atomic sample. The maximum achievable Rydberg fraction $f \approx \Omega^2/4\Delta^2$ is limited by the product of the pulse length and the decay rate from the dressed state. As an example, this can be simply estimated for the experimental parameters from section 6.1, in particular for the $32S$ Rydberg state and a pulse length of $t = 100\,\text{ms}$. Restricting the maximum atom losses to an arbitrary value of 50%, one obtains the condition $f < 1/(2\Gamma_r t) \approx 10^{-4}$. Here, the decay rate $\Gamma_r = 50.6\,\text{kHz}$ of the $32S$ Rydberg state, including blackbody radiation at 298 K [103], is assumed. At a detuning of $\Delta = 100\,\text{kHz}$, corresponding to the optimal detuning for the current density (see section 6.1), the Rabi frequency is limited to $\Omega = 2\,\text{kHz}$. As can be seen from Figure 3.5, the expected density change due to Rydberg dressing at these parameters is on the order of only a percent. This is well below the experimental noise level and hence in line with the experimental observation of no effect.

Finally, a rather technical problem is related to the preparation of the condensate. A very pure BEC is required, since any non-condensed atoms take part in the collective light shift, but do not lead to a deformation of the condensate. One can account for a residual thermal cloud by simply introducing a constant offset density ρ_{Offs} in the energy functional $\partial_\rho E_{\text{eff}}(\rho)$ (equation (3.13) in section 3.1). As can be seen in Figure 6.3, the effect of Rydberg dressing on the condensate is significantly reduced, even at very small offset densities ρ_{Offs}. This is due to the fact that the main impact of Rydberg dressing, according to Figure 3.2, is expected at low densities. While the chances to observe Rydberg dressing seemed already borderline considering only the previous discussion, the additional reduction of the expected effect, caused by the residual thermal cloud, finally makes the observation of Rydberg dressing most likely impossible in the present setup.

However, there are two paths towards a possible experimental realization. One involves samples at reduced dimensionality, such as optical lattices [141, 222], thereby reducing the effective atomic density. The use of three-dimensional samples, instead, would demand a significant increase in Rabi frequency. The effect of Rydberg dressing scales roughly as ~Ω^4/Δ^3 (equations 3.14 and 3.15), while the decay rate of the dressed state is only scaling as the Rydberg fraction ~Ω^2/Δ^2 (see equation 1.12). Increasing the laser detuning Δ by the same amount as the Rabi frequency Ω, one can thus expect a stronger dressing effect at the same loss rate. For the parameters of the present setup (see section 4.1), a modification of the peak density on the order of ten percent requires a more than hundred times larger laser power. Based on current laser techniques, this is not feasible so far.

7 High Rydberg states in a BEC

The great leap forward of this dissertation was the extension of Rydberg excitation to states at high principal quantum numbers $n > 100$ and high atomic densities $\rho \approx 10^{14}\,\mathrm{cm}^{-3}$ in a Bose-Einstein condensate. At these high principal quantum numbers, the Rydberg blockade restricts the number of Rydberg atoms inside the condensate to one (see paragraph 1.2.3 and further discussion in section 7.3). This results in an intriguing system, where the extent of a Rydberg atom approaches the radial size of the BEC (see sketch in Figure 7.1). This is pushing into a regime of strong interaction between the Rydberg atom and the surrounding gas, since there can be up to several tens of thousands of ground state atoms inside the wavefunction of the Rydberg electron. In this and the following chapter, the first results of this newly opened field of research are presented.

The main results are extracted from a single set of data from spectroscopy of Rydberg S-states in a BEC at different principal quantum numbers ranging from $n = 100$ to $n = 202$. The two

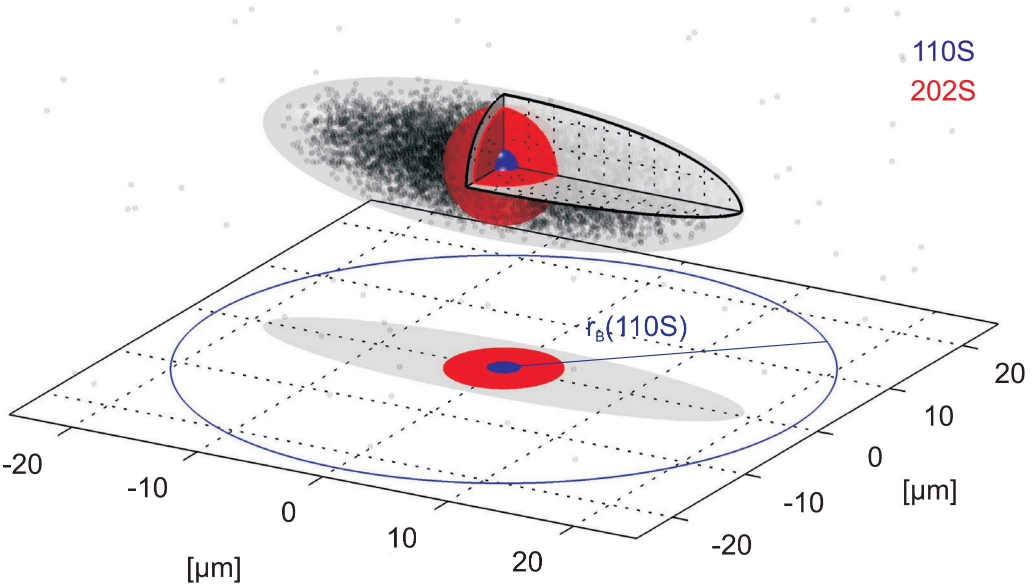

Figure 7.1: Size comparison of the system: A Rydberg atom inside a Bose-Einstein condensate of $N = 8 \cdot 10^4$ atoms. The scheme shows the extent of the Rydberg electron wavefunction for the 110S (blue) and 202S (red) states, the lowest and highest state under investigation, as spheres. The densities of the BEC and the surrounding thermal cloud are to scale. As can be seen from the projection, the lower bound $r_B\ (110S)$ for the blockade radii is much larger than the size of the condensate. This makes clear that there can be only one Rydberg excitation at a time inside the BEC. For the higher Rydberg states, the extent of the Rydberg atom approaches the radial size of the condensate.

observables in these measurements are the change of BEC atom number and aspect ratio in time of flight absorption imaging. The data allows evaluation from different perspectives providing insight into various phenomena. This chapter focuses on the point of view of the Rydberg atom. At the beginning, this includes basic findings on the perturbation of Rydberg states by background gas atoms, a field that has been pioneered experimentally by Amaldi and Segrè in the 1930ies [2, 3]. The validity of the same theoretical concepts, developed by Fermi [14], is shown, but here in a completely different parameter regime, at much higher Rydberg states. Furthermore, the collective excitation and the decay of the Rydberg atom in a high density environment are studied.

The role of the BEC is emphasized later in the next chapter 8. There the new features of the combination of a single Rydberg atom and a BEC are explored, interfacing a single quantum system, the Rydberg electron, and a many-body quantum system, the Bose-Einstein condensate.

7.1 Rydberg spectroscopy

Rydberg S-states with principal quantum numbers n between 110 and 202 were investigated spectroscopically both in a BEC and in a thermal sample (see Figure 7.2). Two different measurement techniques had to be applied, which are described explicitly in section 5.3. The zero position of the frequency axis is defined as the spectral position of the respective Rydberg state measured in a thermal cloud at a peak density of about $10^{12}\,\mathrm{cm}^{-3}$. This is a good approximation for the line position of free Rydberg atoms. At such densities, the Rydberg electron on average is interacting with 7 to 310 ground state atoms inside the Rydberg atom. However, the resulting shift is less than $100\,\mathrm{kHz}$ and hence below the present spectral resolution at these high Rydberg states. In the condensate, the density is around two orders of magnitude higher and leads therefore to a sizeable energy shift due to the scattering of the Rydberg electron from the ground state atoms on the order of some MHz. Besides the line shift, also the width and the amplitude of the spectral lines in Figure 7.2 show a nontrivial scaling with the principal quantum number n of the Rydberg state. These quantities are discussed in the following paragraphs. The theoretical basics can be found in section 3.2.

7.1.1 Line shift

The spectral positions of the Rydberg states in the condensate relative to the position measured in a thermal cloud were extracted from Figure 7.2. The dependency of this effect on the density of ground state atoms is known to be linear (see paragraph 3.2.2). Since the measurements were taken at slightly varying atom numbers, the line shift shown in Figure 7.3 is normalized onto the same peak density for all principal quantum numbers. This essentially only affects the measurement at $n = 125$, as this data point was taken at a 7% higher peak density than the other measurements. The line shift can be fully understood based on Fermi's description of low energy electron scattering (see section 3.2). In the first approximation, the electron atom scattering length is assumed to be energy-independent and one can thus expect a line shift, which is only depending on the density ρ of ground state atoms inside the Rydberg atom. Using

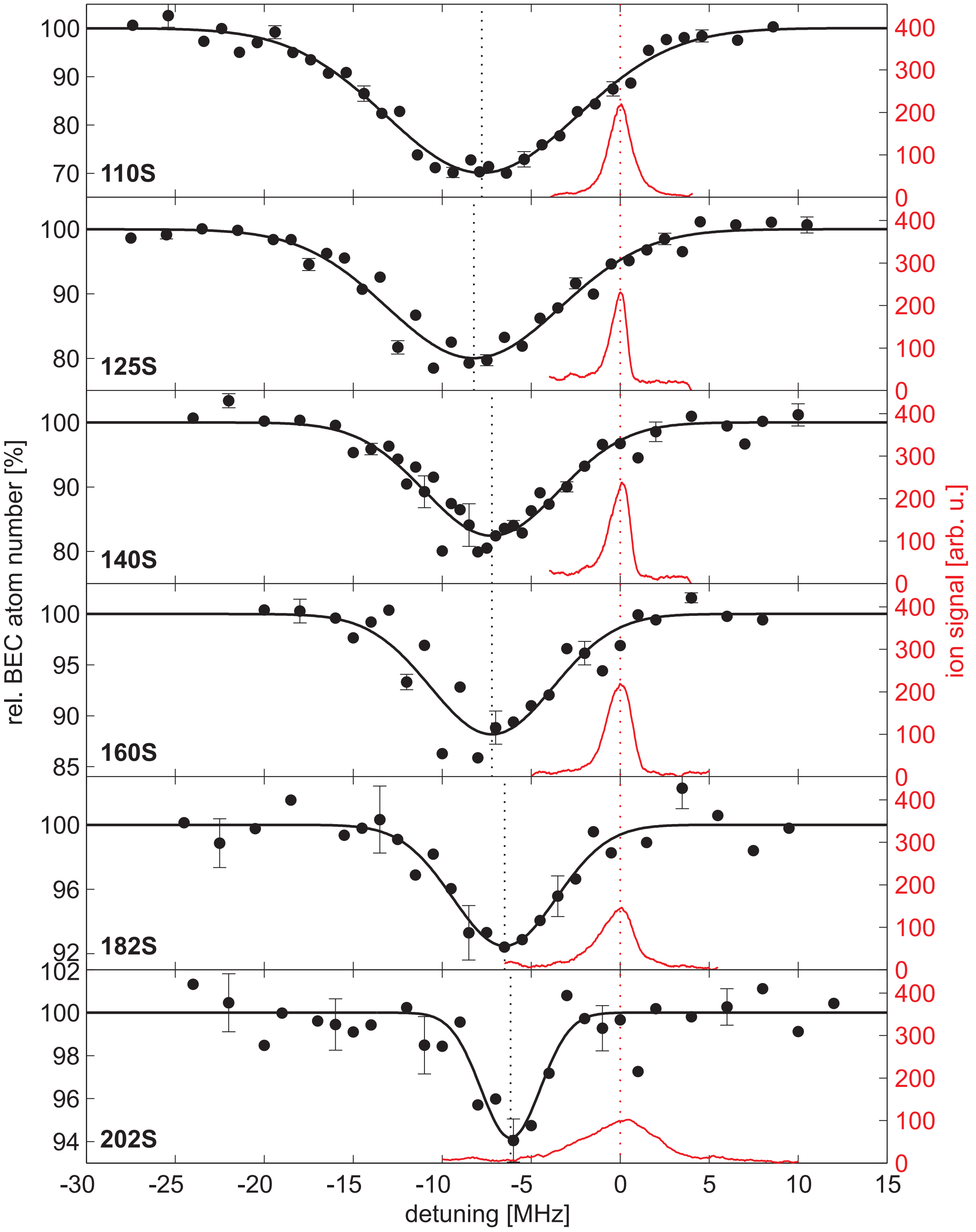

Figure 7.2: Spectral lines of different Rydberg S-states. The black data points (left axis) were measured in a BEC, the red lines (right axis) were taken in a thermal sample. For the measurements at the two lowest Rydberg states, $n = 110$ and $n = 125$, a Rydberg atom was excited 300 times; for the other states 500 cycles of excitation and ionization were chosen.

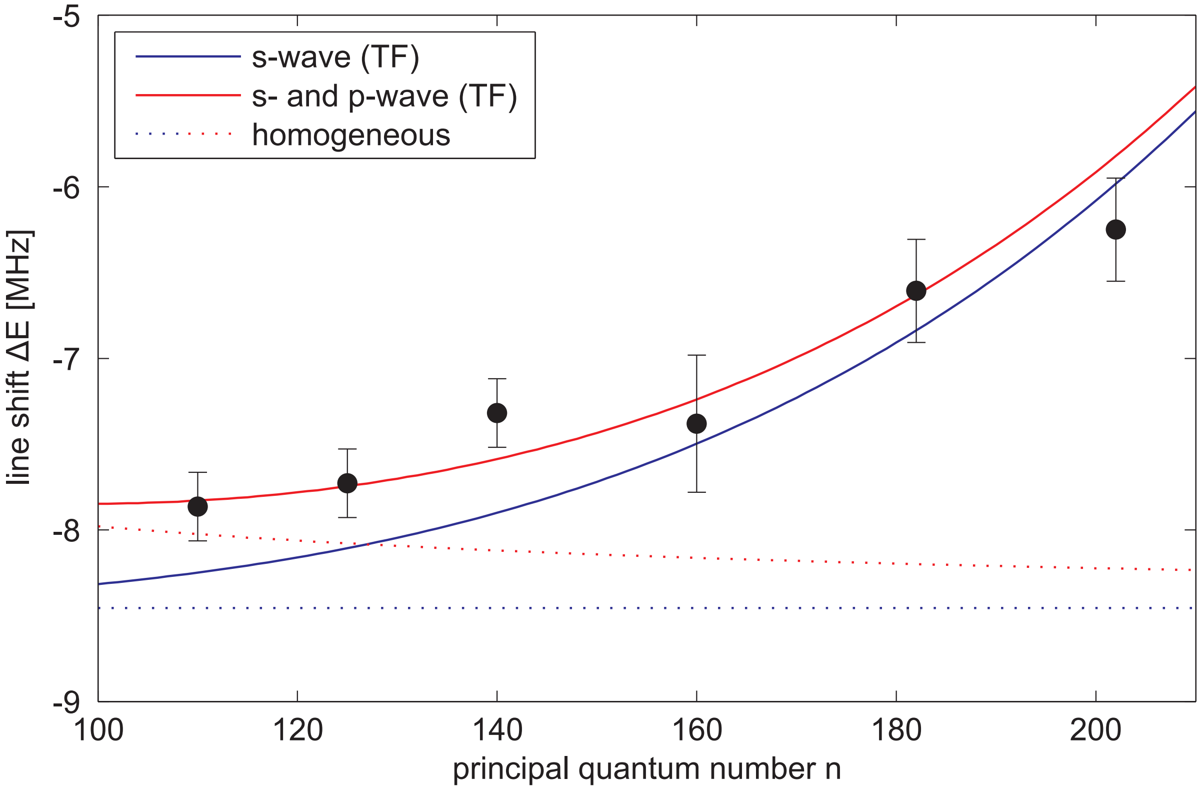

Figure 7.3: Line shifts of Rydberg S-states in a BEC versus principal quantum number n. The line positions are extracted from Figure 7.2 and normalized onto the same BEC peak density. The solid lines are theory curves assuming an energy-independent s-wave scattering length $a_0 = -16.1$ [157] as well as taking correction up to p-wave scattering into account. The dotted lines are calculated for a homogeneous condensate neglecting the Thomas-Fermi density distribution.

the mean peak density $\rho = 9.3 \cdot 10^{13}\,\mathrm{cm}^{-3}$ over one sequence[1], one would expect a constant shift of $-8.5\,\mathrm{MHz}$. However, the absolute line shift is found to be lower and decreasing at higher principal quantum numbers n. These observations can be explained with a simple model, assuming that the Rydberg atom is always excited at the centre of the condensate, the position of highest atomic density. This makes sense, because the collective enhancement of the Rabi-frequency (see section 7.3) is also maximal at this position. As the radius of the higher Rydberg states approaches the radial size of the condensate, the effective density inside the Rydberg atom is significantly lower than the peak density of the BEC. This can be included into the calculation by introducing a mean effective density $\overline{\rho}$, averaging the Thomas-Fermi density distribution (see section 2.2) over the volume of the Rydberg atom, given as a sphere with radius $R(n) = 2a_0(n - \delta_0)^2$:

$$\overline{\rho} = \rho_0 \left(1 - \frac{2}{5}\frac{R^2}{r_0^2} - \frac{1}{5}\frac{R^2}{z_0^2}\right) \tag{7.1}$$

---

[1] The BEC atom number is decreasing from $8.0 \cdot 10^4$ to $5.0 \cdot 10^4$ during one sequence due to off-resonant scattering from the intermediate P-level (see sections 5.1 and 7.3).

Inserting this into Fermi's expression of the interaction energy due to electron-atom scattering (equation 3.33) already explains the order of magnitude and the overall trend of the observed line shift. Here, the zero energy $^3S^e$ triplet electron-Rubidium scattering length $a = -16.1\,a_0$ was taken from the calculations in [157], which agree well with measurements [77]. Further refinement can be obtained by accounting for the energy dependence of the scattering length and including the p-wave scattering potential (see paragraph 3.2.2). As can be seen in Figure 7.3, this leads to slightly better agreement with the data. However, the correction is within the experimental error and decreasing at higher principal quantum numbers n. This means, that the original approximation by Fermi, where the kinetic energy of the electron is neglected, is largely justified in this system. The Rydberg electron can therefore in good approximation be regarded as a quasi-free electron in a Bose-Einstein condensate.

The positively charged Rydberg core can also lead to a contribution to the line shift of high Rydberg states [14]. Ground state atoms inside the Rydberg atom can be polarized since the charge of the core in this region is not completely shielded by the Rydberg electron. As discussed in paragraph 3.3.1, this effect is still expected to be well below $100\,\text{kHz}$ even at the highest densities achieved in the current setup and thus below the experimental resolution.

7.1.2 Line broadening

The linewidth of the Rydberg lines in the BEC, extracted from the Gaussian fits in Figure 7.2, is shown in Figure 7.4. The behaviour of the broadening seems unexpected at first glance. In contrast to the measurements in the thermal cloud, where the linewidth is increasing with principal quantum number, here the width is decreasing at higher Rydberg states. The linewidth measured in the thermal sample is obviously dominated by the homogeneity of the electric field. Already a minor increase of the sample temperature and therefore the size of the cloud leads to a further increase of the linewidth. Since the polarizability α increases with the principal quantum number as $(n - \delta_0)^7$, the effect of any residual electric field gradient is expected to increase dramatically with n. In the BEC, there seems to be at least one other dominant broadening mechanism present, because the linewidth is much larger than the one measured in thermal samples and due to the different scaling with the principal quantum number n. A full modelling of the lineshape in the BEC has not been undertaken so far, but there are at least some broadening mechanisms which are estimated in the following.

First of all, there is an inhomogeneous broadening of the line expected, as it is possible to excite Rydberg atoms at different positions and hence different local densities in the condensate. This broadening can be expected to be on the order of the total line shift (see Figure 7.3). As the linewidth measured at the lower Rydberg states is much larger than the shift, an additional important mechanism must be present.

Another source of broadening is the random position of the atoms inside the potential generated by the scattering of the Rydberg electron. The three dimensional potential has the mean value $\overline{V}$ and the variance $(\Delta V)^2$. According to the central limit theorem [170], for large atom numbers N inside the Rydberg electron wavefunction, the distribution of total line shifts approaches a normal distribution with mean $N\overline{V}$ and variance $N(\Delta V)^2$. The resulting full width at half maximum (FWHM) is therefore proportional to $\sqrt{N}$, leading also to a broadening decreasing with principal quantum number n (see also discussion in paragraph 3.2.2).

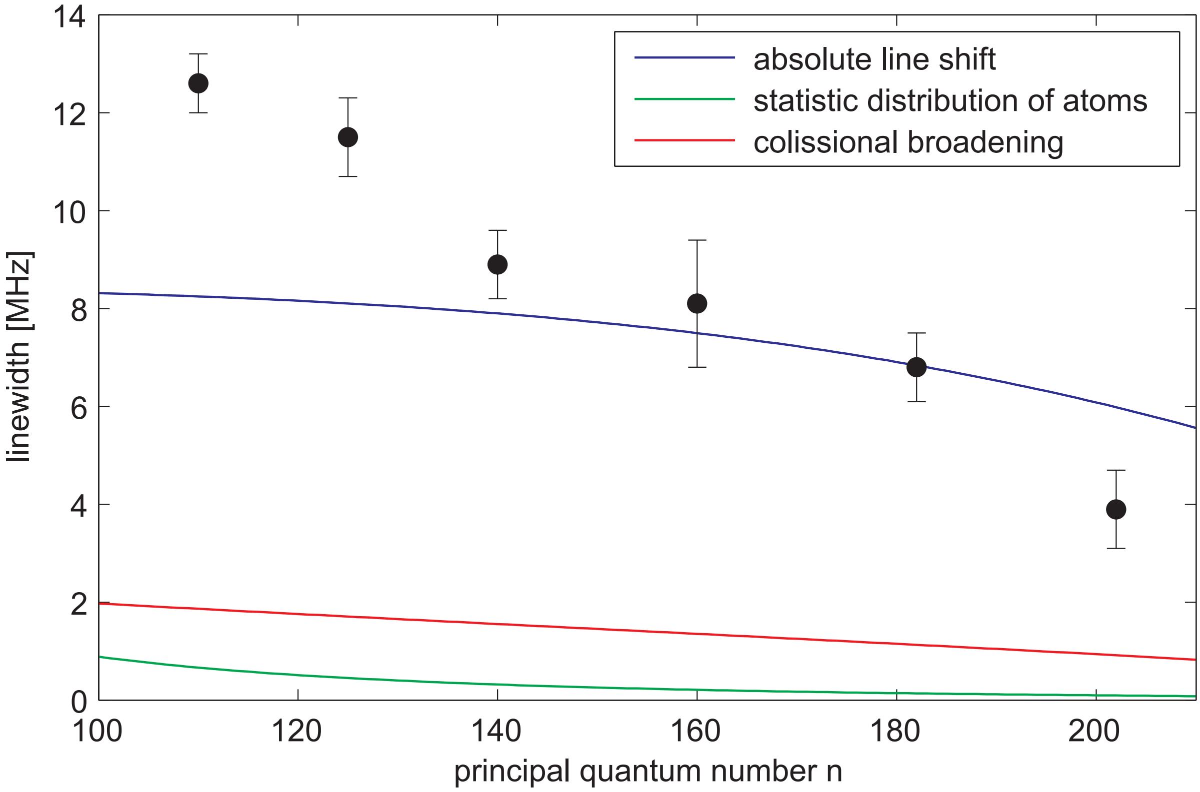

Figure 7.4: Line broadening of Rydberg S-states in a BEC versus principal quantum number n. The linewidths (FWHM) are extracted from the Gaussian fits in Figure 7.2. The solid lines show theoretically expected contributions from different effects: The blue line is the line shift from Figure 7.3, which provides the order of magnitude and overall trend of the inhomogeneous broadening due to the density distribution in the BEC. The green line accounts for the random placement of the atoms inside the scattering potential of the Rydberg electron. The red line is the contribution of classical pressure or collisional broadening.

Finally, also a broadening due to the scattering of the Rydberg atom from the single ground state atoms can be expected. The line broadening observed by Amaldi and Segrè [2, 3] has not been explained by the Fermi model [14]. The first interpretation has been given in 1937 by Reinsberg [226] in terms of impact pressure broadening. The resulting linewidth is proportional to the scattering rate Γ_{scat}. Assuming a geometrical cross section of $4\pi a^2$, this scattering rate can be estimated using a semiclassical approximation for the momentum k of the Rydberg electron (cf. equation 3.44):

$$k(R) = \sqrt{\frac{2m_e}{\hbar^2}\left(-\frac{Ryd}{(n-\delta_0)^2} + \frac{1}{(4\pi\epsilon_0)}\frac{e^2}{R}\right)} \tag{7.2}$$

with the Rydberg constant Ryd, the quantum defect δ_0, and the vacuum permittivity ϵ_0. The scattering rate can than be estimated as:

$$\Gamma_{\text{scat}} = \int 4\pi a^2 \frac{\hbar}{m} k(R)\,|\Psi(R)|^2\, d\vec{R} \tag{7.3}$$

Using the approximation of an energy-independent scattering length a [157], this expression is inversely proportional to the principal quantum number n, as expected from the Bohr model. The resulting linewidth (FWHM) $\Delta f = \Gamma_{\text{scat}}/\pi$ is shown in Figure 7.4. Further measurements at different powers and pulse lengths of the excitation lasers (see section 7.3) show that there is at least one dominant decoherence process present; collisional broadening as described above could be an explanation of this observation.

All three broadening effects mentioned here are individually each smaller than the measured linewidth, but on the right order of magnitude. Furthermore, they all show the correct trend in the principal quantum number so that it seems reasonable that a combination of them can explain the observations.

7.2 Decay of Rydberg atoms

7.2.1 Dependence on principal quantum number and density

A characteristic property of Rydberg states is their long lifetime compared to lower excited atomic states. For Rydberg states with low angular momentum $l \ll n$, the main spontaneous decay channel is directed into low lying states, leading to a lifetime increasing with principle quantum number n^{-3} [37]. Additionally, an environment at finite temperature can induce transitions into neighbouring Rydberg states [227]. These two effects have been studied extensively both theoretically [228, 229] and experimentally [230, 231] in the past. However, many more effects have been identified, which reduce the lifetime in Rydberg states. At high Rydberg densities, incoherent amplified emission and coherent superradiance can lead to an enhanced decay rate [232, 233]. Collisions with other atoms in the Rydberg state or in the ground state can cause decay and ionization [234] as well as the spontaneous formation of a plasma [235, 236]. Due to the vast number of processes which can possibly reduce the lifetime of Rydberg states, it is important to determine the actual Rydberg lifetime in the regime under investigation.

The lifetimes of Rydberg S-states with principal quantum numbers n between 110 and 202 are shown in Figure 7.5, both measured in a thermal sample at densities around $10^{12}\,\text{cm}^{-3}$ and in a Bose-Einstein condensate with peak densities reaching $10^{14}\,\text{cm}^{-3}$. Rydberg atoms were excited on the resonance positions determined from the spectral lines in Figure 7.2. The two different measurement techniques which are used in the thermal cloud and in the BEC respectively are described in section 5.3.

Extrapolating empirical scaling laws for spontaneous decay rates [229] to high principle quantum numbers n, one would expect the lifetime to increase from $1.7\,\text{ms}$ to $10.8\,\text{ms}$ from $n = 110$ to $n = 202$. Instead, the lifetime measured in the low density thermal sample seems to be limited to a rather constant value of around $(0.78 \pm 0.08)\,\mu\text{s}$. This value is significantly longer than the lifetimes of Rydberg states with principal quantum numbers in the range between $n = 35$ and $n = 43$ measured previously with the same technique [159], but still much shorter than expected accounting for spontaneous decay only. Decay induced by blackbody radiation mainly leads to a redistribution of the population over neighbouring Rydberg states [37]. Since both measurement techniques applied here are not state selective, this effect can be neglected in the interpretation of the results presented here. This is also fully consistent with the results at low principal quantum numbers n [159]. Moreover, the lifetime observed in the condensate at peak

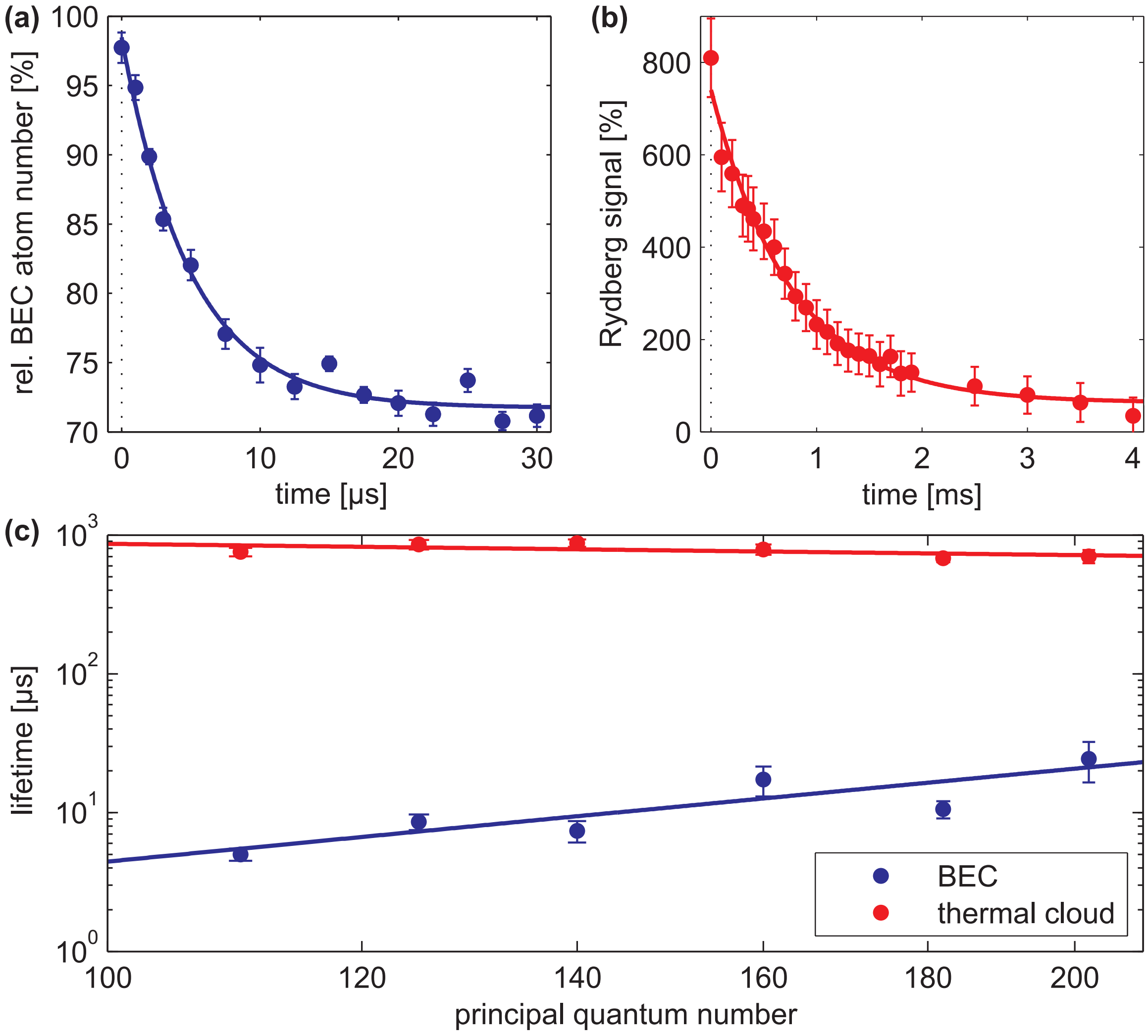

Figure 7.5: Measurements of the lifetime for different Rydberg S-states in the BEC and in the thermal cloud. (a) and (b) show exemplarily the exponential decay of the signal measured for the $110S$ state in the BEC and in a thermal sample. In (c), the dependence of the lifetime on the principal quantum number n is shown. The lines are fitted power laws with exponents 2.2 ± 0.1 (BEC) and -0.3 ± 0.2 (thermal cloud) respectively.

densities up to $10^{14}\,\mathrm{cm}^{-3}$ shows further reduced values on the order of $10\,\mu\mathrm{s}$ which are now increasing with principal quantum number $(n - \delta_0)^{-2.2\pm0.1}$. The exponent differs from the value of about -3 expected for spontaneous decay [228, 229].

A full explanation of this effect is elusive so far (see also further studies and discussion in paragraph 7.2.2). However, the data suggests that there is a dominant decay mechanism which is depending on the number of ground state atoms inside the wavefunction of the Rydberg electron: The lifetime measured in the thermal cloud is about two orders of magnitude longer than in the BEC. This factor corresponds to the difference in density between the two sets of measurements. Since the thermal cloud is much larger than the size of one Rydberg atom, the density of ground state atoms inside the Rydberg atoms can be assumed as homogeneous. The number of atoms inside the Rydberg atom is then constant (see discussion in paragraph 3.2.3) and leads therefore to a lifetime largely independent of the principal quantum number. In contrast to that, in the BEC, the average density inside the Rydberg electron wavefunction decreases for large principal quantum numbers, because the radius of the Rydberg atom can become almost as large as the Thomas-Fermi radius of the condensate (see Figure 7.1). This could explain the increase in lifetime at higher principal quantum numbers. Nevertheless, the exact observed scaling cannot be explained within such a model (cf. paragraph 7.1.1). Further evidence for this hypothesis is provided by lifetime measurements at different positions in the condensate discussed in paragraph 7.2.1. For Rydberg states with low principal quantum numbers (around $n < 80$ at a density of $10^{12}\,\mathrm{cm}^{-3}$), such a process is not expected to play a role since there is on average less than one atom inside the Rydberg electron wavefunction. This explains why this effect has not been observed in previous measurements. Additional investigations in order to clarify the nature of the decay channels are discussed in the following paragraphs.

7.2.2 Possible decay processes

As discussed in the previous paragraph 7.2.1, the origin of the reduced lifetimes both observed in the thermal cloud and in the BEC is not clear yet. However, some processes that are in principle possible can be ruled out. Due to the Rydberg blockade (see paragraph 1.2.3), the density of Rydberg atoms in all samples studied in this work is much lower than required for superradiance effects [232]. The density of ground state atoms is also still small enough so that a collective enhancement of the decay into the ground state is suppressed [233].

Another possibility would be a decay by state changing collisions [237] of the Rydberg atom and the dense background gas of ground state atoms [238]. As calculated in paragraph 7.1.2, the classical scattering rate of the Rydberg electron from the ground state atoms is quite large, ranging from 6 MHz at $n = 110$ to 3 MHz at $n = 202$ respectively. In a classical picture, the Rydberg electron is moving through a dense medium, experiencing a friction force. Since the electron is loosing kinetic energy, it would decay back into the ground state in a cascade. At this point, however, the quantization of the Rydberg energy levels becomes important. The states closest to the initial Rydberg state are still at least a few GHz apart, orders of magnitude more than the energy that could be transfered in a classical scattering event[2]. A more rigorous treatment [239, 240] also shows that the probability for any inelastic collision of the Rydberg electron with ground state atoms is negligibly small at ultracold temperatures, which prevail in this experiment. In order to check this experimentally, the threshold for field ionization was measured directly after excitation and $t_d = 3\,\mu\mathrm{s}$ after the exciting laser pulse. The experimental sequence is similar to the one used for recording the Rydberg spectra in section 7.1, but with an additional electric field pulse of variable strength after a wait of t_d (see inset of Figure 7.6). The resulting relative BEC atom number measured after time of flight for different electric field strengths E is shown in Figure 7.6. The dashed lines denote the classical field ionization threshold [37]

$$E_{\text{ion}}(n) = \frac{1}{16}\frac{e}{4\pi\epsilon_0 a_0^2}\,(n-\delta_0)^{-4} \tag{7.4}$$

in steps of ten principal quantum numbers. At low electric fields, there is no effect of the first

---

[2] With the classical mean electron velocity $v = 2Ryd/\hbar \cdot a_0/(n-\delta_0) = 2.0 \cdot 10^4\,\mathrm{m/s}$ of the $110S$ state the energy transferred in a straight central elastic collision is about 6.9 MHz.

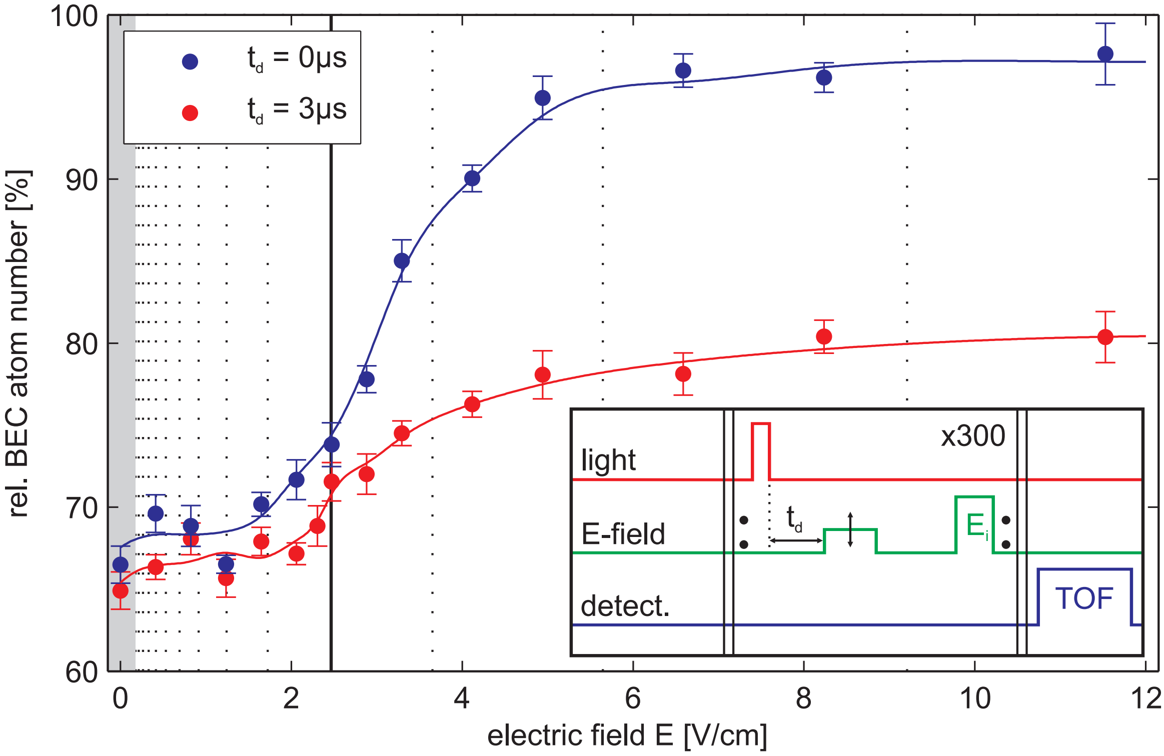

Figure 7.6: Investigation of the decay of the $110S$ Rydberg state. The BEC atom loss was measured while varying the electric field strength of pulses with a delay time of $t_d = 3\,\mu\text{s}$ (red) and immediately after Rydberg excitation (blue). The dotted vertical lines indicate the classical ionization threshold for Rydberg states in steps of ten principal quantum numbers n. The solid black line corresponds to the value for $n = 110$. In the grey shaded area, the electric field is not strong enough to extract a possibly existing ion from the condensate during the electric field pulse. The experimental sequence is depicted in the inset.

electric field pulse and strong atom losses (see paragraph 3.2.4) are observed, since the Rydberg atom can interact with the condensate during the full period of $10\,\mu\text{s}$ until the clearing pulse at the end of each sequence. As soon as the classical ionization threshold E_{ion} is reached (black solid line in Figure 7.6), the measured BEC atom losses decrease rapidly, since the Rydberg atom is ionized before it can lead to a significant atom loss. At a finite delay time $t_d = 3\,\mu\text{s}$ between the light pulse and the first electric field pulse, the measured relative BEC atom number does not go up to 100% due to the losses accumulated during t_d. Nevertheless, the onset of the decreased atom losses is at the same electric field strength as for $t_d = 0\,\mu\text{s}$, at the value expected for the $110S$ Rydberg state according to equation (7.4).

The first conclusion from this observation is that during the delay of $t_d = 3\,\mu\text{s}$, which is a considerable fraction of the lifetime $(5.0 \pm 0.5)\,\mu\text{s}$ of this state measured in the condensate (see Figure 7.5), the Rydberg atom is not decaying to states with significantly lower principal quantum numbers. This means that the Rydberg atoms must decay either directly to low energy levels, as they mainly do in spontaneous decay [37], or directly to the continuum. Possible processes could involve associative ionization, so called Hornbeck-Molnar ionization, or ion pair formation. In the first process, also termed autoionization, a positively charged molecular ion is formed [241]:

$$\text{Rb}(nS) + \text{Rb}(5S) \longrightarrow \text{Rb}_2^+ + e^- \tag{7.5}$$

In the second process, the high electron affinity of Rubidium allows to capture the Rydberg electron, leading to a formation of a positively and negatively charged ion:

$$\text{Rb}(nS) + \text{Rb}(5S) \longrightarrow \text{Rb}^+ + \text{Rb}^- \tag{7.6}$$

Both processes have been experimentally observed in hot Rubidium vapour [242, 243] and are discussed as a possible relevant decay process of ultralong-range Rydberg molecules [13]. In the present case, especially Hornbeck-Molnar ionization seems to be a probable explanation, since positively charged molecular Rb_2^+ ions have been experimentally observed in experiments with ultralong-range Rydberg molecules [12]. In order to distinguish the two processes experimentally, one could reduce the spatial extent of the condensate with respect to the size of the Rydberg atom. In the present setup, this is possible e.g. by lowering the magnetic offset field of the trap (see section 4.1). If the decay process is dominated by Hornbeck-Molnar ionization, then the observed lifetime remains constant. In contrast to that, ion pair formation is strongly reduced, if the Rydberg electron is located mainly outside the BEC.

Another important conclusion from the measurements described in this paragraph is that the BEC atom losses observed after time of flight are really caused during the finite interaction time of a Rydberg atom with the condensate. As can be seen in Figure 7.6, the relative atom losses nearly completely vanish if the Rydberg atom is extracted immediately after excitation. The required electric field is very close to the classical field ionization threshold. Any ions possibly existent before field ionization would be extracted already at much lower fields (see grey shaded area in Figure 7.6). This is the prerequisite for the interpretation of the experiments in paragraph 7.2.1 as a measurement of the lifetime of the Rydberg atom in the condensate and the basis for the explanation of the loss mechanism in section 8.1.

7.2.3 Dependence on spectral position

As discovered in paragraph 7.2.1, the lifetime of high Rydberg states is limited by a process depending on the number of ground state atoms inside the Rydberg atom. This number can be controlled spectroscopically by exciting Rydberg atoms at different densities and thus different laser detunings as pointed out in the discussion of the line broadening in paragraph 7.1.2. The lifetime of Rydberg atoms in the BEC therefore depends on the spectral position of the Rydberg excitation. For the $110S$ state, the lifetime was measured for different laser detunings from the Rydberg resonance in the thermal sample (see Figure 7.7). Since the experimental effort to obtain this data is quite high, only few data points are available. However, the lifetime is clearly decreasing with increasing red detuning. This means that the lifetime observed in the centre of the condensate is more than a factor of two shorter than the one in the outer regions at lower density. Although the data does not allow a quantitative analysis, it provides further evidence for two important conclusions. First, it is possible to control the position of the Rydberg excitation by spectroscopic means (see also paragraph 8.2.1) and second, the lifetime is really limited by a process depending on the number of ground state atoms inside the Rydberg electron wavefunction (see paragraph 7.2.1).

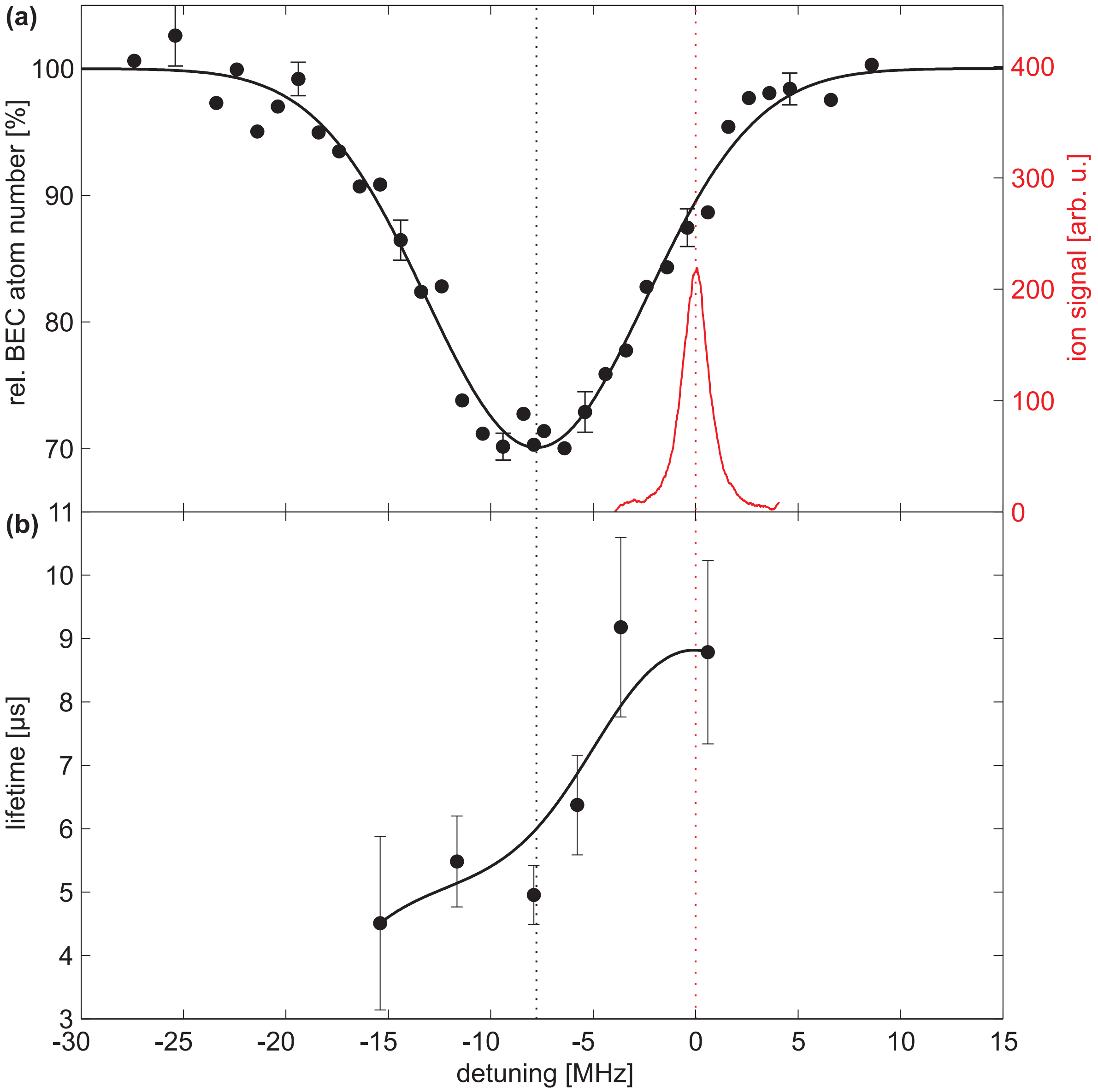

Figure 7.7: Lifetime of the $110S$ Rydberg state in a BEC versus spectral position. (a) The spectral lines measured in the BEC and in a thermal sample from Figure 7.2 (a) are shown as a reference. The lifetime measured in the condensate (b) shows a clear dependence on the spectral position. The black line is a guide to the eye.

7.3 Collective excitation

Strong mutual interaction between Rydberg atoms leads to the Rydberg blockade. This phenomenon results in a region around one Rydberg atom, where further excitations with the same driving laser field are prohibited (see paragraph 1.2.3). If the atoms are indistinguishable, the excitation is shared among all N_c atoms inside the blockade sphere, forming a so called super atom [113]. A clear indication for this effect is the emergence of Rabi oscillations, which are enhanced by a factor of $\sqrt{N_c}$ with respect to the single atom Rabi frequency Ω. This collective enhancement has been directly observed for two atoms [114, 115] in the past. For larger systems, inhomogeneities in the density and the coupling laser field reduce the visibility of collective Rabi oscillations, leading to saturation curves with an enhanced initial slope [118, 84]. Therefore, collective Rabi oscillations of many-body systems have so far only be observed in the case of only one excitation [116, 117].

The experiments in this work have been performed in a completely different regime than the work cited above. Here, not only the number of atoms inside the blockade sphere, but also inside the Rydberg atom itself is large. As discussed in paragraph 7.1.1, this leads to a density-dependent energy shift on the order of some MHz. For this reason, the simple concept of the Rydberg blockade described in paragraph 1.2.3 is not necessarily applicable. The Rydberg S-states investigated in this work show a purely repulsive van-der-Waals interaction (see section 1.2). Thus, a Rydberg excitation in the low density region of the condensate, at a detuning close to zero with respect to the resonance position in the thermal cloud, could possibly tune a second excitation more in the centre of the BEC into resonance. The zero crossings of the combined interaction and density-dependent potentials then in principle allow to create quasi crystalline ordered structures of Rydberg atoms [244]. More important for the work presented here is the case of large red detunings, when Rydberg atoms are excited preferentially in the centre of the condensate. In this case, the density gradient and the Rydberg-Rydberg interaction are of the same sign and there is consequently no antiblockade effect present. On the contrary, the blockade by a single excitation is then even more effective. This justifies a posteriori the assumption that only one Rydberg atom at a time is excited in the condensate in the present experiments (see introduction of chapter 7).

However, it is now not obvious whether and to what extent collective effects play a role in the excitation process. In order to study the excitation dynamics, the relative change of atom number after time of flight has been measured for different laser powers and pulse lengths on the $110S$ Rydberg state. The laser detuning was kept at the resonance position of the spectrum in the uppermost panel of Figure 7.2. Since the Rabi frequency Ω_b on the upper transition is technically limited by the available laser power and the beam waist in the focus, the effective two-photon Rabi frequency Ω was changed via the power of the red laser. In Figure 7.8a, the Rydberg induced relative BEC atom losses after time of flight are plotted versus the single atom excitation pulse area Ωt. The effective single atom Rabi frequency $\Omega = \Omega_r \Omega_b / 2\Delta_p$ (see paragraph 1.1.4) is calculated [96] from the measured powers and beam waists using the dipole matrix elements from [84].

For all three pulse lengths, at very high pulse areas Ωt, the Rydberg induced loss is reduced and the relative BEC atom number approaches 100%. This can be explained by the atom losses induced by spontaneous scattering of photons via the intermediate $5P_{3/2}$ state [198]. Both the

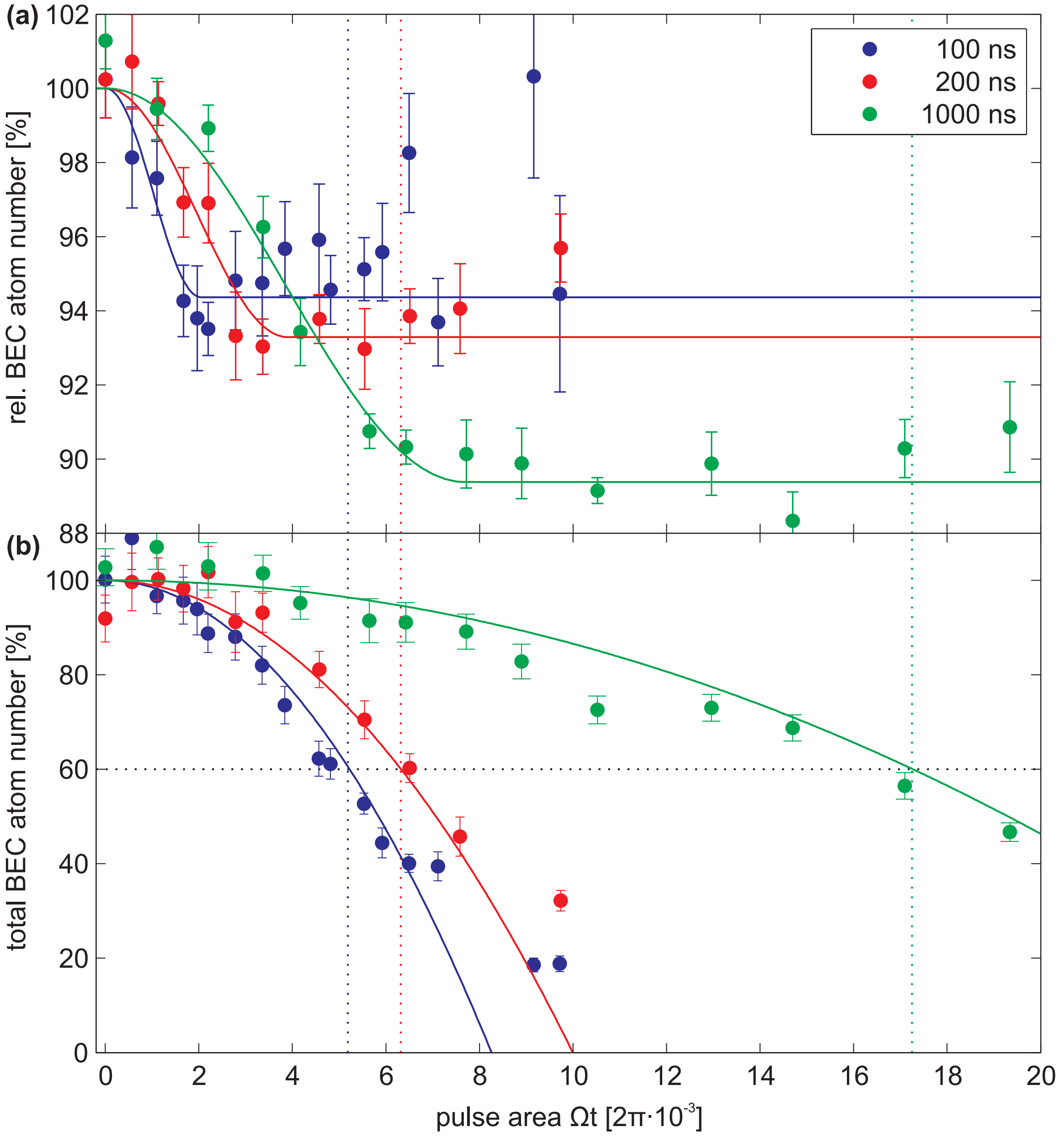

Figure 7.8: Saturation curves for the $110S$ state: atom loss versus pulse area Ωt for three different pulse lengths. (a) Relative change of BEC atom number due to Rydberg excitation. The solid lines are fitted saturation curves. (b) Reduction of the total BEC atom number due to off-resonant scattering from the intermediate level. The solid lines are quadratic fits. For the assumed confidence region the total atom must not exceed 40% (dotted lines).

pulse area Ωt and the scattering rate Γ_{scat} increase with the Rabi frequency Ω_r of the lower transition. While the increase of the pulse area Ωt is linear in Ω_p, the scattering rate Γ_{scat} scales quadratically at large detunings $\Delta_p = 500\,\text{MHz} \gg \Omega_r$ from the intermediate level (see section 5.1):

$$\Gamma_{\text{scat}} = \frac{\Omega_r^2}{4\Delta_p^2} \cdot \Gamma_p \tag{7.7}$$

Here $\Gamma_p = 6.07\,\text{MHz}$ is the decay rate of the $5P_{3/2}$ state [94]. The off-resonant scattering leads to a heating of the atoms, which causes significant losses from the condensate. The quadratic decrease of BEC atom number due to this effect alone is shown in Figure 7.2 (b). As the total BEC atom number drops, the absolute and at some point also the relative Rydberg induced atom loss decrease since the density-dependent line shift (see section 7.1.1) tunes the Rydberg state out of resonance. At the same time, the noise level increases as the BEC becomes very small. The onset of this effect is moving to values for shorter pulse lengths as the pulse area Ωt is proportional to the Rabi frequency Ω_r of the lower transition, whereas the scattering rate according to equation (7.7) is scaling with Ω_r^2 (see also appendix B.2.1). The confidence range is assumed to reach down to total BEC atom numbers of 60% of the initial number, denoted as dotted lines in Figure 7.2.

Even well within this confidence range, no Rabi oscillations are visible. Instead, an initial quadratic increase and a saturation onto a constant value for higher pulse areas Ωt appears. It is important to note here that the origin of these saturation curves is completely different to previous measurements performed in a thermal cloud [118, 84]. In a large inhomogeneous sample, the saturation is a result of the superposition of signals stemming from different super atoms. In this case, each super atom undergoes collective Rabi oscillations at a different frequency, depending on the local density and power of the driving laser field. The superposition of these different oscillations gives rise to a saturation curve [84]. The present case is rather comparable to the situation in [116], where one Rydberg atom in the $102S_{1/2}$ state was excited from a sample smaller than the blockade radius. At peak densities of $10^{12}\,\text{cm}^{-3}$, this resulted in a single super atom consisting of up to 400 atoms.

In the experiments presented here, however, the density is roughly two order of magnitude higher, so that there are on average many atoms inside the Rydberg atom (see Figure 7.1). The scattering of the Rydberg electron from the ground state atoms inside its wavefunction (see section 3.2) has basically two effects. First of all, the energy of the Rydberg state depends on the local density and therefore on the position of the particular atom within an inhomogeneous density distribution, given here by the Thomas-Fermi distribution of the condensate. This means that in case of large density gradients over a blockade volume not all atoms actually contribute to the collective state forming the super atom. The number of atoms taking part in the collective dynamics is thus reduced. Secondly, the transfer of momentum onto a BEC atom constitutes a measurement process determining the position of the Rydberg atom. On the first scattering event, the collective state is hence projected onto the basis of localized Rydberg excitations and the coherent collective evolution stops. The scattering rate Γ_{scat} of the Rydberg electron calculated according to equation (7.3) for the $110S$ state is $6.0\,\text{MHz}$. This means that the Rydberg excitation process is collectively enhanced; but as soon as a Rydberg atom is excited, the coherent collective dynamics stops quasi immediately since the average time $1/\Gamma_{\text{scat}} = 170\,\text{ns}$ for a scattering event is short compared to the excitation dynamics. After an initial increase with $\sin^2(\sqrt{N_c}\Omega t)$, the probability to excite a Rydberg atom then saturates at unity.

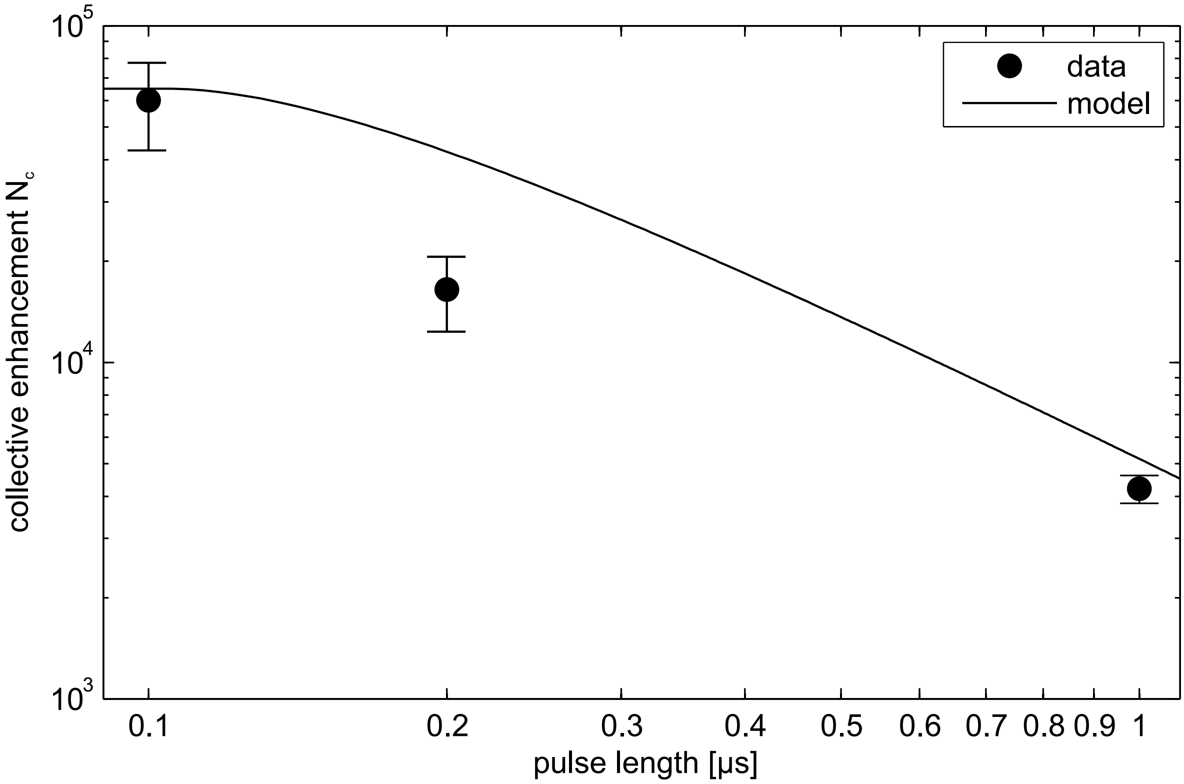

Figure 7.9: Collective enhancement versus pulse length. The number N_c of atoms contributing to the collective enhancement of the excitation process for different pulse lengths is extracted from the initial quadratic rise of the saturations curves in Figure 7.8. The solid line is the result of the model described in the text.

Saturation curves of this shape were fitted in the confidence region in Figure 7.8, with the amplitude and the collective Rabi frequency as fitting parameters. Due to the atom losses from light scattering, the amplitudes of the signal for different pulse lengths can not be compared directly. This observable is explained later in detail in section 8.1; important for the interpretation here is only the fact that the measured BEC atom loss is proportional to the probability of having a Rydberg excitation in the condensate. From the collective Rabi frequency, the number N_c of atoms contributing to the collective enhancement at the beginning of the excitation and consequently the size of the super atom can be extracted (see Figure 7.9). The collective enhancement by the atom number N_c is larger at short excitation pulses, as can be immediately seen in Figure 7.8 from the faster decrease of the observed BEC atom number with increasing pulse area Ωt.

In order to understand this trend, a simple model can be applied, where again the Rydberg excitation is assumed to be located in the centre of the condensate (cf. section 7.1). The interaction of the Rydberg electron and the ground state atoms inside its wavefunction causes a shift of the Rydberg state, depending on the local density ρ of ground state atoms (see section 3.2). Therefore, only a certain fraction of the atoms inside a range $\Delta\rho$ of densities, where this line shift is smaller than the excitation bandwidth Δf, can participate in the coherent dynamics. With the line shift from equation (3.33), this argument leads to the simple estimate:

$$h\Delta f > \frac{2\pi\hbar^2 a}{m_e}\Delta\rho \tag{7.8}$$

The fraction of BEC atoms N_c/N taking part in the collective dynamics can then be calculated from the Thomas-Fermi density distribution as the number of atoms inside a shell of densities $\Delta\rho$ around the center of the condensate with peak density ρ_0:

$$\frac{N_c}{N} = \left(\frac{\Delta\rho}{\rho_0}\right)^{3/2}\left(\frac{5}{2} - \frac{3}{2}\frac{\Delta\rho}{\rho_0}\right) \tag{7.9}$$

The dominant contribution to the excitation bandwidth Δf is the Fourier width[3] $0.886/t$ of the excitation pulse with finite duration t. The result of this estimate is plotted as a solid line in Figure 7.9, assuming a mean BEC atom number of $N = 6.5 \cdot 10^4$. For the shortest pulse length $t = 100\,\mathrm{ns}$, the Fourier width is with $8.9\,\mathrm{MHz}$ larger than the line shift in the condensate at this state (see paragraph 7.1.1). As a consequence, almost the whole condensate is contributing to the collective dynamics, forming a super atom consisting of around 60000 atoms. The simple estimate nicely reproduces the trend and order of magnitude. For longer pulses, the collective enhancement is restricted to fewer and fewer atoms. At $t = 1\,\mu\mathrm{s}$, where most of the experiments in this work were performed, still more than 4000 atoms contribute to the super atom. It is this enhancement factor that allows to excite Rydberg atoms in the condensate fast enough with the available laser powers and constraints due to scattering of the red light at the intermediate P-level (see section 5.1).

---

[3] The numerical factor comes from the FWHM of the sinc^2 function, the Fourier transform of a rectangular pulse of the electric field squared.

8 Coupling a single electron to a BEC

The evaluation of the results in the last chapter were focused on point of view of the Rydberg atom. Now, the reaction of the BEC on the Rydberg electron forming an impurity in the superfluid is discussed. This chapter covers an interpretation of the Rydberg spectroscopy experiments (see section 7.1) in the BEC from a different perspective as well as additional measurements probing the effects onto the condensate.

As discussed in the theory part (section 3.3), the interaction of the positively charged Rydberg core is negligible compared to the impact of the Rydberg electron. Furthermore, the observed line shift of Rydberg states at high densities in paragraph 7.1.1 could be fully explained by Fermi's free electron model [14] alone. Therefore, it seems reasonable to treat the system as a single electron impurity inside the Bose-Einstein condensate. The combination of these two elements is forming a hybrid system, consisting of a single quantum particle, the electron, and a quantum many-body system, the BEC. The quantum nature of the Rydberg electron already became obvious in paragraph 7.2.2, where the decay of the Rydberg atom was studied. The properties of the condensate as a quantum liquid are required in this chapter to understand the BEC atom loss, observed in time of flight absorption imaging. The discussion of this mechanism in this chapter explains the basis for the spectroscopic results provided in the previous chapter 7. As an additional observable, now the shape of the condensate emerges. The measurements show that the whole condensate is set into a collective oscillation by the electron impurity.

At first glance, it seems surprising that an electron impurity, a single particle, five orders of magnitude lighter than a ^{87}Rb atom, can lead to such a strong effect onto a BEC consisting of several hundreds of thousands of atoms. Much heavier single positively charged ion impurities have already been created in a BEC [160, 180]. But so far, a collective response of a Bose-Einstein condensate to a single impurity has not been observed in such systems yet. A simple estimate of the coupling strength of an impurity immersed in a BEC was discussed in paragraph 3.3.2. Within this model, the interaction strength of an electron is two orders of magnitude stronger than that expected for a positively charged ion. The fact that there is a significant impact of the Rydberg electron onto the BEC becomes also obvious by comparing the size and depth of the scattering potential (see section 3.2), created by the electron with the length and energy scales of the BEC (see Figure 8.1). Even though the electron scattering potential is small on the scale of Rydberg states, where the distance to the next level is at least several GHz, it is sizeable on BEC energy scales. In particular, it is orders of magnitude stronger than the polarization potential due to the Rydberg core Rb$^+$, except for very small distances, smaller than the minimum mean interparticle distance of $\overline{d} = 0.2\,\mu$m at a BEC peak density of $\rho = 10^{14}\,\mathrm{cm}^{-3}$. The mean potential depth, averaged over the size of the Rydberg atom, is on the same order as the chemical potential μ of the condensate. At the lowest principal quantum number $n = 110$ studied in this work, the scattering potential even exceeds the chemical potential by nearly one order of magnitude. For long interaction times of the Rydberg atom with the condensate, one can thus

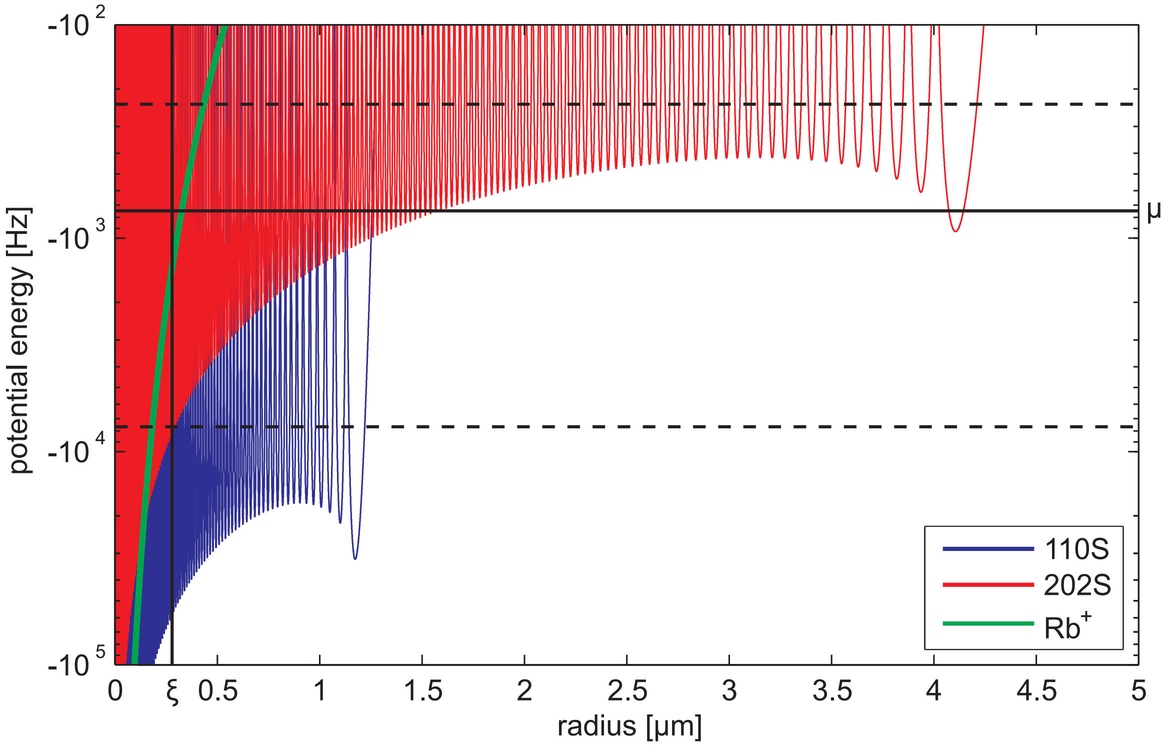

Figure 8.1: Comparison of length and energy scales of the system. The electron scattering potentials (see section 3.2) for the $110S$ and $202S$ Rydberg states are shown together with the polarization potential from the Rydberg core Rb^+. The mean potentials (black dashed lines) are on the order of the chemical potential $\mu = 745\,\mathrm{Hz}$ of the condensate with $N = 8 \cdot 10^4$ atoms (horizontal black line). The spatial extent of the scattering potential for all Rydberg states under investigation is much larger than the healing length $\xi = 274\,\mu\mathrm{m}$ of the BEC.

expect a significant modification of the density distribution of the BEC atoms. In particular, this would lead to an accumulation of atoms inside the wavefunction of the Rydberg atom.

For short interaction times t, where the Fourier width $\propto 1/t$ is larger than the potential depth, however, the momentum scale is more important (see paragraph 3.2.4). For all Rydberg states investigated in this work, the spatial extent of the scattering potential, given by the outermost lobe of the electron wavefunction at $2a_0(n-\delta_0)^2$ is much larger than the healing length $\xi = 274\,\mathrm{nm}$ of the condensate (see paragraph 2.3.1). This means that the Fourier transform of the potential has a dominant component at low momenta on the BEC scale. The Rydberg electron can therefore excite phonons in the condensate.

8.1 Coupling to BEC excitations

First evidence, that the interaction of a Rydberg electron with a BEC leads to the excitation of phonons in the condensate, is provided by the BEC atom losses observed in the spectroscopy experiments in section 7.1. Some atom losses are caused by each Rydberg atom being ionized and extracted from the cloud during the sequence. However, the observed atom losses are much larger than one would expect from this effect alone. The maximum atom losses per Rydberg

quantum number n	110	125	140	160	182	200
atom loss ΔN	50 ± 3	36 ± 3	15 ± 2	11 ± 2	7.1 ± 1.0	5.7 ± 1.3
lifetime τ [µs]	5.0 ± 0.5	8.6 ± 1.1	7.4 ± 1.3	17 ± 4	11 ± 2	24 ± 8

Table 8.1: Mean BEC atom loss ΔN per Rydberg atom and Rydberg lifetime τ in the condensate for different principal quantum numbers n. The maximum atom loss per Rydberg excitation is extracted from the Gaussian fits in Figure 7.2. The given values of the lifetime in the BEC are measured independently (see Figure 7.7).

excitation in time of flight imaging are shown in Figure 8.2. The relative atom loss evaluated as described in paragraph 5.3.2 is taken from the Gaussian fits in Figure 7.2. In order to obtain absolute numbers, these values are multiplied with the BEC atom numbers, measured at the end of each sequence (typically $5.0 \cdot 10^4$ atoms), and divided by the number of excitations per sequence. The loss, which is caused by ionizing the Rydberg atom alone, has been subtracted and the resulting values were normalized onto the same experimental peak density (similar as in paragraph 7.1.1). Both corrections have only a negligible effect well below the experimental uncertainty. The result is the mean number of BEC atoms lost per Rydberg atom since the Rabi frequency for all measurements was chosen on the plateau of the saturation curves in Figure 7.8 and the Rydberg blockade allows only one excitation at a time in the condensate. The values are listed in Table 8.1 together with the Rydberg lifetime measured in the BEC from paragraph 7.2.1. Up to 50 BEC atoms are lost per Rydberg excitation. This number decreases from lower to higher principal quantum numbers n. As the discussion in appendix B.2.2 shows, this observation can not be explained by classical scattering theory, as it is possible in similar experiments with ionic impurities [160]. Contributions by collisions of the positively charged Rydberg core [160, 180], as well as three-body recombination with two neutral atoms [245], are expected to be at least two orders of magnitude smaller than the effects observed here (see paragraph 3.3.2).

It turns out that the experimental data can be reproduced with good accuracy, assuming that the Rydberg electron is creating Bogoliubov excitations in the condensate, which are detected as atom losses in time of flight imaging. The underlying theory is discussed in depth in paragraph 3.2.4. Here, just the fundamental line of reasoning and some additionally required approximations are outlined in order to provide an intuitive understanding of the processes involved. The calculation assumes that at the beginning of each Rydberg excitation, the BEC is in its ground state. As excitations are present in the condensate already after the first laser pulse, this is certainly not the case in the experiment. However, the measured effect scales linear with the number of Rydberg excitations in the relevant range (see appendix B.2.3), so that effects of excitations already present in the condensate can be neglected on the current level of precision. The scattering potential of the Rydberg electron (see section 3.2) acts as a time-dependent perturbation onto the condensate. Perturbation theory is applied to calculate the number of Bogoliubov excitations in the BEC (see equation 3.52). The interaction time of the Rydberg electron with the condensate is limited by the finite lifetime τ of the Rydberg atom (see paragraph 7.2.1) and the experimental sequence, since any Rydberg atom is extracted after a fixed time $t_d = 10\,\mu\text{s}$ (see paragraph 5.3.2). The Fourier transform of the time-dependent interaction potential determines which modes are excited in the condensate. The time dependence leads to a finite Fourier width, allowing energetically a broad energy band of excitations ranging from $0\,\mathrm{kHz}$ to about $16\,\mathrm{kHz}$. This band is large compared to the energy scale of the BEC, orders of magnitude larger than the chemical potential $\mu = 745\,\mathrm{Hz}$. It is then the shape of the scattering potential (see Figure 3.15c) that largely determines which modes are populated according to the dispersion relation (see equation 2.29) within the energetically allowed range. As has been shown in paragraph 3.2.4, excitations of phonon and free particle type are created in the experimentally relevant parameter range. After a time of flight, both phonon and free particle excitations can be detected as atom losses, since all atoms that carry a sufficient momentum q_{min} are leaving the condensate as the trap is switched off. This way, also the residual thermal cloud is removed. The minimum momentum can be estimated to be on the order of $q_{\text{min}} \approx 0.13\,\hbar/\xi$ from lattice diffraction experiments (see Figure 5.3 in section 5.1) and the size of the condensate after time of flight. As discussed in theory paragraph 3.2.4, for high principal quantum numbers around $n = 200$ this cutoff leads to a significant fraction of excited atoms not detected as atom losses (see Figure 3.16b). However, the absolute influence of this modification is next to negligible compared to the experimental uncertainty in this regime.

The treatment presented here can be compared to the Raman-Nath regime in lattice diffraction of atoms [204]. This concept was originally derived for the diffraction of light by high frequency sound waves [246], describing the limit of short interaction time t. In this regime, the atoms are interacting shortly with a thin periodic phase grating $U(z) = U_0\,\cos^2(kz)$, formed by a standing wave light field [247]. During this time, the atoms do not move, but only accumulate a certain phase $U_0/\hbar \cdot t$ induced by the light field potential. The phase shift is much smaller than π, leading to a small fraction of the atoms acquiring a fixed momentum $2k$ which is determined by the Fourier transform of the periodical potential $U(z)$. The probability for an atom to be scattered out of the condensate is to first order proportional to the square of the accumulated phase $(U_0/\hbar \cdot t)^2$ [176].

Likewise in the present case, there is a dominant scaling of the atom losses with the square of the Rydberg lifetime τ (see paragraph 3.2.4). Since so far there is no theoretical model describing the experimentally observed reduction of the Rydberg lifetime τ at high densities and high principal quantum numbers, measured values from section 7.2 are used for the theoretical calculations. Therefore in Figure 8.2, the measured atom loss from Table 8.1 is plotted normalized onto τ^2. This way, the uncertainty in the measured Rydberg lifetime τ has only little influence on the theory curves, but mainly affects the experimental data. The residual dependence on the lifetime τ is weak, so that assuming a constant value of $10\,\mu\mathrm{s}$ for all principal quantum numbers n (lines) already reproduces the overall effect very well. Inserting the measured values of τ into the theory allows for a complete quantitative reproduction of the observations within the errorbars, without any adjustable parameter (squares in Figure 8.2). As expected, the corrections to the scattering potential, which depend on the electron momentum, only play an important role at low principal quantum numbers (see also discussion in paragraph 3.2.2). The improved agreement between theory and experiment is even better visible in the linear plot in appendix B.2.4, where also the role of excitations in the phonon regime is discussed. As already discussed in the theory part (see Figure 3.16), the relative contribution of phonons to the measured atom loss is around 50%. The fact that the experimentally observed atom losses can only be explained taking phonon excitations into account, provides clear evidence that the single Rydberg electron is really coupling to the excitation spectrum of the condensate. This insight is also important for the understanding of further observations, presented in the following section 8.2.

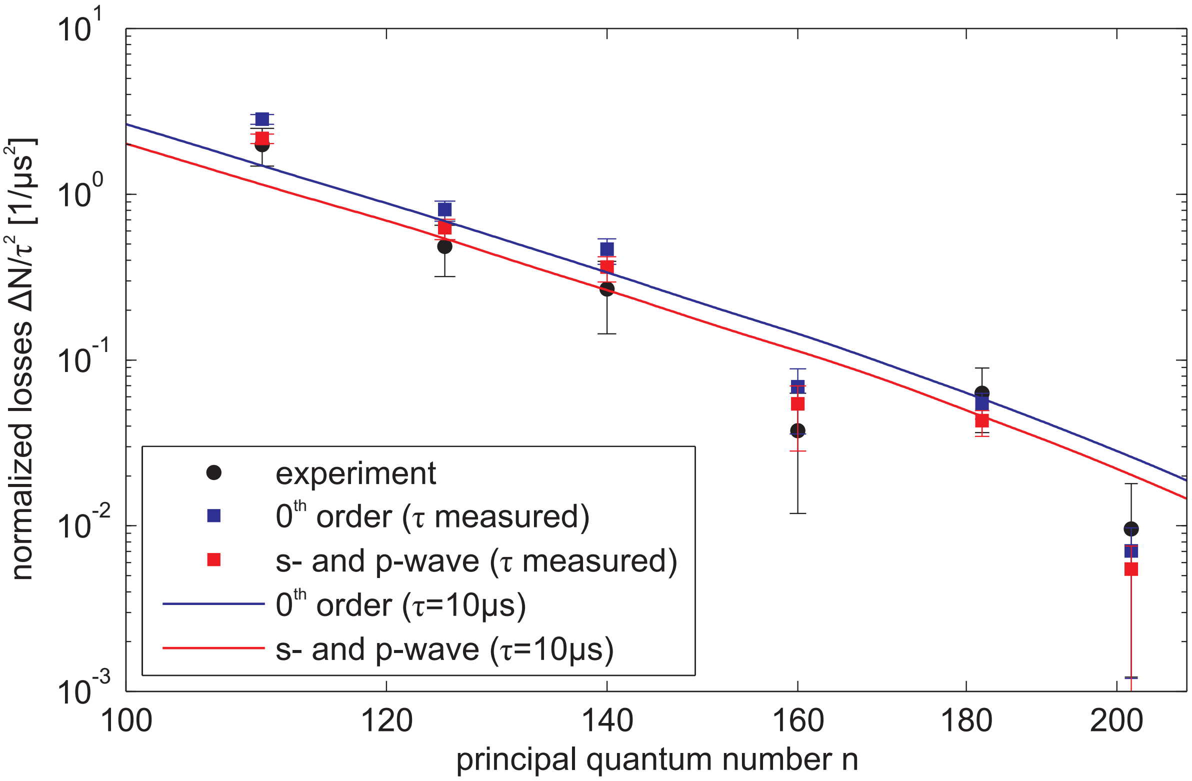

Figure 8.2: Rydberg induced BEC atom loss after time of flight for different principal quantum numbers n. The maximum atom loss per Rydberg excitation is normalized onto the lifetime squared τ^2 of the Rydberg state in the BEC (both quantities from Table 8.1; the losses are corrected for the loss by the field ionization of the Rydberg atom). Theory values, taking the measured lifetime into account (squares) and assuming a constant lifetime of $\tau = 10\,\mu\text{s}$ (solid lines), are shown in the approximation to zeroth order in the electron momentum k (blue) and taking terms up to linear in k into account (red) respectively.

8.2 Excitation of BEC shape oscillations

In the previous section 8.1, the atom losses from the condensate observed after time of flight could be explained by the creation of excitations in the BEC. All atoms that acquire a sufficient momentum above a certain threshold q_{min} leave the condensate during time of flight. Accordingly, the excitations at low momentum can lead to a modification of the density distribution of the condensate. In the following, this deformation of the condensate, observed in the BEC spectroscopy experiments in section 7.1, is discussed. It turns out that the findings are caused by a collective shape oscillation of the whole condensate, which the Rydberg electron is coupling to.

8.2.1 Deformation of condensate

The absorption images of the condensate contain information about the size and the shape of the BEC. So far, only the BEC atom number has been evaluated (see Figure 7.2). An anisotropic deformation of the condensate, preserving the cylindrical symmetry, can be quantified using the aspect ratio $\epsilon = r_\mathrm{r}/r_\mathrm{z}$, the ratio between radial size r_r and axial size r_z of the condensate after time of flight. This number is plotted in Figure 8.3 together with the atom loss and the Rydberg spectra measured in the thermal cloud for reference. For the lower Rydberg states, there is a strong change of the measured aspect ratio ϵ. The Gaussian fits are a guide to eye showing a clear shift of the maximum mechanical effect to the red side of the loss feature. The condensate there becomes more elongated after time of flight, partially compensating for the atom losses in the radial direction. This is illustrated by the insets in Figure 8.3a, where the difference of an absorption image with Rydberg excitation and a reference measurement with detuned blue laser is shown at two different laser detunings. The spectral positions were chosen so that the integrated total atom loss is the same for both examples. On the blue side, the atom loss is isotropic, resulting in a blue spot in the difference picture at the position of the condensate. On the red side, the deformation of the condensate in radial direction partially compensates the atom losses, leading to a red stripe where the atom number after time of flight is not changing.

The observation of this mechanical effect of the Rydberg electron onto the BEC provides further evidence for the conclusions drawn in the previous discussions. Both the line broadening in paragraph 7.1.2 and the dependence of the measured lifetime on the spectral position (see Figure 7.7) suggest that the position of the Rydberg atom inside the inhomogeneous density distribution of the condensate can be controlled spectroscopically. The density-dependent interaction energy of the Rydberg electron with the ground state atoms (see section 3.2) allows to excite Rydberg atoms only at positions in the sample with a certain density. This assumption is also backed by the collective enhancement of the Rydberg excitation that is limited to a certain density range around the peak density (see section 7.3).

The dependence of the observed BEC deformation on the laser detuning from the Rydberg state can be explained from the same principle. Due to the energy shift from Rydberg electron-atom scattering (equation 3.33), a Rydberg excitation at large red detuning from the non-interacting Rydberg state (as measured at low densities) is pinpoint at high densities; this leads to a scattering potential, well localized in the centre of the condensate. Then, a slow mechanical response of the BEC atoms on the millisecond timescale, given by the inverse trap frequencies, can be expected from the resulting time averaged potential. At smaller red detunings, the Rydberg excitation is restricted to a larger range and eventually to a shell of equal density around the centre of the BEC. During repeated excitations, the Rydberg electron is then positioned randomly inside such a shell, so that the average effect onto the condensate averages to zero. This only holds true for excitations at low momenta, well within the phonon regime, where the atoms do not gain enough momentum to leave the condensate at once.

The achievable degree of localization of the Rydberg atom around the centre of the condensate can be estimated by equating the excitation linewidth $h\Delta f$ and the density-dependent line shift from equation (3.33). The resulting resolution $\Delta\rho$ in the density ρ of ground state atoms reads (cf. section 7.3):

$$\Delta\rho = \frac{m_e}{\hbar|a|}\Delta f \tag{8.1}$$

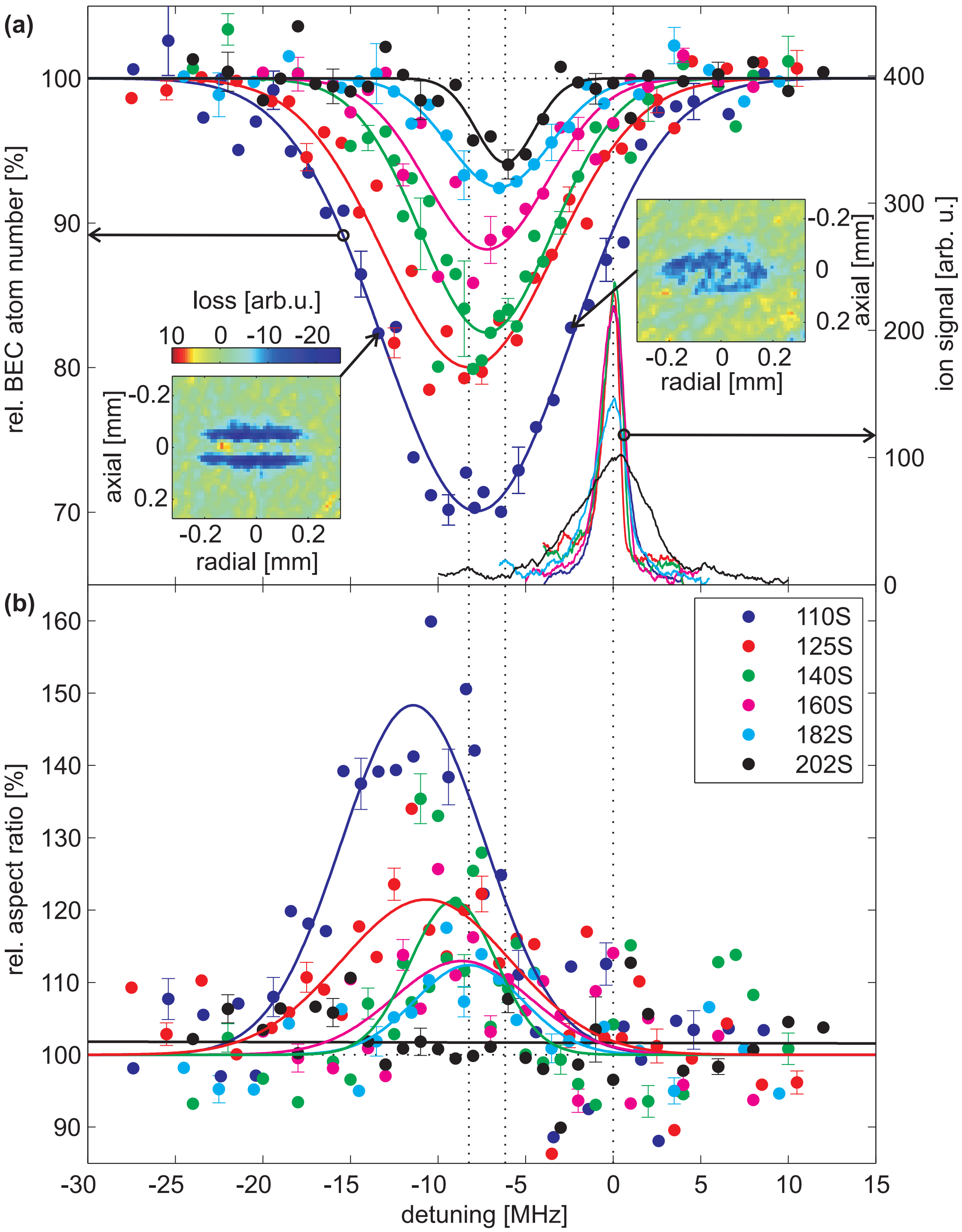

Figure 8.3: Rydberg excitation spectra for different principal quantum numbers n. Relative change of the BEC atom number (a) and aspect ratio (b) after time of flight. The solid lines are Gaussian fits to the data. The zero position is determined as the position of the Rydberg line in the thermal cloud, as shown for reference. The change of aspect ratio is illustrated in the insets of (a), which show difference pictures of the condensate at two distinct spectral positions of the $110S$ state, where the overall losses are the same. The data is from the same measurements as Figure 7.2.

As the excitation linewidth over the size of the condensate is limited by the finite pulse length of $t = 1\,\mu\mathrm{s}$, the resulting spectral resolution in density is expected to be on the order of $\Delta\rho \approx 9.0 \cdot 10^{12}\,\mathrm{cm}^{-3}$. At a mean peak density of the condensate of around $\rho_0 = 8.6 \cdot 10^{13}\,\mathrm{cm}^{-3}$, this corresponds to a resolution of $32\,\%$ of the Thomas-Fermi radii around the center of the condensate. In the present case, this provides a spatial resolution of $1.9\,\mu\mathrm{m}$ in the radial direction, which is much smaller than the optical resolution in the setup. Of course this value is only valid for the lowest two Rydberg states investigated, since already at $n = 140$ the size of the Rydberg atom exceeds this value. Note that this localization actually forms an additional excitation blockade mechanism in addition to the Rydberg dipole blockade (see paragraph 1.2.3) and the Coulomb blockade [248].

8.2.2 BEC shape oscillations

In order to further clarify the origin of the deformation, the dynamics of the BEC deformation are studied in Figure 8.3. Here, the hold time of the condensate after a sequence of 200 Rydberg excitations was varied. The measured relative change of aspect ratio ϵ at the $110S$ state is shown in Figure 8.4 for two different laser detunings on the red and blue flank of the Rydberg line in the condensate (see Figure 7.2). Both measurements show a clear sinusoidal oscillation at the

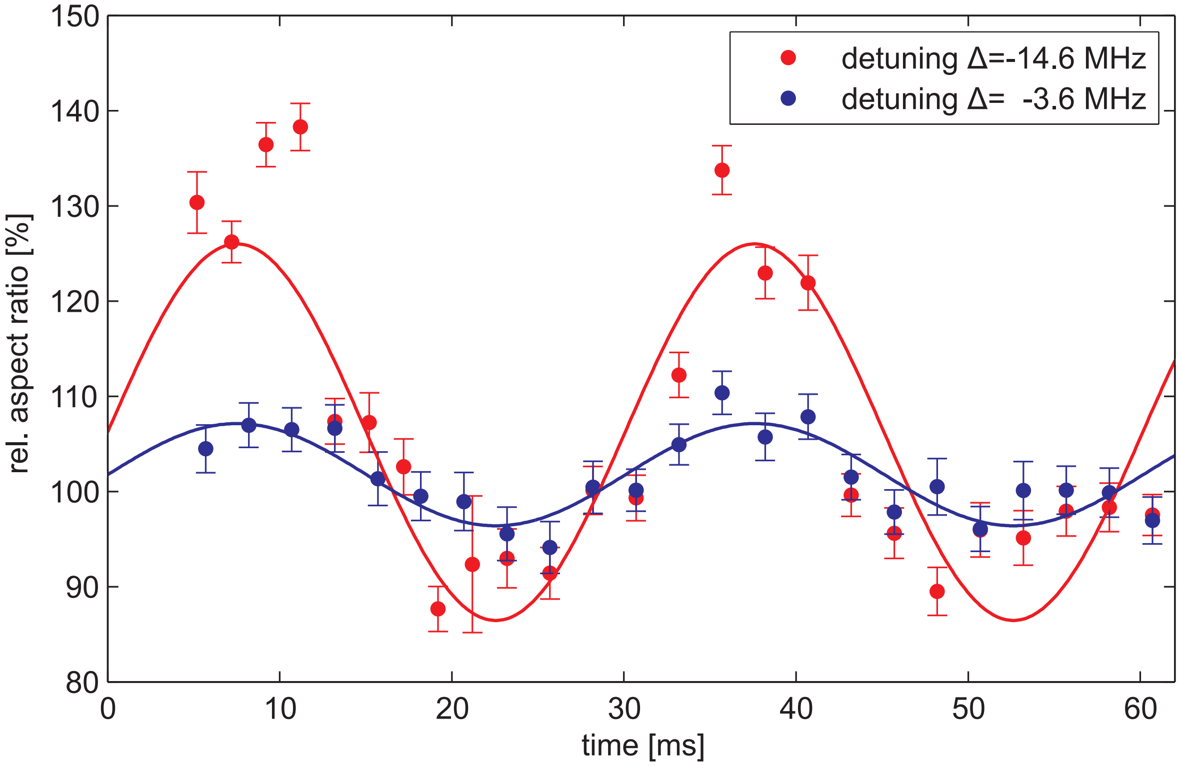

Figure 8.4: Shape oscillations of the BEC induced by the $110S$ state. The relative change of aspect ratio is shown for different hold times in the trap and two different laser detunings. The sequence of 200 Rydberg excitations lasts from 0 ms to 3.2 ms. Except for the number of pulses, it is identical to the one described in paragraph 5.3.2. The solid lines are sinusoidal fits with fixed phase.

same frequency, but with different amplitudes. This means, that the BEC deformation observed in the BEC spectroscopy experiments (see Figure 8.3) is due to a collective shape oscillation of the whole BEC that is excited at different strength and imaged at a fixed time. Since the period of this oscillation is longer than the Rydberg sequence, the contributions of all Rydberg excitations add up in phase. As explained in paragraph 8.2.1, the amplitude on the blue side is lower, since the effect of repeated excitations on a shell around the centre of the condensate is reduced due to the averaging.

The type of shape excitation can be determined by its frequency. Analytical expressions for collective excitations of harmonically trapped Bose-Einstein condensates in the Thomas-Fermi regime are reviewed in paragraph 2.3.2. Taking all measurements at different principle quantum numbers n (see Figure 8.5) into account, one obtains an average frequency of $\nu_{\text{osc}} = (35.2 \pm 0.8)\,\text{Hz}$. Within the errorbars, this is perfectly matching the eigenfrequency of $\sqrt{5/2}\omega_z = 35.4\,\text{Hz}$ expected for the slow $m_l = 0$ quadrupolar mode (see paragraph 2.3.2). For this mode, the radial and axial size of the condensate are oscillating out of phase. However, it turns out that in the present setup the oscillation in the axial direction after time of flight [196] is too small to be resolved. Therefore, in the following only the radial size of the BEC is evaluated. Figure 8.5a shows the oscillation of the radial size of the condensate after time of flight for different Rydberg S-states. The laser detuning was chosen on the blue flank of the loss signal in Figure 7.2 at half maximum of the atom loss, where the mechanical effect onto the condensate is large. In order to quantify this effect, the amplitude and the offset of sinusoidal fits are shown in Figure 8.5b and Figure 8.5c. The oscillation amplitude becomes weaker for higher principal quantum numbers in agreement with the observations in Figure 8.3. The offset of the oscillation is expected to decrease due to atom losses from the condensate (see section 8.1), since the Thomas-Fermi radii of the condensate scale with the BEC atom number to the power of $1/5$. The expected change in offset from the measured atom loss is shown in Figure 8.5c. The order of magnitude is correct, as well as the overall trend. The experimentally observed change in offset is about a factor of two larger than expected. A quantitative understanding is more involved since the effect of the Rydberg excitation alone is relatively small compared to the impact of the red Rydberg laser (see appendix B.2.5). For the measurements presented here, this effect has been subtracted; however, assuming the condensate to be unperturbed might be therefore a poor approximation, even though it lead to very good results in section 8.1. This is one of the reasons why the observation of any deformation of the condensate beyond shape oscillations has been elusive so far, even though such effects could be expected from the shape and strength of the scattering potential (Figure 8.1). The other reason is the finite spatial resolution of the Rydberg excitation, leading to a washing out of the time-averaged potential.

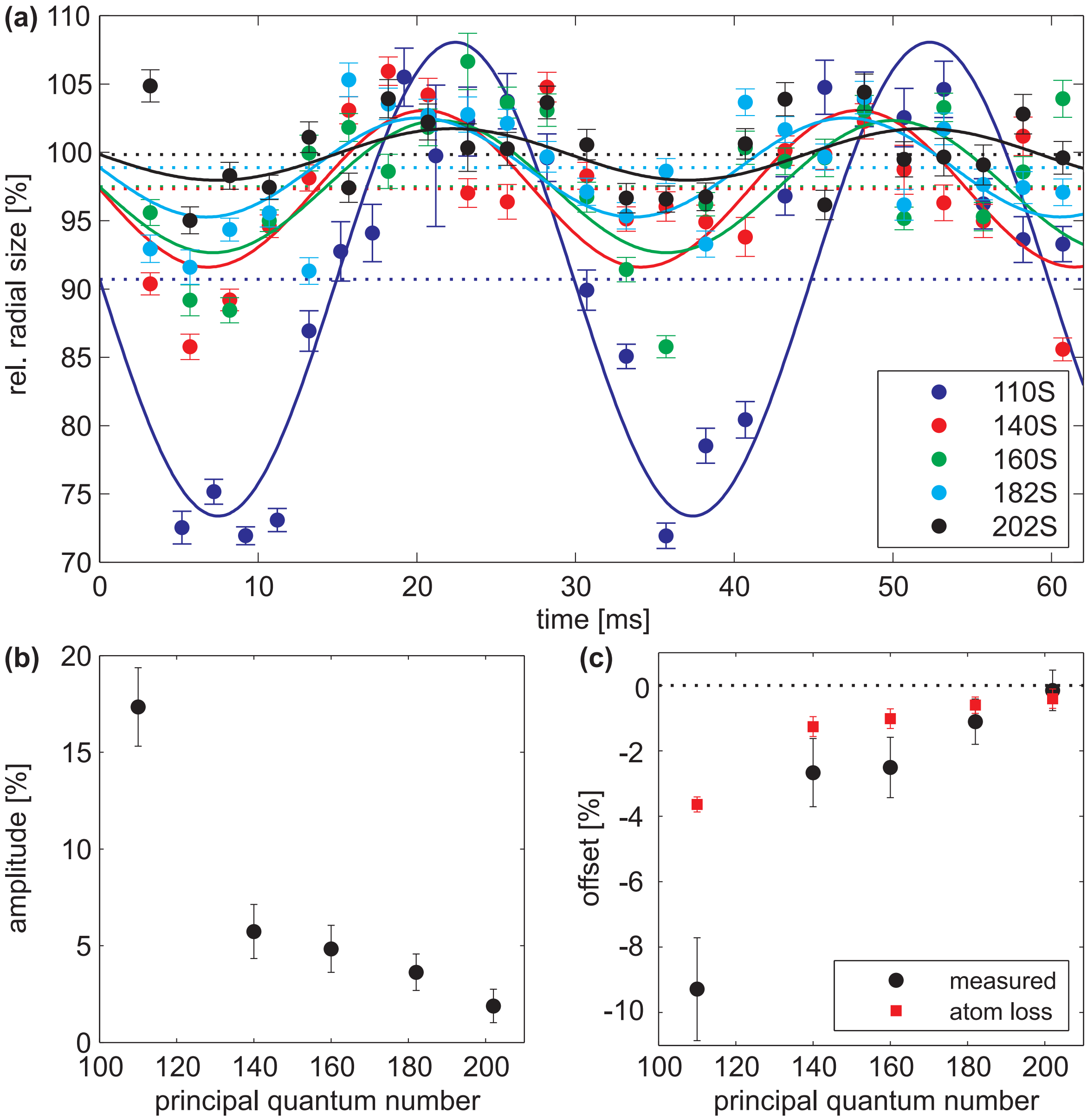

Figure 8.5: Shape oscillations of the BEC, induced by Rydberg atoms in different S-states. (a) The relative change of the radial size of the condensate (Thomas-Fermi radius) is shown for different hold times in the trap and different Rydberg states. The sequence of 200 Rydberg excitations lasts from 0 ms to 3.2 ms. The amplitude (b) and the offset (c) of the sinusoidal fits (solid lines in a) are shown for different principal quantum numbers. In (c), additionally the change of the offset expected from the measured atom loss is shown as red squares.

Conclusion and Outlook

> *Now this is not the end. It is not even the beginning of the end. But it is, perhaps, the end of the beginning.*
>
> Sir Winston Churchill

The overall goal of this thesis was to observe the impact of few Rydberg excitations onto a large atomic sample. In a first approach, an atomic sample was dressed with a low lying Rydberg state. Due to the Rydberg blockade, the excitation is shared among all atoms inside a blockade volume, leading to a small admixture of the Rydberg state to each atom. This way, the strong interaction between two Rydberg atoms causes a small additional interaction energy for all dressed atoms. Many ambitious theoretical proposals exist, that are based on this idea, some even for parameters close to the present experimental configuration. However, in this work, further principal as well as technical problems were identified, that impede an experimental realization in the present setup. A new model has been developed in the framework of this thesis, providing more insight and an intuitive explanation for the collective processes involved. Moreover, it allowed for more precise estimates of the effect of Rydberg dressing, which can be expected for the current situation. This way, clear requirements, that have to be satisfied for an experimental realization, could be derived. One possible path involves significant changes of the trapping geometries to reduce the effective atomic density, such as optical lattices or samples at reduced dimensionality. Approaches based on the current setup, instead, would require a hundred times higher laser power than currently available.

The focus then turned from the Rydberg-Rydberg interaction to the direct interaction between one single Rydberg atom and a large number of atoms in the ground state. This interaction was found to be dominated by the short-range interaction of the Rydberg electron with all atoms located inside its orbit.

In order to enter this regime, the current experimental setup had to be pushed to the limits. High atomic densities around $10^{14}\,\mathrm{cm}^{-3}$, as present in a Bose-Einstein condensate, and Rydberg states at high principal quantum numbers $n > 100$ had to be combined, allowing the Rydberg electron to interact with a large number of atoms. This imposed orders of magnitude higher technical demands to the control of electric fields and to the timing of the experimental sequence than previous experiments. On the one hand, much shorter switching times within one sequence and, on the other hand, much longer total measurement times were required. The latter demanded long term stability on much larger timescales and long, uninterrupted operation of the experiment. Finally, Rydberg states at principle quantum numbers even above $n = 200$ could be achieved. Rydberg atoms at more than a factor of two higher principal quantum numbers have been already observed in different laboratories [249, 250] and lower Rydberg states have been studied in a high density environment already in the 1930ies [2, 3, 74]. However, it is the combination of both, high Rydberg states and Bose-Einstein condensed samples at high densities, that constitutes the major advance in this work.

The experimental results were first discussed from the point of view of the Rydberg atom. It was shown that the density-dependent energy shifts can be fully explained, based on the concept of low energy electron-atom scattering as developed by Enrico Fermi already in 1934 [14]. Besides the line shift, also a broadening and a density-dependent reduction of the lifetime of high Rydberg states were observed. Moreover, the influences onto the Rydberg blockade and the collective excitation of Rydberg atoms were studied.

For all experimental observations so far, the role of the positively charged Rydberg core was negligible. Due to the Rydberg blockade, there is only one excitation at a time in the condensate. The system can thus be considered as a BEC with a single electron impurity, where the Rydberg atom effectively only serves as an electron trap with variable size. However, studying the decay of the Rydberg atom, it could be shown in this thesis that the motion of the electron in this trap is not classical. Instead, the Rydberg electron seems to stay in its quantum state, until it finally decays in a sudden event. This formed the basis to understand the impact of the Rydberg electron onto the condensate.

In collaboration with a theory group, in particular David Peter and Hans Peter Büchler, a simple model was developed, that can explain the Rydberg induced atom losses from a condensate observed after a time of flight. This model is based on the creation of Bogoliubov type excitations in the BEC. It could be shown that a significant contribution of the measured signal comes from phonon type excitations at low momenta. In the limit of very low momenta, these phonons can extend over the whole condensate, causing collective shape oscillations, that were indeed experimentally observed. Measuring the dependence of these shape oscillations on the laser frequency used for Rydberg excitation, evidence was provided that the interaction of the Rydberg electron with the BEC allows to position a Rydberg atom in the condensate much more precisely than the optical resolution.

This thesis started a new field of intriguing research. The results have opened up paths in different directions. Some of them are already followed by different groups. In the following, a short overview of both work already started and possible ideas is given. In particular, the first idea is currently being realized using the present experimental setup, while current work on a next generation apparatus is undertaken to implement some of the other proposals.

Ultralong-range Rydberg molecules

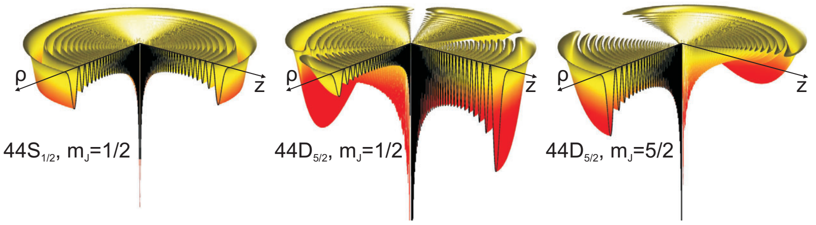

Figure 8.6: Molecular potentials for different ultralong-range Rydberg molecules in cylindrical coordinates (ρ, z). The potential to zeroth order in the electron momentum is plotted weighted with the radius r.

The first idea actually goes one step back and is motivated by one of the problems occurring in the quest for Rydberg dressing on Rydberg D-states. On the red side of the $44D_{5/2}$, $m_J = 5/2$ state, a whole band of lines was found. These lines can be identified as states of ultralong-range Rydberg molecules. Here, one or more atoms in the ground state are bound by the elastic scattering of the Rydberg electron. Similar molecules, formed by Rydberg S-states, have been already studied previously [12, 13]. The main difference of the Rydberg D-states is that their Rydberg electron wavefunction shows an additional angular dependence, that translates directly into the molecular potential (see Figure 8.6). More appealing than the D-state molecules with magnetic quantum number $m_J = 5/2$, already observed in this work, are states with $m_J = 1/2$. Here, ground state atoms can be bound in two potential wells, located around the poles and the equatorial plane respectively.

Another interesting direction in the field of ultralong-range Rydberg molecules is to study the bound states based on Rydberg S-states at much higher principal quantum numbers than previous work [12]. At constant atomic densities, here, the Franck-Condon factor for the photoassociation of molecules with more than one ground state atom [77] increases. While the binding energy per atom is decreasing roughly as the principal quantum number $(n - \delta_0)^{-6}$, the formation of larger and larger polymers can be expected until the binding energy per atom reaches the experimental spectral resolution. Then, there is a transition to the regime of a mean energy shift of the Rydberg atom by all atoms distributed randomly inside, as it has been studied in this work. For a resolution of $100\,\mathrm{kHz}$, this transition is expected at principal quantum numbers around $n = 80$ for Rydberg S-states.

Single photon absorber

Turning to the parameter regime investigated in this thesis, a direct application can be found in quantum optics. Here, the Bose-Einstein condensate can serve as a single photon absorber [251]. Two properties of the combination of high Rydberg states and a high density environment are important. First, the Rydberg blockade for Rydberg states at principal quantum numbers $n \geq 100$ excludes multiple excitations in the condensate at the present parameters. Therefore, only one photon at a time is subtracted from the incident light field. Second, and more important is the interaction of the Rydberg electron with a large number of atoms within its orbit. In this work, evidence was provided that this interaction causes a strong dephasing. The scattering of the Rydberg electron at the ground state atoms acts as a measurement process, that projects the superposition state onto the state of one localized Rydberg atom. This stops the coherent evolution, as soon as there is one atom excited. Thereby, it is assured that the Rydberg state is not transferred coherently back to the ground state by stimulated emission. Since the BEC is optically thick, the BEC then forms an element, that almost deterministically absorbs a single photon from an arbitrary light field. Such an element could not only be used to generate nonclassical states of light [252], but could also form one building block of a single photon counter. Here, an array of atomic clouds, e.g. in an optical lattice, has to be combined with a detection scheme for Rydberg atoms, such as field ionization and ion detection or EIT imaging [253].

Phonon-mediated coupling of electrons

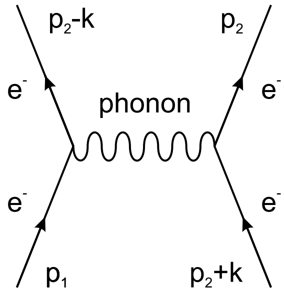

Figure 8.7: Feynman diagram of phonon-mediated coupling of two electrons

A microscopic model explaining the mechanism of superconductivity, the phenomenon of absolutely vanishing electrical resistance of a material below a certain critical temperature, is provided by the BCS theory [254]. Within this model, electrons, that experience an attractive potential, form so called Cooper pairs that condense into a superfluid state. In most conventional superconductors, the attractive interaction between the electrons is formed by a temporal polarization of the surrounding lattice, which is caused by collective modes of motion of the ionic cores, i.e. phonon modes. There is experimental evidence that electron-phonon coupling also plays a role in high-temperature superconductors [255]. Even though the actual underlying processes of superconductivity are more involved, a clean model system, which allows to study the very first building block, the interaction of two electrons mediated by phonons in the surrounding material, is certainly of fundamental interest. The system studied in this thesis makes it possible to prepare a single electron in a Bose-Einstein condensate, forming a medium close to the absolute ground state. The excitation of phonons by the electron in the BEC has been already demonstrated in this work. So far, no evidence has been found that phonons, which are already present in the condensate or excited by previous Rydberg electrons, influence the subsequent excitation of a Rydberg atom. However, the time between the single excitations was so short that phonons, travelling at the Bogoliubov speed of sound $c_s \approx 2\,\frac{\mathrm{nm}}{\mu\mathrm{s}}$ (see equation 2.32), could not propagate notably. First evidence for the coupling of an electron to phonons could possibly be provided in an experiment, where two pulse trains of Rydberg excitations are separated by a variable delay time on the order of few milliseconds. The study of a clean model system, consisting of only two Rydberg electrons, separated in time and coupled by phonons, seems out of reach of the resolution of the present setup.

Crystalline structures of Rydberg atoms

Another idea that is more straightforward, based on the results of this work, deals with the creation of quasi-crystalline structures of Rydberg atoms. One proposal for realizing such a system is based on the strong interaction between Rydberg atoms [256]. Such a dynamical crystallization [257] requires chirped Rydberg excitation pulses [244]. Other proposals use Rydberg dressing to prepare e.g. supersolid crystals [85, 86, 217]. The experimental realization of this approach, however, is even more difficult, as proven in this work. Instead, the interaction between Rydberg electrons and ground state atoms inside their wavefunction could be used. In an inhomogeneous dense sample, such as provided by a typical BEC, the zero crossings of the combined Rydberg-Rydberg interaction and density-dependent scattering potentials allow to excite ordered shells of Rydberg atoms. Such crystals could even have technical relevance, for example as sources for cold ion and electron beams, required for nanoscale imaging and milling applications [258].

Electron orbital imaging

An idea, which is closer to an experimental realization, focuses on the Rydberg electron itself. The excitation of phonons in the BEC, as observed in this work, is caused by the imprint of the potential, which is created by the elastic scattering of the Rydberg electron from ground state atoms in the condensate. The response of the BEC density distribution to this potential could be used to make the orbital of the Rydberg electron visible. The length scales of the structures expected for high principal quantum numbers are on the order of micrometers and therefore well above the resolution limit of state of the art imaging. Various techniques like dark ground imaging [259], phase-contrast imaging [260], polarization contrast imaging [261, 262] and adapted forms of absorption imaging [263] allow to measure precisely the density distribution of a BEC in situ. It seems therefore well within reach to image a single electron orbital. This technique would be more direct than results of high harmonics generation from intense femtosecond laser pulses [264] and photoionization microscopy [265].

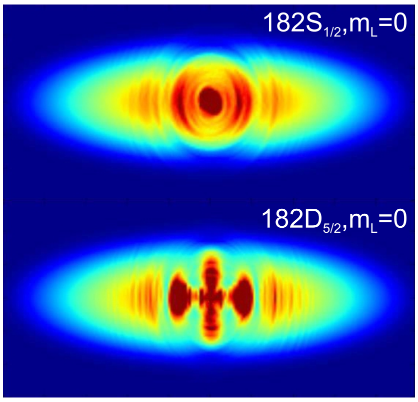

Figure 8.8: BEC density distribution of a BEC modified by 50 subsequent Rydberg excitations calculated for the current experimental parameters [266].

So far, two problems prevented an experimental realization. The results discussed in this work show that the mechanical effect of the Rydberg laser dominated the deformation of the condensate. Current effort aims to overcome this effect by applying different Rydberg excitation schemes and modified experimental sequences. If one does not require the deterministic excitation within a short time, much longer light pulses at lower power can be applied. Thereby, detrimental light forces can be significantly reduced. A more principal problem is connected to the short lifetime, that was observed in this thesis for Rydberg states at BEC densities. Since the timescale of a possible modification of the BEC density distribution is much larger, several subsequent Rydberg excitations are required. Theoretical calculations done in a collaboration with Tomasz Karpiuk, Mirosław Brewczyk and Kazimierz Rzążewski show that around 50 Rydberg excitations at a rate below $100\,\mathrm{kHz}$ lead to a sufficiently strong effect (see Figure 8.8), provided that the atoms are placed with a precision better than $1\,\mu\mathrm{m}$. The required level of spatial resolution can be met by a next generation experimental setup, which allows to tightly focus the Rydberg laser. Alternatively, a strongly inhomogeneous density distribution of the BEC can provide an almost equally good spatial resolution, as could be shown in this work. The estimated resolution of just below $2\,\mu\mathrm{m}$, achieved in the present setup, could be improved using an atomic trap with higher trapping frequencies.

Cold ion impurity and polaron physics

The experiments presented in this work demonstrated that the role of the positively charged Rydberg core is negligible compared to the impact of the electron. Even though the coupling strength of a charged impurity to a Bose-Einstein condensate is decreasing with its mass m_i roughly as $1/\sqrt{m_i}$, the scattering length is increasing as $\sim\sqrt{m_i}$. For the present case of ^{87}Rb, the electron-atom scattering length is $-16.1\,a_0$, whereas the ion-atom scattering length is expected to be on the order of $5000\,a_0$. This value is roughly twice the mean interparticle distance at typical BEC peak densities. One impurity ion can therefore interact with multiple atoms at the same time. In this regime of many-body interaction, the impurity gets dressed by the surrounding atoms, forming a quasi-particle. These so called polarons play a role in some important phenomena in solid state physics, ranging from the colossal magnetoresistance effect to high-temperature superconductivity [267]. They have been already observed in liquid helium [188, 268] and in ultracold Fermi gases [269, 270, 271, 272]. Ion impurities in Bose-Einstein condensates are discussed as promising candidates to reach a regime of strong coupling, that has been elusive in solid state systems so far [273, 182, 183]. In this regime, mesoscopic molecular ions [181] are expected to be formed, that can be self-trapped in the condensate or even lead to a bosenova-type collapse of the BEC [184]. Current approaches, realizing single ion impurities in Bose-Einstein condensates using ion traps [160, 180], are limited by residual micromotion of the ion in the trap [274]. Thus, the regime of s-wave scattering, as required for strongly coupled polaron physics, could not be reached yet.

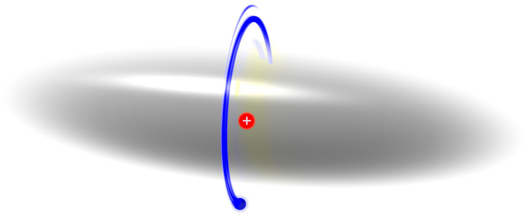

Figure 8.9: Schematic view of a circular Rydberg atom in a Bose-Einstein condensate (grey).

Rydberg excitation in a Bose-Einstein condensate, as presented in this thesis, provide a promising alternative approach. The temperature of the positively charged Rydberg core is mainly determined by the temperature of the atomic cloud and can thus be easily below 1 µK, if the Rydberg atom is excited from an ultracold sample. Since the ionic charge is screened by the Rydberg electron, the Rydberg atom is not accelerated by electric fields. Therefore, no sophisticated ion trapping techniques are required to hold the ion in place for sufficiently long interaction times. However, in the present case of a condensate of rubidium ^{87}Rb atoms in the $5S_{1/2}(F = 2, m_F = 2)$ state, the interaction of the Rydberg electron with the BEC is much larger than any effect that could be expected from the ion. One idea to overcome the effect of the Rydberg electron is based on Rydberg states with high angular momentum along the quantization axis $m_l = l = n - 1$. In such so called circular states, the Rydberg electron is localized on a toroidal Bohr-like orbit around the Rydberg core. At sufficiently large principal quantum numbers n, the Rydberg electron is then located outside the Bose-Einstein condensate. Circular states can be efficiently excited, either using microwave adiabatic transfer [275] or by varying crossed electric and magnetic fields [276].

Another approach would be to increase the interaction strength of the Rydberg core above the one of the Rydberg electron, using e.g. a Feshbach resonance of the $Rb^+ - Rb$ scattering. However, no Feshbach resonance can be expected at least in the present case of atoms in the $m_F = 2$ state and ions created from the same atomic state [277].

Appendix

A Appendix: Theory

In this chapter, additional material is presented in order to further elucidate and substantiate the discussions in chapter 3. It contains explicit calculations and proofs, as well as a benchmark for the numeric calculations in paragraph 3.2.4.

A.1 Rydberg dressing

A.1.1 Eigenenergy of a blockaded N-atom system

The crucial step in order to calculate the energy of a fully blockaded system, consisting of N atoms within one blockade sphere, is the diagonalization of the $(N+1)$-dimensional Hamiltonian H_N (equation 3.7). As stated in paragraph 3.1.2, the characteristic polynomial $\det\left(H_N - \mathbb{1}E\right)$, determining the energy eigenvalues, is given by equation (3.8):

$$\det\left(H_N - \mathbb{1}E\right) = \left[E^2 + h\Delta E - h^2\frac{N\Omega^2}{4}\right]\left(-h\Delta - E\right)^{N-1} \tag{A.1}$$

Now, the proof for this expression is provided by mathematical induction.

For one atom $N = 1$, the statement is obviously true:

$$\det\left(H_1 - \mathbb{1}E\right) = \begin{vmatrix} -E & h\Omega/2 \\ h\Omega/2 & -h\Delta - E \end{vmatrix} = E^2 + h\Delta E - h^2\frac{\Omega^2}{4} \tag{A.2}$$

Setting this polynomial in E equal to zero, one obtains exactly the result of the AC Stark effect of a single atom, as described in paragraph 1.1.3 (cf. equation 1.11). Although redundant for the proof, also the case of two atoms $N = 2$ is shown explicitly:

$$\det\left(H_2 - \mathbb{1}E\right) = \begin{vmatrix} -E & h\Omega/2 & h\Omega/2 \\ h\Omega/2 & -h\Delta - E & 0 \\ h\Omega/2 & 0 & -h\Delta - E \end{vmatrix} = \left[E^2 + h\Delta E - h^2\frac{\Omega^2}{2}\right]\left(-h\Delta - E\right) \tag{A.3}$$

This is to demonstrate that a simple treatment, without any change of basis, leads to the same result as the more elegant calculation in paragraph 3.1.1. There, the asymmetric linear combination of the two singly excited states was eliminated (cf. equation 3.1), as it is not coupled to the ground state by the light field.

It remains to show that the hypothesis (A.1) is true for $N+1$ atoms:

$$
\begin{aligned}
\det\left(H_{N+1}-\mathbb{1}E\right) = & \begin{vmatrix} & & & h\Omega/2 \\ & H_N-\mathbb{1}E & & 0 \\ & & & \vdots \\ h\Omega/2 & 0 & \ldots & -h\Delta-E \end{vmatrix} \\
=&(-h\Delta-E)\det\left(H_N-\mathbb{1}E\right) \\
&+(-1)^{N+1}h\frac{\Omega}{2}\begin{vmatrix} h\Omega/2 & -h\Delta-E & 0 & \dots & 0 \\ h\Omega/2 & 0 & -h\Delta-E & 0 & \vdots \\ \vdots & 0 & \ddots & \ddots & 0 \\ \vdots & \vdots & \ddots & \ddots & -h\Delta-E \\ h\Omega/2 & 0 & \cdots & 0 & 0 \end{vmatrix} \\
=&(-h\Delta-E)\det\left(H_N-\mathbb{1}E\right) \\
&+(-1)^{N+1}h\frac{\Omega}{2}(-1)^{N}h\frac{\Omega}{2}\begin{vmatrix} -h\Delta-E & 0 & \dots & 0 \\ 0 & -h\Delta-E & \ddots & \vdots \\ \vdots & \ddots & \ddots & 0 \\ 0 & \cdots & 0 & -h\Delta-E \end{vmatrix} \\
=&(-h\Delta-E)\det\left(H_N-\mathbb{1}E\right)-h^2\frac{\Omega^2}{4}(-h\Delta-E)^N \\
=&(-h\Delta-E)\left[E^2+h\Delta E-h^2\frac{N\Omega^2}{4}\right](-h\Delta-E)^{N-1}-h^2\frac{\Omega^2}{4}(-h\Delta-E)^N \\
=&\left[E^2+h\Delta E-h^2\frac{(N+1)\Omega^2}{4}\right](-h\Delta-E)^N \\
\equiv&\det\left(H_{N+1}-\mathbb{1}E\right)
\end{aligned}
\tag{A.4}
$$

In the third last line, the induction hypothesis (A.1) has been inserted in order to show that, indeed, the identity for $\det\left(H_{N+1}-\mathbb{1}E\right)$ holds.

Q.E.D.

The energy eigenvalues resulting from the characteristic polynomial (A.1) are:

$$E_{1/2} = \frac{h}{2}\left(\pm\sqrt{N\Omega^2+\Delta^2}-\Delta\right) \tag{A.5}$$

$$E_{3,\dots,-N+1} = -h\Delta \tag{A.6}$$

The ground state of the system has thus the energy

$$E_1 = \frac{h}{2}\left(-\sqrt{N\Omega^2+\Delta^2}-\Delta\right) \tag{A.7}$$

This is the result (3.9), stated in paragraph 3.1.2 for red detuing $\Delta < 0$.

A.2 Creation of Bogoliubov excitations

In this section, some additional details on the treatment of a Rydberg electron in a Bose-Einstein condensate are given. This comprises some elementary calculations required for the perturbative treatment in paragraph 2.3.1, as well as a comparison of the numerical calculations, used in this work, to the analytical results in [171].

A.2.1 Interaction operator in momentum representation

Expressing the scattering potential $V_{\text{scat}}(\vec{r})$ in the Hamiltonian (3.45) by its Fourier components $V_{\text{scat}}(\vec{k})$, one obtains

$$\hat{H}_{\text{int}} = \int \rho(\vec{r}) \frac{1}{V} \sum_{\vec{k}} V_{\text{scat}}(\vec{k}) e^{i\vec{k}\vec{r}/\hbar} s(t)\, d\vec{r} \tag{A.8}$$

Here, the symmetry of the scattering potential $V_{\text{scat}}(\vec{r})$ (see paragraph 3.2.2) has been exploited to obtain simpler expressions[1]. Since the summation runs over all momenta $\vec{k}$, one can flip the sign of $\vec{k}$. The symmetry of the scattering potential $V_{\text{scat}}(\vec{r})$ also translates into the Fourier space and with $V_{\text{scat}}(\vec{k}) = V_{\text{scat}}(-\vec{k})$, one can write equation (A.8) as:

$$\hat{H}_{\text{int}} = \frac{1}{V} \sum_{\vec{k}} \int \rho(\vec{r}) e^{-i\vec{k}\vec{r}/\hbar}\, d\vec{r}\, V_{\text{scat}}(\vec{k}) s(t) \tag{A.9}$$

Introducing the Fourier components $\rho_{\vec{k}}$ [173] of the atomic density (see equation 3.46) immediately leads to the expression in equation (3.47):

$$\hat{H}_{\text{int}} = \frac{1}{V} \sum_{\vec{k},\vec{p}} \hat{a}^{\dagger}_{\vec{p}-\vec{k}} \hat{a}_{\vec{p}}\, V_{\text{scat}}(\vec{k}) s(t) \tag{A.10}$$

A.2.2 Interaction operator in Bogoliubov operators

The result, derived in the previous paragraph A.2.1 for the interaction Hamiltonian $\hat{H}_{\text{int}}$, can also be written in terms of creation and annihilation operators of Bogoliubov excitations by inserting the transformation (2.20) into equation (A.10). In the ground state, the lowest mode $\vec{p} = 0$ is macroscopically occupied and the particle creation and annihilation operators can be approximated by $\hat{a}_0^{\dagger} \approx \hat{a}_0 \approx \sqrt{N_0}$ (see section 2.1). Applying the interaction operator $\hat{H}_{\text{int}}$ onto the ground state $|0\rangle$ and separating the terms with zero momentum out of the sum in equation (3.47)

---

[1] This step is only performed in order to match the notation in [171] and is later reversed in the calculation of equation (3.49).

leads to:

$$\begin{aligned}
\hat{H}_{\text{int}}\,|0\rangle &= \frac{1}{V}\sum_{\vec{k},\vec{p}} \hat{a}^{\dagger}_{\vec{p}-\vec{k}}\hat{a}_{\vec{p}}\,V_{\text{scat}}(\vec{k})s(t)\,|0\rangle \\
&= \frac{1}{V}\left[N_0 V_{\text{scat}}(0) + \sum_{\vec{k}\neq 0}\sqrt{N_0}V_{\text{scat}}(\vec{k})\hat{a}^{\dagger}_{\vec{k}} + \sum_{\vec{p}\neq 0}\sqrt{N_0}V_{\text{scat}}(\vec{p})\hat{a}_{\vec{p}}\right. \\
&\qquad \left. + \sum_{\vec{p}\neq 0,\vec{k}\neq\vec{p}} V_{\text{scat}}(\vec{k})\hat{a}^{\dagger}_{\vec{p}-\vec{k}}\hat{a}_{\vec{p}}\right] s(t)\,|0\rangle \\
&= \frac{1}{V}\left[N_0 V_{\text{scat}}(0) + \sum_{\vec{k}\neq 0}\sqrt{N_0}V_{\text{scat}}(\vec{k})(u_k+v_k)\hat{b}^{\dagger}_{\vec{k}} + \sum_{\vec{p}\neq 0,\vec{k}\neq\vec{p}} V_{\text{scat}}(\vec{k})u_{p-k}v_p\hat{b}^{\dagger}_{\vec{p}-\vec{k}}\hat{b}_{\vec{p}}\right. \\
&\qquad \left. + \sum_{\vec{p}\neq 0} V_{\text{scat}}(0)|v_p|^2\right] s(t)\,|0\rangle
\end{aligned} \tag{A.11}$$

In the last step, equation (2.30) and the commutation relation of the Bogoliubov operators (see paragraph 2.3.1) have been used. The second-last term describes processes, where two quasi-particles are excited simultaneously. The first and last term lead only to a constant energy shift:

$$\langle 0|\,\hat{H}_{\text{int}}\,|0\rangle\,/s(t) = \frac{1}{V}V_{\text{scat}}(0)\left(N_0 + \sum_{\vec{p}\neq 0}|v_p|^2\right) = \overline{V}_{\text{scat}}N \tag{A.12}$$

Here, the total atom number N, including the quantum depletion (see equation 2.35), and the mean scattering potential $\overline{V}_{\text{scat}} = 1/V\int V_{\text{scat}}(\vec{r})d\vec{r} = V_{\text{scat}}(\vec{k}=0)/V$ have been identified in order to recover the energy shift, obtained already in paragraph 3.2.3, using the central limit theorem [170]. Neglecting this constant shift and the second order term, the relevant part of the interaction Hamiltonian can finally be written as:

$$\hat{H}_{\text{int}}/s(t) = \frac{\sqrt{N_0}}{V}\sum_{\vec{q}\neq 0} V_{\text{scat}}(\vec{q})\left(u_q - v_q\right)\left(\hat{b}^{\dagger}_{\vec{q}} - \hat{b}_{-\vec{q}}\right) \tag{A.13}$$

Here, a zero term (see equation 2.30) has been added. In this form, the result is equivalent to the one given in [171].

A.2.3 Numerical vs. analytical calculation

The calculations of the number of atoms ΔN affected by the excitation of a Rydberg atom in paragraph 3.2.4 are performed numerically, based on the Rydberg electron wavefunctions from [79]. However, an analytical solution is possible, if one neglects terms to higher order in the electron momentum in the electron-atom scattering potential (see paragraph 3.2.2). Then, an analytical expression of the Fourier transformed probability density of the Rydberg electron

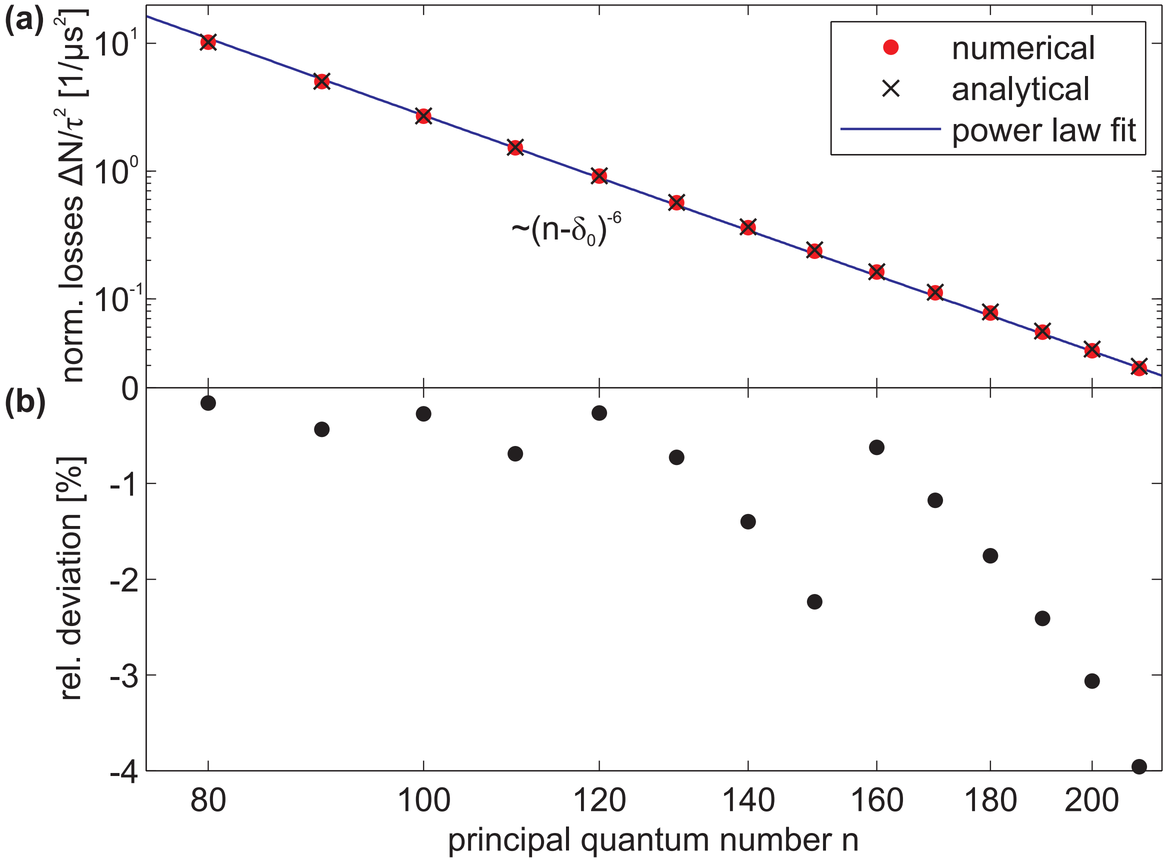

Figure A.1: Comparison of numerical and analytical [171, 177] calculation of atom losses induced by Bogoliubov excitation. In (a), the number ΔN of atoms lost from a condensate, caused by one Rydberg excitation, is shown for different principal quantum numbers n. A homogeneous condensate density of $\rho = 8.6 \cdot 10^{13}\,\mathrm{cm}^{-3}$ over the size of the Rydberg atom is assumed. In both calculations, the integration has been cut at momenta smaller than $q = 4.9 \cdot 10^5\,\hbar/m \approx 0.13\,\hbar/\xi$ (see discussion in paragraph 3.2.4 and section 8.1). As in Figure 8.2, the number ΔN of lost atoms is normalized onto the lifetime squared τ^2 of the Rydberg state in the BEC, which is here kept fixed at a constant value of $\tau = 10\,\mu\mathrm{s}$. Both the numerical (red dots) and the analytical solution (black crosses) are consistent with a $(n - \delta_0)^{-6}$ scaling (blue line). The relative deviation of the numerical result from the analytical solution is shown in (b).

in the limit of large principal quantum numbers n can be used [177]. In order to benchmark the numerical evaluation, the results to zeroth order in the electron momentum are compared to the results of an analytical calculation in Figure A.1. Both curves largely comply with a $(n - \delta_0)^{-6}$ power law. The two results agree within a few percent; at low principal quantum numbers n, the difference is even less than one percent. The deviation at higher n is caused by the fact that the overall result there becomes very small and hence the relative error increases. However, even in this regime, the error is way below the corrections to the scattering potential, linear in the electron momentum, and below the experimental uncertainty.

B Appendix: Experiment

In this chapter, additional experimental data and different evaluations of the measurements discussed in part III are presented. Section B.1 contains data on Rydberg dressing, measured in various parameter regimes in order to further confirm the conclusions drawn in chapter 6. Section B.2 is mostly focused on complimentary evaluations of the data, which is discussed in chapters 7 and 8, but includes also some additional measurements. While not absolutely necessary for the line of thought, this information provides significant confirmation of the reasoning in the main text.

B.1 Rydberg dressing

In this section, additional measurements on dressing a Bose-Einstein condensate with different Rydberg S-states (paragraph B.1.1) and a Rydberg D-state close to a Förster resonance (paragraph B.1.2) are shown. These results agree qualitatively with the results in chapter 6. However, they further demonstrate that it is not possible to observe a significant effect of Rydberg dressing with the current apparatus, even in different parameter regimes.

B.1.1 Rydberg dressing with S-states

In section 6.1, the weak dressing of a Bose-Einstein condensate with different Rydberg S-states was discussed. For the measurements presented in Figure 6.1, a relatively long sequence, lasting $t = 100\,\mathrm{ms}$, was chosen to allow for the dressed BEC to reach its ground state. In this case, the Rabi frequency Ω close to resonance of the Rydberg state is limited by the decay of the dressed state. In first approximation, the number of lost atoms then scales as $\Gamma_r \Omega^2 t^2$ (see paragraph 1.1.2), where Γ_r is the decay rate of the particular Rydberg state. Alternatively, one can also apply a relatively short Rydberg excitation pulse. Then, much larger Rabi-frequencies can be realized, at which there is a significant change of the Rydberg dressed ground state of the BEC predicted from the calculations in paragraph 3.1.4. However, this treatment only describes the ground state of the system and it is not clear yet, how strong effects can be expected in an experiment, where the Rydberg dressing potential is only pulsed for a very short time. Nevertheless, one can presume a momentum transferred onto the atomic cloud, that finally leads to a deformation during time of flight. In Figure B.1, the result of measurements with a short dressing laser pulse are shown. In this sequence, the blue Rydberg laser is switched on adiabatically (see section 4.1), before the red Rydberg laser is turned on as a square pulse for $1\,\mathrm{ms}$. The Rabi frequency was chosen such that the total atom losses from the BEC do not exceed 50%. In contrast to the measurements with a longer sequence (see Figure 6.1), there is no loss feature

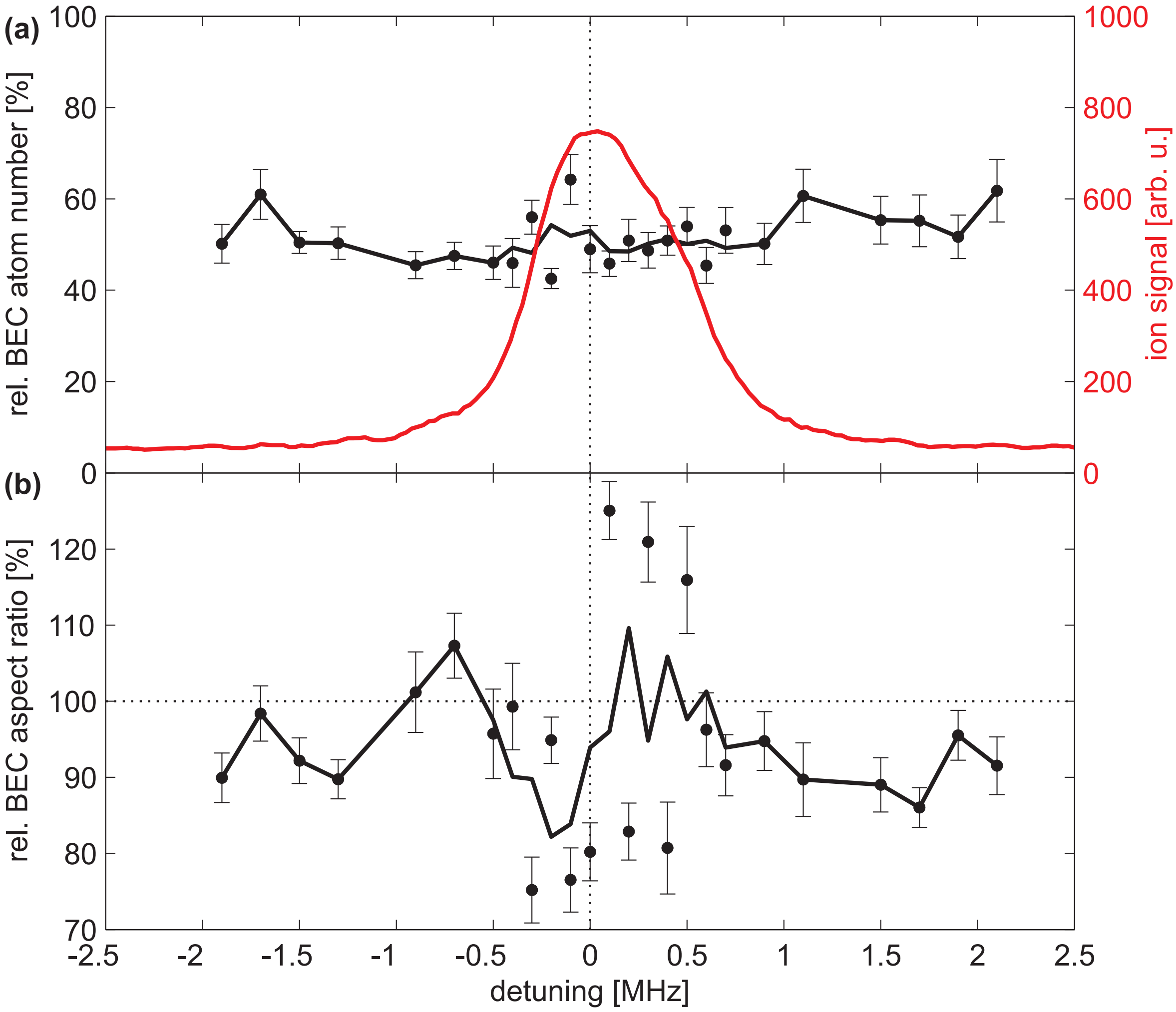

Figure B.1: Dressing a repulsive Rydberg S-state to a Bose-Einstein condensate. The condensate, consisting of $2 \cdot 10^4$ atoms, is dressed for 1 ms at fixed Rabi frequency $\Omega = 23.3\,\mathrm{kHz}$ and variable detuning Δ to the $32S$ Rydberg state. The relative change of BEC atom number (a) and aspect ratio (b) was extracted from absorption images, taken after a time of flight of 50 ms. In (a), additionally the ion signal from reference measurements in a thermal sample is shown (excitation pulse length 2 µs). The solid black lines are a moving average (spectral resolution ~0.3 MHz) as a guide to the eye.

visible in the BEC atom number. Obviously, the decay from the Rydberg state does not play a role any more; the Rabi frequency Ω is only limited by the atom losses created by off-resonant scattering from the intermediate $5P_{3/2}$ state (see section 5.1). This results from the fact that this process is only scaling linear with the pulse length t. Combining equations (5.1) and (1.15), the total atom loss ΔN_{loss} can be expressed in terms of the decay rate Γ_p of the intermediate state, the two-photon Rabi frequency Ω, and the Rabi frequency Ω_b driving the upper transition (cf. discussion in section 7.3 and paragraph B.2.1):

$$\Delta N_{\mathrm{loss}} \sim \Gamma_{\mathrm{scat}} t = \Gamma_p \frac{\Omega^2}{\Omega_b^2} t \tag{B.1}$$

Even though there seems to be some effect visible in the aspect ratio, the noise level is too high to provide a definite result. Anyway, most applications of Rydberg dressing (see chapter 6) require longer experimental sequences to allow for the system to reach its ground state.

B.1.2 Rydberg dressing with D-states

In this paragraph, additional measurements on dressing a Bose-Einstein condensate with a Rydberg state close to a Förster resonance are shown. This comprises measurements at different

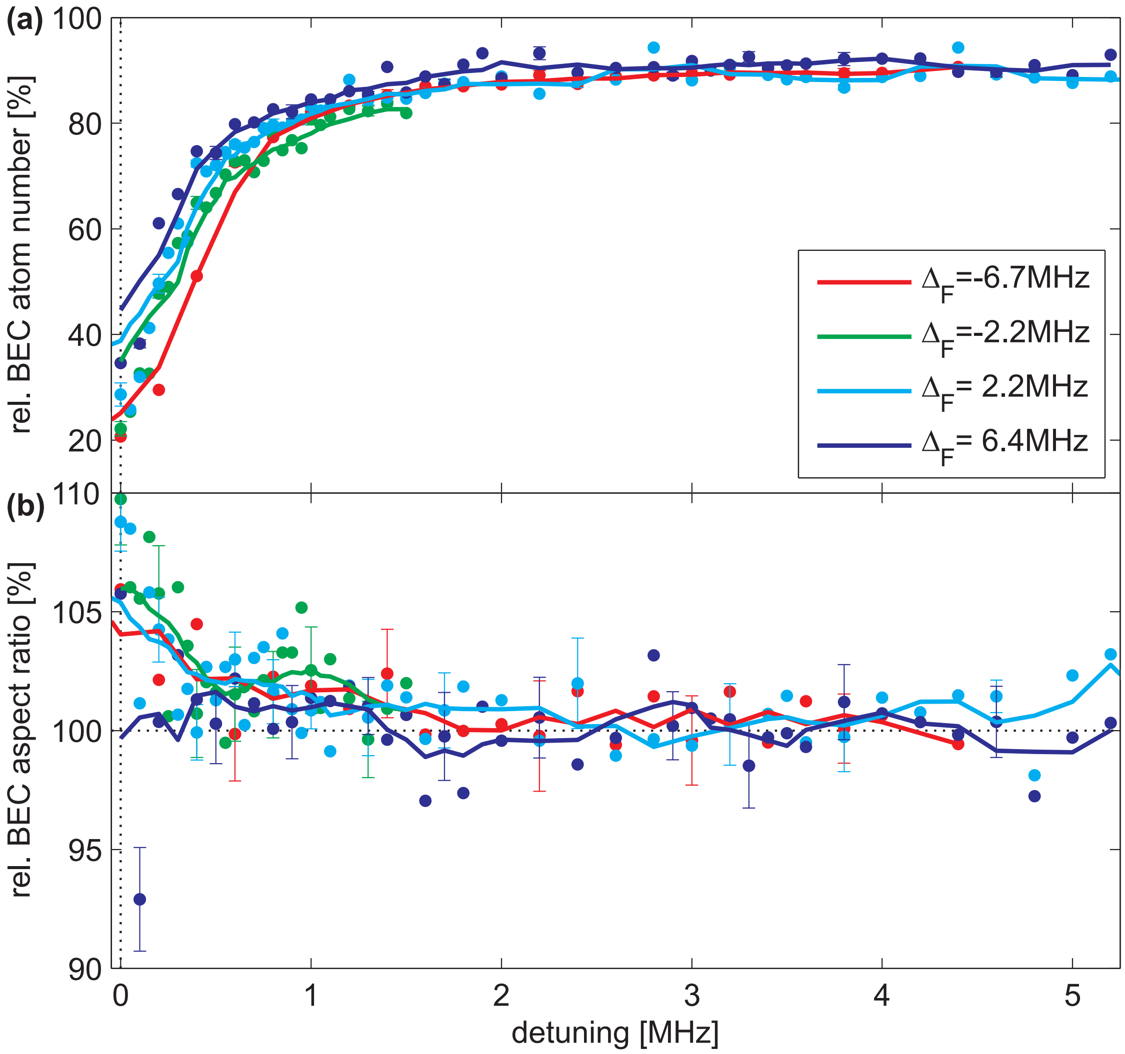

Figure B.2: Dressing of a Rydberg D-state to a Bose-Einstein condensate. The condensate, consisting of $8 \cdot 10^4$ atoms, is dressed for 100 ms at fixed Rabi frequency $\Omega = 2.6\,\text{kHz}$ and variable detuning Δ to the $44D_{5/2}$, $m_F = 5/2$ Rydberg state for different Förster defects Δ_F. The relative change of the BEC atom number (a) and the aspect ratio (b) was extracted from absorption images, taken after a time of flight of 50 ms. The solid lines are a moving average (spectral resolution ~0.5 MHz) as a guide to the eye.

Förster defects Δ_F (see Figure B.2) and different sequence lengths (see Figure B.3). The additional data further confirms the conclusions drawn in section 6.2. That is, there is no effect of Rydberg dressing observed above the noise level.
In particular, the results for all Förster defects Δ_F in Figure B.2 seem to agree within the experimental error. Only one single data point at a Förster defect of $\Delta_F = 6.4\,\mathrm{MHz}$ and low laser detuning Δ seems to deviate. This point, however, seems to be clearly an outlier without any significance.
Also the measurements for different sequence lengths in Figure B.3 largely agree, at least qual-

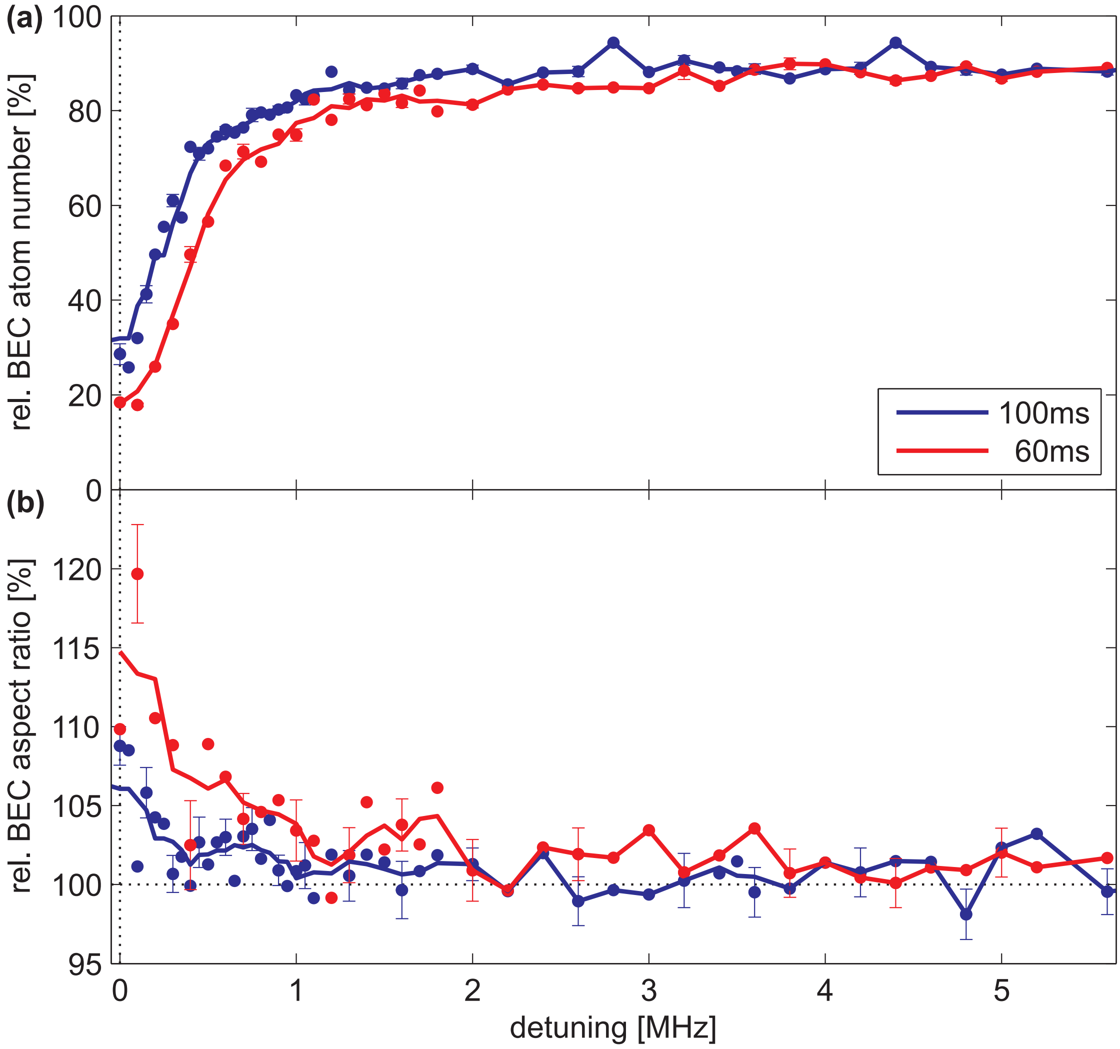

Figure B.3: Dressing of a Rydberg D-state to a Bose-Einstein condensate. The condensate, consisting of $8 \cdot 10^4$ atoms, is dressed for 100 ms and 60 ms respectively at variable detuning Δ to the $44D_{5/2}$, $m_F = 5/2$ Rydberg state for a Förster defect of $\Delta_F = 2.2\,\mathrm{MHz}$. The Rabi frequencies $\Omega = 2.6\,\mathrm{kHz}\,/3.4\,\mathrm{MHz}$ have been adjusted to the pulse lengths. The relative change of the BEC atom number (a) and the aspect ratio (b) was extracted from absorption images, taken after a time of flight of 50 ms. The solid lines are a moving average (spectral resolution ~0.5 MHz) as a guide to the eye.

itatively. The slightly higher losses on resonance for the shorter sequence are caused by the different Rabi frequency. The change in aspect ratio at low detunings, also visible in Figure B.2, is presumably connected to the strong atom loss at red detuning. As already discussed in section 6.2, this effect is most likely not connected to Rydberg dressing.

B.2 High Rydberg states in a BEC

This section contains additional material connected to chapters 7 and 8. Further evaluations (paragraphs B.2.1 and B.2.4) and complementary approaches for the interpretation of the data (paragraph B.2.2) are shown, together with additional data (paragraphs B.2.3 and B.2.5), for the sake of completeness.

B.2.1 Atom losses due to light scattering

In section 7.3, measurements of the BEC atom losses, induced by spontaneous scattering of photons via the intermediate $5P_{3/2}$ state, are presented for different pulse areas Ωt (see Figure 7.8b). In Figure B.4, these losses are plotted versus the calculated probability $\Gamma_{\text{scat}} t$ for a

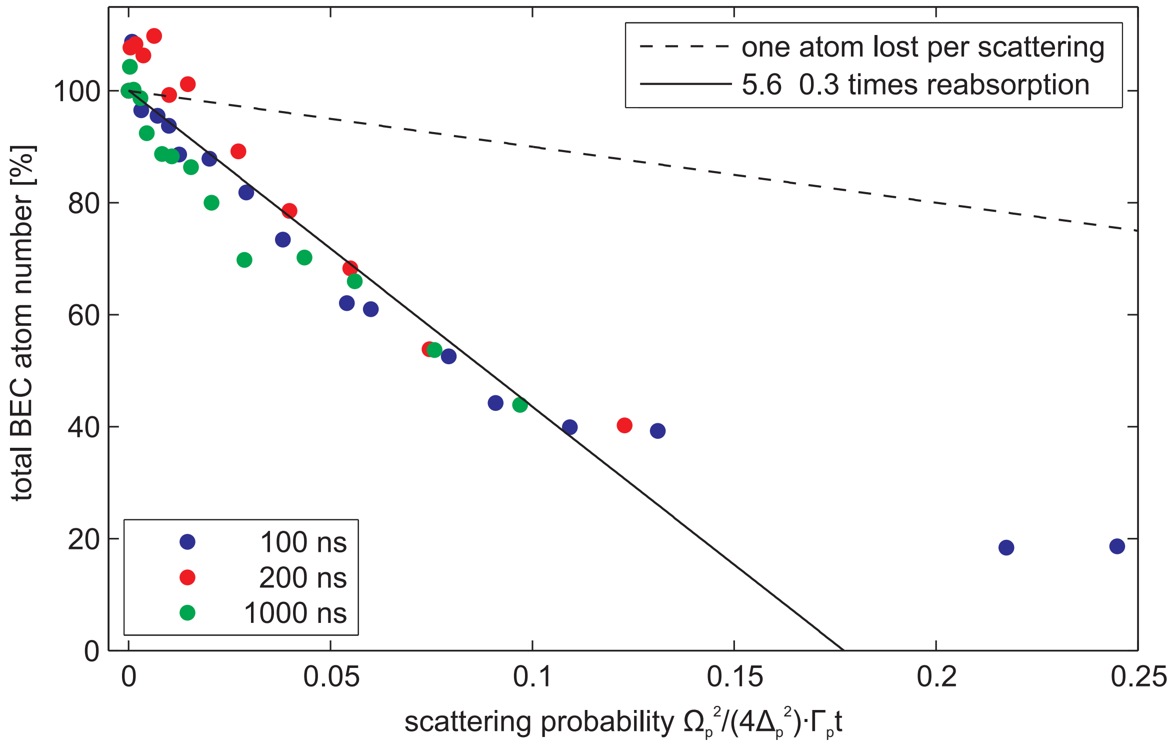

Figure B.4: Atom losses due to scattering from the intermediate P-level. The data from Figure 7.8 is shown versus the calculated probability for an atom to scatter a photon of the red Rydberg laser. The black dotted line assumes that one scattered photon leads to exactly one atom lost. The black solid line is a linear fit.

scattering event. As expected, the data points taken at different excitation pulse lengths collapse on one single line, except for few points at the highest atom losses. The fitted slope of this line (solid line) is (5.6 ± 0.3) times higher than expected if one assumes that every scattering event leads to exactly one atom lost (dotted line). This can be explained by reabsorption of scattered photons within the condensate. The mean free path of a fluorescence photon can be estimated as $l = 1/(\sigma_0\rho)$, using the free space absorption cross section $\sigma_0 \approx 4\pi/k_0^2$ [278]. For the wavelength $\lambda = 780\,\text{nm}$ of the D_2 line and a BEC peak density of $\rho = 10^{14}\,\text{cm}^{-3}$, this results in a mean free path of around $l = 52\,\text{nm}$, which is much smaller than the size of the condensate. This simple calculation clearly overestimates the effect of reabsorption. Light scattering not necessarily happens in the condensate or directed to the centre of the condensate and the cross section σ_0 drops very quickly proportional to the atomic density ρ towards the edge of the BEC. However, it seems probable that, on average, a few reabsorption events will take place. Only for larger atom losses, the size of the condensate is reduced so much that there is a deviation from the linear dependence, explaining the observation shown in Figure B.4.

B.2.2 BEC atom losses due to classical electron atom scattering

A classical approach to explain the losses of BEC atoms observed in time of flight imaging in section 8.1 is based on the scattering of the electron and the BEC atoms, similar to the treatment of a single ion impurity [160]. The expression of the scattering rate Γ_{scat} is already given in equation (7.3) in the context of the broadening of the Rydberg line, measured in the condensate (see paragraph 7.1.2). In a classical picture, it is reasonable to assume that every single scattering event leads to an atom loss, since the energy transferred in an elastic collision (see footnote 2 on page 101) is much larger than the chemical potential $\mu = 745\,\text{Hz}$ of the condensate. As in paragraph 7.1.1, the Rydberg atom is assumed to be localized in the centre of the condensate and the Thomas-Fermi density distribution of the BEC is taken into account. The interaction time is limited both due to the finite Rydberg lifetime τ (see paragraph 7.2.1) and the experimental sequence, where any Rydberg atom is extracted after a fixed time $t_d = 10\,\mu\text{s}$ (see paragraph 5.3.2). Therefore, the number N_{scat} of scattering events per Rydberg excitation reads:

$$N_{\text{scat}} = \int_0^{t_d} \Gamma_{\text{scat}} e^{-t/\tau}\, dt = \Gamma_{\text{scat}}\tau \left(1 - e^{-t_d/\tau}\right) \tag{B.2}$$

The result using the energy-independent scattering length $a = -16.1\,a_0$ [157] is shown in Figure B.5. The overall trend and order of magnitude match, but do not reproduce the measured data at higher principal quantum numbers n. This is not very surprising, since the classical picture of the Rydberg electron, transferring energy onto the atoms while slowly decaying back to the ground state, turned out to be wrong in paragraph 7.2.2.

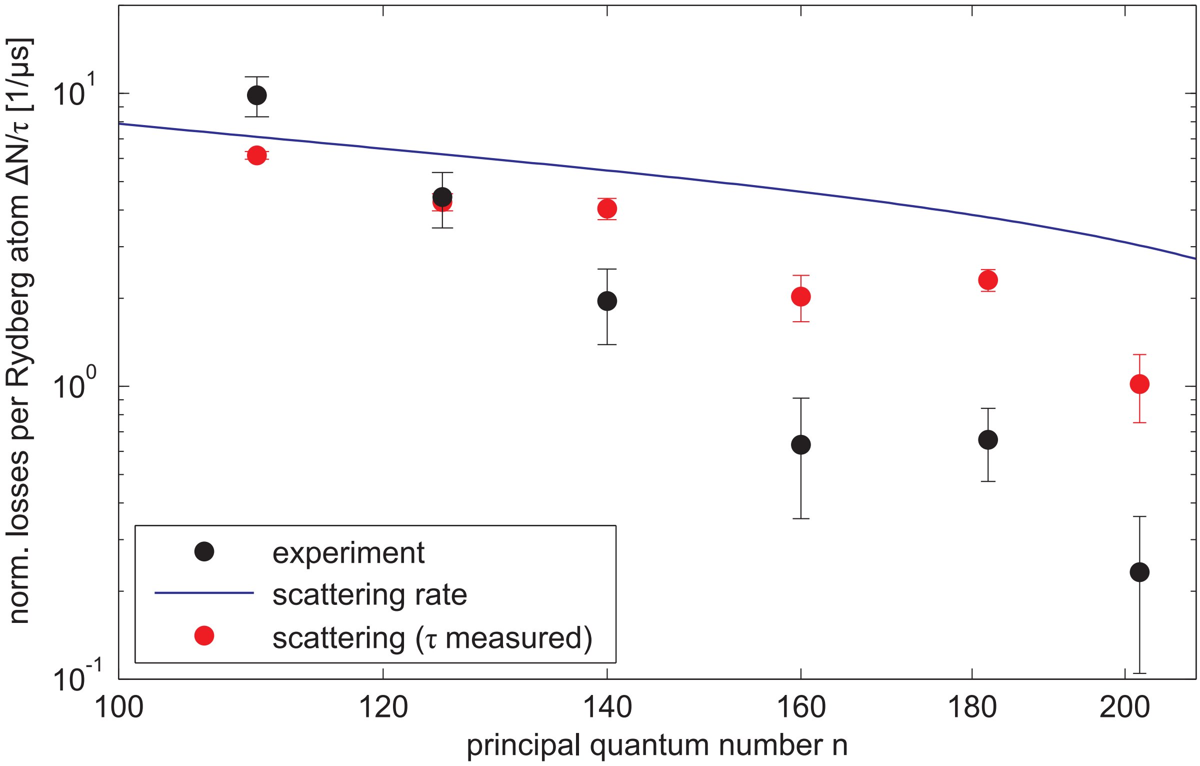

Figure B.5: Rydberg induced BEC atom loss after time of flight for different principal quantum numbers n. The maximum atom loss per Rydberg excitation is normalized onto the lifetime τ of the Rydberg state in the BEC (both quantities from Table 8.1. These values are corrected for the loss by the field ionization of the Rydberg atom). The calculated scattering rate Γ_{scat} (blue solid line) and the number of scattering events, taking the measured lifetime into account (red squares), cannot reproduce the experimental observations for higher Rydberg states.

B.2.3 BEC atom losses for different sequence lengths

For the modelling of the BEC atom losses in section 8.1, the condensate is assumed to be in its ground state at the beginning of each Rydberg excitation. In the experiment, this is certainly not the case, since already the first Rydberg excitation creates excitations persistent in the condensate. However, one can estimate whether this approximation will cause some crucial deviation. A good indication, that one can neglect excitations already present in the condensate, can be obtained experimentally by measuring the BEC atom loss in time of flight imaging for different numbers of Rydberg excitations in one sequence. This was done exemplarily for the $110S$ Rydberg state (see Figure B.6). Since this measurement was taken at $5\,\%$ lower Rabi frequency than the spectroscopic measurements in Figure 7.2, the fitted atom loss per Rydberg excitation is with 26.2 ± 2.3 slightly lower than in the measurements in section 8.1. However, the losses are still linear for up to 400 Rydberg excitations in one condensate, which is much larger than the number of pulses used for the measurement of the spectral line of this Rydberg state in Figure 7.2. This provides experimental evidence that, within the current experimental error, effects of quasiparticle excitations already present in the condensate can be neglegted in good approximation.

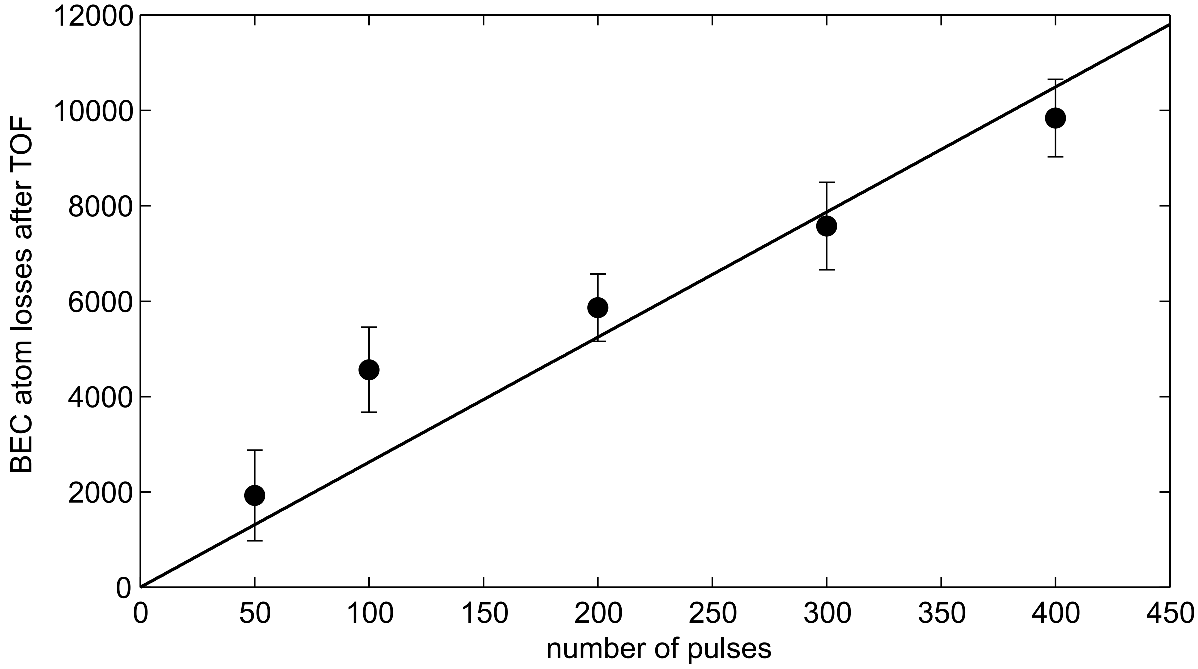

Figure B.6: Absolute BEC atom losses in time of flight imaging for different number of pulses. The laser detuning was kept fixed at $-11.4\,\mathrm{MHz}$ to the $110S$ state, close to the maximum of the BEC atom loss. The Rabi frequency was around $5\,\%$ smaller than the one for the spectroscopic measurements in Figure 7.2. The solid line is a linear fit with slope 26.2 ± 2.3 atoms per Rydberg excitation light pulse.

B.2.4 Absolute BEC atom losses

In section 8.1, the BEC atom loss in time of flight imaging is plotted normalized to the squared lifetime τ^2 of the Rydberg states (see Figure 8.2). This way, the uncertainty in the measured lifetime τ of the Rydberg states translates mostly into the experimental data. For comparison, here the absolute BEC atom losses are shown in Figure B.7. Even though the theory data now show large errorbars, it becomes obvious that the corrections linear in the electron momentum k in the scattering potential (see paragraph 3.2.2) indeed play a significant role. At low principal quantum numbers n, they lead to much better agreement with the experimental data. Furthermore, the calculated contribution of excitations in the phonon regime, at quasi-momenta $q < \hbar/\xi$, to the observed atom losses is indicated. Consistent with the results discussed in paragraph 3.2.4, the fraction is on the order of 50%.

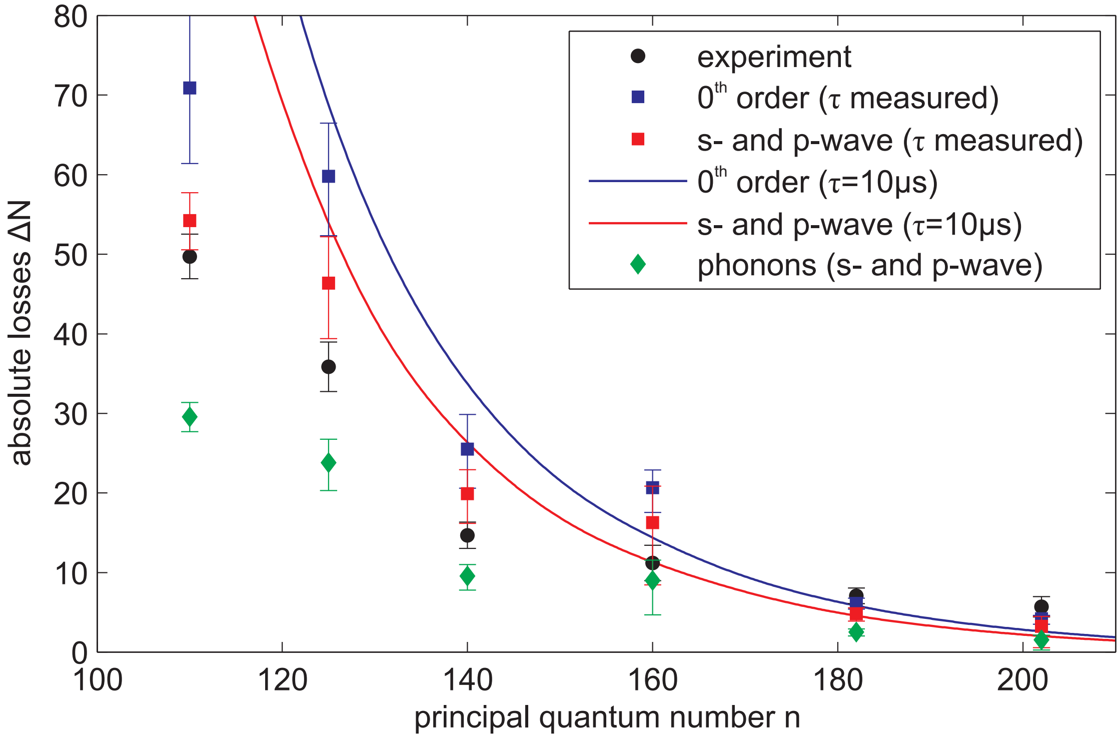

Figure B.7: Absolute Rydberg induced BEC atom loss after time of flight for different principal quantum numbers n. The losses are corrected for the loss by field ionization of the Rydberg atom and normalized on the peak density. Theory values taking the measured lifetime τ into account (squares) and assuming a constant lifetime of $\tau = 10\,\mu s$ (solid lines) are shown, both in the approximation to zeroth order in the electron momentum k (blue) and taking terms up to linear in k into account (red). Furthermore, the calculated contribution of phonon excitations including s- and p-wave scattering is indicated (green diamonds).

B.2.5 Induced BEC shape oscillations

As mentioned in paragraph 8.2.2, the switching of the red Rydberg laser alone creates a BEC shape oscillation due to the momentum transfer by off-resonant scattering (see also appendix B.2.3). Additional reference measurements, where the blue Rydberg laser is detuned by more than $40\,\mathrm{MHz}$, allow to extract the pure effect of the Rydberg excitation onto the condensate as shown in Figure 8.5. The underlying raw data is plotted in Figure B.8. It becomes obvious that the effect of the Rydberg excitation, while being clear and considerable, is small compared to the effect of the off-resonant red laser light. This makes the interpretation not straightforward and probably hinders the observation of any mechanical effects beyond collective oscillations of the condensate. Since the detuning to the intermediate $5P_{3/2}$ is constantly $500\,\mathrm{MHz}$ throughout all measurements, the amplitude of the reference oscillation is determined only by the power of the red Rydberg laser. This value was adjusted for each Rydberg state in the procedure described in section 8.1.

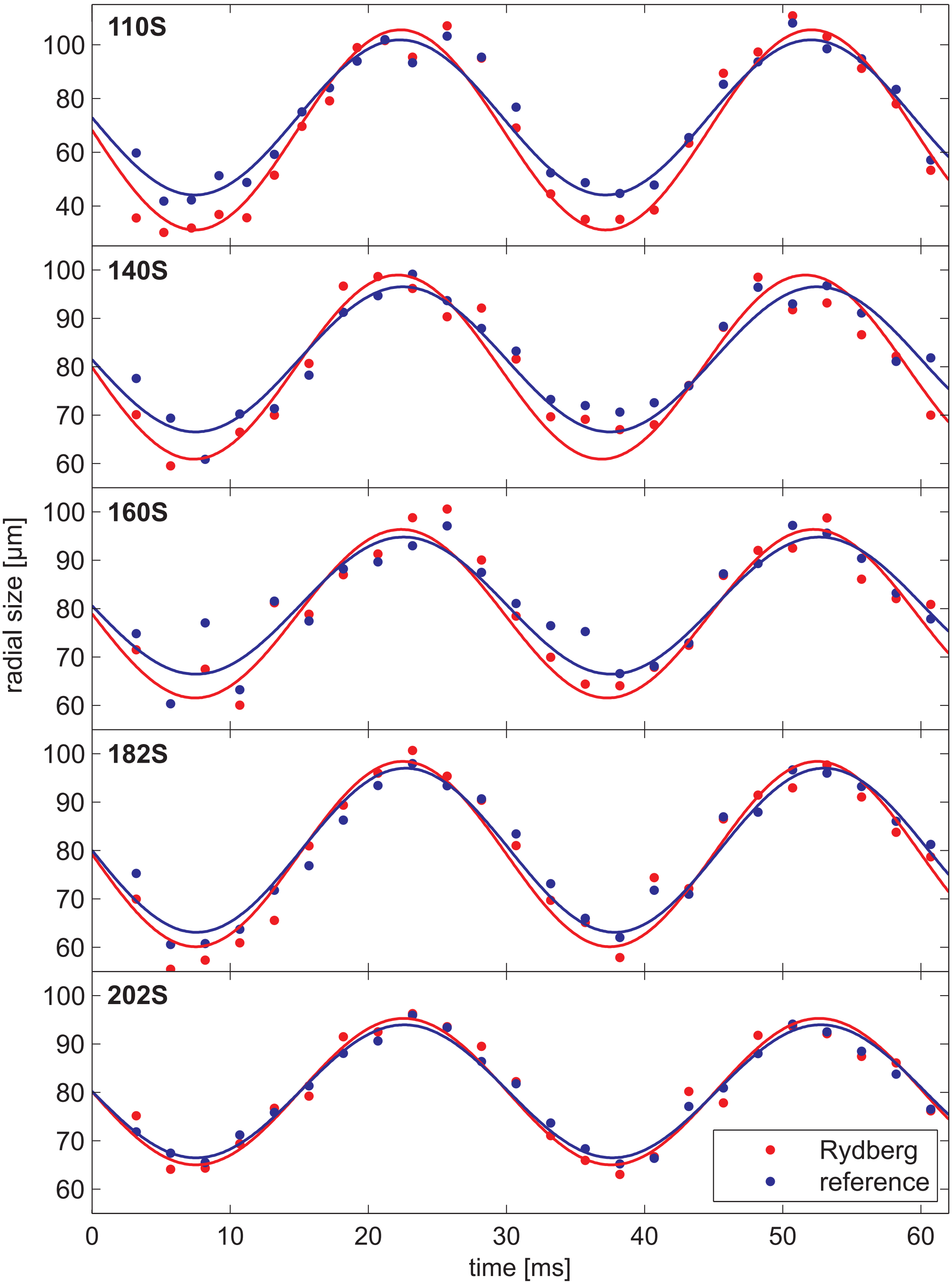

Figure B.8: Shape oscillations of the BEC induced different Rydberg states. The radial size of the condensate (Thomas-Fermi radius) was measured for different hold times in the trap and different Rydberg states. Both measurements with Rydberg excitation (red) and with detuned lasers (blue) for reference are shown. The sequence of 200 Rydberg excitations lasts from 0 ms to 3.2 ms.

Bibliography

[1] S. Haroche, *Nobel lecture: Controlling photons in a box and exploring the quantum to classical boundary*, Rev. Mod. Phys., **85**, 1083–1102 (2013).

[2] E. Amaldi and E. Segrè, *Effect of pressure on high terms of alkaline spectra*, Nature, **133**, 141 (1934).

[3] E. Amaldi and E. Segrè, *Effetto della pressione sui termini elevati degli alcalini*, Nuovo Cimento, **11**, 145–156 (1934).

[4] M. H. Anderson, J. R. Ensher, M. R. Matthews, C. E. Wieman and E. A. Cornell, *Observation of Bose-Einstein condensation in a dilute atomic vapor*, Science, **269**, 198–201 (1995).

[5] K. B. Davis, M. O. Mewes, M. R. Andrews, N. J. van Druten, D. S. Durfee, D. M. Kurn and W. Ketterle, *Bose-Einstein condensation in a gas of sodium atoms*, Phys. Rev. Lett., **75**, 3969–3973 (1995).

[6] I. Bloch, J. Dalibard and S. Nascimbène, *Quantum simulations with ultracold quantum gases*, Nature Physics, **8**, 267–276 (2012).

[7] M. Saffman, T. G. Walker and K. Mølmer, *Quantum information with Rydberg atoms*, Rev. Mod. Phys., **82**, 2313–2363 (2010).

[8] J. Honer, H. Weimer, T. Pfau and H. P. Büchler, *Collective many-body interaction in Rydberg dressed atoms*, Phys. Rev. Lett., **105**, 160404 (2010).

[9] J. E. Johnson and S. L. Rolston, *Interactions between Rydberg-dressed atoms*, Phys. Rev. A, **82**, 033412 (2010).

[10] J. Nipper, J. B. Balewski, A. T. Krupp, S. Hofferberth, R. Löw and T. Pfau, *Atomic pair-state interferometer: Controlling and measuring an interaction-induced phase shift in Rydberg-atom pairs*, Phys. Rev. X, **2**, 031011 (2012).

[11] J. Nipper, *Interacting Rydberg atoms: Coherent control at Förster resonances and polar homonuclear molecules*, Ph.D. thesis, Universität Stuttgart (2012).

[12] V. Bendkowsky, B. Butscher, J. Nipper, J. P. Shaffer, R. Löw and T. Pfau, *Observation of ultralong-range Rydberg molecules*, Nature, **458**, 1005–1008 (2009).

[13] V. Bendkowsky, *Ultralong-range Rydberg molecules: Invesitagion of a novel binding*, Ph.D. thesis, Universität Stuttgart (2010).

[14] E. Fermi, *Sopra lo spostamento per pressione delle righe elevate delle serie spettrali*, Nuovo Cimento, **11**, 157–166 (1934).

[15] N. N. Bogoliubov, *On the theory of superfluidity*, J. Phys. (USSR), **11**, 23 (1947).

[16] J. Fraunhofer, *Bestimmung des Brechungs- und Farbenzerstreuungs-Vermögens verschiedener Glasarten, in Bezug auf die Vervollkommnung achromatischer Fernrohre*, Denkschriften der Königl. Akademie der Wissenschaften zu München, **5**, 193–226 (1814-15).

[17] N. Bohr, *On the Constitution of Atoms and Molecules*, Phil. Mag. Series 6, **26**, 1–25 (1913).

[18] H. E. White, *Introduction to Atomic Spectra*, McGraw-Hill Book Company, Inc., New York and London (1934).

[19] G. J. Stoney, *On the cause of the interrupted spectra of gases*, Phil. Mag. Series 4, **41**, 291–296 (1871).

[20] A. Schuster, *On harmonic ratios in the spectra of gases*, Proc. Roy. Soc. London, **31**, 337–347 (1881).

[21] J. J. Balmer, *Notiz über die Spektrallinien des Wasserstoffs*, Annalen der Physik, **25**, 80–87 (1885).

[22] W. N. Hartley, *On homologous spectra*, J. Chem. Soc., Trans., **43**, 390–400 (1883).

[23] J. R. Rydberg, *On the structure of the line-spectra of the chemical elements*, Phil. Mag. Series 5, **29**, 331–337 (1890).

[24] G. D. Liveing and J. Dewar, *On the spectra of sodium and potassium*, Proceedings of the Royal Society of London, **29**, 398–402 (1879).

[25] A. R. P. Rau and M. Inokuti, *The quantum defect: Early history and recent developments*, American Journal of Physics, **65**, 221–225 (1997).

[26] T. Lyman, *The spectrum of hydrogen in the region of extremely short wave-lengths*, Astrophysical Journal, **23**, 181 (1906).

[27] F. Paschen, *Zur Kenntnis ultraroter Linienspektra. I. (Normalwellenlängen bis 27000 Å.-E.)*, Annalen der Physik, **332**, 537–570 (1908).

[28] M. Planck, *Über das Gesetz der Energieverteilung im Normalspektrum*, Annalen der Physik, **309**, 553–563 (1901).

[29] J. Mehra and H. Rechenberg, *The Historical Development of Quantum Theory*, Springer, New York (2001).

[30] A. Sommerfeld, *Zur Quantentheorie der Spektrallinien*, Annalen der Physik, **356**, 1–94 (1916).

[31] R. W. Wood, *The complete Balmer series in the sodium spectrum*, Astrophysical Journal, **29**, 97 (1909).

[32] M. L. Zimmerman, M. G. Littman, M. M. Kash and D. Kleppner, *Stark structure of the Rydberg states of alkali-metal atoms*, Phys. Rev. A, **20**, 2251–2275 (1979).

[33] *Wikimedia commons*, commons.wikimedia.org.

[34] T. P. Hezel, C. E. Burkhardt, M. Ciocca, L.-W. He and J. J. Leventhal, *Classical view of the properties of Rydberg atoms: Application of the correspondence principle*, American Journal of Physics, **60**, 329–335 (1992).

[35] N. Bohr, *Über die Serienspektra der Elemente*, Z. Phys., **2**, 423–469 (1920).

[36] R. F. Stebbings and F. B. Dunning, editors, *Rydberg States of Atoms and Molecules*, Cambridge University Press (1983).

[37] T. F. Gallagher, *Rydberg Atoms*, Cambridge Monographs on Atomic, Molecular, and Chemical Physics, Cambridge University Press, Cambridge (1994).

[38] C. Guerlin, J. Bernu, S. Deléglise, C. Sayrin, S. Gleyzes, S. Kuhr, M. Brune, J.-M. Raimond and S. Haroche, *Progressive field-state collapse and quantum non-demolition photon counting*, Nature, **448**, 889–893 (2007).

[39] D. Jaksch, J. I. Cirac, P. Zoller, S. L. Rolston, R. Côté and M. D. Lukin, *Fast quantum gates for neutral atoms*, Phys. Rev. Lett., **85**, 2208–2211 (2000).

[40] M. D. Lukin, M. Fleischhauer, R. Cote, L. M. Duan, D. Jaksch, J. I. Cirac and P. Zoller, *Dipole blockade and quantum information processing in mesoscopic atomic ensembles*, Phys. Rev. Lett., **87**, 037901 (2001).

[41] S. N. Bose, *Plancks Gesetz und Lichtquantenhypothese*, Z. Phys., **26**, 178–181 (1924).

[42] A. Einstein, *Quantentheorie des einatomigen idealen Gases*, Sitzungsberichte der Preußischen Akademie der Wissenschaften, pages 261–267 (1924).

[43] P. Kapitza, *Viscosity of liquid helium below the λ-point*, Nature, **141**, 74 (1938).

[44] J. F. Allen and A. D. Misener, *Flow of liquid helium II*, Nature, **141**, 75 (1938).

[45] F. London, *The λ-phenomenon of liquid helium and the Bose-Einstein degeneracy*, Nature, **141**, 643–644 (1938).

[46] L. Tisza, *Transport phenomena in helium II*, Nature, **141**, 913 (1938).

[47] D. G. Henshaw and A. D. B. Woods, *Modes of atomic motions in liquid helium by inelastic scattering of neutrons*, Phys. Rev., **121**, 1266–1274 (1961).

[48] S. Balibar, *Looking back at superfluid helium*, Comptes rendus de la conférence "Bose-Einstein condensation", Institut Henri Poincaré, Paris, Birkhäuser Verlag, Basel (2003).

[49] I. Carusotto, *Sorting superfluidity from Bose-Einstein condensation in atomic gases*, Physics, **3**, 5 (2010).

[50] P. Nozières and D. Pines, *Theory Of Quantum Liquids: Superfluid Bose liquids*, Westview Press (1994).

[51] C. E. Hecht, *The possible superfluid behaviour of hydrogen atom gases and liquids*, Physica, **25**, 1159–1161 (1959).

[52] D. G. Fried, T. C. Killian, L. Willmann, D. Landhuis, S. C. Moss, D. Kleppner and T. J. Greytak, *Bose-Einstein condensation of atomic hydrogen*, Phys. Rev. Lett., **81**, 3811–3814 (1998).

[53] C. J. Pethik and H. Smith, *Bose-Einstein condensation in dilute gases*, Cambridge University Press, Cambridge, 2nd edition (2008).

[54] W. C. Stwalley and L. H. Nosanow, *Possible "new" quantum systems*, Phys. Rev. Lett., **36**, 910–913 (1976).

[55] T. J. Greytak, D. Kleppner, D. G. Fried, T. C. Killian, L. Willmann, D. Landhuis and S. C. Moss, *Bose-Einstein condensation in atomic hydrogen*, Physica B: Condensed Matter, **280**, 20–26 (2000).

[56] S. Chu, *Nobel lecture: The manipulation of neutral particles*, Rev. Mod. Phys., **70**, 685–706 (1998).

[57] C. N. Cohen-Tannoudji, *Nobel lecture: Manipulating atoms with photons*, Rev. Mod. Phys., **70**, 707–719 (1998).

[58] W. D. Phillips, *Nobel lecture: Laser cooling and trapping of neutral atoms*, Rev. Mod. Phys., **70**, 721–741 (1998).

[59] D. E. Pritchard, *Cooling neutral atoms in a magnetic trap for precision spectroscopy*, Phys. Rev. Lett., **51**, 1336–1339 (1983).

[60] W. Petrich, M. H. Anderson, J. R. Ensher and E. A. Cornell, *Stable, tightly confining magnetic trap for evaporative cooling of neutral atoms*, Phys. Rev. Lett., **74**, 3352–3355 (1995).

[61] K. B. Davis, M.-O. Mewes, M. A. Joffe, M. R. Andrews and W. Ketterle, *Evaporative cooling of sodium atoms*, Phys. Rev. Lett., **74**, 5202–5205 (1995).

[62] H. F. Hess, G. P. Kochanski, J. M. Doyle, N. Masuhara, D. Kleppner and T. J. Greytak, *Magnetic trapping of spin-polarized atomic hydrogen*, Phys. Rev. Lett., **59**, 672–675 (1987).

[63] N. Masuhara, J. M. Doyle, J. C. Sandberg, D. Kleppner, T. J. Greytak, H. F. Hess and G. P. Kochanski, *Evaporative cooling of spin-polarized atomic hydrogen*, Phys. Rev. Lett., **61**, 935–938 (1988).

[64] M. R. Andrews, C. G. Townsend, H.-J. Miesner, D. S. Durfee, D. M. Kurn and W. Ketterle, *Observation of interference between two Bose condensates*, Science, **275**, 637–641 (1997).

[65] M.-O. Mewes, M. R. Andrews, D. M. Kurn, D. S. Durfee, C. G. Townsend and W. Ketterle, *Output coupler for Bose-Einstein condensed atoms*, Phys. Rev. Lett., **78**, 582–585 (1997).

[66] I. Bloch, T. W. Hänsch and T. Esslinger, *Atom laser with a cw output coupler*, Phys. Rev. Lett., **82**, 3008–3011 (1999).

[67] E. D. Tannenbaum, *Gravimetric radar: Gravity-based detection of a point-mass moving in a static background*, arXiv:1208.2377 (2012).

[68] L. Pitaevskii and S. Stringari, *Bose-Einstein Condensation*, Oxford University Press, Oxford (2003).

[69] R. W. Wood and R. Fortrat, *The principal series of sodium*, Astrophysical Journal, **43**, 73–80 (1916).

[70] W. Ritz, *Magnetische Atomfelder und Serienspektren*, Annalen der Physik, **330**, 660–696 (1908).

[71] W. M. Hicks, *On the relation between lines of the same spectral series*, Astrophysical Journal, **44**, 229 (1916).

[72] C. Füchtbauer and F. Gössler, *Verschiebung und unsymmetrische Verbreiterung von Absorptionslinien durch Fremdgase*, Naturwissenschaften, **21**, 675–676 (1933).

[73] C. Füchtbauer and F. Gössler, *Verschiebung und unsymmetrische Verbreiterung von Absorptionslinien durch Fremdgase*, Z. Phys., **87**, 89–104 (1934).

[74] C. Füchtbauer, P. Schulz and A. F. Brandt, *Verschiebung von hohen Serienlinien des Natriums und Kaliums durch Fremdgase, Berechnung der Wirkungsquerschnitte von Edelgasen gegen sehr langsame Elektronen*, Z. Phys., **90**, 403–415 (1934).

[75] L. D. Landau and L. M. Lifshitz, *Course of Theoretical Physics, Volume III: Quantum Mechanics (Non-Relativistic Theory)*, Pergamon Press, Oxford, 3rd edition (1977).

[76] Omont, A., *On the theory of collisions of atoms in Rydberg states with neutral particles*, J. Phys. France, **38**, 1343–1359 (1977).

[77] V. Bendkowsky, B. Butscher, J. Nipper, J. B. Balewski, J. P. Shaffer, R. Löw, T. Pfau, W. Li, J. Stanojevic, T. Pohl and J. M. Rost, *Rydberg trimers and excited dimers bound by internal quantum reflection*, Phys. Rev. Lett., **105**, 163201 (2010).

[78] B. Butscher, J. Nipper, J. B. Balewski, L. Kukota, V. Bendkowsky, R. Löw and T. Pfau, *Atom-molecule coherence for ultralong-range Rydberg dimers*, Nature Physics, **9**, 970–974 (2010).

[79] B. Butscher, *A Rydberg Interferometer*, Ph.D. thesis, Universität Stuttgart (2011).

[80] W. Li, T. Pohl, J. M. Rost, S. T. Rittenhouse, H. R. Sadeghpour, J. Nipper, B. Butscher, J. B. Balewski, V. Bendkowsky, R. Löw and T. Pfau, *A homonuclear molecule with a permanent electric dipole moment*, Science, **334**, 1110–1114 (2011).

[81] E. Arimondo and J. Ye, *Ultracold atoms: An exotic quantum object*, Nature Physics, **9**, 694–695 (2013).

[82] K. Singer, J. Stanojevic, M. Weidemüller and R. Côté, *Long-range interactions between alkali Rydberg atom pairs correlated to the ns-ns, np-np and nd-nd asymptotes*, J. Phys. B: At. Mol. Opt. Phys., **38**, S295–S307 (2005).

[83] R. Heidemann, U. Raitzsch, V. Bendkowsky, B. Butscher, R. Löw and T. Pfau, *Rydberg excitation of Bose-Einstein condensates*, Phys. Rev. Lett., **100**, 033601 (2008).

[84] R. Heidemann, *Rydberg excitation of Bose-Einstein condensates: Coherent collective dynamics*, Ph.D. thesis, Universität Stuttgart (2008).

[85] N. Henkel, R. Nath and T. Pohl, *Three-dimensional roton excitations and supersolid formation in Rydberg-excited Bose-Einstein condensates*, Phys. Rev. Lett., **104**, 195302 (2010).

[86] G. Pupillo, A. Micheli, M. Boninsegni, I. Lesanovsky and P. Zoller, *Strongly correlated gases of Rydberg-dressed atoms: Quantum and classical dynamics*, Phys. Rev. Lett., **104**, 223002 (2010).

[87] *Mars climate orbiter mishap investigation board phase I report*, available online at ftp.hq.nasa.gov/pub/pao/reports/1999/MCO_report.pdf.

[88] C. J. Foot, *Atomic Physics*, Oxford Master Series in Atomic, Optical and Laser Physics, Oxford University Press, Cambridge (2005).

[89] M. P. A. Jones, *Atom-light interactions*, available online at massey.dur.ac.uk/mpaj/notes_main.pdf.

[90] R. Loudon, *The Quantum Theory of Light*, Oxford University Press, Cambridge, 3rd edition (2000).

[91] M. Fleischhauer, A. Imamoglu and J. P. Marangos, *Electromagnetically induced transparency: Optics in coherent media*, Rev. Mod. Phys., **77**, 633–673 (2005).

[92] G. Alzetta, A. Gozzini, L. Moi and G. Orriols, *An experimental method for the observation of r.f. transitions and laser beat resonances in oriented Na vapour*, Il Nuovo Cimento B Series 11, **36**, 5–20 (1976).

[93] S. H. Autler and C. H. Townes, *Stark effect in rapidly varying fields*, Phys. Rev., **100**, 703–722 (1955).

[94] D. A. Steck, *Rubidium 87 D line data*, available online at steck.us/alkalidata (revision 2.1.4) (2010), 23 December 2010.

[95] E. Brion, L. H. Pedersen and K. Mølmer, *Adiabatic elimination in a lambda system*, J. Phys. A: Mathematical and Theoretical, **40**, 1033 (2007).

[96] U. Krohn, *Universal scaling and coherence properties of an ultracold Rydberg gas*, Ph.D. thesis, Universität Stuttgart (2008).

[97] D. Comparat and P. Pillet, *Dipole blockade in a cold Rydberg atomic sample*, J. Opt. Soc. Am. B, **27**, A208–A232 (2010).

[98] A. Tauschinsky, C. S. E. van Ditzhuijzen, L. D. Noordam and H. B. v. L. van den Heuvell, *Radio-frequency-driven dipole-dipole interactions in spatially separated volumes*, Phys. Rev. A, **78**, 063409 (2008).

[99] W. R. Anderson, M. P. Robinson, J. D. D. Martin and T. F. Gallagher, *Dephasing of resonant energy transfer in a cold Rydberg gas*, Phys. Rev. A, **65**, 063404 (2002).

[100] K. Afrousheh, P. Bohlouli-Zanjani, D. Vagale, A. Mugford, M. Fedorov and J. D. D. Martin, *Spectroscopic observation of resonant electric dipole-dipole interactions between cold Rydberg atoms*, Phys. Rev. Lett., **93**, 233001 (2004).

[101] K. Afrousheh, P. Bohlouli-Zanjani, J. A. Petrus and J. D. D. Martin, *Determination of the* $^{85}\mathrm{Rb}$ ng*-series quantum defect by electric-field-induced resonant energy transfer between cold Rydberg atoms*, Phys. Rev. A, **74**, 062712 (2006).

[102] T. J. Carroll, S. Sunder and M. W. Noel, *Many-body interactions in a sample of ultracold Rydberg atoms with varying dimensions and densities*, Phys. Rev. A, **73**, 032725 (2006).

[103] I. I. Ryabtsev, D. B. Tretyakov, I. I. Beterov and V. M. Entin, *Observation of the Stark-tuned Förster resonance between two Rydberg atoms*, Phys. Rev. Lett., **104**, 073003 (2010).

[104] A. Reinhard, K. C. Younge, T. C. Liebisch, B. Knuffman, P. R. Berman and G. Raithel, *Double-resonance spectroscopy of interacting Rydberg-atom systems*, Phys. Rev. Lett., **100**, 233201 (2008).

[105] T. J. Carroll, K. Claringbould, A. Goodsell, M. J. Lim and M. W. Noel, *Angular dependence of the dipole-dipole interaction in a nearly one-dimensional sample of Rydberg atoms*, Phys. Rev. Lett., **93**, 153001 (2004).

[106] A. Reinhard, T. C. Liebisch, B. Knuffman and G. Raithel, *Level shifts of rubidium Rydberg states due to binary interactions*, Phys. Rev. A, **75**, 032712 (2007).

[107] M. Saffman and T. G. Walker, *Creating single-atom and single-photon sources from entangled atomic ensembles*, Phys. Rev. A, **66**, 065403 (2002).

[108] Y. O. Dudin and A. Kuzmich, *Strongly interacting Rydberg excitations of a cold atomic gas*, Science, **336**, 887–889 (2012).

[109] T. Peyronel, O. Firstenberg, Q.-Y. Liang, S. Hofferberth, A. V. Gorshkov, T. Pohl, M. D. Lukin and V. Vuletić, *Quantum nonlinear optics with single photons enabled by strongly interacting atoms*, Nature, **488**, 57–60 (2012).

[110] S. Baur, D. Tiarks, G. Rempe and S. Dürr, *Single-photon switch based on Rydberg blockade*, Phys. Rev. Lett., **112**, 073901 (2014).

[111] I. Mourachko, D. Comparat, F. de Tomasi, A. Fioretti, P. Nosbaum, V. M. Akulin and P. Pillet, *Many-body effects in a frozen Rydberg gas*, Phys. Rev. Lett., **80**, 253–256 (1998).

[112] D. Tong, S. M. Farooqi, J. Stanojevic, S. Krishnan, Y. P. Zhang, R. Côté, E. E. Eyler and P. L. Gould, *Local blockade of Rydberg excitation in an ultracold gas*, Phys. Rev. Lett., **93**, 063001 (2004).

[113] V. Vuletic, *Quantum networks: When superatoms talk photons*, Nature Physics, **2**, 801–802 (2006).

[114] E. Urban, T. A. Johnson, T. Henage, L. Isenhower, D. D. Yavuz, T. G. Walker and M. Saffman, *Observation of Rydberg blockade between two atoms*, Nature Physics, **5**, 110–114 (2009).

[115] A. Gaëtan, Y. Miroshnychenko, T. Wilk, A. Chotia, M. Viteau, D. Comparat, P. Pillet, A. Browaeys and P. Grangier, *Observation of collective excitation of two individual atoms in the Rydberg blockade regime*, Nature Physics, **5**, 115–118 (2009).

[116] Y. O. Dudin, L. Li, F. Bariani and A. Kuzmich, *Observation of coherent many-body Rabi oscillations*, Nature Physics, **8**, 790–794 (2012).

[117] M. Ebert, A. Gill, M. Gibbons, X. Zhang, M. Saffman and T. G. Walker, *Atomic Fock state preparation using Rydberg blockade*, Phys. Rev. Lett., **112**, 043602 (2014).

[118] R. Heidemann, U. Raitzsch, V. Bendkowsky, B. Butscher, R. Löw, L. Santos and T. Pfau, *Evidence for coherent collective Rydberg excitation in the strong blockade regime*, Phys. Rev. Lett., **99**, 163601 (2007).

[119] U. Raitzsch, V. Bendkowsky, R. Heidemann, B. Butscher, R. Löw and T. Pfau, *Echo experiments in a strongly interacting Rydberg gas*, Phys. Rev. Lett., **100**, 013002 (2008).

[120] T. G. Walker and M. Saffman, *Zeros of Rydberg-Rydberg Förster interactions*, J. Phys. B: At. Mol. Opt. Phys., **38**, S309 (2005).

[121] T. Pohl and P. R. Berman, *Breaking the dipole blockade: Nearly resonant dipole interactions in few-atom systems*, Phys. Rev. Lett., **102**, 013004 (2009).

[122] H. Deng, G. Weihs, C. Santori, J. Bloch and Y. Yamamoto, *Condensation of semiconductor microcavity exciton polaritons*, Science, **298**, 199–202 (2002).

[123] J. Kasprzak, M. Richard, S. Kundermann, A. Baas, P. Jeambrun, J. M. J. Keeling, F. M. Marchetti, M. H. Szymaska, R. André, J. L. Staehli, V. Savona, P. B. Littlewood, D. B. and L. S. Dang, *Bose-Einstein condensation of exciton polaritons*, Nature, **443**, 409–414 (2006).

[124] S. O. Demokritov, V. E. Demidov, O. Dzyapko, G. A. Melkov, A. A. Serga, B. Hillebrands and A. N. Slavin, *Bose-Einstein condensation of quasi-equilibrium magnons at room temperature under pumping*, Nature, **443**, 4430–433 (2006).

[125] R. Balili, V. Hartwell, D. Snoke, L. Pfeiffer and K. West, *Bose-Einstein condensation of microcavity polaritons in a trap*, Science, **316**, 1007–1010 (2007).

[126] J. D. Plumhof, T. Stöferle, L. Mai, U. Scherf and R. F. Mahrt, *Room-temperature Bose-Einstein condensation of cavity exciton-polaritons in a polymer*, Nature Materials, **13**, 247–252 (2014).

[127] J. Klaers, J. Schmitt, F. Vewinger and M. Weitz, *Bose-Einstein condensation of photons in an optical microcavity*, Nature, **468**, 545–548 (2010).

[128] F. Dalfovo, S. Giorgini, L. P. Pitaevskii and S. Stringari, *Theory of Bose-Einstein condensation in trapped gases*, Rev. Mod. Phys., **71**, 463–512 (1999).

[129] W. Ketterle, D. S. Durfee and D. M. Stamper-Kurn, *Making, probing and understanding Bose-Einstein condensates*, Proceedings of the International School of Physics "Enrico Fermi", Course CXL, IOS Press, Amsterdam (1999).

[130] E. P. Gross, *Structure of a quantized vortex in boson systems*, Il Nuovo Cimento Series 10, **20**, 454–477 (1961).

[131] L. P. Pitaevskii, *Vortex lines in an imperfect Bose gas*, Soviet Physics JETP-USSR, **13** (1961).

[132] R. Löw, *Versatile setup for experiments with rubidium Bose Einstein condensates: From optical lattices to Rydberg matter*, Ph.D. thesis, Universität Stuttgart (2006).

[133] S. Stringari, *Collective excitations of a trapped Bose-condensed gas*, Phys. Rev. Lett., **77**, 2360–2363 (1996).

[134] M.-O. Mewes, M. R. Andrews, N. J. van Druten, D. M. Kurn, D. S. Durfee, C. G. Townsend and W. Ketterle, *Collective excitations of a Bose-Einstein condensate in a magnetic trap*, Phys. Rev. Lett., **77**, 988–991 (1996).

[135] M. Abramowitz and I. A. Stegun, *Handbook of Mathematical Functions: with Formulas, Graphs, and Mathematical Tables*, Dover books on mathematics, Dover, New York (1972).

[136] D. M. Stamper-Kurn, H.-J. Miesner, S. Inouye, M. R. Andrews and W. Ketterle, *Collisionless and hydrodynamic excitations of a Bose-Einstein condensate*, Phys. Rev. Lett., **81**, 500–503 (1998).

[137] D. S. Jin, J. R. Ensher, M. R. Matthews, C. E. Wieman and E. A. Cornell, *Collective excitations of a Bose-Einstein condensate in a dilute gas*, Phys. Rev. Lett., **77**, 420–423 (1996).

[138] D. S. Jin, M. R. Matthews, J. R. Ensher, C. E. Wieman and E. A. Cornell, *Temperature-dependent damping and frequency shifts in collective excitations of a dilute Bose-Einstein condensate*, Phys. Rev. Lett., **78**, 764–767 (1997).

[139] J. B. Balewski, A. T. Krupp, A. Gaj, S. Hofferberth, R. Löw and T. Pfau, *Rydberg dressing: Understanding of collective many-body effects and implications for experiments*, arXiv:1312.6346 (2013).

[140] I. Bouchoule and K. Mølmer, *Spin squeezing of atoms by the dipole interaction in virtually excited Rydberg states*, Phys. Rev. A, **65**, 041803 (2002).

[141] T. Macrì and T. Pohl, *Rydberg dressing of atoms in optical lattices*, Phys. Rev. A, **89**, 011402 (2014).

[142] J. Javanainen, *Noncondensate atoms in a trapped Bose gas*, Phys. Rev. A, **54**, R3722–R3725 (1996).

[143] L. Vestergaard Hau, B. D. Busch, C. Liu, Z. Dutton, M. M. Burns and J. A. Golovchenko, *Near-resonant spatial images of confined Bose-Einstein condensates in a 4-Dee magnetic bottle*, Phys. Rev. A, **58**, R54–R57 (1998).

[144] J. Nipper, J. B. Balewski, A. T. Krupp, B. Butscher, R. Löw and T. Pfau, *Highly resolved measurements of Stark-tuned Förster resonances between Rydberg atoms*, Phys. Rev. Lett., **108**, 113001 (2012).

[145] C. Wittig, *The Landau-Zener formula*, J. Phys. Chem. B, **109**, 8428–8430 (2005).

[146] H. Geiger and E. Marsden, *On a diffuse reflection of the α-particles*, Proceedings of the Royal Society of London. Series A, **82**, 495–500 (1909).

[147] E. Rutherford, *The scattering of α and β particles by matter and the structure of the atom*, Philosophical Magazine Series 6, **21**, 669–688 (1911).

[148] E. D. Bloom, D. H. Coward, H. DeStaebler, J. Drees, G. Miller, L. W. Mo, R. E. Taylor, M. Breidenbach, J. I. Friedman, G. C. Hartmann and H. W. Kendall, *High-energy inelastic $e - p$ scattering at 6° and 10°*, Phys. Rev. Lett., **23**, 930–934 (1969).

[149] M. Breidenbach, J. I. Friedman, H. W. Kendall, E. D. Bloom, D. H. Coward, H. DeStaebler, J. Drees, L. W. Mo and R. E. Taylor, *Observed behavior of highly inelastic electron-proton scattering*, Phys. Rev. Lett., **23**, 935–939 (1969).

[150] C. Ramsauer, *Über den Wirkungsquerschnitt der Gasmoleküle gegenüber langsamen Elektronen*, Annalen der Physik, **369**, 513–540 (1921).

[151] J. S. Townsend and V. A. Bailey, *The motion of electrons in gases*, Philosophical Magazine Series 6, **42**, 873–891 (1921).

[152] L.-V. de Broglie, *Recherches sur la théorie des quanta*, Ann. de Phys., 10^{e} série, t. III (1925), translated by A. F. Kracklauer.

[153] L. P. Presnyakov, *Broadening of highly excited atomic levels in an atmosphere of alkali-metal atoms*, Phys. Rev. A, **2**, 1720–1725 (1970).

[154] V. A. Alekseev and I. I. Sobel'man, *A spectroscopic method for the investigation of elastic scattering of slow electrons*, Sov. Phys. JETP, **22**, 882–888 (1966).

[155] G. F. Chew, *The inelastic scattering of high energy neutrons by deuterons according to the impulse approximation*, Phys. Rev., **80**, 196–202 (1950).

[156] J. E. G. Farina, *On the impulse approximation*, J. Phys. A: Mathematical and General, **11**, 1915–1932 (1978).

[157] C. Bahrim, U. Thumm and I. I. Fabrikant, *^3S_e and ^1S_e scattering lengths for e^- + Rb, Cs and Fr collisions*, J. Phys. B: At. Mol. Opt. Phys., **34**, L195–L201 (2001).

[158] C. Reinsberg, *Zur Theorie der Druckverschiebung der Spektrallinien in der Nähe des Serienendes*, Z. Phys., **93**, 416 (1934).

[159] J. Balewski, *Hochauflösende Photoassoziationsspektroskopie von Rydberg-Dimeren und Trimeren*, Diplomarbeit, Universität Stuttgart (2009).

[160] C. Zipkes, S. Palzer, C. Sias and Köhl, *A trapped single ion inside a Bose-Einstein condensate*, Nature, **464**, 388–391 (2010).

[161] E. Fermi, *Sul moto dei neutroni nelle sostanze idrogenate*, Ric. Scientifica, **7**, 13–52 (1936), translated by G. M. Temmer in Enrico Fermi, *Collected Papers Volume I*, university of Chicago press, 1962.

[162] C. H. Greene, A. S. Dickinson and H. R. Sadeghpour, *Creation of polar and nonpolar ultra-long-range Rydberg molecules*, Phys. Rev. Lett., **85**, 2458–2461 (2000).

[163] J. Holtsmark, *Der Ramsauereffekt im Argon*, Z. Phys., **55**, 447–446 (1929).

[164] J. Holtsmark, *Der Wirkungsquerschnitt des Kryptons für langsame Elektronen*, Z. Phys., **66**, 49–58 (1930).

[165] O. Hinckelmann and L. Spruch, *Low-energy scattering by long-range potentials*, Phys. Rev. A, **3**, 642–648 (1971).

[166] M. I. Chibisov, A. A. Khuskivadze and I. I. Fabrikant, *Energies and dipole moments of long-range molecular Rydberg states*, J. Phys. B: At. Mol. Opt. Phys., **35**, L193 (2002).

[167] C. Bahrim and U. Thumm, *Low-lying* $^3P^o$ *and* $^3S^e$ *states of* Rb^-*,* Cs^-*, and* Fr^-, Phys. Rev. A, **61**, 022722 (2000).

[168] E. L. Hamilton, C. H. Greene and H. R. Sadeghpour, *Shape-resonance-induced long-range molecular Rydberg states*, J. Phys. B: At. Mol. Opt. Phys., **35**, L199 (2002).

[169] C. H. Greene, E. L. Hamilton, H. Crowell, C. Vadla and K. Niemax, *Experimental verification of minima in excited long-range Rydberg states of* Rb_2, Phys. Rev. Lett., **97**, 233002 (2006).

[170] G. Pólya, *Über den zentralen Grenzwertsatz der Wahrscheinlichkeitsrechnung und das Momentenproblem*, Mathematische Zeitschrift, **8**, 171–181 (1920).

[171] J. B. Balewski, A. T. Krupp, A. Gaj, D. Peter, H. P. Büchler, R. Löw, S. Hofferberth and T. Pfau, *Coupling a single electron to a Bose-Einstein condensate*, Nature, **502**, 664–667 (2013).

[172] D. M. Stamper-Kurn, A. P. Chikkatur, A. Görlitz, S. Inouye, S. Gupta, D. E. Pritchard and W. Ketterle, *Excitation of phonons in a Bose-Einstein condensate by light scattering*, Phys. Rev. Lett., **83**, 2876–2879 (1999).

[173] P. Nozières and D. Pines, *Theory Of Quantum Liquids: Normal Fermi liquids*, W. A. Benjamin Inc., New York, Amsterdam (1966).

[174] J. Javanainen and J. Ruostekoski, *Off-resonance light scattering from low-temperature Bose and Fermi gases*, Phys. Rev. A, **52**, 3033–3046 (1995).

[175] R. Graham and D. Walls, *Spectrum of light scattered from a weakly interacting Bose-Einstein condensed gas*, Phys. Rev. Lett., **76**, 1774–1775 (1996).

[176] Y. B. Ovchinnikov, J. H. Müller, M. R. Doery, E. J. D. Vredenbregt, K. Helmerson, S. L. Rolston and W. D. Phillips, *Diffraction of a released Bose-Einstein condensate by a pulsed standing light wave*, Phys. Rev. Lett., **83**, 284–287 (1999).

[177] D. Peter, private communication.

[178] A. Robert, O. Sirjean, A. Browaeys, J. Poupard, S. Nowak, D. Boiron, C. I. Westbrook and A. Aspect, *A Bose-Einstein condensate of metastable atoms*, Science, **292**, 461–464 (2001).

[179] D. Ciampini, M. Anderlini, J. H. Müller, F. Fuso, O. Morsch, J. W. Thomsen and E. Arimondo, *Photoionization of ultracold and Bose-Einstein-condensed Rb atoms*, Phys. Rev. A, **66**, 043409 (2002).

[180] S. Schmid, A. Härter and J. H. Denschlag, *Dynamics of a cold trapped ion in a Bose-Einstein condensate*, Phys. Rev. Lett., **105**, 133202 (2010).

[181] R. Côté, V. Kharchenko and M. D. Lukin, *Mesoscopic molecular ions in Bose-Einstein condensates*, Phys. Rev. Lett., **89**, 093001 (2002).

[182] J. Tempere, W. Casteels, M. K. Oberthaler, S. Knoop, E. Timmermans and J. T. Devreese, *Feynman path-integral treatment of the BEC-impurity polaron*, Phys. Rev. B, **80**, 184504 (2009).

[183] W. Casteels, J. Tempere and J. Devreese, *Polaronic properties of an ion in a Bose-Einstein condensate in the strong-coupling limit*, Journal of Low Temperature Physics, **162**, 266–273 (2011).

[184] R. M. Kalas and D. Blume, *Interaction-induced localization of an impurity in a trapped Bose-Einstein condensate*, Phys. Rev. A, **73**, 043608 (2006).

[185] F. Reif and L. Meyer, *Study of superfluidity in liquid He by ion motion*, Phys. Rev., **119**, 1164–1173 (1960).

[186] G. W. Rayfield and F. Reif, *Evidence for the creation and motion of quantized vortex rings in superfluid helium*, Phys. Rev. Lett., **11**, 305–308 (1963).

[187] D. S. Fisher, B. I. Halperin and P. M. Platzman, *Phonon-ripplon coupling and the two-dimensional electron solid on a liquid-helium surface*, Phys. Rev. Lett., **42**, 798–801 (1979).

[188] A. F. Borghesani, *Ions and electrons in liquid helium*, International series of monographs in physics, Oxford University Press, Oxford (2007).

[189] P. Massignan, C. J. Pethick and H. Smith, *Static properties of positive ions in atomic Bose-Einstein condensates*, Phys. Rev. A, **71**, 023606 (2005).

[190] J. Bardeen, G. Baym and D. Pines, *Interactions between He^3 atoms in dilute solutions of He^3 in superfluid He^4*, Phys. Rev. Lett., **17**, 372–375 (1966).

[191] J. Bardeen, G. Baym and D. Pines, *Effective interaction of He^3 atoms in dilute solutions of He^3 in He^4 at low temperatures*, Phys. Rev., **156**, 207–221 (1967).

[192] R. Löw, *A versatile setup for experiments with rubidium Bose-Einstein condensates: From optical lattices to Rydberg matter*, Ph.D. thesis, Universität Stuttgart (2006).

[193] E. W. Streed, A. P. Chikkatur, T. L. Gustavson, M. Boyd, Y. Torii, D. Schneble, G. K. Campbell, D. E. Pritchard and W. Ketterle, *Large atom number Bose-Einstein condensate machines*, Rev. Sci. Instrum., **77**, 023106 (2006).

[194] M.-O. Mewes, M. R. Andrews, N. J. van Druten, D. M. Kurn, D. S. Durfee and W. Ketterle, *Bose-Einstein condensation in a tightly confining dc magnetic trap*, Phys. Rev. Lett., **77**, 416–419 (1996).

[195] W. D. Phillips and H. Metcalf, *Laser deceleration of an atomic beam*, Phys. Rev. Lett., **48**, 596–599 (1982).

[196] Y. Castin and R. Dum, *Bose-Einstein condensates in time dependent traps*, Phys. Rev. Lett., **77**, 5315–5319 (1996).

[197] V. M. Entin, E. A. Yakshina, D. B. Tretyakov, I. I. Beterov and I. I. Ryabtsev, *Spectroscopy of the three-photon laser excitation of cold rubidium Rydberg atoms in a magneto-optical trap*, JETP, **116**, 721–731 (2013).

[198] R. Löw, H. Weimer, J. Nipper, J. B. Balewski, B. Butscher, H. P. Büchler and T. Pfau, *An experimental and theoretical guide to strongly interacting Rydberg gases*, J. Phys. B: At. Mol. Opt. Phys., **45**, 113001 (2012).

[199] M. Viteau, J. Radogostowicz, M. G. Bason, N. Malossi, D. Ciampini, O. Morsch and E. Arimondo, *Rydberg spectroscopy of a Rb MOT in the presence of applied or ion created electric fields*, Opt. Express, **19**, 6007–6019 (2011).

[200] R. Grimm, M. Weidemüller and Y. B. Ovchinnikov, *Optical dipole traps for neutral atoms*, Adv. At. Mol. Opt. Phys., **42**, 95–170 (2000).

[201] M. Anderlini, E. Courtade, D. Ciampini, J. H. Müller, O. Morsch and E. Arimondo, *Two-photon ionization of cold rubidium atoms*, J. Opt. Soc. Am. B, **21**, 480–485 (2004).

[202] E. Courtade, M. Anderlini, D. Ciampini, J. H. Müller, O. Morsch, E. Arimondo, M. Aymar and E. J. Robinson, *Two-photon ionization of cold rubidium atoms with a near resonant intermediate state*, J. Phys. B: At. Mol. Opt. Phys., **37**, 967–979 (2004).

[203] C. Tresp, *A setup for highly precise excitation and detection of Rydberg atoms*, Master Thesis, Universität Stuttgart (2012).

[204] O. Morsch and M. Oberthaler, *Dynamics of Bose-Einstein condensates in optical lattices*, Rev. Mod. Phys., **78**, 179–215 (2006).

[205] P. L. Gould, G. A. Ruff and D. E. Pritchard, *Diffraction of atoms by light: The near-resonant Kapitza-Dirac effect*, Phys. Rev. Lett., **56**, 827–830 (1986).

[206] M. S. O'Sullivan and B. P. Stoicheff, *Scalar polarizabilities and avoided crossings of high Rydberg states in Rb*, Phys. Rev. A, **31**, 2718–2720 (1985).

[207] M. Greiner, O. Mandel, T. Esslinger, T. W. Hänsch and I. Bloch, *Quantum phase transition from a superfluid to a Mott insulator in a gas of ultracold atoms*, Nature, **415**, 39–44 (2002).

[208] N. Navon, S. Nascimbène, F. Chevy and C. Salomon, *The equation of state of a low-temperature Fermi gas with tunable interactions*, Science, **328**, 729–732 (2010).

[209] J. Simon, W. S. Bakr, R. Ma, M. E. Tai, P. M. Preiss and M. Greiner, *Quantum simulation of antiferromagnetic spin chains in an optical lattice*, Nature, **472**, 307–312 (2011).

[210] B. Yan, S. A. Moses, B. Gadway, J. P. Covey, K. R. A. Hazzard, A. M. Rey, D. S. Jin and J. Ye, *Observation of dipolar spin-exchange interactions with lattice-confined polar molecules*, Nature, **501**, 521–525 (2013).

[211] T. Lahaye, T. Koch, B. Fröhlich, M. Fattori, J. Metz, A. Griesmaier, S. Giovanazzi and T. Pfau, *Strong dipolar effects in a quantum ferrofluid*, Nature, **284**, 672–675 (2007).

[212] K.-K. Ni, S. Ospelkaus, M. H. G. de Miranda, A. Pe'er, B. Neyenhuis, J. J. Zirbel, S. Kotochigova, P. S. Julienne, D. S. Jin and J. Ye, *A high phase-space-density gas of polar molecules*, Science, **322**, 231–235 (2008).

[213] S. Ospelkaus, K.-K. Ni, D. Wang, M. H. G. de Miranda, B. Neyenhuis, G. Quéméner, P. S. Julienne, J. L. Bohn, D. S. Jin and J. Ye, *Quantum-state controlled chemical reactions of ultracold potassium-rubidium molecules*, Science, **327**, 853–857 (2010).

[214] C. Chin, R. Grimm, P. Julienne and E. Tiesinga, *Feshbach resonances in ultracold gases*, Rev. Mod. Phys., **82**, 1225–1286 (2010).

[215] T. Lahaye, C. Menotti, L. Santos, M. Lewenstein and T. Pfau, *The physics of dipolar bosonic quantum gases*, Reports on Progress in Physics, **72**, 126401 (2009).

[216] S. Giovanazzi, A. Görlitz and T. Pfau, *Tuning the dipolar interaction in quantum gases*, Phys. Rev. Lett., **89**, 130401 (2002).

[217] F. Cinti, P. Jain, M. Boninsegni, A. Micheli, P. Zoller and G. Pupillo, *Supersolid droplet crystal in a dipole-blockaded gas*, Phys. Rev. Lett., **105**, 135301 (2010).

[218] F. Maucher, N. Henkel, M. Saffman, W. Królikowski, S. Skupin and T. Pohl, *Rydberg-induced solitons: Three-dimensional self-trapping of matter waves*, Phys. Rev. Lett., **106**, 170401 (2011).

[219] N. Henkel, F. Cinti, P. Jain, G. Pupillo and T. Pohl, *Supersolid vortex crystals in Rydberg-dressed Bose-Einstein condensates*, Phys. Rev. Lett., **108**, 265301 (2012).

[220] S. Möbius, M. Genkin, A. Eisfeld, S. Wüster and J. M. Rost, *Entangling distant atom clouds through Rydberg dressing*, Phys. Rev. A, **87**, 051602 (2013).

[221] M. Mattioli, M. Dalmonte, W. Lechner and G. Pupillo, *Cluster luttinger liquids of Rydberg-dressed atoms in optical lattices*, Phys. Rev. Lett., **111**, 165302 (2013).

[222] F. Cinti, T. Macrì, W. Lechner, G. Pupillo and T. Pohl, *Defect-induced supersolidity with soft-core bosons*, Nature Communications, **5**, 3235 (2014).

[223] B. Butscher, V. Bendkowsky, J. Nipper, J. B. Balewski, L. Kukota, R. Löw, T. Pfau, W. Li, T. Pohl and J. M. Rost, *Lifetimes of ultralong-range Rydberg molecules in vibrational ground and excited states*, J. Phys. B: At. Mol. Opt. Phys., **44**, 184004 (2011).

[224] T. Weber, J. Herbig, M. Mark, H.-C. Nägerl and R. Grimm, *Bose-Einstein condensation of cesium*, Science, **299**, 232–235 (2003).

[225] S. Zhang, F. Robicheaux and M. Saffman, *Magic-wavelength optical traps for Rydberg atoms*, Phys. Rev. A, **84**, 043408 (2011).

[226] C. Reinsberg, *Zur Theorie der Verbreiterung der Spektrallinien einer Serie durch Fremdgase*, Z. Phys., **105**, 460–467 (1937).

[227] W. E. Cooke and T. F. Gallagher, *Effects of blackbody radiation on highly excited atoms*, Phys. Rev. A, **21**, 588–593 (1980).

[228] F. Gounand, *Calculation of radial matrix elements and radiative lifetimes for highly excited states of alkali atoms using the Coulomb approximation*, Journal de Physique, **40**, 457–460 (1979).

[229] I. I. Beterov, I. I. Ryabtsev, D. B. Tretyakov and V. M. Entin, *Quasiclassical calculations of blackbody-radiation-induced depopulation rates and effective lifetimes of Rydberg nS, nP, and nD alkali-metal atoms with $n \leq 80$*, Phys. Rev. A, **79**, 052504 (2009).

[230] A. L. d. Oliveira, M. W. Mancini, V. S. Bagnato and L. G. Marcassa, *Measurement of Rydberg-state lifetimes using cold trapped atoms*, Phys. Rev. A, **65**, 031401 (2002).

[231] V. A. Nascimento, L. L. Caliri, A. L. de Oliveira, V. S. Bagnato and L. G. Marcassa, *Measurement of the lifetimes of S and D states below $n = 31$ using cold Rydberg gas*, Phys. Rev. A, **74**, 054501 (2006).

[232] F. Gounand, M. Hugon, P. R. Fournier and J. Berlande, *Superradiant cascading effects in rubidium Rydberg levels*, J. Phys. B: At. Mol. Opt. Phys., **12**, 547 (1979).

[233] T. Wang, S. F. Yelin, R. Côté, E. E. Eyler, S. M. Farooqi, P. L. Gould, M. Koštrun, D. Tong and D. Vrinceanu, *Superradiance in ultracold Rydberg gases*, Phys. Rev. A, **75**, 033802 (2007).

[234] I. Beigman and V. Lebedev, *Collision theory of Rydberg atoms with neutral and charged particles*, Physics Reports, **250**, 95–328 (1995).

[235] M. P. Robinson, B. L. Tolra, M. W. Noel, T. F. Gallagher and P. Pillet, *Spontaneous evolution of Rydberg atoms into an ultracold plasma*, Phys. Rev. Lett., **85**, 4466–4469 (2000).

[236] M. Robert-de Saint-Vincent, C. S. Hofmann, H. Schempp, G. Günter, S. Whitlock and M. Weidemüller, *Spontaneous avalanche ionization of a strongly blockaded Rydberg gas*, Phys. Rev. Lett., **110**, 045004 (2013).

[237] R. K. Janev and A. A. Mihajlov, *Excitation and deexcitation processes in slow collisions of Rydberg atoms with ground-state parent atoms*, Phys. Rev. A, **20**, 1890–1904 (1979).

[238] E. de Prunelé and J. Pascale, *Theoretical model for the collision of high Rydberg atoms with neutral atoms or molecules*, J. Phys. B: At. Mol. Opt. Phys., **12**, 2511–2528 (1979).

[239] A. P. Hickman, *Relation between low-energy-electron scattering and l-changing collisions of Rydberg atoms*, Phys. Rev. A, **19**, 994–1003 (1979).

[240] A. P. Hickman, *Approximate scaling formula for collisional angular-momentum mixing of Rydberg atoms*, Phys. Rev. A, **23**, 87–94 (1981).

[241] A. Kumar, B. C. Saha, C. A. Weatherford and S. K. Verma, *A systematic study of Hornbeck Molnar ionization involving Rydberg alkali atoms*, Journal of Molecular Structure: THEOCHEM, **487**, 1 – 9 (1999).

[242] L. Barbier, M. T. Djerad and M. Chéret, *Collisional ion-pair formation in an excited alkali-metal vapor*, Phys. Rev. A, **34**, 2710–2718 (1986).

[243] W. L. M Chéret, L Barbier and R. Deloche, *Penning and associative ionisation of highly excited rubidium atoms*, J. Phys. B: At. Mol. Opt. Phys., **15**, 3463–3477 (1982).

[244] R. M. W. van Bijnen, S. Smit, K. A. H. van Leeuwen, E. J. D. Vredenbregt and S. J. J. M. F. Kokkelmans, *Adiabatic formation of Rydberg crystals with chirped laser pulses*, J. Phys. B: At. Mol. Opt. Phys., **44**, 184008 (2011).

[245] A. Härter, A. Krükow, A. Brunner, W. Schnitzler, S. Schmid and J. H. Denschlag, *Single ion as a three-body reaction center in an ultracold atomic gas*, Phys. Rev. Lett., **109**, 123201 (2012).

[246] C. Raman and N. S. Nagendra Nath, *The diffraction of light by high frequency sound waves: Part I.*, Proceedings of the Indian Academy of Sciences - Section A, **2**, 406–412 (1935).

[247] C. Keller, J. Schmiedmayer, A. Zeilinger, T. Nonn, S. Dürr and G. Rempe, *Adiabatic following in standing-wave diffraction of atoms*, Applied Physics B, **69**, 303–309 (1999).

[248] D. V. Averin and K. K. Likharev, *Coulomb blockade of single-electron tunneling, and coherent oscillations in small tunnel junctions*, Journal of Low Temperature Physics, **62**, 345–373 (1986).

[249] J. Neukammer, H. Rinneberg, K. Vietzke, A. König, H. Hieronymus, M. Kohl, H. J. Grabka and G. Wunner, *Spectroscopy of Rydberg atoms at* $n \approx 500$*: Observation of quasi-Landau resonances in low magnetic fields*, Phys. Rev. Lett., **59**, 2947–2950 (1987).

[250] S. Ye, X. Zhang, T. C. Killian, F. B. Dunning, M. Hiller, S. Yoshida, S. Nagele and J. Burgdörfer, *Production of very-high-*n *strontium Rydberg atoms*, Phys. Rev. A, **88**, 043430 (2013).

[251] J. Honer, R. Löw, H. Weimer, T. Pfau and H. P. Büchler, *Artificial atoms can do more than atoms: Deterministic single photon subtraction from arbitrary light fields*, Phys. Rev. Lett., **107**, 093601 (2011).

[252] M. Dakna, T. Anhut, T. Opatrný, L. Knöll and D.-G. Welsch, *Generating Schrödinger-cat-like states by means of conditional measurements on a beam splitter*, Phys. Rev. A, **55**, 3184–3194 (1997).

[253] G. Günter, M. Robert-de Saint-Vincent, H. Schempp, C. S. Hofmann, S. Whitlock and M. Weidemüller, *Interaction enhanced imaging of individual Rydberg atoms in dense gases*, Phys. Rev. Lett., **108**, 013002 (2012).

[254] J. Bardeen, L. N. Cooper and J. R. Schrieffer, *Theory of superconductivity*, Phys. Rev., **108**, 1175–1204 (1957).

[255] A. Lanzara, P. V. Bogdanov, X. J. Zhou, S. A. Kellar, D. L. Feng, E. D. Lu, T. Yoshida, H. Eisaki, A. Fujimori, K. Kishio, J. I. Shimoyama, T. Noda, S. Uchida, Z. Hussain and Z. X. Shen, *Evidence for ubiquitous strong electron-phonon coupling in high-temperature superconductors*, Nature, **412**, 510–514 (2001).

[256] F. Robicheaux and J. V. Hernández, *Many-body wave function in a dipole blockade configuration*, Phys. Rev. A, **72**, 063403 (2005).

[257] T. Pohl, E. Demler and M. D. Lukin, *Dynamical crystallization in the dipole blockade of ultracold atoms*, Phys. Rev. Lett., **104**, 043002 (2010).

[258] B. J. Claessens, M. P. Reijnders, G. Taban, O. J. Luiten and E. J. D. Vredenbregt, *Cold electron and ion beams generated from trapped atoms*, Physics of Plasmas, **14**, 093101 (2007).

[259] M. R. Andrews, M.-O. Mewes, N. J. van Druten, D. S. Durfee, D. M. Kurn and W. Ketterle, *Direct, nondestructive observation of a Bose condensate*, Science, **273**, 84–87 (1996).

[260] M. R. Andrews, D. M. Kurn, H.-J. Miesner, D. S. Durfee, C. G. Townsend, S. Inouye and W. Ketterle, *Propagation of sound in a Bose-Einstein condensate*, Phys. Rev. Lett., **79**, 553–556 (1997).

[261] C. C. Bradley, C. A. Sackett and R. G. Hulet, *Bose-Einstein condensation of lithium: Observation of limited condensate number*, Phys. Rev. Lett., **78**, 985–989 (1997).

[262] F. Kaminski, N. Kampel, M. Steenstrup, A. Griesmaier, E. Polzik and J. Müller, *In-situ dual-port polarization contrast imaging of Faraday rotation in a high optical depth ultracold ^{87}Rb atomic ensemble*, The European Physical Journal D, **66**, 1–8 (2012).

[263] G. E. Marti, R. Olf and D. M. Stamper-Kurn, *A collective excitation interferometer for rotation sensing with a trapped Bose-Einstein condensate*, arXiv:1210.0033 (2012).

[264] J. Itatani, J. Levesque, D. Zeidler, H. Niikura, H. Pepin, J. C. Kieffer, P. B. Corkum and D. M. Villeneuve, *Tomographic imaging of molecular orbitals*, Nature, **432**, 867–871 (2004).

[265] A. S. Stodolna, A. Rouzée, F. Lépine, S. Cohen, F. Robicheaux, A. Gijsbertsen, J. H. Jungmann, C. Bordas and M. J. J. Vrakking, *Hydrogen atoms under magnification: Direct observation of the nodal structure of stark states*, Phys. Rev. Lett., **110**, 213001 (2013).

[266] T. Karpiuk, M. Brewczyk, K. Rzążewski, J. B. Balewski, A. T. Krupp, A. Gaj, R. Löw, S. Hofferberth and T. Pfau, *Detecting and imaging single Rydberg electrons in a Bose-Einstein condensate*, arXiv:1402.6875 (2014).

[267] P. Hannaford, *Condensed-matter physics: Repulsive polarons found*, Nature, **485**, 588–589 (2012).

[268] J. Classen, C.-K. Su and H. J. Maris, *Observation of exploding electron bubbles in liquid helium*, Phys. Rev. Lett., **77**, 2006–2008 (1996).

[269] A. Schirotzek, C.-H. Wu, A. Sommer and M. W. Zwierlein, *Observation of Fermi polarons in a tunable Fermi liquid of ultracold atoms*, Phys. Rev. Lett., **102**, 230402 (2009).

[270] S. Nascimbène, N. Navon, K. J. Jiang, L. Tarruell, M. Teichmann, J. McKeever, F. Chevy and C. Salomon, *Collective oscillations of an imbalanced Fermi gas: Axial compression modes and polaron effective mass*, Phys. Rev. Lett., **103**, 170402 (2009).

[271] C. Kohstall, M. Zaccanti, M. Jag, A. Trenkwalder, P. Massignan, G. M. Bruun, F. Schreck and R. Grimm, *Metastability and coherence of repulsive polarons in a strongly interacting Fermi mixture*, Nature, **485**, 615–618 (2012).

[272] M. Koschorreck, D. Pertot, E. Vogt, B. Fröhlich, M. Feld and M. Köhl, *Attractive and repulsive Fermi polarons in two dimensions*, Nature, **485**, 619–622 (2012).

[273] F. M. Cucchietti and E. Timmermans, *Strong-coupling polarons in dilute gas Bose-Einstein condensates*, Phys. Rev. Lett., **96**, 210401 (2006).

[274] A. Härter, A. Krükow, A. Brunner and J. Hecker Denschlag, *Minimization of ion micromotion using ultracold atomic probes*, Applied Physics Letters, **102**, 221115 (2013).

[275] R. G. Hulet and D. Kleppner, *Rydberg atoms in "circular" states*, Phys. Rev. Lett., **51**, 1430–1433 (1983).

[276] D. A. Anderson, A. Schwarzkopf, R. E. Sapiro and G. Raithel, *Production and trapping of cold circular Rydberg atoms*, Phys. Rev. A, **88**, 031401 (2013).

[277] K. Jachymski, private communication.

[278] Y. Castin, J. I. Cirac and M. Lewenstein, *Reabsorption of light by trapped atoms*, Phys. Rev. Lett., **80**, 5305–5308 (1998).

Danksagung

Zum Abschluss möchte ich an dieser Stelle all jenen danken, die auf unterschiedliche Weise zu den Ergebnissen in dieser Arbeit beigetragen haben.

Ein großer Dank gebührt zunächst Tilman Pfau, nicht nur für die Aufnahme in seine Arbeitsgruppe. Durch seinen fortwährenden Einsatz für das gesamte Institut ist es ihm gelungen, dauerhaft ein sehr produktives Umfeld zu gewährleisten. Seine Intuition und sein wissenschaftlicher Überblick haben wesentlich zu den erzielten Erfolgen beigetragen.

Unmittelbar anschließend möchte ich dem gesamten, mittlerweile stark angewachsenen, kalten Rydberg-Team danken, angefangen bei meinen direkten Vorgängern, Vera, Björn und Johannes. Sie haben das Experiment zu den ersten großen Erfolgen geführt und mit der Untersuchung der weitausgedehnten Rydberg-Moleküle die Grundlage für meine Arbeit gelegt. Vera hat mir sehr viele Dinge geduldig erklärt und von Björn habe ich unzählige Tipps und Tricks im Labor und am PC bekommen. Mit Johannes durfte ich eine besonders spannende, sehr produktive und einfach gute Zeit am Experiment verbringen. Unsere gemeinsamen Abende im Labor werde ich nicht vergessen.

Großer Dank gebührt auch dem derzeitigen Team; Alexander für die Unterstützung auch in weniger erfolgreichen Zeiten und Anita für die Entscheidung, am Tiefpunkt der Erfolgskurve das Team zu verstärken und für die Hilfe bei den Anstrengungen das Experiment wieder nach vorne zu bringen. Ich hoffe, dass zu den aktuellen, viel versprechenden Daten noch viele weitere gute Ergebnisse kommen werden. Viel Erfolg wünsche ich auch Philipp, der erst kürzlich zum Team gestoßen ist und Teile dieser Arbeit korrekturgelesen hat.

Danke auch an Robert für den Aufbau der Kammer, sowie die Hilfe mit der alten Technik und Sebastian für die intensiven Diskussionen, die schlussendlich immer zu guten Resultaten geführt haben.

Für die wertvolle Theorieunterstützung und erfolgreiche Zusammenarbeit möchte ich ganz herzlich David und Hans Peter Büchler danken.

Den Teams an den beiden neuen kalten Rydberg-Experimenten bin ich insbesondere wegen der leihweisen Überlassung eines Rydberg-Lasersystems zu Dank verpflichtet. Explizit genannt sei hier Christoph, der dieses Lasersystem aufgebaut hat und bei der Faserverbindung der beiden Labore mitgewirkt hat. Michael war mir zudem immer ein kompetenter Ansprechpartner in Sachen Elektronik. Ich hoffe, dass sich die vielen Ideen, die wir nicht realisieren konnten, an der neuen Apparatur als umsetzbar erweisen und auch dort den verdienten Erfolg bringen.

Schließlich möchte ich den vielen hilfsbereiten Kollegen im gesamten Institut danken, insbesondere unserer geduldigen Administration, Astrid, Bea, den beiden Karins, Nadine und Oli.

Prof. Wrachtrup danke ich sowohl für die Übernahme des Mitberichts als auch für den noch genau einen freien Prüfungstermin und Prof. Büchler für den Prüfungsvorsitz.

Sehr dankbar bin ich schließlich Frederike und meiner Familie für deren Rückhalt und Unterstützung, insbesondere in den letzten fünf Jahren.

„The exceptionally precise control of the motional and internal degrees of freedom of ultracold atoms and ions has enabled the engineering and manipulation of new and unusual quantum states of matter. […]

Jonathan Balewski and colleagues used laser light to excite a single atom in an atomic rubidium condensate to its Rydberg state - a highly excited state with a very large principal quantum number, n=110-200. They created and investigated an unusual quantum object: a single electron whose orbit encloses the entire condensate. This system exhibits strong coupling between the electron and the collective mechanical motion of the condensate. The electron orbit encircles tens of thousands of atomic nuclei, in contrast to an exotic atom, where an electron orbits around a nucleus with at least one nucleon replaced by another unstable particle. […]

The results reported by Balewski and colleagues will deliver new opportunities in quantum optics and quantum information science. The strong interactions of the Rydberg atoms provide robustness and speed for these quantum technologies. Strong coupling of the electron to the condensate phonons could be used to produce phonon-mediated interactions between several electrons within the condensate, and may also act as an exotic qubit or offer a testing ground for strongly correlated electron physics.“

Ennio Arimondo and Jun Ye,
Nature Physics 9, 694 (2013)